ROLES OF LARGE LOOPS IN CATALYTIC VERSATILITY OF CATALASE-PEROXIDASES: SIGNIFICANCE OF PERIPHERAL STRUCTURES IN IMPROVISING ENZYME FUNCTIONS

by

Shalley Nidhish Kudalkar

A dissertation submitted to the Graduate Faculty of
Auburn University
in partial fulfillment of the
requirements for the Degree of
Doctor of Philosophy

Auburn, Alabama
May 7, 2012

Approved by

Douglas C. Goodwin, Chair, Associate Professor of Chemistry and Biochemistry
Holly R. Ellis, Associate Professor of Chemistry and Biochemistry
Christian R. Goldsmith, Assistant Professor of Chemistry and Biochemistry
Christopher J. Easley, Assistant Professor of Chemistry and Biochemistry

Abstract

Catalase-peroxidases are bifunctional enzymes that catalyze the removal of hydrogen peroxide by two distinct pathways (catalase and peroxidase). They are central to antibiotic resistance in *Mycobacterium tuberculosis* and may be virulence factors in several dangerous human pathogens. These enzymes also hold much promise for engineering new enzymes to combat long-standing problems (e.g., environmental contamination by toxic pollutants). Currently, understanding of catalase-peroxidase structure and function is lacking to facilitate new drug development and enzyme engineering. The purpose of the research described in this dissertation is to understand the molecular basis for the unique catalytic abilities of catalase-peroxidases to fully capitalize on their potential. The versatile catalytic abilities of these enzymes arise from an active site that is normally restricted to one activity (i.e., peroxidase). This is facilitated by three structures which are quite distant from the active site: a C-terminal domain and two large loops (LL1 and LL2). Given that catalase-peroxidases have two large loops absent from their fellow peroxidases, it is reasonable to suggest that these loops may serve to fine tune the active site for bifunctionality. Indeed, deletion of any of these structures has a substantial impact on catalase-peroxidase active site environment and catalytic function (e.g., selective loss of catalase activity). The main emphasis of this dissertation is to explore the roles of these two

large loops i) by identifying additional roles of LL1 in the unique catalytic properties of KatGs, and ii) by targeting the intersubunit interactions between LL2 apex and C-terminal domain. Site directed and deletion variants targeting LL2 apex and its length and various portions of LL1 (Y226F KatG, KatG$^{\Delta 209-228}$, KatG$^{\Delta 200-214}$, KatG$^{\Delta LL1}$) were generated and investigated by heme environmental spectroscopy, steady-state and transient-state kinetic techniques. For LL1, all the variants including tyrosine showed a complete loss of catalase activity but the deletion variants showed substantial increase in peroxidase activity compared to wild type (wt KatG) and Y226F KatG. This increase in peroxidase activity was traceable to rapid reduction of high oxidation state intermediates by exogenous electron donors, and coincident prevention of enzyme inactivation by peroxides. The steady-state kinetic parameters of KatG$^{\Delta 200-214}$ were comparable to wt KatG. In case of LL2, deletion variants showed near to complete loss of catalase activity with variable effects on peroxidase activity. The peroxidase activity with respect to H_2O_2 showed a substantial rate of turnover (even in excess of wt KatG) at sufficiently high H_2O_2 concentrations, along with two orders of magnitude lower apparent second order rate constants suggesting deficiency in the correct association of H_2O_2 in the active site leading towards it reduction to H_2O. However, peroxidase kinetic parameters with respect to ABTS suggested that electron transfer to the heme by exogenous electron donors is unaffected and in some cases even enhanced. Concomitant with the shift in activity was a change in heme coordination from predominantly hexacoordinate high-spin to predominantly pentacoordinate high-spin. In contrast to deletion variants, the apex substitution variants of LL2 showed similar spectroscopic characteristics compared to wt KatG with little to no effect on the catalytic activities. The results of these studies emphasize the fact that both large loops despite of their peripheral locations

serve to fine-tune the active site for its bifunctionality by acting as a gate keeper (LL1) to limit the typical peroxidase activity in favor of catalase activity and by maintaining the unique interaction occurring at 30Å from the active site between LL2 and C-terminal domain.

Acknowledgments

I would like to express my deepest gratitude to my advisor, Dr. Douglas Goodwin, for his excellent guidance, caring, patience, and providing me with an excellent atmosphere. His continual support and guidance throughout my research work made this dissertation a success.

I am thankful to my committee members Dr. Holly Ellis, Dr. Christian Goldsmith, and Dr. Christopher Easley, for their support and suggestions. I am also thankful to Dr. Angela Calderon for agreeing to take on the role of the university reader. I am grateful to Dr. Duin for all his help and advice with EPR.

I would also like to extend my sincere thanks to Dr. Robert Moore, Elizabeth Ndonsta, Yu Wang, Haijun Duan, and Mick for their valuable suggestions and co-operation.

My sincere thanks go to my best friend, Vinod, for his support and advice. I would like to thank my sisters- Meenakshi and Triveni, and brother- Paritosh for all their love and encouragement. I dedicate this work to my mother for her affection and prayers, to my daughter Nishqa, and to my husband, Nidhish, whose unconditional love and motivation made this research possible.

Table of Contents

List of Figures

List of Tables

Chapter One: Literature Review

Enzymes are exceptional catalysts that are capable of astounding rate enhancement with great specificity under mild conditions. They catalyze reactions in enzymatic pathways with excellent chemo-, regio-, and stereo-selectivities. Naturally, there is substantial interest in harnessing these capabilities for reactions which lack suitable catalysts. Thus, there is a considerable interest in engineering new enzymes for novel applications demanded by, among others, the agricultural, food and pharmaceutical industries and also as a tool for molecular biology. The problems which could be addressed with appropriately engineered enzymes are potentially global in scope (e.g., like contamination of the environment with unmanageable toxic waste, etc.), opening the possibility for substantial impact for humankind.

Although the potential benefits to be achieved from enzyme engineering are substantial, the barriers to successful enzyme engineering are equally formidable. Primary among these obstacles is a lack of understanding of a highly complex structure-function relationship. Unlocking the secrets of this complex relationship can be approached in a number of ways, but it would seem that nature has mastered the art of manipulating structure to produce a broad panel of highly functional catalysts. Thus, a potentially fruitful strategy for enzyme engineering may be drawn from examples of the process accomplished naturally in biological systems.

Here it is important to point out that successful enzyme engineering must depend not only on a coherent strategy, but also on a workable methodology. We would argue that at least in part, the failure of efforts in enzyme engineering have been due to flawed strategy. In other words, these approaches have represented great methodology but faulty strategy. Clearly, either one on its own is insufficient. If methods are applied without the right strategies, the fine balance which nature has achieved in enzyme engineering can be disrupted and consequently give rise to proteins that are unstable, cannot fold properly, and have no catalytic activity no matter how elegant the methodology may be. On the other hand, if the strategy is applied without appropriate methods success cannot be achieved on any reasonable time scale. Here we would part with nature as the methods employed there take far too long.

Taken together, our approach is to use nature to inform strategy, but employ methodology provided by molecular biology to allow for pursuit of these strategies at a reasonable rate. A fundamental thread of the research presented in this dissertation is that catalase-peroxidases (also known to the field as KatG) represent an example where very clear elements of an enzyme engineering strategy can be discerned. Catalase-peroxidases are heme containing enzymes. These enzymes catalyze the removal of hydrogen peroxide by two distinct pathways: catalase and peroxidase. Unique structural features enable KatGs to carry out this bifunctionality using a single active site. The purpose of this literature review is to address questions like: What can be learned about the development of the catalytic properties of KatG? What does this elucidate in terms of a strategic approach that might be pursued? How might the function of KatG be manipulated?

This chapter will first establish how proteins containing the heme cofactor are rich resources for exploring and understanding the structure-function relationship. In order to understand this structure-function relationship various structural levels of heme proteins will be discussed in terms of their impact on the functions of these proteins. Generally, four structural levels dictate catalytic activity of heme proteins: the structure of heme cofactor itself, the characteristics of protein derived heme ligands, the non-ligand heme environment and the global structure of the protein. This chapter will detail the work done so far to understand these structural levels and will present some important examples which signify their role in heme protein functions. In doing so, it will become evident that voluminous data are present in literature, but they primarily support the first three structural levels with little dedicated to the fourth level (i.e., the contribution of the global structure of these proteins has received little attention). For this reason, various heme enzymes will be discussed with particular attention to their structure–function relationship. It is here that the importance of global structure of the protein (which includes unique structures peripheral and distant from the active site) in manipulating the catalytic activity of protein surfaces will be addressed. Through the examples provided in this chapter, the rationale for this research on roles of important peripheral structures in maintaining the active site architecture and consequently the catalytic versatility of catalase-peroxidases will come into focus.

1.1. Heme and Heme Proteins

Heme is not only easily monitored by several spectroscopic techniques, but it is also highly versatile and widely used in nature as a cofactor. It is a prosthetic group that binds iron

within a tetrapyrrole, and although there is more than one type of heme used in biology, the diversity of function heme fills corresponds much more to the diversity of protein scaffolds which surround it rather than differences in covalent structure of the heme itself. Thus, heme is a cofactor used in oxygen storage and transport, substrate oxidation, ligand sensing, electron transfer, and other processes (*1*). As with any protein, heme-dependent proteins are usually classified into different superfamilies based on their structural and /or functional similarities. These superfamilies might have a primary function (oxygen carrier, substrate oxidation etc.), but a considerable functional overlap can be seen among them.

The heme structure consists of a tetrapyrrole ring system complexed with iron. The four pyrrole rings are linked by methylene bridges giving rise to highly conjugated and roughly planar porphyrin. Usually, the heme iron is octahedrally coordinated by six heteroatoms. The four equatorial ligands are nitrogens from each of pyrrole and the remaining two axial ligands lie above and below the plane of the heme. Heme proteins collectively perform three main functions: catalysis of redox reactions using peroxides or oxygen plus externally supplied electrons (e.g., cytochrome P450, peroxidases, catalases, and catalase–peroxidases), storage and/or transport (e.g., myoglobin, and hemoglobin) and, electron transfer (e.g., cytochrome c) (*2*). The ability of this simple metalloorganic compound to perform diverse functions is dictated by four structural levels: heme structure itself, identity of protein derived heme-ligands, the non-ligand protein environment and, finally the global structure of the protein.

Although many forms of heme exist in nature, the three most abundant forms of heme are heme *a*, heme *b*, and heme *c* (Figure 1.1). Heme *a* and heme *b* differ at R_1 and R_3 positions. In

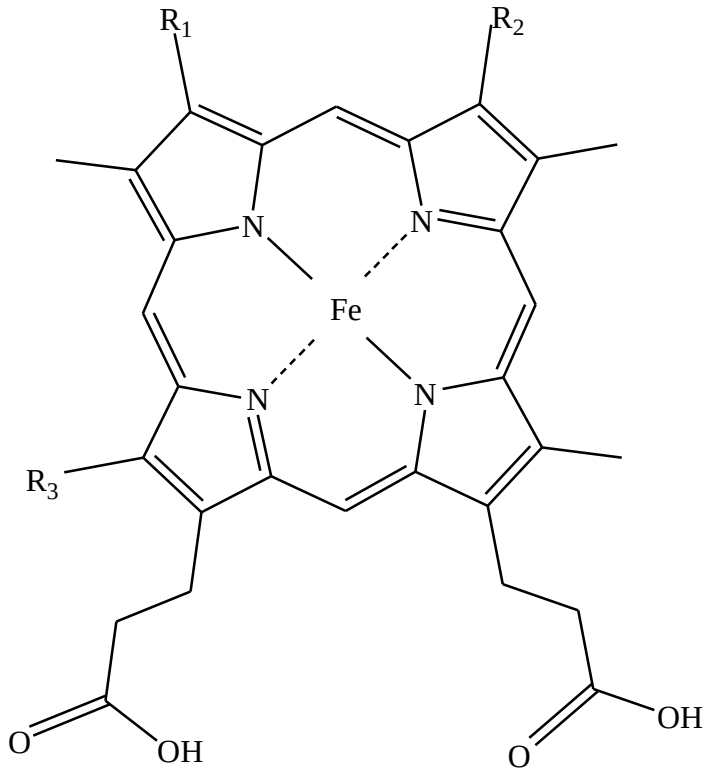

	Heme *a*	**Heme *b***	**Heme *c***
Chemical formula	$C_{49}H_{56}O_6N_4Fe$	$C_{34}H_{32}O_4N_4Fe$	$C_{34}H_{36}O_4N_4S_2Fe$
Functional group at R_1	hydroxyehtylfarnesyl	-CH=CH_2	-CH-CH_3-SH
Functional group at R_2	-CH=CH_2	-CH=CH_2	-CH-CH_3-SH
Functional group at R_3	-CH=O	-CH_3	-CH_3

Figure 1.1: Heme. Structures were taken from the PubChem Public Chemical Database using the CID numbers: heme *a* - 5288529, heme *b* - 4973, heme c – *2*5202875 (*3*)

heme *b* they are vinyl and methyl groups, respectively, whereas hydroxyethylfarnesyl side chain occupies R_1 and formyl group is present at R_3 in heme *a*. These differences make heme *a* more hydrophobic and electron-withdrawing, increasing its reduction potential. For this reason, heme *a* is found in mammalian cytochrome c oxidases, enzymes present at the end of electron transport chain (*4*). Heme *c* differs from heme *b* by becoming covalently attached to the protein through two thioether linkages at R_1 and R_2. Due to these thioether bonds proteins containing heme *c* (e.g., cytochrome *c*) are chemically and thermally stable (*5*). The covalent linkage is suggested to provide structural support to the proteins as there is not much effect on the reduction potential of the proteins containing heme *c (6)*. One less commonly used form of heme exists in nature as heme *d*, it is found in *Penicillium vitale* catalase and *E.coli* catalase (*7, 8*).

Heme b (protoporphyrin IX) is the most widely used in nature and is the prosthetic group found in all the heme enzymes discussed in this chapter. This kind of heme is found in hemoglobins, myoglobins, cytochrome P450s, and heme-based sensor proteins. Figure 1.2 shows various heme *b* ligand environments. For the heme proteins that do not directly bind an exogenous ligand, the axial ligands to the heme iron are supplied by protein itself. For example, in cytochrome b_{550} has two histidine ligands (*9*). By contrast, in heme proteins which do bind oxygen, hydrogen peroxide, or other small exogenous ligands, only one axial site (the so called "proximal side") is occupied by a protein-based ligand. The so-called distal side of the heme is either unoccupied or a weakly associated water molecule. Histidine is widely used as the proximal ligand in heme proteins (e.g., hemoglobin, myoglobin) and heme peroxidases. Exceptions include cysteinate sulfur in P450s (*10*) and haloperoxidases (*11*), and phenolate oxygen of a tyrosine residue in heme catalases (*12*). Whether ligated on the proximal side by

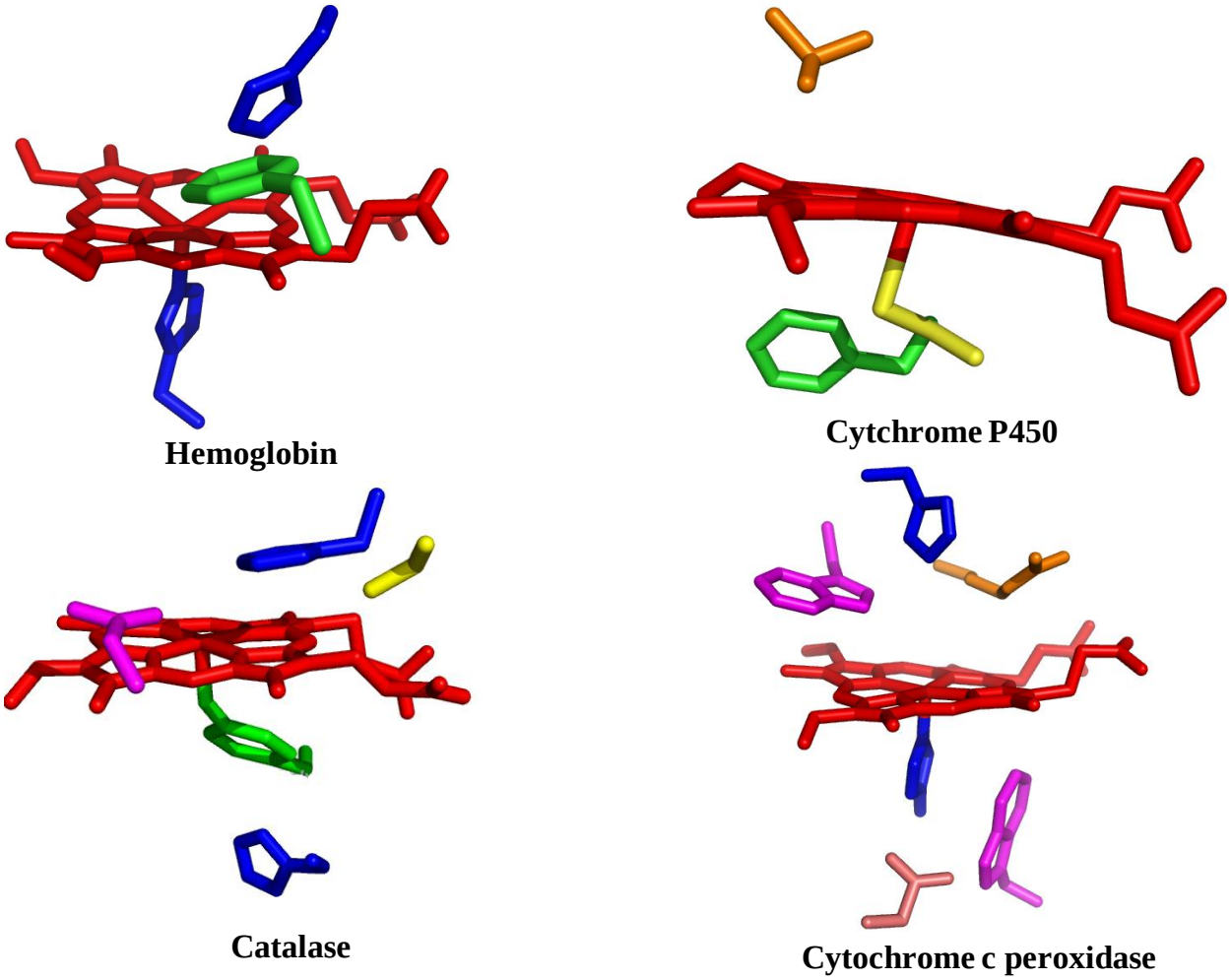

Figure 1.2: Various heme b ligand environments. Propionate groups of all structures are oriented towards right**.** Amino-acids color codes are as follows: Histidine - Blue, Phenylalanine/ Tyrosine – Green, Tryptophan – Magenta, Aspartate – Pink, Arginine – Dark yellow, Threonine – Orange, and Cystiene/Serine-yellow.

histidine, cysteine, or tyrosine, the distal side of the heme invariably forms part of catalytic site. Depending on the enzyme's status in the catalytic cycle, the distal side can either be unoccupied or occupied, and if occupied is very often by an oxygen atom derived from H_2O, O_2 or peroxide.

The non-ligand heme environment also influences the immediate active center environment. This includes the amino-acid residues not directly bound to the heme. These residues modulate the activity by maintaining the polarity of distal and proximal pocket of heme. They also regulate the accessibility of the substrate to heme center and heme edge by optimizing the access channel for the particular substrate. This non-ligand heme environment can provide new function to a protein. For example, haloperoxidases and cytochrome P450s both have cysteine as the proximal ligand but both catalyze very different reactions (*13*). Haloperoxidases mediate the oxidation of halides by hydrogen peroxide whereas cytochrome P450 catalyzes a monooxygenation reaction (*13*, *14*). This difference is due to the way substrate channel is located in both the enzyme. In P450s, the edge of the heme is buried, whereas the heme iron center is accessible to the substrates making oxo-transfer a dominant reaction. In contrast, the heme edge of chloroperoxidases is more accessible allowing chlorination of number of aliphatic substrates (*11*).

Up to now, it has been shown that the nature of heme, protein derived heme ligands, and non-ligand heme environment modulate the function of heme enzymes. However, the global structure of the proteins, comprising of the unique structures peripheral and distant to the active site, is simultaneously a crucial part of heme enzyme function and the least understood. The lack of exploration of this fourth structural level can be attributed to two main reasons. First, it is difficult to specifically identify the important peripheral structures to target and how to address

them. Secondly, it's been thought that this structural level is not nearly as important as the active site itself. However, years of synthesis and characterization of inorganic model complexes demonstrate, if nothing else that the whole protein is important. Also, nature and our own experience show that true *change of* function may not necessarily result from active site manipulation. Here, bifunctional catalase-peroxidase (KatG) is an ideal model to identify the unique distant structural features and help to explore their role in maintaining its bifunctionality. Also, it points out that nature regards and addresses such structures in devising new catalysts.

In terms of catalase-peroxidase function, there are three superfamilies that are particularly relevant: typical catalases, non-animal peroxidases, and animal peroxidases. In this chapter, these superfamilies will be discussed to better understand how the entire protein structure influences the heme environment to promote one function over the other.

1.2. Catalases

Catalases are ubiquitous enzymes. All aerobic organisms, whether prokaryotic or eukaryotic and even aero-tolerant anaerobes (e.g., the archeal *Methanosarcina barkeri*) (*15*) have at least one enzyme with *catalatic* activity. Catalases are organized into three main groups based on the variety of subunit sizes, different heme prosthetic groups, and the variety of sequence groups: the "classic" monofunctional heme-containing enzymes, the catalase-peroxidases, and the non-heme or Mn-containing catalases. In addition, a diverse group of heme-containing proteins, such as chloroperoxidase, plant peroxidases, and myoglobin, exhibit low levels of

catalatic activity. This can be attributable to the presence of heme which alone can exhibit a very low catalase activity (*16*).

Catalases catalyze decomposition of hydrogen peroxide (H_2O_2) to water and oxygen and the overall reaction can be simply represented as in reaction 1.1.

$$2H_2O_2 \longrightarrow 2H_2O + O_2 \qquad \textbf{(1.1)}$$

Catalases from all three groups follow essentially a two-step process for the decomposition of H_2O_2: H_2O_2 reduction followed by H_2O_2 oxidation. There are two distinct stages in the reaction pathway for the heme and non-heme catalases, however the mechanism involved in these two stages differ considerably for classic catalases versus that for non-heme catalases. This section will limit itself to a consideration of heme containing proteins with catalatic activity. In heme catalases, the first stage involves oxidation of heme iron using H_2O_2 as substrate in order to form a ferryl porphyrin π cation radical intermediate (compound I) and H_2O (*16*). In the second stage, compound I acts as two–electron oxidant, producing O_2 and regenerating the ferric form the enzyme (Figure 1.3). The catalase activity is typically monitored by either one of two common methods: monitoring the dioxygen evolved during catalysis using a Clark electrode (*17*) or monitoring the decrease in H_2O_2 by decrease in absorbance at 240 nm (*18*).

In eukaryotes, catalases are present in the peroxisomes, where H_2O_2 is generated via oxidative processes (e.g., β-oxidation of long chain fatty acids) (*19*). H_2O_2 is capable of initiating cellular damage by direct reaction with certain biomolecular components, but more often reactive species derived from H_2O_2 (e.g., hydroxyl radical) are the true damage-causing agent. Thus, catalases remove H_2O_2 and prevent the cells from encountering harmful reactive species.

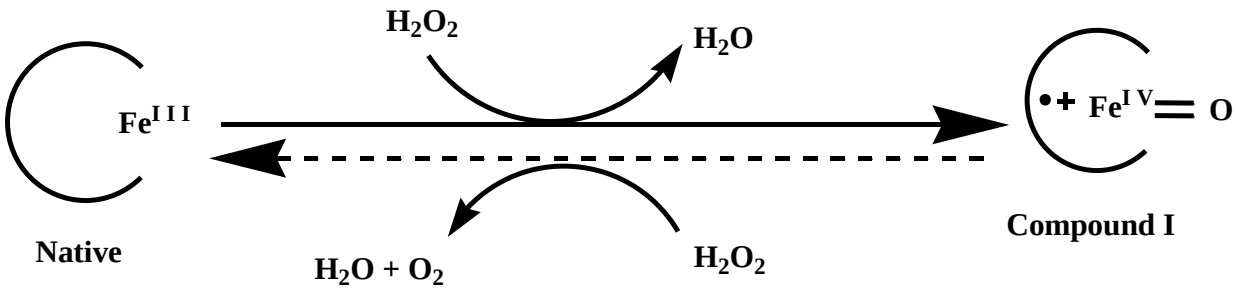

Figure 1.3: Catalytic cycle of catalases

More than 300 catalase sequences have been reported to date, and comparisons of these sequences reveal a strong sequence homology for about 400 amino acid residues (*20, 21*). Out of these, 12 residues are fully conserved and seven other residues differ in only one or two of the sequences. The distal histidine is one of the fully conserved residues as are the active site asparagine and the fifth ligand to the heme iron (i.e., the proximal tyrosine). Despite the sequence similarities catalases are divided into well-defined subgroups based on the polypeptide length: large subunit catalases (>700 residues per subunit) and small subunit catalases (<500 residues per subunit). Hyderoperoxidase II (HPII) from *E.coli* is the largest of the heme catalases with 753 residues per subunit. A crystal structure has been solved for the enzyme, and it is used here as a representative for all catalase structures (*20*). Beside size, the small and large subunit catalases have two other characteristic differences. The first is that small subunit catalases contain heme *b*, which is modified to heme *d* in large subunit catalases (Figure 1.4), This heme is an oxidized protoporphyrin IX and is produced through the auto catalytic modification of the pyrrole ring opposite to the essential histidine producing a *cis*-hydroxychlorin γ-spirolactone. The second difference is that large subunit catalases carry an extra C-terminal domain with a flavodoxin topology whereas small subunit catalases can bind NADPH cofactor despite the absence of a nucleotide binding motif (*22, 23*).

Monofunctional catalases are homotetramers, 200-340 kDa in size with four prosthetic heme groups. Each subunit contains four distinct structural regions: an amino-terminal domain, an anti-parallel eight-stranded β-barrel domain, the domain connection and the α-helical domain (Figure 1.5). In large subunit catalases, there is a fifth domain at the C-terminal end of the

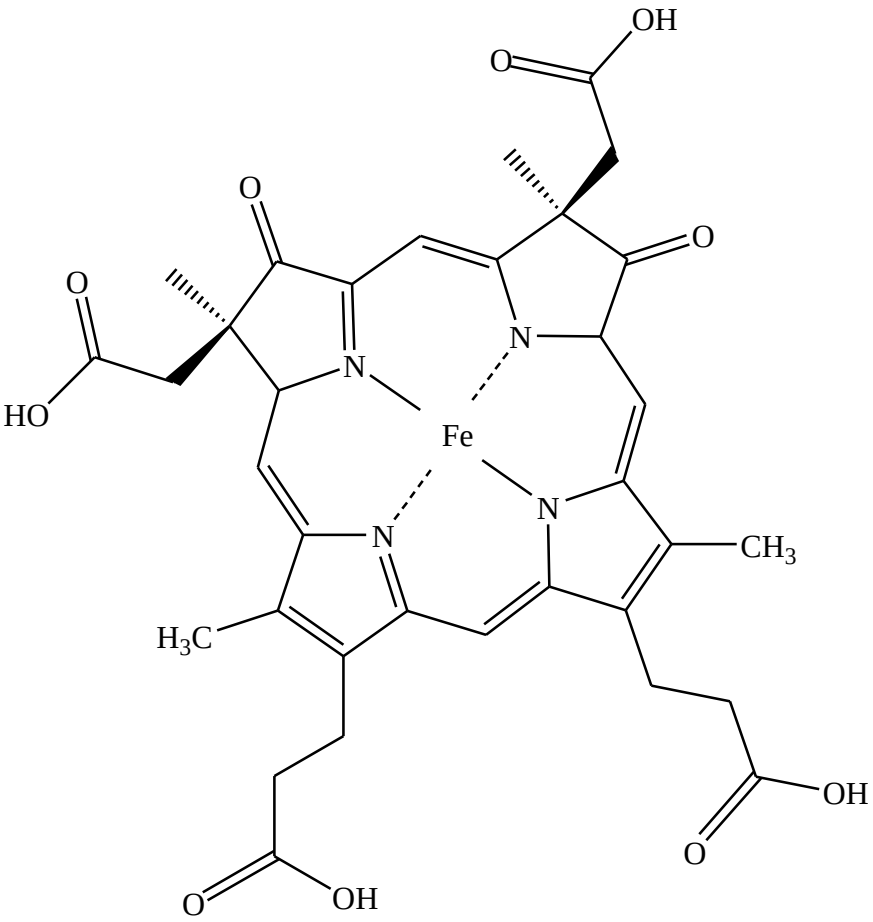

Figure 1.4: Structure of heme d. Structure was taken from the PubChem Public Chemical Database using the CID number: heme *d* - 3581(*3*)

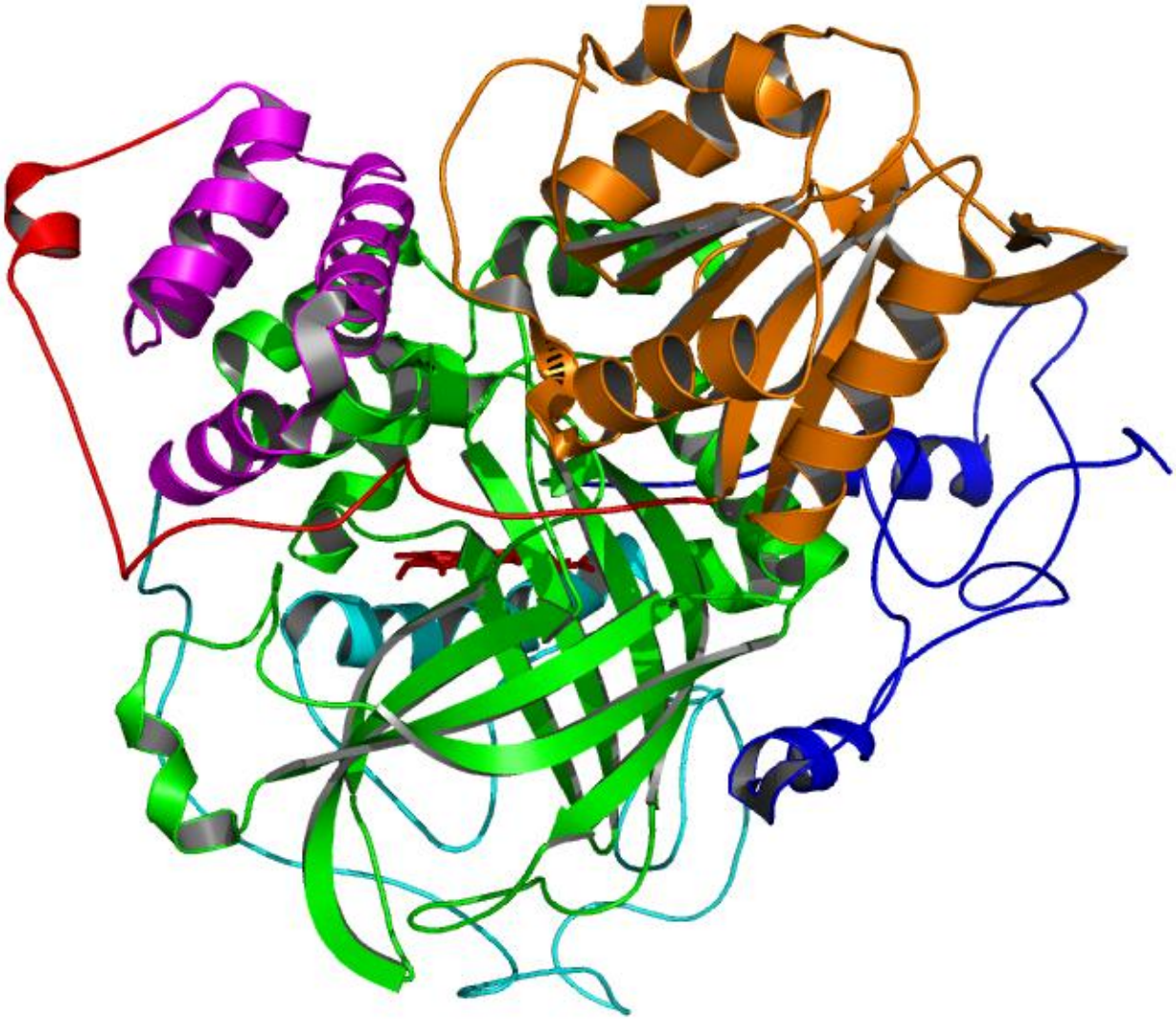

Figure 1.5: Global structure of catalase. Structure was taken from PDB accession domain 1GGE. Different structures are color coded as follows: Amino-terminal arm – Blue, 8-stranded β-parallel domain – Green, Wrapping domain – Cyan, α-helical domain – Magenta, Carboxy-terminal domain – Orange, and Extended hinge joining helical and carboxy domains – Red.

protein. This accounts at least in part for the greater molecular weight of the subunits in these enzymes (*7, 24-29*).

The N-terminal domain forms a hairpin structure and is involved in intersubunit interactions, the extent of which increases with the length of this amino-terminal- domain (*24*). This domain is buried between adjacent subunits and may serve to stabilize the homotetramers (*25*). The essential distal histidine is situated in C-terminus of the N-terminal domain. The position and reactivity of distal histidine is controlled by a hydrogen bond network formed between highly conserved residues from the β-barrel domain. The anti-parallel β-barrel domain is the largest domain, and it is a highly conserved part of the molecule. This domain consists of an eight-stranded antiparallel β-barrel with six α–helical insertions in the turns between the strands. The first half of the domain contains amino-acid residues which define the distal side of the heme pocket, and in the small subunit enzymes, the second half continues to the NADPH binding pocket.

The wrapping domain is an extended region of about 110 residues that connects the globular β-barrel and α-helical domains. Even though the domain has a low content of secondary structures, it contains α -helix with the amino-acid residues which define the heme proximal side including the essential tyrosine. This domain participates in extensive intersubunit interactions particularly with residues from the amino-terminal-domain region from another subunit.

The α-helical domain contains four contiguous α-helices and is not highly conserved. This domain binds NADPH. An extra C-terminal domain of about 150 residues has been seen in

in two large catalase, PVC (*7*) and HPII (*26*), structures. This domain contains high content of secondary structure elements organized with a 'flavodoxin-like' topology.

Both the position of the heme and its environment are strongly conserved among catalases, including four amino acid residues which are considered essential for catalysis: the proximal tyrosine ligand, and histidine, asparagine, and serine all on the distal side of the heme (Figure 1.6). The serine is hydrogen bonded to N^{δ} of the histidine and is essential for maintaining the proper orientation and nucleophilic character of the immidazole, and thus stabilizes the distal heme pocket structure. The distal histidine is parallel to the plane of the heme and oriented above pyrrole ring. This unusual orientation seems to favor more extensive $\pi - \pi$ interactions between histidine and porphyrin presumably lowering the reactivity of compound I with reducing substrate (*27*). Conversely, in all other heme-containing proteins with a distal histidine, it is perpendicular to the plane of the heme causing increased reactivity of compound I with reducing substrates especially in peroxidases (*27*). Interestingly, in the catalase distal histidine is absolutely required for the formation of heme d from protoheme b (*28*). The coessential asparagine residue in the distal heme pocket is involved in compound I formation by promoting proton transfer to the histidine. This facilitates peroxide anion binding to heme and stabilizes the transition state for heterolytic cleavage of the O – O bond (*29*).

Catalases are very clearly more disposed toward two-electron reduction of compound I rather than two sequential one-electron steps via compound II. One feature of the catalase structure that contributed to this is a particularly large, narrow hydrophobic main substrate access channel at the lowest section which allows only diffusion of small molecules with low polarity.

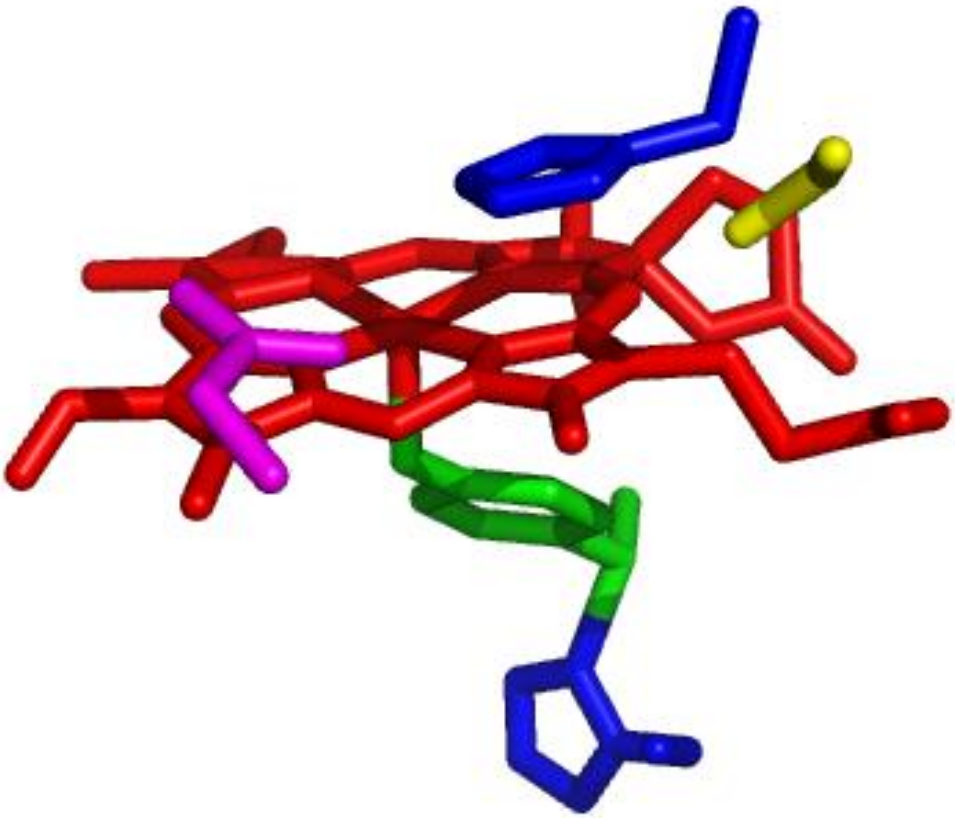

Figure 1.6: Active Site of *Escherichia coli* HPII catalase with important distal and proximal residues. Amino acids are coded to following color scheme: Histidine - Blue, Tyrosine – Green, Asparaginine – Magenta, Serine-Yellow.

This limits the rate of one electron reduction of compound I by lowering the rate of diffusion of bulky organic substrates through the lower half of the access channel. Three channels have been shown to connect the active site heme with the surface in the crystal structure of CatF (*12*) and HPII variants (*35*). The main channel is perpendicular to the heme plane and provides the access for substrate H_2O_2 as shown by molecular modeling (*36, 37*). The second minor channel also known as lateral channel as it approaches heme laterally, almost in the plane of the heme and the third channel connects the heme with the central cavity. Not much evidence has been reported about the involvement of these two later channels in substrate transport to the active site heme.

1.3. Peroxidases

Peroxidases are ubiquitous in nature and use various peroxides as electron acceptors to catalyze a number of oxidative reactions. These peroxidases can be heme or non-heme proteins. Non-heme peroxidases are not evolutionarily linked and are classified into five independent families. The largest one is the thiol peroxidase which is divided into two different subfamilies (Glutathione peroxidases and Peroxiredoxines). The remaining four families include alkylhydroperoxidase, non-heme haloperoxidase, NADH peroxidase, and manganese catalase (*38*). The non-heme peroxidases are largely outside the scope of this dissertation, and thus will not be discussed in detail.

Most heme-dependent peroxidases are classified into two large superfamilies: i) peroxidase-cyclooxygenase and ii) non-animal peroxidases. As the name suggests, the non-animal

superfamily has representatives from fungal, plant and bacterial species (*39, 40*). Peroxidase-cyclooxygenases are found primarily in vertebrate organisms (*41*), however, because the members of this superfamily were first identified in mammals, it is also referred to as the mammalian/animal peroxidases superfamily. Interestingly, significant similarity in amino acid sequences have also been encountered in various invertebrates like arthropods, mollusks, crayfish, *Caenorhabditis elegans* and dorsophilla, so they are mainly identified as animal peroxidases (*42*).

1.3.1. Non-animal peroxidases

This superfamily arose from gene duplication of an ancestral gene and has been divided into three classes based on amino acid sequence alignment and similarity of biological function (*39, 40*). Class I contains intracellular peroxidases like ascorbate peroxidase (APX) and yeast cytochrome c peroxidase (CcP) (*39, 43*). Due to the generation of H_2O_2 as a byproduct of photosynthesis and respiration, APX plays a critical role in protection of chloroplasts of higher plants (*44*). As the name suggests, APX uses ascorbate as reducing substrate to facilitate H_2O_2 reduction to water (*45*). In contrast, CcP uses ferrocytochrome c to reduce toxic peroxide to water (*39*). The primary context of CcP is as mitochondrial enzyme where it confronts H_2O_2 generated as a result of misfiring in the respiratory electron transport chain (*46, 47*).

Class II of the non-animal superfamily is composed of secretory fungal peroxidases. This class includes lignin peroxidases (LiP) and manganese-dependent peroxidases (MnP), each named after one of its substrates , and *Coprinus cinereus* peroxidases (ARP or CiP) named after

its source black inkcap mushroom from Basidiomycete family (*39*). The main role of class II peroxidase is to degrade lignin in wood, and participate in secondary metabolism under conditions of limited supply of nutrients (*48*).

Class III of the superfamily includes the secretory plant peroxidases, such as horseradish peroxidase (HRP-C), as well as soybean, barley, and peanut peroxidases. In contrast to class I , class III peroxidases are not primarily used for H_2O_2 detoxification, but rather are associated with a broad range of physiological processes in the plant life cycle. These peroxidases are involved in phytohormone (e.g., indole-3-acetic acid) catabolism, wound healing, and cell wall metabolism (*39, 45, 48*). In addition, class III peroxidases can generate H_2O_2 and hydroxyl radical (ROS) in a controlled manner during the oxidative burst, hypersensitive response or cell elongation (*49*).

Non-animal peroxidases are monomeric proteins with molecular weights ranging from 35 to 45 kDa and contain heme *b*. Evaluation of typical non-animal peroxidase structures reveals two structural subdomains (proximal and distal) which appear to have arisen from an early gene duplication event. The major secondary structural component in the overall structure of non-animal peroxidases is the α-helix. There are 10 α-helices (A–J) which are linked by loops and turns, and only a minor contribution from β-structures in the overall peroxidase structure. The heme group sits in the pocket formed by two anti-parallel helices, B on the distal side and F on the proximal side. Class I and II peroxidases posses additional helical groups like short helix B' between helices B and C which is absent in class III, however class III contains three additional helices, D' , F' , F" (*50*). The proximal subdomain contributes proximal histidine ligand to the

heme iron and evolutionary conserved aspartate. Class I peroxidases lack any disulphide bridges, carbohydrate moieties and calcium ions. In contrast, class II and III enzymes are glycoproteins with four conserved disulphide bridges and two calcium ions. Although, the position of disulphide bridges and calcium ion binding sites differ in both classes of enzymes (*39, 51*), the presence of these features does provide a substantial stabilization of the active site conformation, particularly as it relates to the coordination state of the active site heme.

Across the three classes of non-animal peroxidases there is a remarkable conservation of active site structure and catalytic residues. The active site of all non-animal peroxidases contains heme *b* prosthetic group ligated to the imidazole Nε of the proximal histidine (*52*). A strong hydrogen bond is present between $N\varepsilon_2$ of the proximal histidine and conserved aspartate residue. This increases the anionic character of the histidine and is proposed to help peroxidases stabilize highly oxidized ferryl intermediates (*52, 53*). On the distal side, a strictly conserved histidine is positioned about 5 Å above the heme iron. This residue acts as a general base, serving to deprotonate H_2O_2 and is important for the formation of compound I. The distal side also contains a strictly conserved arginine which is also involved in compound I formation by acting as an electrostatic catalyst to offset a negative charge that develops across the O-O bond of the substrate H_2O_2 and facilitates the formation of H_2O (*54, 55*).

A tryptophan residue in class I peroxidases and phenylalanine in class II and III peroxidases (except *Arthromyces ramosus* peroxidases, which has leucine) is present in the distal and proximal side of heme (*39, 56-58*). In CcP of class I peroxidase the proximal tryptophan acts as a cation radical site of compound I (*59, 60*). The site of protein radical was confirmed to be

proximal tryptophan adjacent to proximal histidine by site-directed mutagenesis studies (*61*) and EPR studies of compound I with deuterium labeled tryptophan residues (*60*). But in case of APX, porphyrin radical is observed even though APX and CcP share sequence and structural similarities. However, the crystal structure of APX shows a K^+ ion in the proximal cavity of heme which is absent in CCP (*62*). The K^+ ion increases the redox potential of the proximal tryptophan making it more difficult to oxidize. Consequently, in compound I of APX the free radical is present as a porphyrin radical rather than tryptophan radical (*63*). In class II and class III peroxidases, tryptophan is replaced by phenylalanine. Because electron withdrawal from this side chain is far more difficult, the radical remains centered in the porphyrin π electron system (*57, 58*).

In class II peroxidases two calcium ions, one near the proximal phenylalanine or leucine and second at the distal side of the heme, are present (*64*). The distal calcium ion is required for activity because it maintains the structural integrity of class II peroxidases. In MnP loss of this calcium ion disrupts active site such that the distal histidine becomes sixth ligand to the heme iron and induces a shift in the spin state from high-spin (active) to low spin (inactive) (*65*). As with class II peroxidases, heme environment in class III peroxidases is also sensitive to the presence or absence of calcium ion but a much less dramatic effect on the activity in the absence of calcium ions has been observed (*50, 66, 67*).

According to the crystal structures obtained to date, the active site of peroxidases show the presence of at least four ordered water molecules, three in the distal pocket and one in the proximal one (*51, 68*). The proximal water molecule is hydrogen bonded to the proximal

aspartate. Though the exact hydrogen bond network differs between peroxidases, the general pattern of the distal cavity water molecules involves an extensive network of hydrogen bonds connecting the distal histidine, distal arginine and pyrrole IV propionate of the heme (*51*). One of the water molecules is situated right above the heme but is typically taken to be far away for the direct coordination. But in some peroxidases (e.g., in CcP0 it is ligated to heme at the sixth position giving rise to high-spin hexacoordinate heme (*69*). The week coordination of this distal water molecule at the sixth position of the heme has been shown to be very important in catalysis for some of the heme peroxidases (*70*).

All heme peroxidases utilize heme iron to transfer electrons from a reducing substrate (RH) to H_2O_2 (reaction 1.2). The overall reaction can be written as:

$$H_2O_2 + 2RH \longrightarrow 2H_2O + 2R^{\cdot} \qquad \textbf{(1.2)}$$

Figure 1.7 shows the detailed catalytic cycle of a typical heme peroxidase (*39*). The first step is same as that of the catalases, which is the oxidation of resting ferric enzyme by one equivalent of H_2O_2 to generate H_2O molecule and compound I**.** Compound I is then reduced by one-electron from a reducing substrate to generate one equivalent of substrate radical ($R^{\cdot}$) and compound II (oxo-ferryl species). Lastly, Compound II is reduced back to resting state with the concomitant one-electron transfer from the reducing substrate to generate another equivalent of substrate radical and one equivalent of H_2O. The main difference in compound I and compound II is their heme states. Unlike compound I which contains a porphyrin π-cation radical, compound II is a fully covalent ferryl-oxo heme intermediate (*39*).

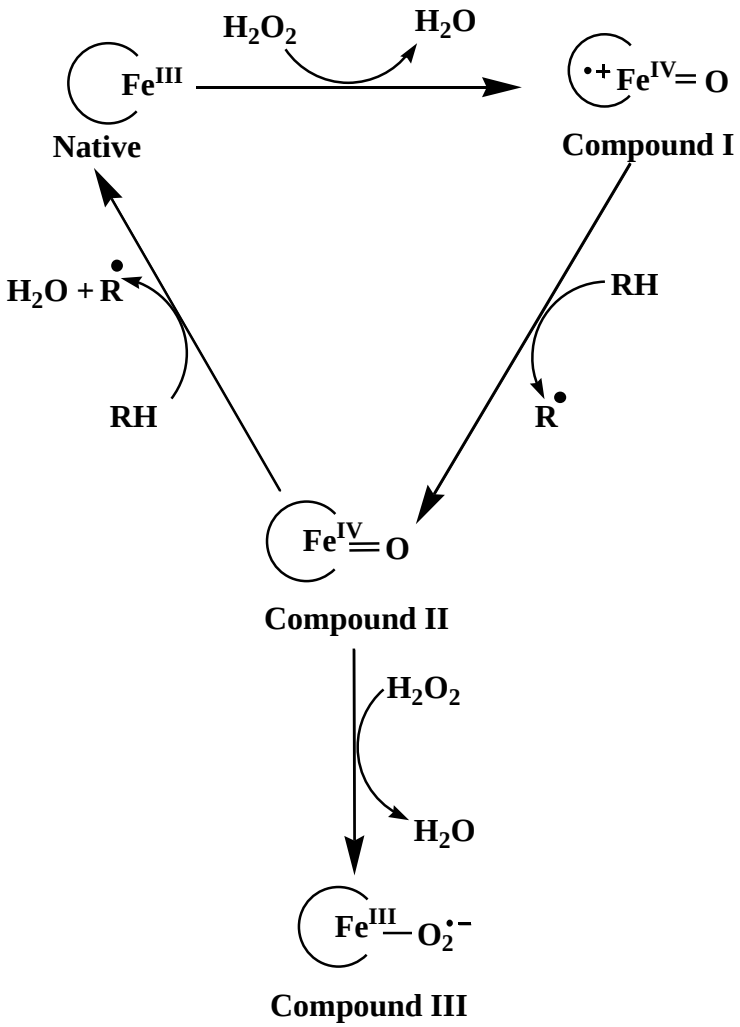

(RH: reducing substrate)

Figure 1.7: Catalytic cycle of peroxidases

In the presence of excess H_2O_2, compound III, a ferrous dioxy/ferric-superoxide inactive intermediate, can be formed by three different routes. Compound III is formed by the reaction of compound II with H_2O_2. Native peroxidase reaction with superoxide ($O_2^{\cdot-}$) or its protonated form ($HO_2^{\cdot}$) can produce it too. Finally, reaction of ferrous enzyme with O_2 produces compound III (*39*). Compound III is an inactive species in monofunctional peroxidases and it's a dead end for the peroxidase cycle. In the absence of H_2O_2, the reversion of compound III is relatively slow and in the presence of excess of H_2O_2, the additional reaction of compound III leads to irreversible inactivation of the peroxidases (*71, 72*). However, the presence of efficient reducing substrates can prevent this irreversible inactivation (*73, 74*). The formation of compound III via later two routes is irreversible (*75*).

1.3.2. Animal-peroxidases

The animal and non-animal peroxidase superfamily have evolved independently, providing a good example of convergent evolution (*42*). Animal peroxidases differ substantially in sequence, overall structure and nature of the prosthetic group compared to non-animal peroxidases. The most obvious structural difference between these two superfamilies is the nature of the prosthetic group. In contrast to the members of the non-animal superfamily that have noncovalently bound heme *b* at the active site, the heme group of peroxidases from mammalian superfamily is post-translationally modified to form ester bonds with the protein via highly conserved aspartate and glutamate residues (Figure 1.8) (*76, 77*). The most well known animal peroxidases are myeloperoxidase (MPO) and lactoperoxidase (LPO). These enzymes are important in human biology and contribute in host defense against pathogens (*41, 78*). They play

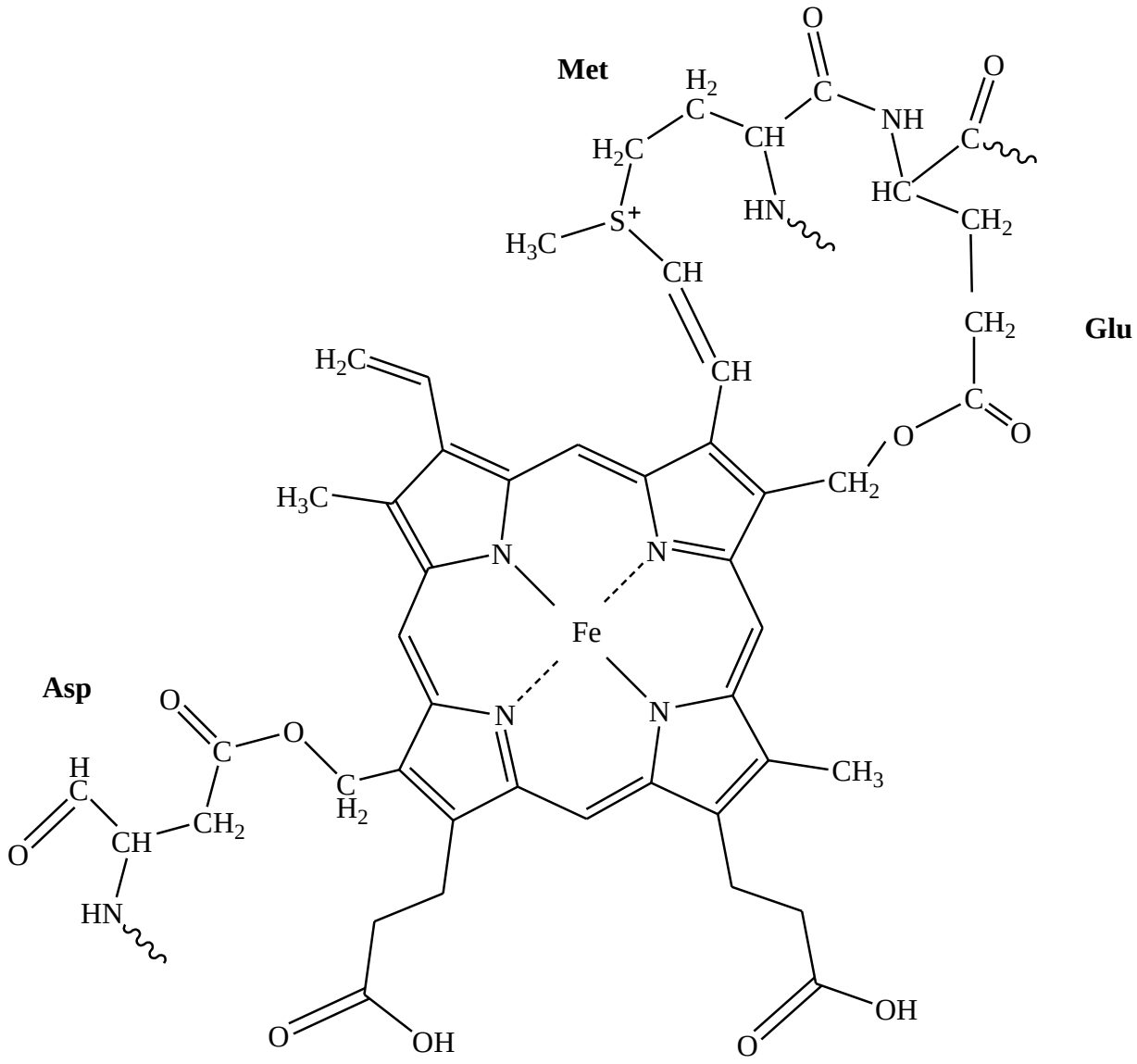

Figure 1.8: Structure of post-translationally modified and covalently linked heme b with the protein via ester bond formation with highly conserved aspartate and glutamate residues

an important part in the innate immune system by oxidizing small ions like halides, pseudohalides, and nitrite to their corresponding oxidation products, for example, hypohalous acids which are used as part of a bactericidal response (*41, 78, 79*). Figure 1.9 depicts the general halide oxidation scheme for animal peroxidases.

MPO is a cationic 146 kDa dimer consisting of two symmetry-related halves (~73 kDa) linked covalently by a disulphide bridge (*80*). Each half contains two polypeptides, a small one composed of 106 amino acids (14.5 kDa), and large one of 467 amino acids (58.5 kDa), a heme prosthetic group, a calcium ion, and five sites of asparagine-linked glycosylation. The secondary structure is dominated by 22 α-helices which comprise 36% of the entire molecule (*79, 81, 82*). Four helices from the large polypeptide, H5, H6, H8, and H12 and one from the small polypeptide, H2, form a core unit containing the heme group.

The active site of MPO contains one heme group which is derivative of ferriprotoporphyrin IX. The modification of methyl groups on pyrrole rings A and C allow the formation of ester linkages with the carboxyl group of glutamate of the large and aspartate of the small polypeptide. In addition, heme is covalently bound to the sulfur atom of a methionine residue via a sulfonium linkage (*82*). Histidine serves as a proximal ligand which forms a hydrogen bond with an asparagine, these two residues are conserved in all animal peroxidases. The modified heme is positioned at the bottom of a deep crevice which allows only H_2O_2 and small anions to access the iron atom (*81*). The formation of compound I in MPO is reversible requiring a larger excess of H_2O_2 for its formation than the typical peroxidases (*39*). For

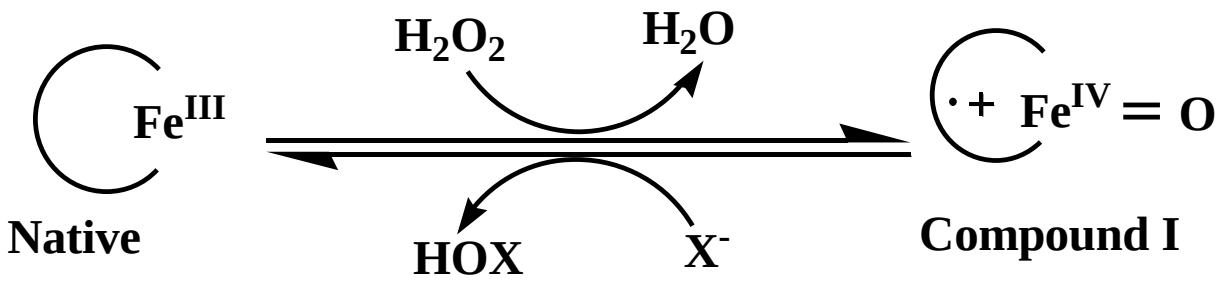

(HOX: hypohalous acid; X^-: halide)

Figure 1.9: General reaction scheme of animal peroxidases

example, HRP is converted to its compound I state upon addition of just one equivalent of H_2O_2 (*39*). The unique feature of MPO is the reaction of compound I with chloride ion to produce hypochlorite ion (*83*). The formation of this bacterial killing hypochlorite ion is the critical part of neutrophil response to bacterial invasion (*39*).

Lactoperoxidase (LPO) also contains covalently liked protoporphyrin IX type heme. LPO is glycoprotein with a single chain that has a molecular mass of ~68 kDa. The LPO structure consists of 20 α-helices, 2 small anti-parallel β-strands, 4 glycosylated asparagines residues; 1 phosphorylated serine, 7 disulphide bridges and a tightly bound Ca^{2+} ion (*84*). Lactoperoxidase also forms compound I upon reaction with H_2O_2, but only stochiometric amounts of H_2O_2 are needed (*39*). However unlike MPO, LPO compound I is unable to oxidize chloride ion, but is capable of oxidizing other halides (like iodine or bromine) and pseudohalides (e.g., thiocyanate) to the corresponding hypohalite ions, which are potent antimicrobials (*85*).

1.4. Catalase-peroxidases

The preceding discussion sufficiently reveals that out of the four levels of protein structure, first three (i.e., heme, protein-derived ligands, non-ligand heme environment) and their effects on a given protein's functional capabilities, are bolstered by a wealth of information. It has also become obvious that comparatively little is known about the fourth level. That is, the mechanism by which distant protein structures influence the active site environment, and thus, contribute to the functional capabilities of heme in different proteins is poorly understood. For reasons to be described in this section, the catalase-peroxidases provide an excellent model to

evaluate this aspect of the protein structure and function. Moreover, the research described in this dissertation takes the advantage of nature's strategies towards enzyme engineering by using catalase-peroxidases as a focal point to understand the mechanism by which distant protein structures control the heme environment and modulate the activities of heme proteins.

Catalase-peroxidases (KatGs) are present in prokaryotes and fungi. These enzymes are capable of decomposing H_2O_2 via two distinct mechanisms using a *single* active site. Though it is an over simplification, the catalytic cycle of KatG can be described by super-positioning of both catalase and peroxidase catalytic cycles (Figure 1.10) (*86-90*). The two cycles are plainly suggested to be diverting at compound I. That is, compound I could either be reduced by hydrogen peroxide (catalase) or an exogenous electron donor (peroxidase). In the catalase cycle, compound I is reduced by using another equivalent of H_2O_2, forming H_2O and O_2. Whereas in peroxidase cycle, compound I undergoes two single-electron reduction steps by an exogenous electron donor. The first reduction produces a substrate radical and compound II. The second reductive step produces ferric enzyme, a second equivalent of substrate radical and one molecule of H_2O.

Despite using a single active site to carry out both the activities, KatGs exhibit a prominent catalases activity and a substantial peroxidase activity with broad specificity. This bifunctionality is unique because typically catalases are poor peroxidases and peroxidases are weak catalases. Thus, the bifunctionality of KatGs raises fundamental questions. The first is to which group of enzymes do KatGs belong, catalases or peroxidases. The answer can be sought by sequence and structural comparison of these groups of enzymes. The overall amino acid

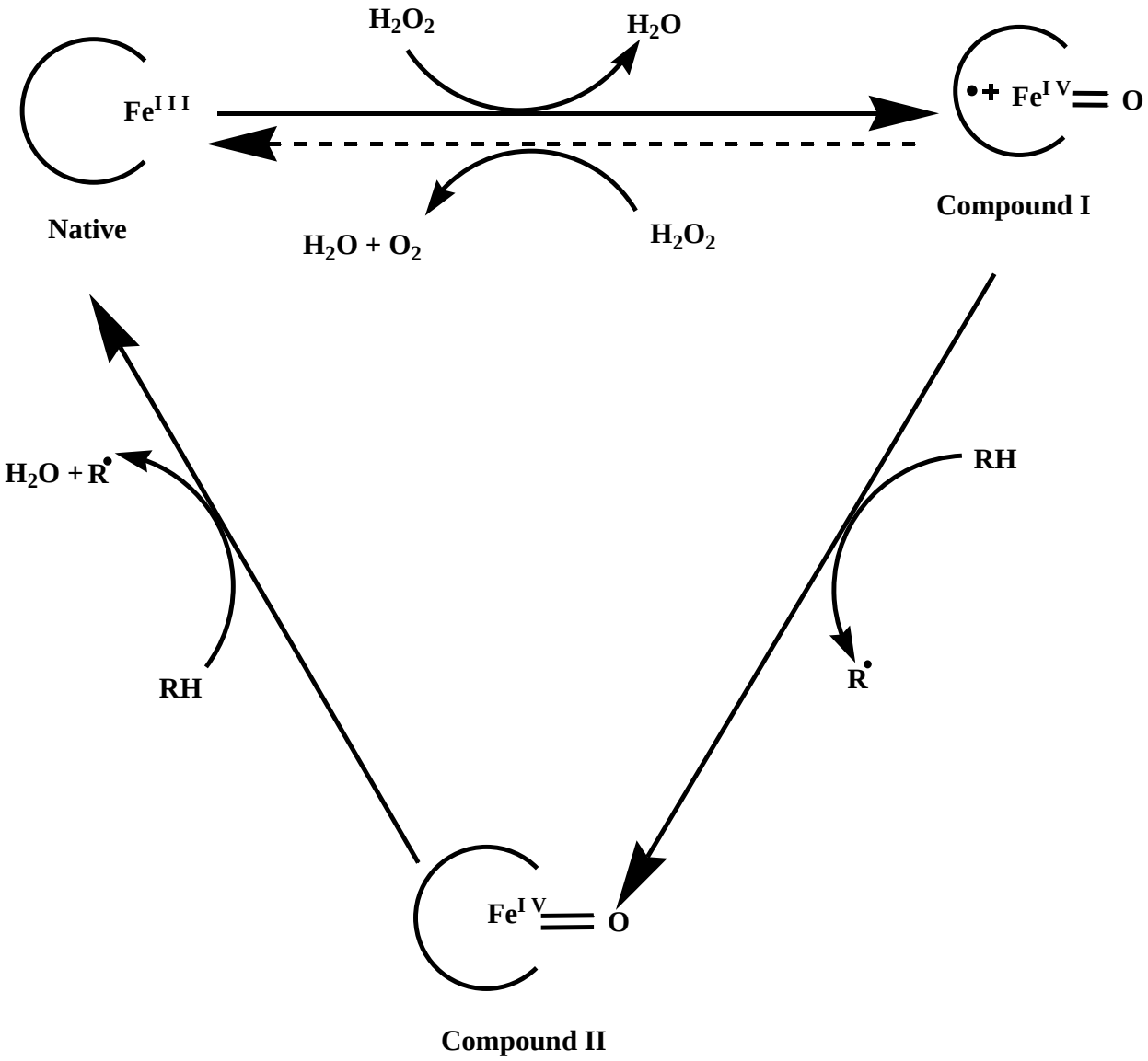

(RH: reducing substrate, R˙: substrate radical)

Figure 1.10: Classical reaction scheme for catalase-peroxidase

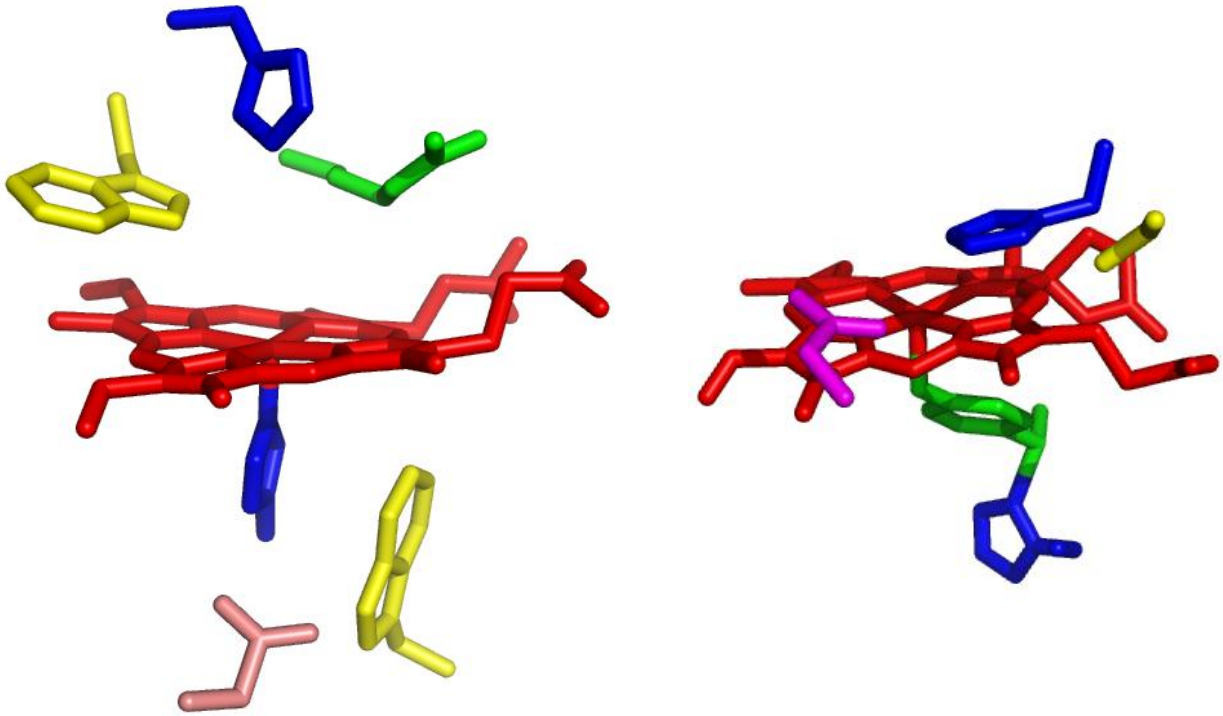

Figure 1.11: Active sites of catalase-peroxidase (right) and monofunctional catalase (left). Amino acids are coded to following color scheme: Histidine - Blue, Tyrosine/Arginine – Green, Asparaginine – Magenta, Serine/Trytophan – Yellow, Aspartate-deep salmon red.

sequence and structural fold of KatG bear no similarity to monofunctional catalases. Even the active site of both the groups bears little resemblance if any to one another (Figure 1.11).

On one hand, monofunctional catalases use either heme b or heme d as the prosthetic group (*29, 30*); KatGs always have heme b in their active sites (*91-94*). Additionally, the proximal and distal active site residues are different in both the groups. On the proximal side of heme, the fifth ligand in catalases is tyrosine whereas in KatGs it is histidine. On the distal side, histidine is the only common residue in both groups of enzyme but its orientation differs in these enzymes. In KatGs, this distal histidine is perpendicular to heme whereas in monofunctional catalases it is parallel. In both the cases, distal histidine allows the proper binding and reduction of peroxide molecule. However, the perpendicular orientation of this histidine in KatGs favors increase reactivity of compound I with reducing substrate. On the other hand, the sequence and structural comparison of KatGs to monofunctional peroxidases shows that these two groups of enzymes are closely related. Indeed, the first three structural levels of these two important groups of enzymes are nearly indistinguishable. The active site of KatG is virtually identical to monofunctional peroxidases with identical distal and proximal catalytic triad of amino-acid residues (Figure 1.12) (*91-94*). On the proximal side of the heme, the essential histidine is the fifth coordination ligand to the heme and it forms hydrogen bond with fully conserved aspartate, which also interacts with the indole nitrogen atom from the proximal tryptophan. The distal side involves three catalytically important residues i.e., arginine-tryptophan-histidine. In KatG, the histidine-arginine pair is important for compound I formation and the distal tryptophan is essential for compound I reduction by H_2O_2 (*95-97*).

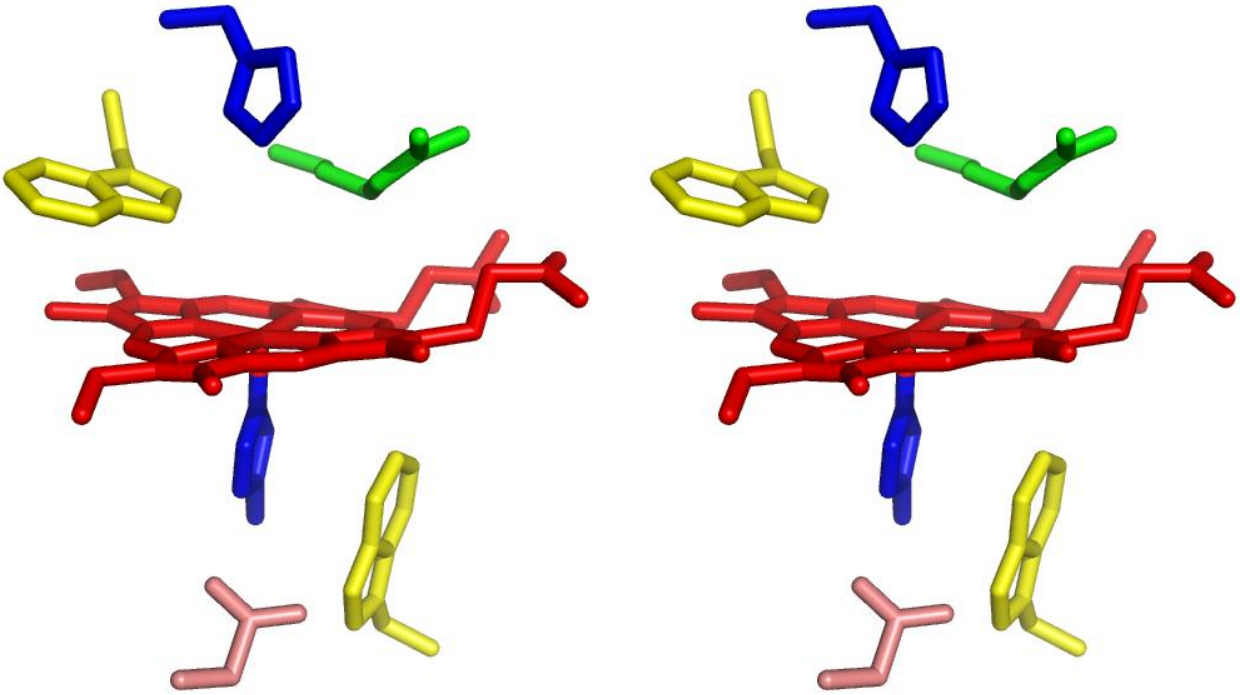

Figure 1.12: Active Sites of catalase-peroxidase (right) and monofunctional peroxidase (left). Amino acids are coded to following color scheme: Histidine - Blue, Arginine – Green, Trytophan – Yellow, Aspartate-deep salmon red.

The highly similar active sites and structural similarities of KatGs to monofunctional peroxidases raises the next essential question. What strategies has nature used to incorporate a new activity into an old scaffold? In other words, what enabled KatGs to utilize monofunctional peroxidase active site to carry out catalase activity? The quest to solve this question has led to understanding the role of peripheral structures of KatGs, which are away from the active site and are generally absent from the monofunctional peroxidases, in maintaining the heme environment of these enzymes to impart the bifunctionality. Solution to this question will not only help us appreciate the nature's preference in utilizing the old scaffold for new activity over developing an entire new enzyme system to incorporate new functions. But, will also aid in deciphering the impact of the fourth structural level of a protein on its function.

Comparisons of the global structures of these two groups of enzymes reveal that KatG contains two extended loops in its active-site bearing N-terminal domain and also carries an additional domain (C-terminal) derived from gene duplication and fusion (Figure 1.13). Most importantly, both extended loops and the C-terminal domain are peripheral to an distant from the active site. The overall structure of the C-terminal domain is similar to that of the N-terminal domain consistent with its origin in gene duplication and fusion (*98, 99*). Both the domains have high α-helical composition with few β-sheets (*91-94*). As in monofunctional peroxidases, there are 10 major α-helices (A-J) in each domain. However, only the N-terminal domain contains the active site and binds heme. This active site is buried inside the N-terminal domain and substrate access to the heme is through a narrow access channel which allows small substrates but is too restricted for the passage of larger substrates (*43*). Even though the C-terminal domain maintains the overall protein architectures of the active site, it does not bind heme or catalyze any reaction

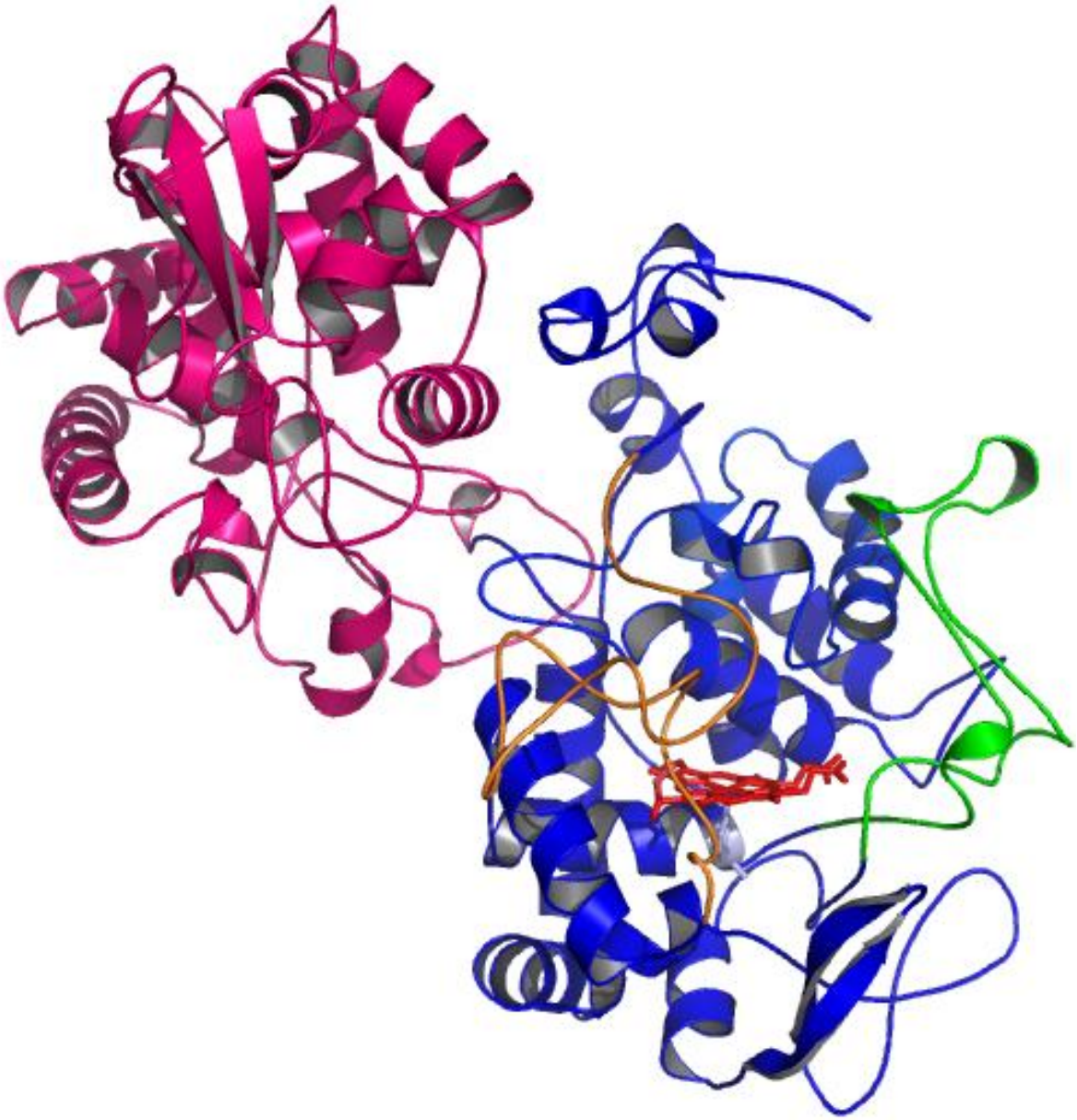

Figure 1.13: C-terminal domain and two large loops of catalase-peroxidase. Structure was taken from PDB accession domain 1SJ2. Different structures are color coded as follows Heme- red, N-terminal domain- Blue, C-terminal domain –Magenta, Large loop 1 (LL1) – Orange, and Large loop 2 (LL2) – Green.

(*98*). Instead the space corresponding to heme pocket in this vestigial active site structure is filled with two small β strands (between helices D' and E') and a 10 amino-acid long loop (between helices F' and G') (*43*, *98*).

Despite being ~30Å away from the active site and inability to bind heme, the C-terminal domain is a crucial component in maintaining the bifunctionality of KatGs (*86*). Loss of the entire C-terminal domain results in complete loss of activity due to coordination of the active site histidine to the heme iron (*86*, *100*). This observation was attributed to collapse of the actives site architecture due to disruption of interdomain interactions (*86*, *100*). The same supporting function of C-terminal domain is performed by distal calcium ion in monofunctional peroxidases, such as lignin and manganese peroxidases (*64*, *80*). One of the inter-domain interactions includes a strictly conserved hydrogen bond network formed between tyrosine from BC loop of the N-terminal domain, and the aspartate from B'C' loop of the C-terminal domain, has been shown to tune the KatG active-site for bifunctionality (*101*). Disruption of this hydrogen bond by substituting tyrosine with alanine yields an enzyme with diminished catalase activity (*101*). It is thus proposed that despite its distance from the active-site, the C-terminal domain serves to support an architectural framework necessary for proper active-site configuration by providing a series of interactions with N-terminal domain.

In addition to the extra C-terminal domain, KatGs contain three large loops (LL1, LL2, and LL3) in the N-terminal domain. LL1 and LL2 are positioned at the opposite edges of the heme and restrict the access channel to the deeply buried active site at the distal side. LL3 is far from the active site and its role in KatG is not well defined (*94*).

LL1 spans between helices D and E and is located at one edge of the heme connecting its distal and proximal pockets (*91-94*). This structure varies considerably in length (36-76 amino acids) among KatGs, but it nevertheless contains a highly conserved sequence of ~10 amino acid residues 'MGLIYVNPEG' its C-terminal end (*43, 102*). Deletion of this loop results in elevated peroxidase activities compared to wild-type KatG with complete loss of catalase activity (*103*) . The strictly conserved residues of LL1, e.g., Tyr249, Ile248, and Glu253 (*Synechocystis* numbering), have been identified as essential for the H_2O_2 *oxidation* which is the hallmark of and unique to catalase turnover (*91-94, 102*). Glu253 creates an acidic entrance to the access channel which is characterized by a pronounced funnel shape and a series of water molecules (*91-94*). The substitution variants Glu253Gln sustains a substantial loss of catalase activity and alters the pH profile of catalase activity with no effect on peroxidase activity (*43*). This observation suggested that the negative charge of Glu253 at the entrance stabilizes and orients the solute matrix essential for H_2O_2 catalysis, particularly its oxidation (*102, 104*).

The hydrogen bond between Ile248 of LL1 and Asp152 is important for the stability of the heme architecture, and perturbation of this hydrogen bond due to Ile248Phe mutation drastically reduces the catalase activity as a result of changes at the proximal heme site (*105*). These changes which are mediated by LL1 and its connection with helices E and F cause an increase in pentacoordinate high spin heme at the expense of hexacoordinate high spin heme form (*105*). Moreover, Asp152 has been shown to be essential for the catalase but not peroxidase activity of KatG (*106*).

All crystal structures for KatG solved so far reveal that the conserved tyrosine residue of LL1 is involved in a covalent adduct at the distal side of the heme. This adduct is formed between $C^{\eta 2}$ of tryptophan and $C^{\varepsilon 1}$ of tyrosine, and between $C^{\varepsilon 2}$ of tyrosine and S^{δ} of methionine (Figure1.14). The formation of this adduct is heme- and peroxide- dependent and is proposed to proceed by a radical-based mechanism initiated by the heme (*107, 108*). The formation of covalent adduct is also proposed to involve the tyrosyl and tryptophanyl radicals (*109*) but no direct insight about this has emerged to date. The existence of covalent adduct in solution has been shown by mass-spectrometry and SDS-PAGE (*107, 110, 111*). None of the three amino acids of the adduct can be substituted without diminishing the catalase activity of KatG, yet such mutants maintain or even exhibit improved peroxidase activity (*92, 96, 108, 112*). Thus, manipulation of this unique adduct affects the electronic nature of the redox intermediates. Mutation of tyrosine to phenylalanine has been shown to cause rapid conversion of compound I to stable compound II due to endogenous electron transfer (*90, 113, 114*). The formation of stable compound II favors the peroxidase activity but eliminates catalase activity (*113, 115*). The mutation also allows the easy conversion and stable formation of compound III, which interferes with the catalase activity (*75, 90, 113, 114*). Moreover, it has been observed that disruption of this adduct weakens the heme binding to the protein. This results in the appearance of hexacoordinate low-spin heme form, along with the loss of the heme prosthetic group, due to binding of strong internal ligand to the heme iron (*116*). Recently, a scheme depicting the catalytic role of this adduct radical has been suggested in catalase reaction of KatG.

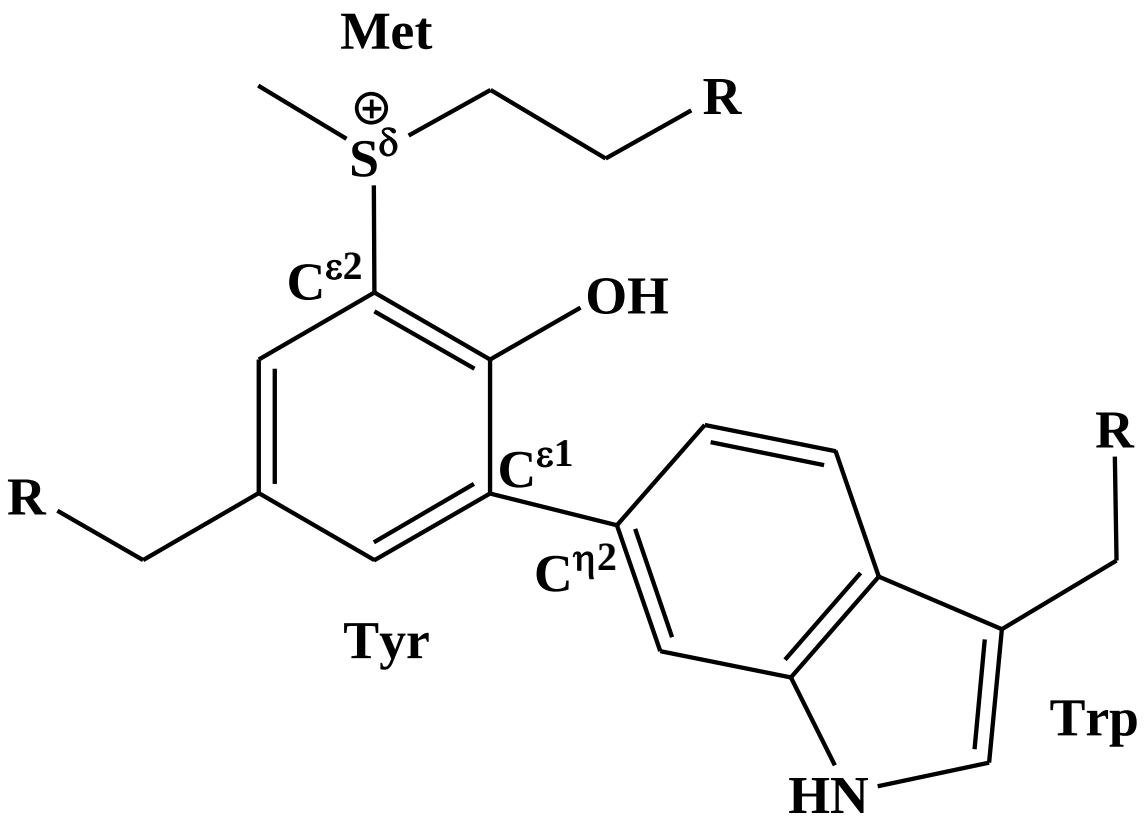

Figure 1.14: Model of (Trp-Try-Met) covalent adduct of catalase-peroxidase

According to this scheme, tyrosine in the adduct can catalyze oxygen formation from superoxide, which dissociates from oxyenzyme during the catalase reaction of KatG (*117*). Other roles for LL1 and its relation to the covalent adduct will be addressed in Chapter Three.

Sequence alignment performed using Clustal X (details presented in Chapter Four) on 20 selected representatives from all known Class I families with one sequence of typical Class II representative shows that in contrast to LL1, LL2 varies little in its length (35-36 amino acids). However, in comparison to LL1, LL2 contains far fewer (~4 amino acids) invariant residues. This loop begins and terminates adjacent to the active site spanning between F and G helices, and its apex protrudes into a hydrophobic pocket in the C-terminal domain of the other subunit. A complete loss of catalase activity, 50% reduction in peroxidase activity, and diminished rate of cyanide binding was evident in the variant lacking the entire LL2 (*87*). However, the mechanism behind this observation was not clearly understood.

Closer examination of the LL2 structure indicated that the ascending and descending limbs of this loop run roughly parallel to the hydrogen bond network formed by distal histidine (His106), Asn136, and Leu130. Thus, removal of entire LL2 was suggested to disrupt the above mentioned hydrogen bond network as two of its residues Glu284 and Trp297 lie fairly close to this network (*87, 103*). In order to determine the underlying mechanism of LL2 participation in the reactivity of KatG, the Goodwin lab has carried out a detailed study involving various amino acid residues of this loop. The data obtained from this study have been complied in Chapter Four of this dissertation.

The preceding discussion demonstrates that the large loops of KatG serve an important role in maintaining the catalytic versatility of the enzyme. To further evaluate these two large loops, they were subjected to modification by substitution and deletion mutagenesis followed by biophysical and kinetic characterization. For Large loop 1, the main goal was to investigate the additional functions of this large structure (36-76 residues long) besides positioning tyrosine correctly for the formation of the covalent adduct. In order to investigate this, various portions of the loop were deleted including or excluding tyrosine 226 and their catalytic properties were compared with wild-type KatG and its tyrosine to phenylalanine variants.

In case of large loop 2, closer examination of this structure revealed an intersubunit interaction happening ~ 35Å away from the active site between its apex and hydrophobic cavity of C-terminal domain of another subunit. Keeping in mind that the removal of entire LL2 eliminated the catalase activity but preserved the peroxidase activity of KatG and also that C-terminal domain is required to maintain both the activities of KatG, we focused on understanding the role of this intersubunit interaction in fine tuning the active site architecture and preserving the activities of KatG. LL2 was targeted in two different ways: first, important residues at the point of contact were either substituted or deleted, and secondly, the length of LL2 was targeted by deleting conserved and non-conserved residues. Both sets of mutations were made to disrupt the intersubunit interaction and to decipher the importance of length preservation in LL2 over residue preservation. The detailed result and observation of this study is compiled in Chapter Four.

1.5. Conclusions

Heme proteins are rich sources to exploit to understand the relationship between protein structure and function. The available three dimensional structures have provided crucial information about heme structure, location and role of important catalytic residues in and around the active site, effect of post-translational modification on protein's catalytic ability and position and importance of peripheral structures of protein with respect to active site. The diverse functionality of heme proteins, even though they all contain small and simple metallo-organic compound heme, is fascinating and points to the factors which manipulate heme to achieve catalytic versatility. These factors include heme structure, protein-derived heme ligands, non-ligand heme environment, and the global structure of the protein. Much interest has been paid to understand the effects of first three structural levels on heme protein activity, and the role of global structure of proteins has been under investigation. This thesis details my contribution to decipher the role of various peripheral structures and interaction arising from these structures on the active site environment and eventually on the activity of heme proteins. We have used *Escherichia coli* catalase-peroxidase (KatG) as a model to evaluate the mechanism by which structures peripheral to enzyme active site influence its architecture and catalytic ability.

KatG catalyzes both catalase and peroxidase reactions using a unique active site. This active site catalyzes substantial catalase turnover even though it bears no resemblance to classical catalases. Instead, the active-site is superimposable on that of classical peroxidases, enzymes which have little if any catalase activity. This diversity in function highlights the effect of structures present outside the active site. Indeed, structural comparison of catalase-peroxidases

with classical peroxidases shows the obvious differences between two groups of enzymes like a gene-duplicated C-terminal domain and two interhelical insertions (LL1 and LL2) unique to catalase-peroxidases. This thesis focuses on understanding the role of these peripheral structures and interactions arising from them with the hope that it will shed some light on the regulation of heme protein function by global protein structure.

Chapter Two: Generation and Characterization of Catalase-peroxidases by Molecular and Biophysical Techniques

2.1. Manipulating the *katG* gene: cloning and mutagenesis

The *katG* gene from *E.coli* (K-12) was cloned and placed in a pET expression vector by Dr. Douglas Goodwin using a PCR-based approach. Primers were designed to amplify the *katG* gene such that the product could be cleaved with *Nde I* at the 5' ATG start codon and by *Xho I* at the 3' end such that the natural stop codon was eliminated. The resulting PCR product and the pET-20b plasmid were each cleaved with *Nde I* and *Xho I*, and the correct fragments were ligated together according to standard procedure (*118*). The candidate plasmids were sequenced to eliminate the possibility of accidental mutations during cloning process. By using the *Xho I* restriction enzyme with the pET-20b vector, the *katG* gene was followed by six codons for histidine and a stop codon. Thus, wtKatG is expressed with a six-histidine tag on its C-terminus.

The pET expression system is a system for the robust expression of recombinant proteins in *E. coli*. The pET expression vectors are designed to allow use of a T7 promoter for bacteriophage T7 RNA polymerase-based transcription of the target gene. This ensures that almost all of the cell's resources are converted to target gene expression, but also minimize expression of the target gene until T7 RNA polymerase is itself expressed. In the BL-21(DE3) expression host, T7 RNA polymerase is under control of the *lacUV5* promoter, and thus, its

expression can be induced by the addition of IPTG.

The pET vector used in the research described in this dissertation was pET-20b. The *katG* gene was inserted following the T7 RNA polymerase promoter. As mentioned above, the *katG* gene was inserted in such a way that the expression would result in a C-terminal six-histdine tag. For the selection purposes, the pET-20b plasmid encodes an ampicillin resistance marker, conferring ampicillin resistance on cells carrying the plasmid.

2.1.1. Site-directed mutagenesis

In vitro site-directed mutagenesis is an invaluable technique for studying protein structure-function relationships and allows for the single substitution of amino acids purported to be critical to function.

2.1.1.1. Quikchange™ technique (Agilent Technologies)

The QuikChange™ approach (Agilent Technologies, La Jolla) was used to make point mutations that resulted in a change of the target codon. This method was performed using thermostable *Pfu*™ DNA polymerase (Agilent Technologies). *Pfu* DNA polymerase was preferred as it replicates both plasmid strands with high fidelity and without displacing the mutant oligonucleotide primers (*119*). The Quikchange procedure utilizes a supercoiled double-stranded DNA (dsDNA) vector (in this study recombinant His-tagged *E.coli* KatG (pKatG1) was used as a template) and two synthetic oligonucleotide primers containing the desired mutation (Figure 2.1). All oligonucleotide primers were purchased from Invitrogen (Carlsbad,CA) and

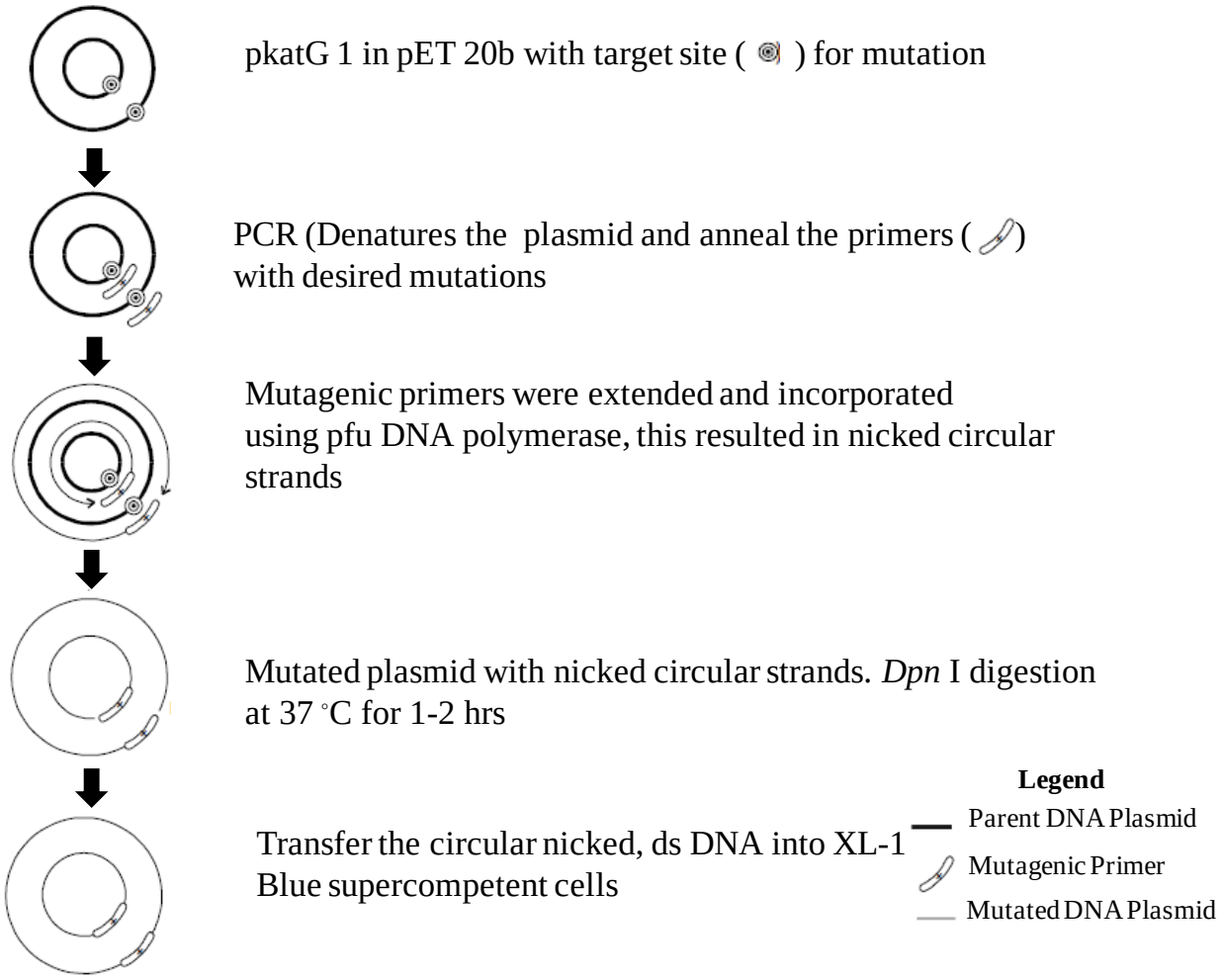

Figure 2.1: Overview of QuikChange™ site-directed mutagenesis method. Scheme adapted from Stratagene QuikChange™ site-directed mutagenesis manual.

designed to be complementary to opposite strands of the vector, the mutation to be introduced and its complement were encoded to the middle of the coding strand and non-coding strand primers, respectively, and were extended during temperature cycling (PCR) by Pfu DNA polymerase. The resulting products contained staggered nicks, and these products were then treated with *Dpn I* endonuclease (New England Biolabs, Ipswich, MA) at 37°C for 1 hr. The target sequence (5´-G(Me)ATC-3´) of *DpnI* endonuclease is specific for methylated and *E.coli* hemimethylated DNA and is used to digest the parental DNA template and to select for DNA with desired mutation (*120*). DNA isolated from almost all *E.coli* strains is dam methylated and therefore susceptible to *Dpn I* digestion. The resulting plasmids were then used to transform the XL1-Blue non-expression host (Agilient Technologies) by electroporation using a Biorad Micropulser™.

2.1.1.2. "Around the Horn" technique

This is also a PCR-based method, but in contrast to QuikChange, it uses non-overlapping oligonucleotide primers to introduce mutations in the expression construct for the target protein (Figure 2.2). The primers are designed in such a way that if the 5' end of the forward primer is at the position "x" in the sequence, the 5' end of the reverse primer is at position "x-1". The PCR products that result from the process have blunt ends and can be ligated using T4 DNA ligase (New England Biolabs) provided that primers are phosphorylated on their 5' ends. In all cases, ligation products were used to transform *E.coli* XL-1 Blue (a non-expression host) by heat shock. Candidate colonies were selected on the basis of ampicillin resistance. Plasmids from the candidate colonies were screened first by diagnostic restriction digests. Positive candidates were

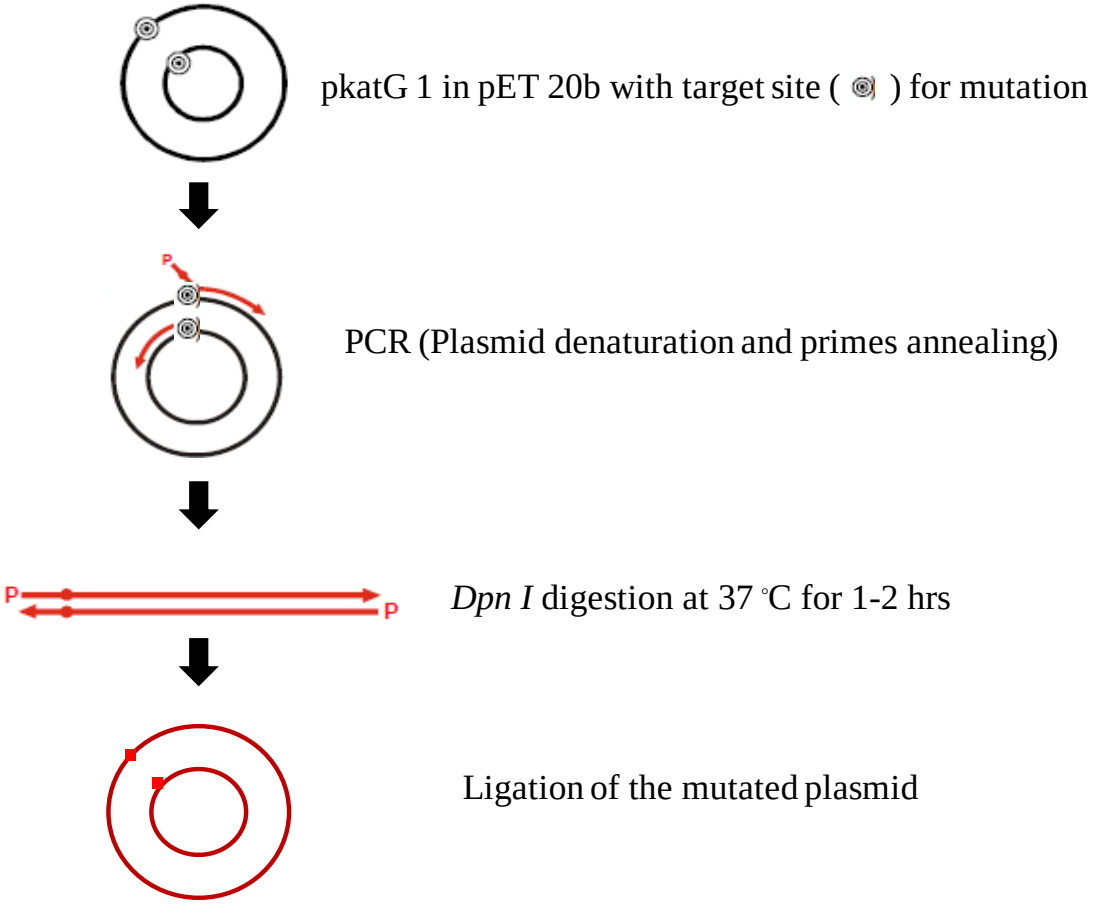

Figure 2.2: Overview of "Around the horn" site-directed mutagenesis method.

then submitted for DNA sequence analysis (Davis Sequencing, Davis, CA) to verify the correct mutations and ensure that no unintended mutations had occurred. Plasmids were used to transform *E.coli* BL-21 [DE3] pLysS (the expression host).

2.1.2. Deletion mutagenesis

2.1.2.1. Seamless®cloning (Stratagene)

To generate the construct for the expression of deletion variants, a deletion protocol was developed based on Seamless®cloning (Stratagene). This method is a PCR-based approach in which primers are designed to include *Eam* 1104 I restriction sites. Consequently all the products were treated with *Eam* 1104 I. *Eam* 1104 I is a type-IIS restriction endonuclease that cleaves target DNA downstream of its recognition sequence (*121*). The unique feature of *Eam* 1104 I is that it cleaves one nucleotide down on the upper strand in the 3' direction and four nucleotides down on the lower strand in 5' direction. This results in overhanging sequence with three nucleotides that can be designed into the primers to suit the investigators needs.

5' – **CTC** **TTC** N▼NN NN – 3'

3' – GAG AAG NNN N▲N – 5'

Primers were designed to amplify pKatG1 leaving out the codons coding for the targeted region, to include a *Eam* 1104 I restriction site, and yield compatible overhanging

sequences upon digestion with *Eam* 1104 I. The overhanging sequences were ligated using T4 DNA ligase. The resulting products were used to transform *E.coli* XL-1 Blue cells by heat shock. Colonies were selected on the basis of ampicillin resistance, and candidate plasmids were verified by DNA sequence analysis at Davis Sequencing.

2.1.2.2 "Around the Horn" technique

To generate deletion variants, non-overlapping primers were designed to exclude the codons corresponding to the targeted deletion. The desired codons were removed either from the forward primers or reverse primers. The desired PCR products were ligated using T4 DNA ligase. The resulting products were used to transform *E.coli* XL-1 Blue cells by heat shock. Colonies were selected on the basis of ampicillin resistance, and candidate plasmids were verified by DNA sequence analysis at Davis Sequencing.

2.2. Expression system

E.coli strain BL21-Gold[DE3]plysS was used to express the proteins studied in this dissertation. First the pET-20b plasmids containing the desired gene were used to transform *E.coli* strain BL21-Gold[DE3]plysS. The 'DE3" in the expression strain indicates that this strain is a lysogen of bactriophage DE3, implying that it contains a chromosomal copy of the gene for T7 RNA polymerase under the control of the *lacUV5* promoter (*122*). Target genes are maintained in a transcriptionally silent mode until induction using the lactose analog, isopropyl-β-D-thiogalactopyranoside (IPTG). In the absence of IPTG, *lac* repressor binds to the *lac*

promoter, and little or no T7 RNA polymerase is expressed. Consequently, none of the T7 promoter-controlled target protein is expressed. Conversely, in the presence of IPTG, the *lac* repressor dissociates from the *lac* promoter allowing for expression of T7 RNA polymerase and as a result the gene for the target protein is subsequently transcribed.

The designation "pLysS" indicates that a plasmid encoding T7 lysozyme is present in the strain. T7 lysozyme is a natural inhibitor of T7 RNA polymerase, and therefore, stops the "leakage" expression of the target protein (*122*). This way pLysS provides more tight control of target protein expression prior to induction. This is especially useful for the expression of toxic proteins. This provides additional stability to the target gene as even in the absence of IPTG, there is some expression of T7 RNA polymerase from the *lacUV5* promoter in λDE3 lysogen. If the target protein is sufficiently toxic to *E..coli*, the "leakage" expression can substantially slow down the cell growth or cause cell death. As a result, the desired cell density for efficient and abundant expression of the target protein can be dramatically dimished.

During transformation of the desired plasmid and expression host were incubated for 30 minutes on ice. The mixture was then heat shocked at 42°C for 20 seconds and then placed on ice water for 2 minutes. Cells were grown in SOC medium for 1 hour with gentle agitation at 37°C. Resulting cells were plated on LB agar plates supplemented with ampicillin and chloramphenicol. Expression was carried out in 0.5 L Lauria-Broth with ampicilin and chloramphenicol at 37°C at 250 rpm. Expression was induced with IPTG (Gold Biotechnology Inc., St. Louis, MO) at mid-log phase (Optical density @ 600= 0.5) and cells were grown for 4

hours. At four hours post-induction cells were harvested by centrifugation at 10000 rpm at 4 °C, supernatant was discarded and pellets were stored in -80°C for protein purification.

Protein expression was analyzed by using the trichloroacetic acid (TCA) precipitation technique (*123*). A quantity of cells sufficient to yield a 0.05 OD_{600} reading (when diluted to 1 ml) was treated with an equal volume of 10% trichloroacetic acid (4 °C) followed by centrifugation. The pellet was then washed with 1 ml acetone, dried and resuspended in SDS-PAGE loading buffer adjusting the pH with 200 mM Tris base. Protein solubility was monitored by taking 1 ml of cells from cultures at four hours post-induction of expression. Cells were centrifuged at 13,200 rpm for 10 minutes. Supernatant was discarded and pellet was homogenized with 75 µl Bugbuster. The solution was centrifuged to separate out the pellet and supernatant. 10 µl of supernatant was mixed with SDS loading buffer. Pellet was resuspended in 40 µl of urea, 10 µl of urea suspended pellet was mixed with SDS loading buffer. Samples from expression and solubility analysis were separated by SDS- PAGE using 7.6% acrylamide resolving gel.

2.3. Protein purification

2.3.1. Soluble protein purification

Cell pellets were resuspended in Bugbuster reagent (EMD4 Biosciences, Madison, WI) and 0.1ml phenylmethylsulfonylfluoride (PMSF). Bugbuster reagent is a protein extraction reagent and was used for the gentle disruption of the cell wall of *E.coli* to release soluble protein. PMSF is a serine protease inhibitor and was used to deactivate proteases from digesting target

protein after cell lysis. Following homogenization, 250 units of benzonase nuclease was added and mixture was incubated at room temperature for 2 hours with gentle stirring. Benzonase nuclease was used to remove nucleic acid contaminants from the protein preparation. This enzyme attacks and degrades all forms of DNA and RNA. The cell lysate was then centrifuged at 10,000 rpm for 20 minutes. Since all the variants contain C-terminal six-histidine tag Nickel-affinity chromatography was used to purify the protein. Nickel is bound to an agarose bead by chelation using nitrilotriacetic acid (NTA) beads. NTA is a tetradentate chelating adsorbent occupying four of six ligand binding sites in the coordination sphere of the nickel ion. The remaining two sites interact with six-histdine tag. Only the target protein containing six-histidine tag binds to resin as all other cellular proteins either do not bind or only weakly bind to the resin. The target protein is eluted with higher concentration of imidazole (Sigma, St. Louis, MO) whereas all other weakly bound proteins elute at lower concentrations of imidazole.

The supernatant obtained after the centrifugation of the cell lysate was loaded on to Ni-NTA column (Qiagen,Valencia,CA) by circulating the solution at 1ml/min through the column bed overnight. Next day, the column was washed with 50mM Tris buffer, 50mM phosphate buffer followed by four different washes of 50mM phosphate, 200mM NaCl pH 7.0 buffer containing increasing imidazole concentrations (2mM, 20mM, 50mM, and 200mM). 2 and 20mM washes removed most non-specifically bound proteins, whereas 50 and 200mM washes eluted the target protein off the column. Excess imidazole was removed by gel filtration chromatography using 50mM phosphate buffer and 50mM NaCl at pH 7.0. Protein was aliquoted in 1.5ml microcentrifuge tubes and stored at -80°C for future use.

2.3.2. Insoluble protein purification

A denaturing protein purification procedure was used for proteins which were expressed in inclusion bodies. In this procedure, after cells were centrifuged down to pellets, the pellets were resuspended in 200 mM phosphate buffer, pH 7.0 (Buffer A) supplemented with 0.1 mM PMSF and 0.1 mg/ml lysozyme, and homogenized. Cells were then lysed by sonication using Branson Sonifier 250 (Branson Ultrasonics Corp., Danbury, CT, USA). Following sonication, benzonase (250 units) was added, and the mixtures were gently stirred at 23 °C for 1 hour. The cell lysates were then centrifuged at 16,000 × g. The pellets, which contained the proteins of interest, were then resuspended in 8M urea and homogenized. Centrifugation at 16,000 × g was repeated. This time urea served to solublize the inclusion-body though they remained in a denatured state. Thus, each supernatant was mixed with Ni-NTA resin and gently agitated at 23 °C overnight. The resin was then loaded into an empty column, washed with 10 mM imidazole in 8 M urea, and then the protein was eluted off the resin with 200 mM imidazole in 8 M urea. Urea and imidazole were then removed by dialysis against buffer A for 36 hours. The bulk dialysis buffer was replaced every six hours.

2.4. Enzyme reconstitution

After purification enzyme was reconstituted by addition of hemin (0.9 equivalents). Due to poor solubility of hemin at neutral and acidic solution, working solutions of hemin were prepared by dissolving solid hemin in 0.1 M KOH. After the addition of hemin, the enzyme was allowed to incubate for 24 hrs at 4°C. Following incubation, reconstituted enzyme was

centrifuged at 13,000 rpm for 5 minutes to remove insoluble hemin, complexes and protein aggregates. All spectral measurements for ferric and ferrous forms of enzyme were carried out by scanning the enzyme between 800 nm to 250 nm at room temperature in 100 mM phosphate buffer, pH 7.0 using Shmiadzu UV-1601 spectrophotometer. The pyridine hemochrome assay was used to determine the concentration of reconstituted enzyme (*124*). This assay is based on the characteristic absorption spectrum of oxidized and reduced form of the hemochrome by replacing the axial ligands with pyridine. Briefly, a reference solution of reconstituted enzyme, 20% pyridine, 0.1 M NaOH and 0.3 mM $K_3Fe(CN)_6$ was made in a cuvette. A reference spectrum was then recorded from 560 nm to 530 nm. A miniscule quantity of sodium dithionite was then added and a second spectrum was recorded. Addition of pyridine, followed by the reducing agent (sodium dithionite) reduces the ferric enzyme to hexacordinate low spin ferrous form. Reconstituted enzyme concentration was calculated by the dividing the absorbance difference between the peak (~ 555 nm) and trough (~ 538 nm) absorbance by the difference in their absorptivities (20.7 mM^{-1} cm^{-1}).

2.5. Spectroscopic characterization of KatG variants

In order to understand the impact of substitutions and deletions within LL1 and LL2 on the structure and catalytic function of KatG, a full panel of spectroscopic and kinetic techniques was brought to bear on each one. Described here are the principles underlying each technique, the general approaches to our analyses of the data, and the information that each provides with regard to KatG structure and catalysis. The particular details of these experiments (e.g.,

instrumental parameters, solution conditions and concentrations used, etc.) will be included in the subsequent chapters in which they are most appropriate.

2.5.1. Circular dichroism (CD) spectroscopy

Circular dichroism occurs when a sample differentially absorbs left-handed circularly polarized (lcp) light and right-handed circularly polarized (rcp) light ($\Delta\varepsilon=\varepsilon_L-\varepsilon_R$). This is a property of a chiral or optically active chromophore. Most biological macromolecules, including proteins, are composed of chiral building blocks and these components often have chromophores in the UV range. CD spectroscopy is a technique in which the CD of a molecule is measured over a range of wavelengths. For proteins, the most frequent application of this technique is to evaluate CD at far UV wavelengths to assess secondary structural content (e.g., α-helix, β-sheets, etc.). Individually, the $n\rightarrow\pi^*$ and $\pi\rightarrow\pi^*$ transitions associated with the peptide bond are very weak and tend to cancel one another. However, in a given secondary structure where the conformational features of peptide bonds are repeated, a cumulative effect is observed which is characteristic for the major types of secondary structures found in proteins.

Effective application of CD spectroscopy depends on comparison against some known standard. In case of using CD as a measure of protein structural stability (with respect to temperature, pH, or otherwise), spectra recorded under conditions favoring the unfolding of a protein are compared against the spectrum recorded under conditions favoring the folded state. Likewise, a CD spectrum for wild-type protein is the standard against which any variant is

measured. Finally, the secondary structural content of an unknown protein can be estimated from its spectral characteristics when compared against CD spectra for proteins of known structure.

Secondary structure of the proteins is determined in the "far-UV" spectral region (190-250 nm). Different secondary structures of proteins such as α helices, β sheets, random coil, type I β-turn, and extended 3_{10}-α helices give rise to characteristics shapes and magnitude of CD spectrum (Figure 2.3) (*125*). The "near-UV" spectral region (250-350 nm) CD spectrum of a protein is helpful for determining certain features of tertiary structure. Aromatic amino-acids and disulphide bonds at this wavelength range produce CD signals which are sensitive to the changes in the overall tertiary structures of proteins. In this study, all the variants prior to reconstitution with hemin were used to record the far-UV CD spectra (180 -300 nm) using a Jasco J-180 spectrapolarimeter. To ensure that absorption by samples was not excessive, low concentrations (5 μM) of protein were prepared in only 5mM phosphate buffer and a minimal pathlength (0.05 cm) CD cuvette was used. Phosphate buffer was used as it is one of the better buffers in terms of its minimal absorption in the UV. Low concentration of sample and buffer ensured maximal signal to noise ratio in the CD spectrum and avoided masking of CD signals by the buffer. The short pathlength of cuvette helped to overcome sample absorption and permitted scanning to lower wavelengths. The instrument was purged with N_2 gas in order to remove O_2 from the lamp housing and the sample compartment which prevented ozone formation and minimized the damage to the optical systems. Also, N_2 atmosphere allowed measurements to be made below 200 nm. In order to improve the quality of the data and to be consistent in data acquisition over the range of variants, experimental parameters like the time constant, the scan rate, the number of scans, and the bandwidth were kept standard.

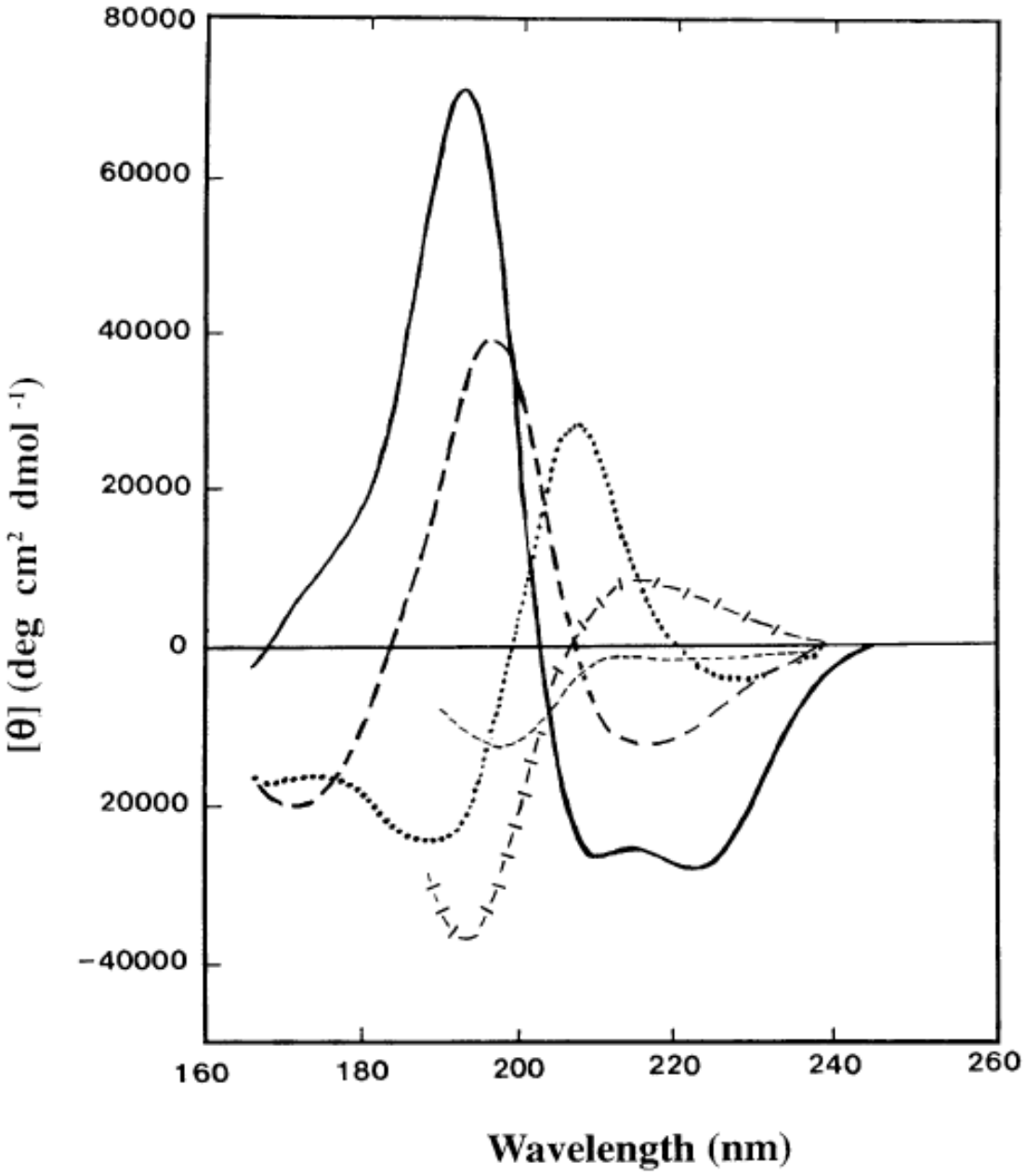

Figure 2.3: Far UV CD spectra associated with various types of secondary structures. Solid line, α-helix; long dashed line, anti-parallel β-sheet; dotted line, type 1 β-turn; cross dashed line, extended 3_{10}- α-helix; short dashed line, irregular structure *(125)*.

2.5.2. UV-visible absorption spectroscopy

Although UV-visible absorption is central to a number of our kinetic studies, the kinetic application of UV-vis will be covered later in this chapter. As a purely, spectroscopic tool, UV-visible absorption has two primary applications. The first is to evaluate KatG as a generic protein based on absorption due to the presence of aromatic amino acid side chains, particularly tryptophan and tyrosine. Phenylalanine does also absorb UV light, but due to its very low molar absorptivity, its contribution to the overall spectrum of KatG is minimal. Likewise, cysteine is recognized to be a contributor, but *E.coli* KatG has only one cysteine side chain. The dominant band in the UV has an absorption maximum at 281 nm. This is the result of a cumulative contribution of 22 tryptophan residues and 15 tyrosine residues, resulting in a particularly and unusually intense absorption band. Indeed, the theoretical molar absorptivity expected from this composition is 144,000 $M^{-1}cm^{-1}$ (*126*). The intensity of absorption at 280 nm is a convenient method of estimating the concentration of purified KatG. The spectrum for KatG from 320-250 nm also serves for the qualitative evaluation of the stability of the protein isolated. A progressively intensifying baseline as one scans further into the UV is indicative of light scattering. Though there are several underlying causes for light scattering in a given sample, one particularly relevant to the work described here is protein aggregation. Substantial light scattering suggestive of protein aggregation is an early indication that a given variant lacks structural stability and is prone to non-specific association and precipitation.

Because KatG is a heme-containing enzyme, UV-visible absorption is also highly useful for evaluating the oxidation state and coordination environment of the heme itself. Generally,

speaking, heme will have at least three prominent absorption bands which arise due to π-π^* transitions in the conjugated π system of the heme. In order of increasing energy and intensity, these bands are called α (Q_{00}), β (Q_{0v}), and γ (Soret). The Soret band (γ) is the most intense band, and is the highest energy transition therefore, occurs at lowest wavelength of the three. In free heme, the Soret band is observed at 380 nm. When incorporated in a protein, the absorption will red shift typically to wavelength greater than 400 nm. When electrons from the porphyrin π-system are transferred from highest energy-filled orbital to lowest energy unfilled orbitals (d_π) of the iron, charge-transfer (CT) bands are observed. The appearance of CT bands depends upon the spin state of heme. The characteristic absorption bands of KatG in its resting state occur at 408 nm (Soret), 502 nm (CT2), and 640 nm (CT1) (Figure 2.4). In the high-spin complex of KatG the α and β bands are largely obscured by the charge transfer bands. However, charge transfer bands are not observed in low-spin complexes and are too weak to observe when the iron is in ferrous state. In low-spin complexes, the charge transfer is blocked due to dropping of a porphyrin π^* electron into a *d* orbital of the iron completely filling the *d* orbitals. The characteristic absorption bands of the low-spin ferricyano-KatG complex occur at 422 nm (Soret), ~542 nm (β), and ~575 nm (α). Thus, it is evident that the ligand environment of heme iron affects its optical absorptions, both at π-π^* and CT transitions.

Isolated KatGs contain heme with the iron in its ferric oxidation state. Ferric iron contains five d-electrons, in the absence of external influences and according to Hund's rule, each occupy one of five degenerate d-orbitals (Figure 2.5). Though a somewhat rudimentary approach, crystal field theory provides a straightforward explanation for the effect of ligands on

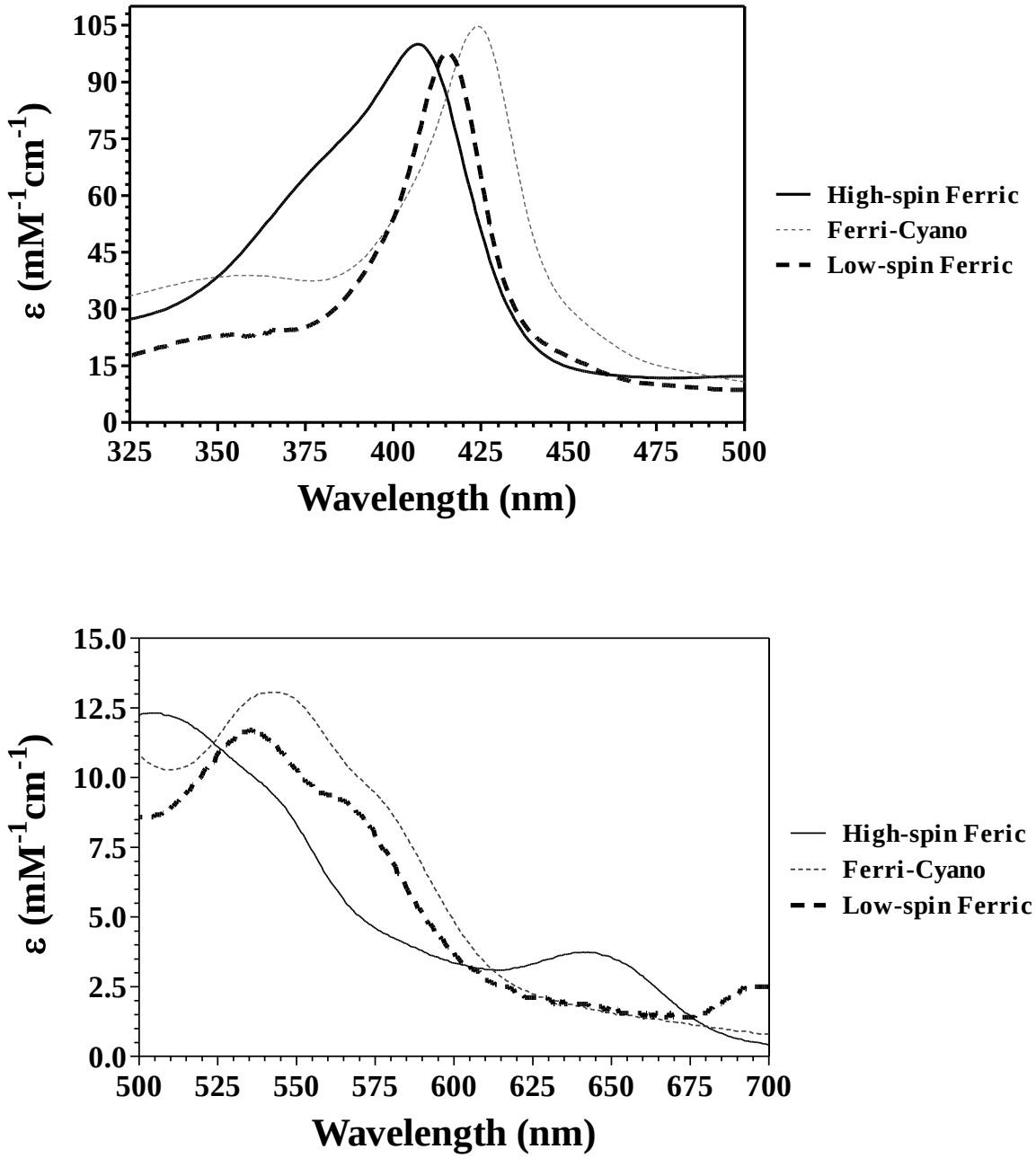

Figure 2.4: Typical absorption spectra for KatG in the Soret (top) and charge transfer (lower) regions.

the energies of the five *d* orbitals. Each of six ligands can provide a lone pair of electrons for bonding to the iron, and in an octahedral complex could occur along the x, y, and z axes. By virtue of electron-electron repulsion, iron *d* orbitals oriented along the axes (i.e., d_{x2-y2} and d_{z2}) will be higher in energy than those oriented between major axes (i.e., d_{xy}, d_{xz}, and d_{yz}). Ligands which destabilize the on-axis orbitals in such a manner that electron pairing energy is less than the energy required to place an electron in a destabilized orbitals (i.e, splitting energy) are strong field ligands (Figure 2.5) whereas, the ligands which do not split the energy levels so severely are weak field ligands. In the presence of strong field ligand iron (III) has a +½ spin (i.e., low spin) whereas in the presence of weak-field ligand it will have +5/2 spin (i.e., high spin).

Other factors can result in further differentiation of the *d* orbital energies, and such is the case in many heme proteins (Figure 2.6). The pyrrole nitrogens of heme are located in the plane of d_{x2-y2} and d_{xy} orbitals of iron and electrons in d_{x2-y2} are pointed towards the bonding pair of electrons of pyrrole nitrogens and are strongly repelled. Also, the electrons in d_{xz} and d_{yz} orbitals are repelled more strongly than in d_{xy} due to the conjugation of the porphyrin. The d_{z2} orbital is sensitive to the fifth and sixth ligands, both of which are located along the z-axis. As stated earlier, in the conjugated π system of the heme, three π-π^* transitions designated as α, β, and γ are observed. The α transition originates from a_{2u} state to π^* (e_g) state. The β band has the same origin but goes to the vibrationally excited levels of the e_g state, and thus is of slightly higher energy. The Soret band (π) is of the highest energy due to the fact that it originates from the lower energy π (a_{1u}) ground state but ends at the same e_g π^* as the α transition (Figure 2.7).

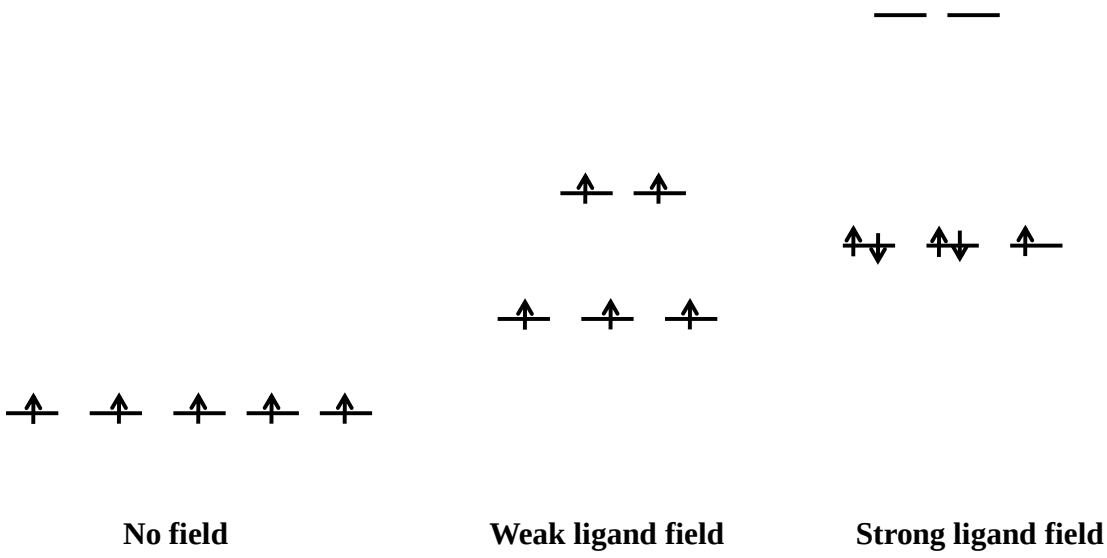

Figure 2.5: Effects of ligands on Fe^{III} *d*-electrons.

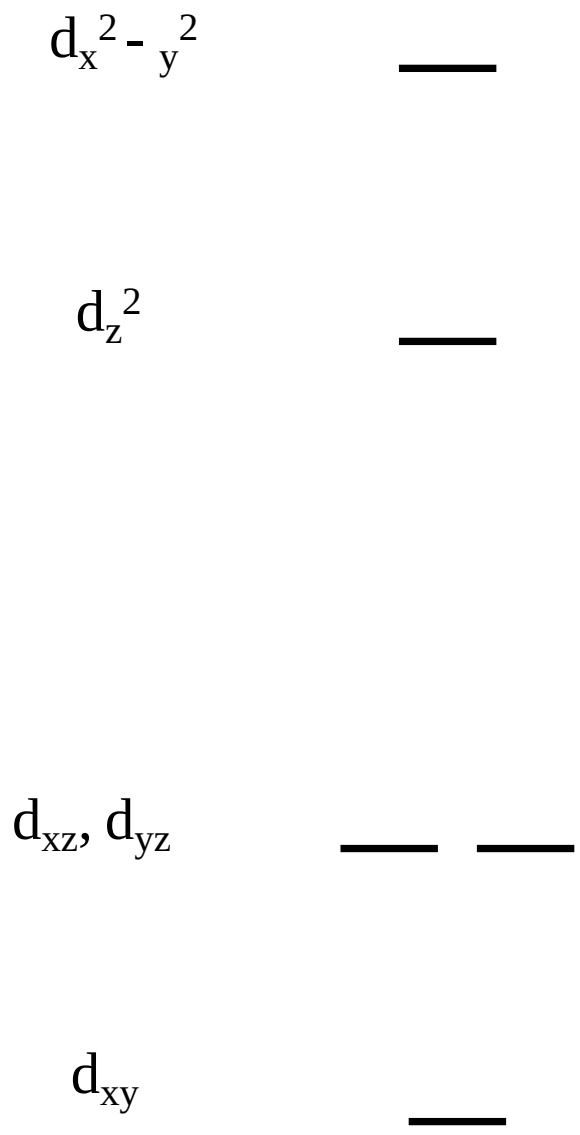

Figure 2.6: Further splitting of *d*-orbital energy levels in heme peroxidases.

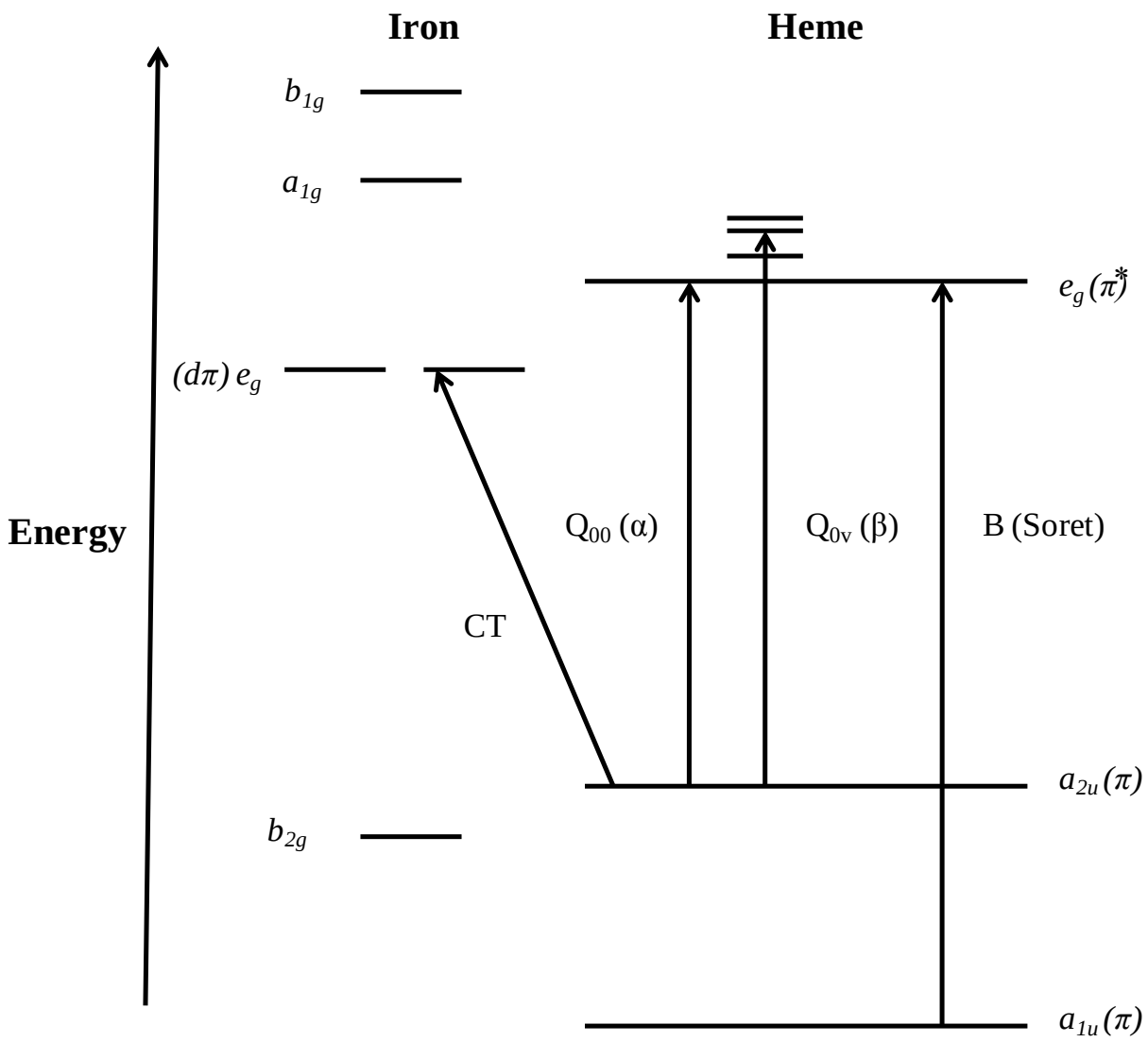

Figure 2.7: Electronic transitions observed in heme peroxidases.

2.5.3. Magnetic Circular Dichroism spectroscopy

Magnetic circular dichroism (MCD) as the name suggests is the measurement of a CD signal in the presence of external magnetic field oriented parallel to the direction of light propagation. The magnetic field or Faraday effect is induced in a particular chromophore through its effect on the electronic properties of the absorbing species as a consequence of Zeeman splitting. Three different types of MCD spectra are evident and are termed as A, B, and C. A and B terms are temperature-independent, whereas the C term is temperature dependent (*127*, *128*).

An "A term" arises when transitions occur from a non-degenerate ground state to a doubly degenerate excited state (Figure 2.8). These transitions require absorption of lcp and rcp light giving rise to derivative shaped signal. A "C term" is same as an "A term" but instead of magnetic field splitting, it splits the ground state (Figure 2.9). This causes difference in the intensity between lcp and rcp resulting in Gaussian shaped signal. A "B term" arises from nondegenerate ground-state and excited-state mixing brought on by the magnetic field and is Gaussian in shape.

MCD spectra have been observed for numerous heme proteins of known oxidation and spin state. This provides a substantial archive for comparison to new and lesser known heme systems like those of KatG. Moreover, the identity of axial ligands and characteristics of their protein environment can be evaluated, but this typically requires access to near infrared wavelengths. The easiest application of MCD to heme proteins is distinguishing between high-spin and low-spin ferrous heme which can be accomplished by monitoring features between 350 and 750 nm.

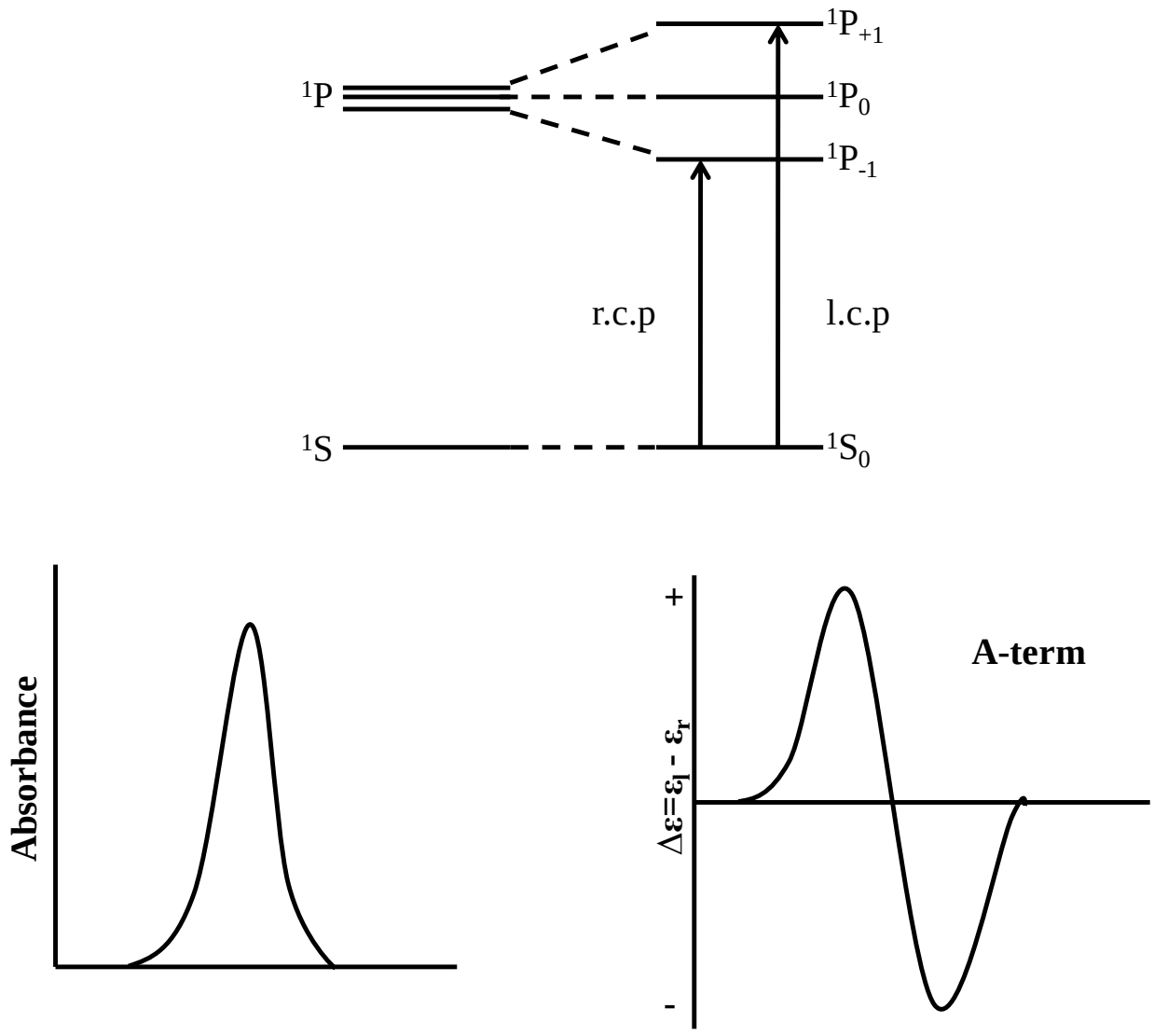

Figure 2.8: Basis for an MCD spectrum: A-term.

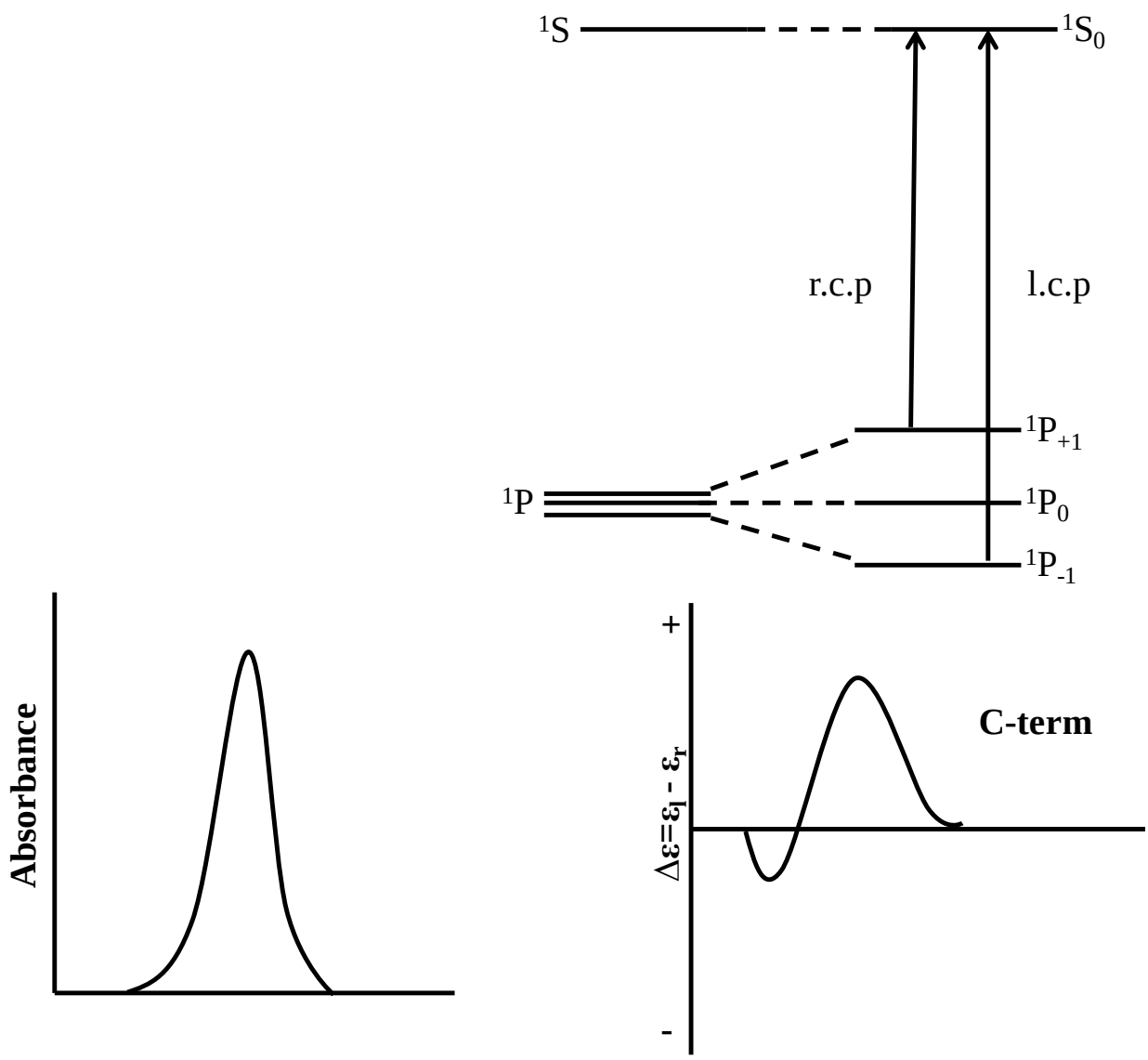

Figure 2.9: Basis for an MCD spectrum: C-term.

The transitions observed in the MCD of ferrous heme are due to the Soret band and α and β bands. An intense "A" term signal is observed near 550 nm in the low-spin ferrous heme due to the α and β band. However, in case of high-spin ferrous heme and also low and high spin ferric heme, the spectra are more complex. This is due to the presence of new transitions like charge transfer bands (and possibly weaker d-d transitions) and the unpaired electrons on the iron which produce a spin degeneracy in the system. Two effects arise due to this ground state spin degeneracy; first a C-term is produced, and second, spin-orbital coupling of iron to porphyrin is observed, which splits the porphyrin energy level (*129, 130*). According to spin-orbital coupling theory high-spin ferrous heme MCD spectrum show Soret absorption maxima near 430-440 nm and exhibit an intense positive MCD and weaker negative MCD signals. Also the features near 550 nm are less intense in case of high-spin ferrous heme. The difference in the intensity due to the α and β band near 550 nm and near absence of Soret maxima in case of low-spin ferrous heme around 435 nm is a good marker for distinguishing the contribution of high- and low-spin ferrous heme (Figure 2.10).

2.5.4. Electron Paramagnetic Resonance (EPR)

Optical spectroscopy is a highly effective and straight forward method for the determination of concentration and enzymatic activity. However, its use as a tool for structural characterization of metal sites in proteins is far more limited. In particular, for heme proteins it should be remembered that the majority of spectral features observed by UV-Vis are due π to π^* transitions in the porphyrin π electron system rather than the metal itself. EPR spectroscopy circumvents these issues and is an ideal technique to characterize the structure and function of

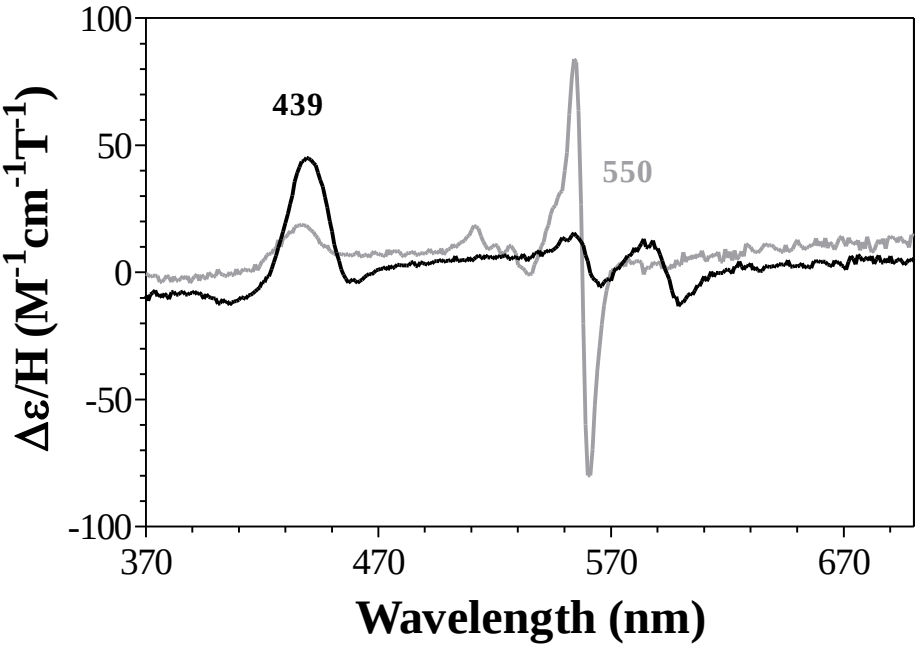

Figure 2.10: Characteristic differences in ferrous MCD spectra of high-spin (black) and low-spin heme (gray).

heme proteins. In heme proteins EPR usually applies to their ferric form and in this state two characteristic families of EPR spectra predominate; low-spin Fe^{3+} (S=1/2) and high-spin Fe^{3+} (S=5/2) (*131*).

The basic principle behind EPR relies on the interaction of a paramagnetic species within the molecule of interest with an external magnetic field. The external magnetic field lifts the degeneracy of the + ½ and – ½ electron spin states such that one is aligned with the magnetic field (m_s = + ½) and the other is aligned against the magnetic field (m_s = - ½) (Figure 2.11). The energy difference between the two spin states is given by the equation 2.1, which is dependent upon the strength of the magnetic field (B) (*132*).

$$\Delta E = E_+ - E_- = h\nu = g\beta B \qquad \textbf{(2.1)}$$

Where B is the strength of the magnetic field in Tesla but usually represented as Gauss, β is the Bohr magnetron (9.274×10^{-24} J T^{-1}), h is Planck's constant (6.626×10^{-34} J s^{-1}), and ν is operating frequency of the spectrometer radiation. Of course, h and β are constants and in the EPR experiment, and the frequency of radiation is held constant at a given level depending on the band EPR (e.g., ν at X-band is 9 GHz). The g-factor is the Zeeman splitting factor, and it is a tensor which specifies the strength of interaction between unpaired electrons and the applied magnetic field, B. In a paramagnetic species, the g-factor depends on the coordination number and geometry of the paramagnetic center and the chemistry of the primary ligands to the heme. This indirectly provides information about the location and environment of the unpaired electrons.

In paramagnetic species, the g-factor is anisotropic meaning that it depends directly on its

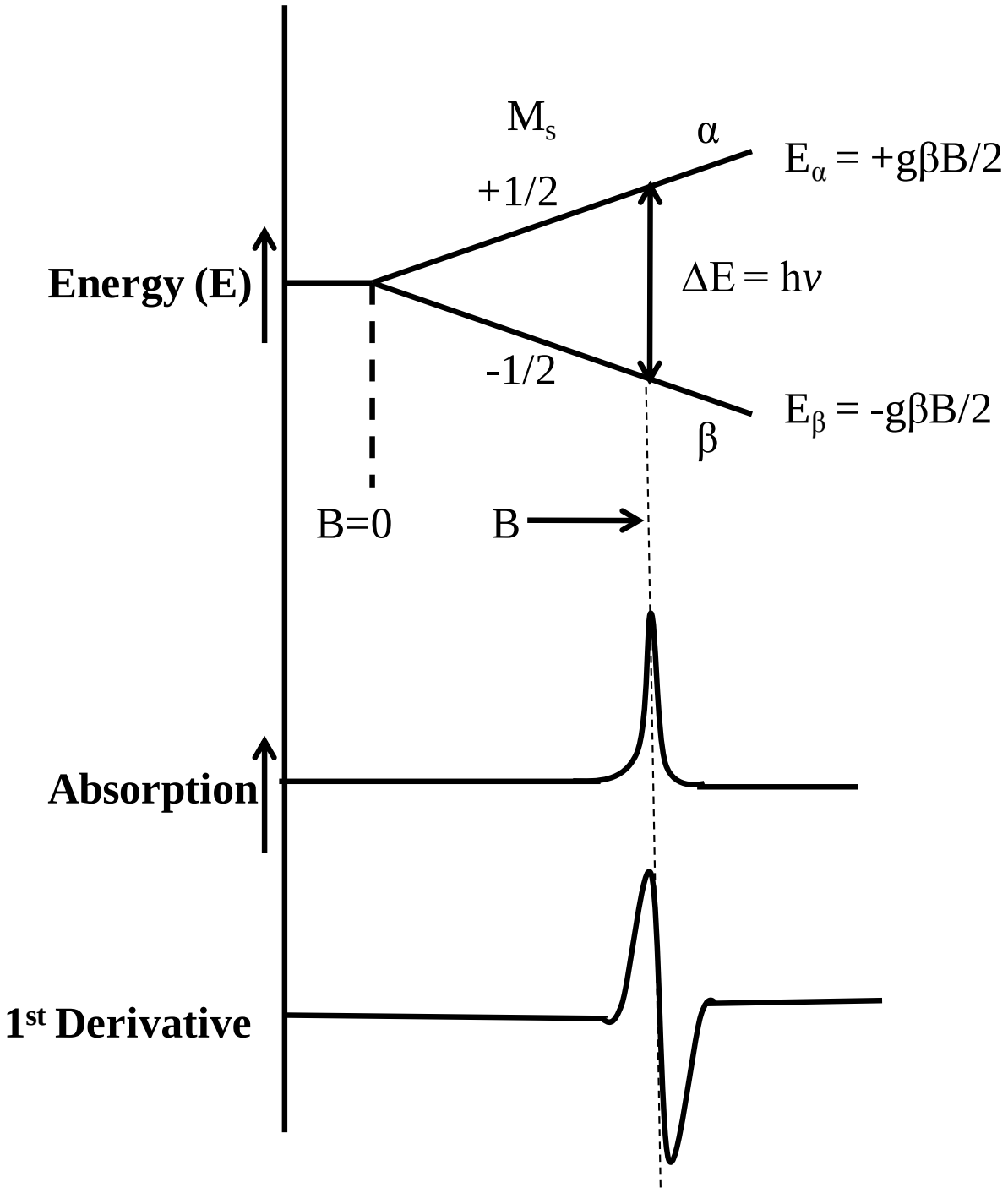

Figure 2.11: Electronic paramagnetic absorption.

orientation in the magnetic field. Thus, for anisotropic species, the g-factor breaks down into different values of g for different orientations depending on the alignment of B along the Cartesian axes (x, y, and z) (*39*). For instance, in case of a heme protein, if the magnetic field is perpendicular to the plane of heme porphyrin it can result in three g-values g_x, g_y, and g_z, and there are three types of symmetry associated with these three g-values (Figure 2.12) (*131*, *133*). When all three g-values are equal ($g_x = g_y = g_z$), the symmetry around heme is isotropic and is not dependent on orientation in the magnetic field. When two g-values are equal, the resulting EPR spectrum is axially symmetric (suggesting an axially symmetric microgeometry for the paramagnet). The unique g-values are $g_{\parallel}$ (parallel to the symmetric axis $=g_z$) and the other two equivalent g-values are referred to as $g_{\perp}$. The axial symmetry has two subsets. One where $g_{\perp} > g_{\parallel}$ and second where $g_{\parallel} > g_{\perp}$. When all the three g-values are unequal ($g_x \neq g_y \neq g_z$) it refers to rhombic case and implies that the microsymmetry around heme iron is no higher than rhombic.

In KatG three EPR spectra are generally observed; hexacoordinate high-spin ferric heme spectrum is dominated by axial with slight contribution from rhombic signal (Figure 2.13, Panel A), pentacoordinate high-spin ferric heme dominated by rhombic signal with minor contribution from axial signal (Figure 2.13, Panel B) and hexacoordinate low-spin ferric heme spectrum (Figure 2.13, Panel C). The EPR of high-spin ferric heme have g-values centered around $g_{\perp}=6$ and $g_{\parallel} =2$, and in low-spin EPR ferric heme three different values of g are seen (*131*).

For the purpose of the work here, EPR was used as a tool to determine the effect of various mutations on spin state and coordination environment of the heme in the active site. It was also used to determine the relative concentrations of the different species in the population.

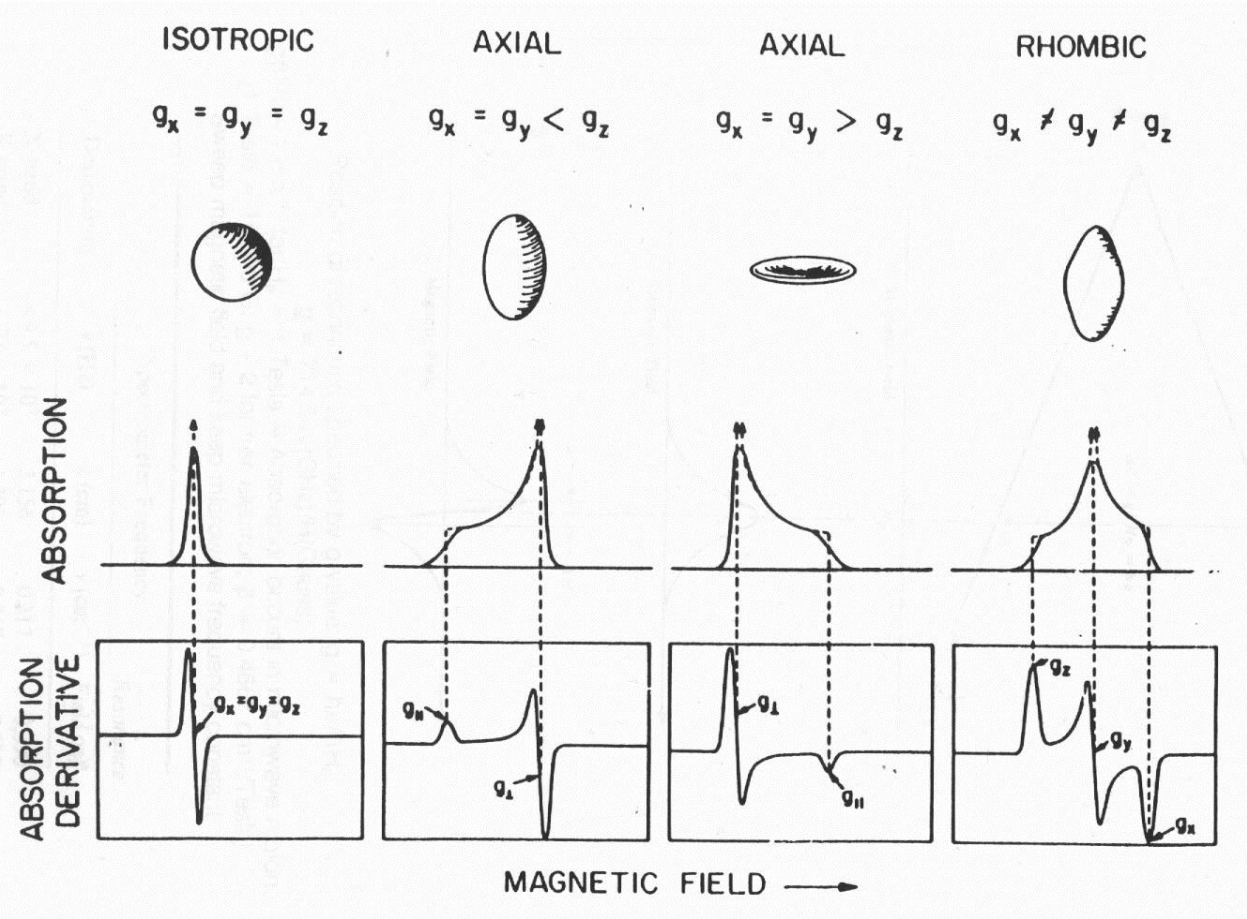

Figure 2.12: EPR absorption derivatives.

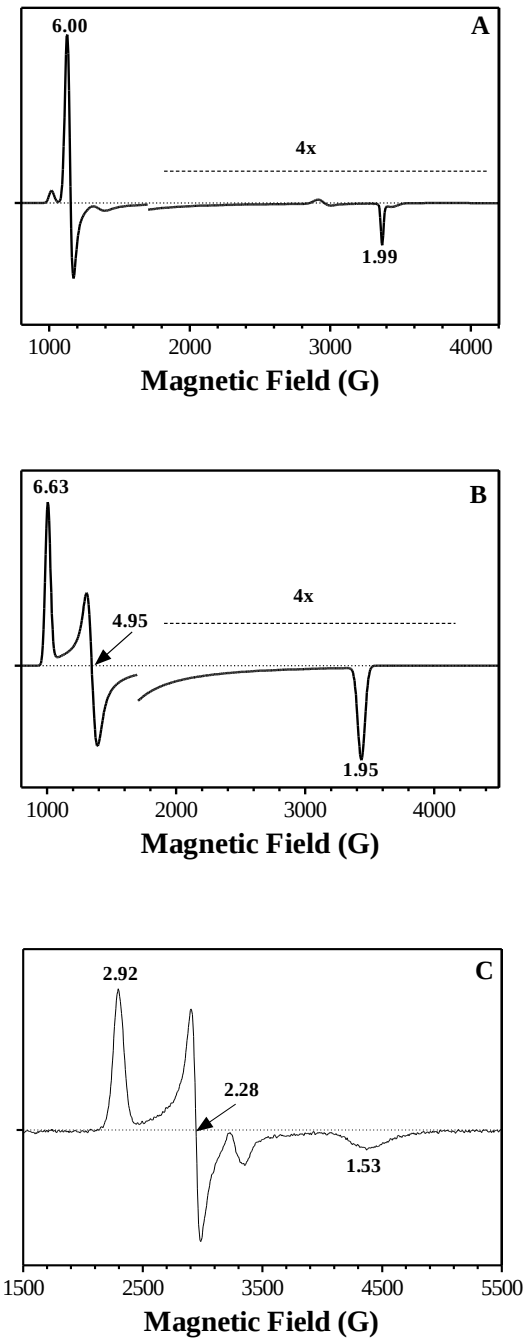

Figure 2.13: Different EPR spectra observed in catalase-peroxidases. High-spin hexacoordinate heme (A), high-spin pentacoordinate heme (B), and low-spin hexacoordinate heme (C). g-values shown in each spectrum are the estimates and can vary to some extent depending upon the heme environment.

To obtain sufficiently intense signals for each EPR spectrum, frozen samples of ~300 μL at ~150μM concentration were prepared in liquid nitrogen and spectra were recorded at low temperature (~10 K). EPR signal magnitude is proportional to population difference, which is dictated by a Boltzman distribution. Low temperature increases the population difference. But this population difference is depleted by microwave excitation and restored by intrinsic spin-lattice relaxation process. Thus, low temperature increases the EPR amplitude and decreases the linewidth by decreasing the spin-lattice relaxation rate, which in turn increases the lifetime of the excited state, and decreases the uncertainty in the excited state (*132*).

The double integration of the absorption derivatives of the individual components was used to quantify the relative amount of each species in EPR spectra. The resultant spin intensity was compared with that of a standard to calculate concentrations of species present. In order to determine how the intensities of the EPR signals obtained from KatG variants were related to the concentrations of the paramagnetic species responsible, spin quantification was carried out using Biomolecular EPR spectroscopy software package available online (*134*). The strategy was to obtain the pure line shapes of all the signals, integrate these line shapes, and then finally measure how much of each there was in every spectrum.

In KatGs, EPR signals were mainly characterized by three effective g-values; two for high-spin heme species (axial and rhombic) and the third one for low-spin heme species. In some cases, axial signal showed two subsets with g-values very close to each other which complicated the spectrum and hence quantitation of different species. Thus, three high spin signals and one low-spin signal were required to obtain the desired simulations. The high spin signals included: two axial signals (AHS1) with g-values of 5.85 and 1.99, and AHS2 with g-values of 5.69 and

1.99 and one rhombic signal (RHS) with g-values of 6.65, 4.95, and 1.95. The low-spin signal was rhombic (RLS) with g-values of 2.93, 2.27, and 1.53. After obtaining the lineshapes of all the individual signals, double integration was carried out. From these integration values, percentages of each paramagnetic species were calculated.

2.6. Kinetic characterization of KatG variants

The spectroscopic tools reviewed above provide valuable insight into the environment around a protein bound heme and the effect of amino acid substitutions or deletions. However, to be of interpretive value these effects must be related to the catalytic performance of the enzyme in question. Steady-state kinetic methods allow for the evaluation of catalytic performance under multiple turnover conditions monitoring the continuous generation of product or consumption of substrate. These studies allow for the determination of general parameters governing enzyme turnover as a function of substrate concentration. Transient-state kinetic methods allow one to evaluate individual steps in the catalytic process to determine the basis for changed steady-state kinetic parameters.

2.6.1. Steady-state kinetic analysis

Catalase and peroxidase activities

One catalase activity assay measures the decomposition of H_2O_2 to H_2O and O_2 in the presence of enzyme at 240 nm ($\varepsilon_{(H2O2)}$ at 240 = 39.4 M^{-1} cm^{-1}) (*135*). This assay is typically carried out at room temperature using pH 7.0 phosphate buffer.

For the peroxidase activity assay, H_2O_2 is reduced and suitable electron donor is subsequently oxidized. The oxidized electron donor absorbs light and can be determined spectrophotometrically. Because the identity of the physiological electron donor of KatG is still unknown, a wide variety of organic and inorganic substances serve as electron donors. In this work, ABTS (2,2'-azino-bis[3-ehtyl benzothiazoline-6-sulphonic acid]) was used as the electron donor. ABTS was chosen because its radical oxidation product relatively stable in aqueous solution, has a high molar absorptivity at 340 nm (ε_{340} = 3.66 x 10^4 M^{-1} cm^{-1}) and its oxidized form absorbs at 417 nm (ε_{417} = 34.7 mM^{-1} cm^{-1}) (*136*). The data from the activity assays were fit to one of the following equations.

When no substrate-dependent inhibition was observed, equation 2.2 (i.e., Michaelis-Menten equation) was used (*137*).

$$\frac{v}{[E]_T} = \frac{k_{cat}[S]}{K_M + [S]} \qquad \textbf{(2.2)}$$

In this equation, v is initial velocity of formation of product, $[E]_T$ is the total enzyme concentration, [S] is substrate concentration, k_{cat} (turnover number) is the maximum number of substrate molecules converted to products per active site per unit time, and K_M (the Michaelis constant) is the concentration required to reach half the maximum velocity. At saturating concentrations of substrate $v/[E]_T$ is equal to k_{cat}, whereas at low substrate concentrations, the slope of $v/[E]_T$ vs [S] approaches the apparent second order rate constant k_{cat}/K_M. k_{cat}/K_M is a measure of efficiency of the enzyme with a given substrate.

This classical Michaelis-Menten equation describes the simplest enzymatic mechanism in which the association of enzyme with substrate is followed by the release of product (equation 2.3) (*137*):

$$E + S \underset{k_{-1}}{\overset{k_1}{\rightleftharpoons}} ES \xrightarrow{k_2} E + P \qquad \textbf{(2.3)}$$

E - free enzyme, S – substrate, ES – the enzyme-substrate complex, P – product, $(k_2 + k_{-1}) / k_1 = K_M$, and $k_2 = k_{cat}$

The mechanism of KatGs is quite complex such that the standard interpretation of Michaelis-Menten parameters cannot be applied even though the catalase activity of KatG does follow the Michaelis-Menten kinetics allowing reasonable estimation of apparent k_{cat} and K_M values. However, peroxidase kinetics pose an additional difficulty due to substrate-dependent inhibition with respect to both H_2O_2 and some electron donors. Thus, in this situation it becomes difficult to observe true saturating conditions. In this case, equation 2.2 was modified to include substrate-dependent inhibition to accommodate a second apparent dissociation constant (K_I) corresponding to the substrate's action as an inhibitor. Hence, equation 2.4 was used when substrate dependent inhibition was detected (*137*).

$$\frac{v}{[E]_T} = \frac{k_{cat}[S]}{K_M + [S] + [S]^2 / K_I} \qquad \textbf{(2.4)}$$

In its simplest form this relationship is seen when a second molecule of substrate binds to ES to give an ES_2 complex that is catalytically inactive, equation 2.5 (*137*):

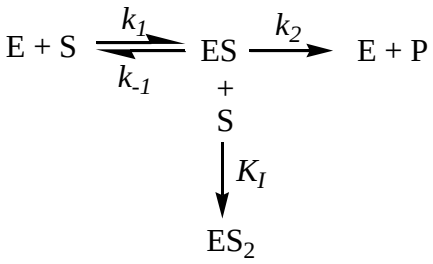

(2.5)

At low concentrations of substrate, rates can still be fit to a Michaelis - Menten equation. But as [S] increases, there is first a maximum value of *v* followed by a decrease.

2.6.2. Transient-state kinetic analysis of KatG

Stopped-flow experiments

Steady-state kinetic measurement usually defines the kinetic boundaries of an enzyme-catalyzed reaction by providing two essential pieces of data on kinetic performance, one corresponding to low concentration of substrate (k_{cat}/K_M) and one corresponding to high concentration of substrate (k_{cat}). In order to measure the rate constants of the individual steps on the reaction pathway and to detect and monitor intermediates involved in the catalytic process, it becomes necessary to measure rates by transient-state methods.

Transient-state kinetic methods are usually applied to the observation of rates that occur in a very short time (i.e., the short period of time from the enzyme encountering the substrate / inhibitor / other ligands to the point of equilibrium). Our instrument can be used to detect and monitor intermediates occurring in this time frame. Stopped-flow apparatus can be used to carry out either single mixing or double mixing experiments. In the work described in this dissertation, stopped-flow was used to observe the reactions of H_2O_2 and ABTS with large loop 1 variants and

also to monitor the rate of cyanide binding in case of large loop 2 variants. A SX.18MV rapid reaction analyzer (Applied Photophysics Surrey, UK) was used to carry out all the stopped-flow measurements. The basic set up of the instrument is shown in Figure 2.14 (*138*).

In single-mixing experiment, the drive motor rapidly fires two solutions (e.g., enzyme in syringe A and substrate in syringe B) together into a mixer. The mixed solution then flows into the observation cell. At this point, a stop syringe limits the volume of the solution used in each experiment and stops the flow of the solution. The flow of the solution into the stop syringe moves the plunger back and triggers the data collection. The mixed solution in the observation cell is illuminated by a light source and the change, as a function of time, in absorbance can be measured.

For large loop 1 variants in single mixing experiments, the enzyme was allowed to react with varying concentrations of H_2O_2 for a defined period of time. This allowed for the formation of higher oxidation states which were monitored initially by diode array to observe the formation and transition of different oxidation states from the native ferric state. Later, rate of formation of these different states were recorded at relevant single wavelengths. The single wavelength was chosen carefully to get an optimal distinction between formation and decay of one species to another.

For large loop 2 variants, the enzyme was allowed to react with varying concentrations of KCN. Full spectra were recorded by diode array to observe the shift in the Soret band as enzyme with high-spin ferric heme species transitioned to low-spin ferric heme form (Figure 2.15).

The kinetic constants for cyanide binding were measured by observing the time course of

Single-Mixing Stopped-Flow

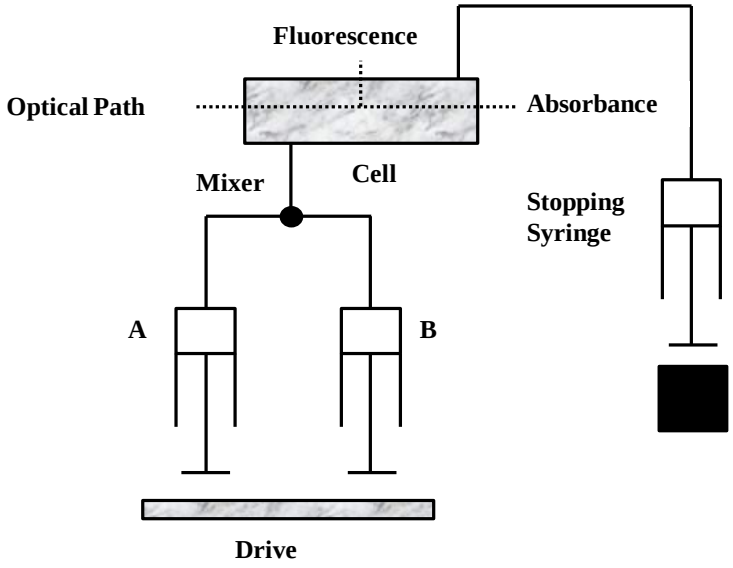

Double-Mixing Stopped-Flow

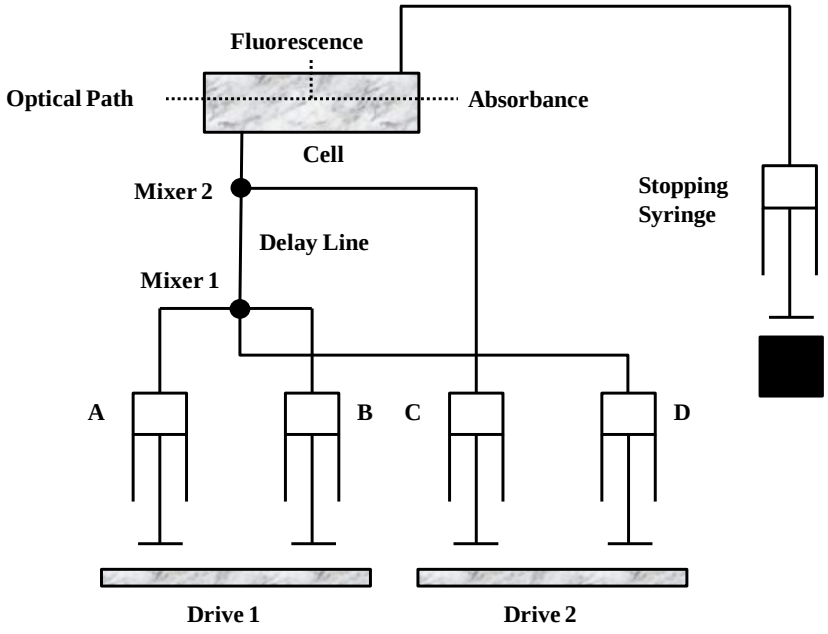

Figure 2.14: Basic setup for stopped-flow instrument. Scheme adapted from http://www.hi-techsci.com

cyanide binding at single wavelength (either 400 or 428 nm). Observed pseudo-first order rates were plotted as a function of cyanide concentration to obtain second-order rate constants for cyanide binding.

In double mixing experiments, three reactants are mixed together in a sequential fashion. The first two syringes (enzyme in syringe A and one substrate in syringe B) drives the two solutions together through mixer 1 into a delay line. The time between the first and second ram firing determines the length of the first reaction. After passing through the delay line, the solution enters the mixer 2 where the third reactant is encountered. Then the mixed solution is passed into the observation cell. This triggers the data collection as described for the single mixing experiment.

In double mixing experiments carried out using large loop 1 variants, enzyme was first allowed to react with H_2O_2 and the reaction mixture was left to incubate in delay line for set period of time. The content of delay line was then mixed with ascorbate and varying concentration of ABTS. The full spectra were recorded by diode array and rate constants for ABTS-dependent reactions were measured at single wavelength. Ascorbate was used as it reduces ABTS radicals as rapidly as they are generated, ensuring a constant substrate concentration during the reaction (*114, 139*). Ascorbate is often a poor substrate for peroxidase enzymes and has been a very effective tool for measuring rapid peroxidase reactions with electron donors and minimizes the interference from the oxidized products. Moreover, the concentration of ascorbate was kept constant in our ABTS stopped-flow studies making its contribution easy to account for.

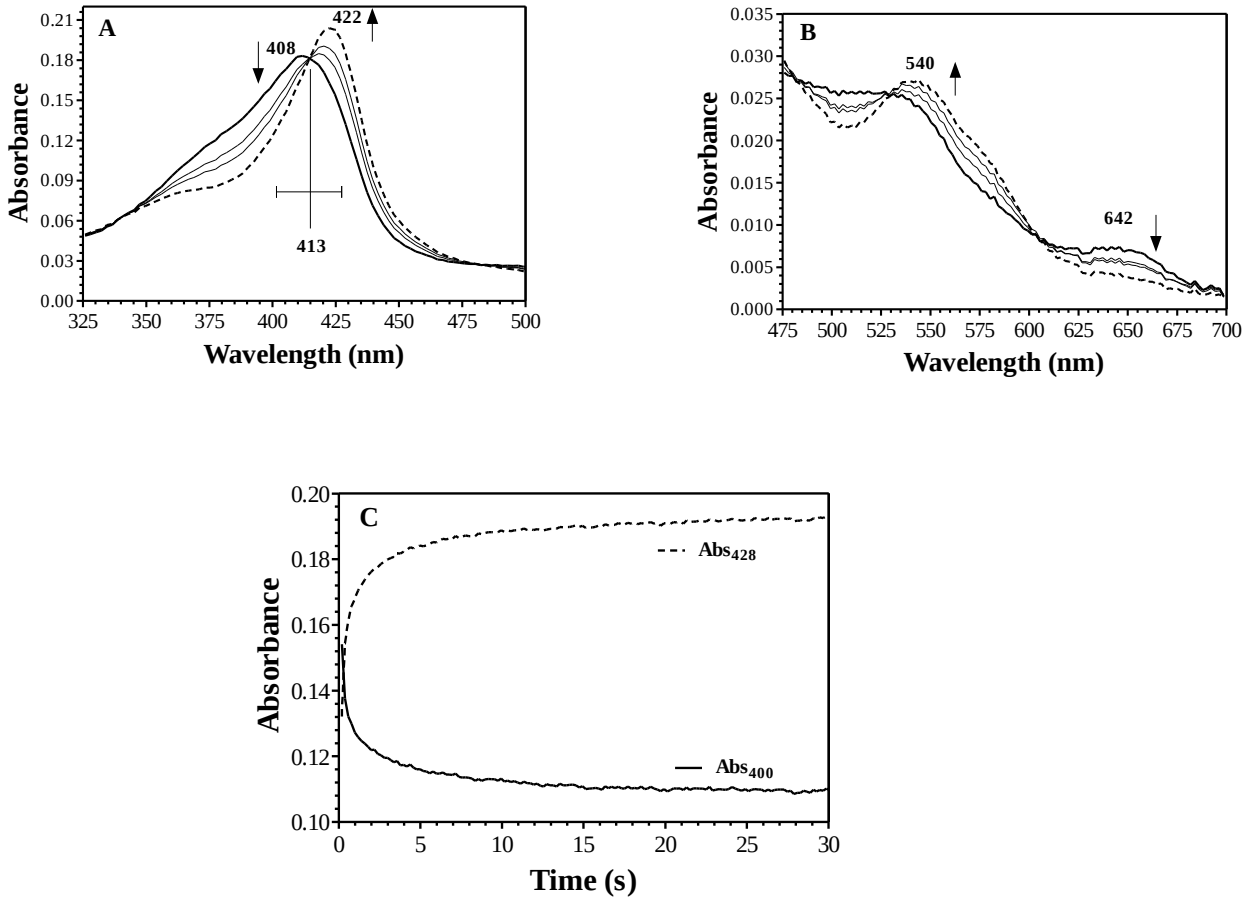

Figure 2.15: Spectral changes (A and B) and typical time traces (C) observed for reaction of ferric enzyme with potassium cyanide. The kinetic constants can be measured by observing the decrease in absorbance at 400 nm or increase in absorbance at 428 nm, as both wavelengths fall on either side of the isosbestic point (413 nm).

Rapid Freeze Quench (RFQ) EPR experiment

In principle, EPR spectroscopy can be used as a method to monitor kinetic event; however, in practice, the time required to tune the spectrometer, and its intrinsically low sensitivity compared to light-absorption spectroscopy, affects its competitiveness. This problem has been overcome by using rapid mixing-freezing method to study the reaction intermediates. This method of quenching a chemical or enzymatic reaction by rapid freezing was first introduced by Bray in 1961 (*140*) and adapted specifically for EPR analyses of the samples (*141*). RFQ-EPR can provide electronic and molecular structural information on biochemical transient intermediates with high time resolution, formed during the reaction whose presence was determined first by stopped-flow experiments. By preparing a series of freeze-quenched samples at various time intervals, a full kinetic profile of the catalytic cycle of an enzyme can be obtained.

The freeze quench experiments are divided into three phases: the mixing, the ageing and finally the freezing (*132*). The frozen reaction products are collected and analyzed by EPR. Briefly, the procedure consists of the rapid mixing of two reactants (e.g., enzyme and substrate), followed by rapid freezing of the mixture in a liquid isopentane bath. The reaction is aged for a user-defined time inside the calibrated ageing loops. A built-in ejection nozzle at the exit of the ageing loop sprays the aged solution towards the dewar, which is filled with isopentane. The temperature is regulated by immersing the dewar in a liquid N_2 bath. Cryosolvent level is maintained as close as possible to the nozzle to minimize flying time. On ejection the reaction is stopped below -130°C and the frozen sample is packed directly into the EPR tubes and analyzed

by EPR spectroscopy.

In KatG, compound I is formed upon reaction of ferric enzyme with alkyl peroxides (*142*). The presence of this compound I species have been observed in various KatGs using optical stopped-flow experiment (*75, 104, 113, 143, 144*). This compound I decays quickly to compound II like species in the absence of exogenous substrates. This is consistent with an endogenous electron transfer pathway producing a tyrosyl radical on tyrosine involved in W-Y-M adduct (*95, 145*). In stopped-flow experiments carried out on LL1 variants, we observed the spectral feature consistent with the presence of both compound I-like and compound-II like species. Thus, RFQ-EPR experiments were carried out on LL1 variants to identify and confirm the electronic nature of these two species and to observe the presence or absence of protein based radical in these variants. The data obtained from these experiments are summarized in chapter 3.

2.7. Conclusions

From this section, it is clear that wide array of instrumentations and techniques were required to study KatGs. These techniques ranged from molecular biology to various spectroscopic instrumentations. Molecular biology provided an opportunity to create new variants by genetic manipulation. In order to study those variants, specific expression and purification methods were employed to obtain the proteins in their native states. The structural impacts of manipulations were studied by spectroscopic techniques like UV-Vis, EPR etc., whereas appropriate kinetic characterizations were performed to observe the changes in proteins' activity and also to identify the intermediates formed in the catalytic mechanisms.

Chapter Three: Tracing the Impact of a Unique Loop in Catalase-peroxidase Catalysis

3.1. Introduction

Catalase-peroxidases (KatGs) are heme-containing enzymes with a multifunctional active site. The enzymes are named after their catalase and peroxidase activities, but they also posses peroxynitritase (*146*), NADH oxidase, isonicotinoyl hydrazide INH lyase, and isonicotinoyl-NAD synthase activities (*89*). Due to the latter two activities, KatG has been implicated as the enzyme responsible for the activation of a frontline antitubercular drug (isoniazid) and is, therefore, central to the treatment of *Mycobacterium tuberculosis* infections (*147, 148*). Depending upon the geographical distribution, in 50-70% of isoniazid-resistance *M. tuberculosis* clinical isolates, *katG* gene is the most commonly targeted gene with 30-90% of the mutation occurring in codon 315 (*149-152*). However, neither the mechanism of isoniazid activation by *M. tuberculosis* KatG nor the mechanism by which mutations to the *katG* gene lead to resistance is fully understood.

The catalytic mechanism of KatG as well as the nature of the interplay between the two dominant activities, catalase and peroxidase, remain a matter of some discussion. It is generally agreed that catalase and peroxidase reactions involve a common path for the formation of a ferryl protoporphyrin IX (PPIX) π-cation radical intermediate (i.e., compound I) but differ in the

mechanism for compound I reduction back to the ferric state. Many have argued that the catalase activity of KatG follows a mechanism similar to that of typical or monofunctional catalases. As such, there are two major steps. In the first step, the ferric enzyme undergoes a two-electron oxidation by one equivalent of H_2O_2, yielding compound I and H_2O (reaction 3.1). In the second step, the enzyme returns to its resting state by reacting with a second equivalent of H_2O_2, this time oxidizing it to O_2 (reaction 3.2). With typical enzymes from the non-animal peroxidase superfamily, compound I is returned to the ferric state by two single-electron reduction steps at the expense of an exogenous electron donor. In the first transfer, compound I is reduced, generating a ferryl intermediate (i.e., compound II) and the first equivalent of the corresponding substrate radical (reaction 3.3). Compound II then oxidizes the second equivalent of the substrate, generating a second radical and returning the enzyme to its ferric starting state (reaction 3.4).

$$H_2O_2 + Fe^{III}(PPIX) \longrightarrow H_2O + Fe^{IV}{=}O(PPIX^{\bullet+}) \quad \textbf{(3.1)}$$

$$H_2O_2 + Fe^{IV}{=}O(PPIX^{\bullet+}) \longrightarrow H_2O + O_2 + Fe^{III}(PPIX) \quad \textbf{(3.2)}$$

$$RH + Fe^{IV}{=}O(PPIX^{\bullet+}) \longrightarrow R^{\bullet} + Fe^{IV}{=}O(PPIX)(H^{+}) \quad \textbf{(3.3)}$$

$$RH + Fe^{IV}{=}O(PPIX)(H^{+}) \longrightarrow R^{\bullet} + H_2O + Fe^{III}(PPIX) \quad \textbf{(3.4)}$$

$$H_2O_2 + Fe^{IV}{=}O(PPIX) \longrightarrow H_2O + Fe^{III}{-}O_2^{\bullet-}(PPIX) \quad \textbf{(3.5)}$$

Though the mechanisms of typical catalases and peroxidases have many similarities, they are distinct from one another in important ways. In peroxidases, compound II is an essential component of the catalytic cycle. With the typical monofunctional catalases, compound II is regarded as an inactive species with respect to catalytic O_2 production. When H_2O_2 concentrations are high and/or exogenous electron donor concentrations are low, peroxidase compound II typically reacts quite easily with H_2O_2 to form a Fe^{III}-$O_2^{\cdot -}$ intermediate known as oxyperoxidase or compound III (reaction 3.5). Compound III is inactive with respect to the turnover of typical peroxidases and is commonly observed in these enzymes. It is also an inactive intermediate for catalases, but compound III is almost never observed with these enzymes (*71, 153-156*).

By any definition, KatG is a robust catalase. Their active sites produce turnover numbers (i.e., apparent k_{cat} values) of around 5000 s^{-1}. Apparent second-order rate constants of 10^6 $M^{-1}s^{-1}$ are typical (*157*). What makes this kinetic performance striking is that the KatG active site bears no resemblance to the typical monofunctional catalase enzymes (e.g., *E.coli* catalase [HPII]). Consistent with its membership in the non-animal peroxidase superfamily, the KatG active site is superimposable on the other Class I members of the superfamily (*56, 62, 91-94*). These enzymes (and all Class II and Class III peroxidases as well) have little if any catalase activity. Indeed, typical k_{cat} values for catalase turnover (which is referred to as pseudocatalase activity) are near 10 s^{-1} (*71, 154*). Due to this strange structure/function relationship the very existence of the catalase-peroxidase raises fundamental questions about heme enzyme structure, catalysis, and evolution. How is an existing enzyme active site with an obvious catalytic function co-opted to accommodate an entirely new function? What does this tell us about how nature has approached

this shift of functional capability? The active sites have changed little between catalase-negative peroxidases and highly catalase active KatG. This would suggest that the structures external to the active site must have some obvious differences.

Indeed, catalase-peroxidases do contain a group of structural components which are absent from their monofunctional counterparts. First, each catalase-peroxidase subunit contains a second domain; a gene-duplicated C-terminal domain which has lost its ability to bind heme or to catalyze any reaction of its own (*71, 91-94, 99, 158*). However, the Goodwin laboratory has demonstrated that the presence of this domain is necessary to maintain catalase-peroxidase structure and function (*86, 100*). In particular, the C-terminal domain supports the architecture of the active site by preventing coordination of the heme iron by so called the distal histidine. Also, the C-terminal domain, when it is expressed and isolated as a separate protein, can restore the function of the N-terminal domain (*100*).

In addition, the active site-bearing N-terminal domain contains three insertions which are absent from typical peroxidases: Large Loop 1 (LL1), Large Loop 2 (LL2), and Large Loop 3 (LL3) (*94*). LL3 is the smallest of the three and shows a great deal of sequence variability. As yet, no specific function has been proposed or assigned for this structure. LL1 and LL2 are highly conserved across all catalase-peroxidases, but in fundamentally different ways. LL2 shows considerably more sequence variability than LL1, but its length is essentially invariant. Conversely, LL1 shows high degree of sequence conservation but the length of the structure is highly variable from one species to another. In spite of these differences, both structures have been shown to be essential for catalase but not peroxidase activity (*87, 90, 108, 113*).

The LL1 contains a strictly conserved sequence of ten amino acids (MGLIYVNPEG) at its C-terminal end. The tyrosine (Y226 by *E. coli* numbering) participates in a unique Trp-Tyr-Met (W-Y-M) covalent adduct as observed in the crystal structures of all catalase-peroxidases structures solved to date (*91-94*). Formation of this covalent adduct is heme and peroxide dependent (*108*), and substitution of any of these three amino-acids results in the loss of catalase activity with either little effect on or enhancement of peroxidase activity (*90, 95-97, 108-110, 113*). The redox cycling of the W-Y-M adduct between its fully covalent and one-electron oxidized states has been suggested to as one mechanism to facilitate the enzyme's catalatic activity (*144*). According to this mechanism the free radical oxidized state of the W-Y-M adduct can serve as an electron acceptor what is typically regarded as the peroxidatic dead end intermediate (Fe^{III}-$O_2^{\cdot -}$). The electron transfer from Fe^{III}-$O_2^{\cdot -}$ to the W-Y-M radical would produce the Fe^{III}-O_2 complex which would immediately dissociates, yielding Fe^{III} enzyme and O_2. At the very least this could serve as a protective mechanism by preventing Fe^{III}-$O_2^{\cdot -}$ accumulation, and may account for the bulk of catalase activity observed in KatG (reactions 3.6-3.9) (*75, 117, 159*).

$$H_2O_2 + Fe^{III}(PPIX)(WYM) \longrightarrow H_2O + Fe^{IV}{=}O(PPIX^{\cdot +})(WYM) \quad \textbf{(3.6)}$$

$$Fe^{IV}{=}O(PPIX^{\cdot +})(WYM) \longrightarrow Fe^{IV}{=}O(PPIX)(WYM^{\cdot +}) \quad \textbf{(3.7)}$$

$$H_2O_2 + Fe^{IV}{=}O(PPIX)(WYM^{\cdot +}) \longrightarrow H_2O + Fe^{III}\text{-}O_2^{\cdot -}(PPIX)(WYM^{\cdot +}) \quad \textbf{(3.8)}$$

$$Fe^{III}\text{-}O_2^{\cdot -}(PPIX)(WYM^{\cdot +}) \longrightarrow Fe^{III}(PPIX)(WYM) + O_2 \quad \textbf{(3.9)}$$

Both LL1 and LL2 contribute to a narrow access channel to the deeply buried heme in the active site. The strictly conserved residues, Ile248, Asn251, and Glu253 (*Synechocystis* numbering), have been identified as essential for the H_2O_2 oxidation required for catalase turnover (*91-94, 102*). Substitution of any of these residues resulted in 50-70 % loss of catalase activity but retention of peroxidase activity. Ile248 maintains the heme architecture by forming a hydrogen bond with Asp152 (*105*), and Glu253 creates an acidic entrance to the access channel which stabilizes and orients the solute matrix essential for H_2O_2 oxidation (*102*). Even though the LL1 structure is 36-76 amino-acids long and it connects distal and proximal pocket of the active site (Figure 3.1), the dominant role which has been articulated for LL1 to this point is to position tyrosine correctly for the formation of W-Y-M adduct. However, this could be accomplished with a much less extensive structure and as such, it raises a question: Does this structure play other roles in regulating catalase and peroxidase activities? In order to investigate this question, three deletion variants were created in *E.coli* KatG; KatG$^{\Delta LL1}$ (Leu193-Asn228), KatG$^{\Delta 209-228}$ (Ser209-Asn228), and KatG$^{\Delta 200-214}$ (Glu200-Lys214) and compared to wt KatG and the substitution variant Y226F KatG. These variants were created by keeping in mind that each deleted different portions of LL1 and only two of them contained the essential tyrosine (Y226). The effects of each deletion on the overall stability and catalytic activity of KatG were monitored by various biophysical techniques.

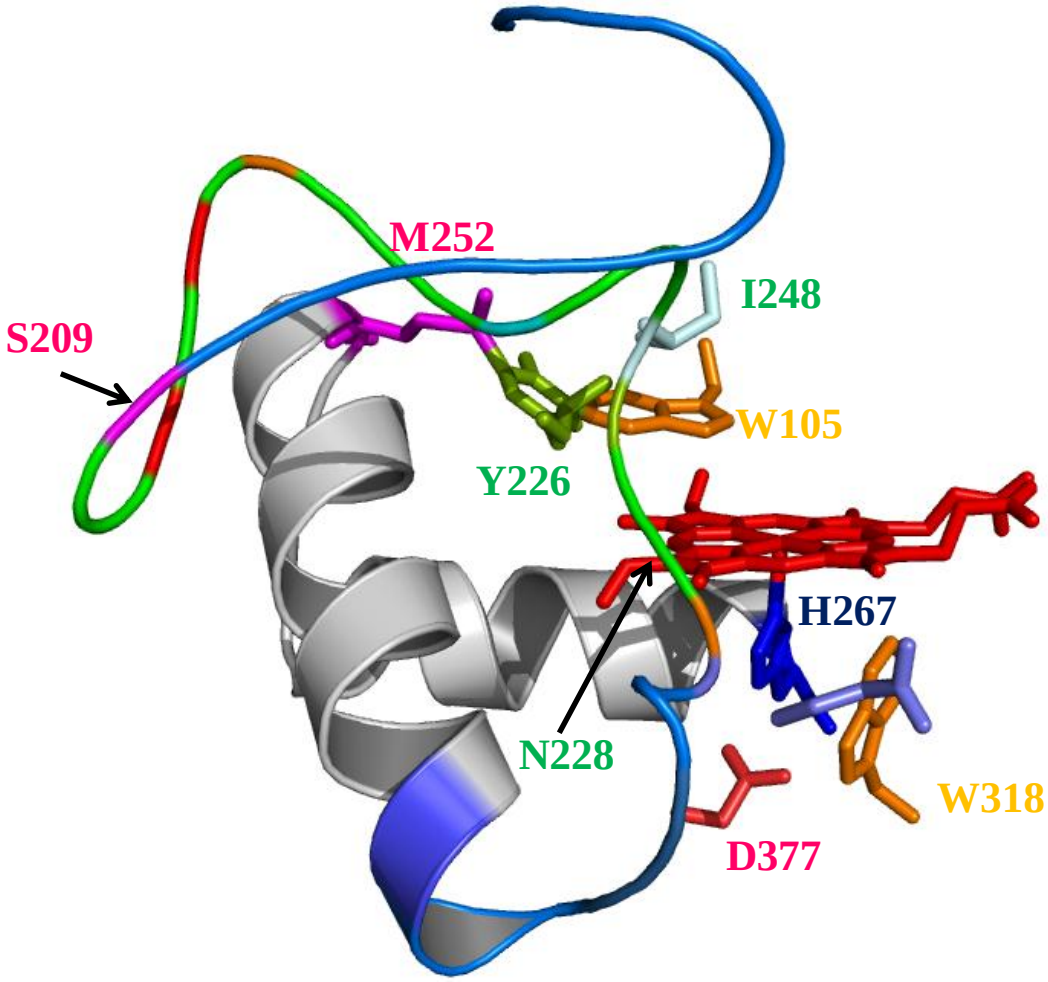

Figure 3.1: LL1 Connecting Distal and Proximal Part of the Active Site in KatG. Structure was taken from PDB accession domain 1SJ2. Different structures are color coded as follows Heme-red, Large loop 1 (LL1) – Green and Blue.

3.2 Materials and Methods

3.2.1. Materials

All oligonucelotide primers were obtained from Invitrogen (Carlsbad, CA). *E. coli* stains (XL-1 Blue and BL-21 [DE3]) and *Pfu* polymerase were purchased from Agilent Technologies (La Jolla, CA). The restriction enzymes were obtained from New England Biolabs (Beverly, MA). QIAprep Spin Miniprep kit and nickel-nitrilotriacetic acid (Ni-NTA) resin were obtained from Qiagen (Valencia,CA). Isopropyl-B-D-thioglactopyranoside (IPTG) was obtained from Gold Biotechnology Inc. (St. Louis, MO). Mono and di-basic sodium phosphate, acetic acid, and sodium acetate were purchased from Fisher (Pittsburgh,PA). Bugbuster and benzonase were purchased from EMD (Madison, WI). Ampicillin, chloramphenicol, imidazole, hemin, sodium dithionite, 2,2'-azino-bis(3-ethylbenzothiazoline-6-sulfonic acid) (ABTS), and hydrogen peroxide (30%), were obtained from Sigma (St. Louis, MO). Water purified through Barnstead Easy Pure II UV ultrapure water system (18.2 MΩ/cm resistivity) was used to make all buffers and media.

3.2.2 Site-directed and deletion mutagenesis

Y226F KatG variant was developed by site-directed mutagenesis using QuikChange™ protocol as described in chapter 2. The primers used were ECCP m23 (+) (5'-GAG ATG GGT CTG AT***C*** T***T***C GTT AAC CC-3') and ECCP m23 (-) (5'-GGG TTA ACG AAG ATC AG CCC ATC TC-3'). The nucleotide substitutions corresponding to the mutations are in bold italics.

PCR product was treated with *Dpn* I to remove starting template and ligated using T4 DNA liagase. The desired plasmids were used to transform *E. coli* XL-1 blue cells by electroporation. The amplicillin resistant colonies were screened by *Hpa* I digest as the successful mutants contain a unique *Hpa* I site. Positive colonies were submitted for full DNA sequence analysis to Davis Sequencing. Corrected mutated plasmids were used to transform *E. coli* BL21-Gold[DE3]plysS.

To generate constructs for the expression of KatG$^{\Delta LL1}$ (wtKatG lacking LL1 insertion), a deletion protocol based on Seamless®cloning was employed. The primers used were ECCPD101 (CC AGC TCT TCC ***CGG*** ATC CGG TTC CCA GAC GTC TTC) and ECCPD102 (ATT TAC TCT TCC ***CCG*** GAA GC CCG GAT CAC AGC). The underlined sequence is the *Eam* 1104I recognition sequence and the ones in bold are the overhanging sequence remained after the hydrolysis with *Eam* 1104I. The desired plasmids were used to transform *E. coli* XL-1 blue cells by electroporation. Positive colonies were submitted for full DNA sequence analysis to Davis Sequencing. Corrected mutated plasmids were used to transform *E. coli* BL21-Gold[DE3]plysS.

The variants KatG$^{\Delta 200\text{-}214}$ and KatG$^{\Delta 209\text{-}228}$ were generated by an alternate mutagenesis method due to the difficulty in obtaining methylated dCTP required for the *Eam*1104I-dependent protocol. The primers were designed by excluding corresponding codons for the deletion and they produced linear PCR product. This alternate procedures required modification of primers to include 5'- phosphoryl group for the blunt ligation of the PCR products. The primer pair for KatG$^{\Delta 200\text{-}214}$ was: 5'-phosphate-GCA CCG CTG GGT GCA ACC GAG ATG GGT CTG-3' and 5'-phospahte-ATC ACC CCA GTT AAC ATC CAG ATC CGG TTC-3'. For KatG$^{\Delta 209\text{-}228}$

following primer pair was used: 5'-phosphate-CCG GAA GGC CCG GAT CAC AGC GGC GAA CCG-3' and 5'-phosphate-ATG ACG GTG AGT CAG CCA GGC TTT TTC ATC-3'. The desired plasmids were used to transform *E. coli* XL-1 blue cells by electroporation. Plasmids from candidate colonies were evaluated by diagnostic restriction digest and DNA sequence analysis. Corrected mutated plasmids were used to transform *E. coli* BL21-Gold[DE3]plysS.

3.2.3. Expression and purification

Y226F KatG, KatG$^{\Delta 209\text{-}228}$, and KatG$^{\Delta 200\text{-}214}$ were expressed in the soluble form whereas KatG$^{\Delta LL1}$ was expressed in inclusion bodies. Expressions of Y226F KatG, KatG$^{\Delta LL1}$, KatG$^{\Delta 209\text{-}228}$, and KatG$^{\Delta 200\text{-}214}$ were carried out as described in chapter 2. Soluble purification protocol was used for Y226F KatG, KatG$^{\Delta 209\text{-}228}$, and KatG$^{\Delta 200\text{-}214}$ whereas insoluble purification was employed for KatG$^{\Delta LL1}$. Concentrations of purified enzyme was estimated according to the method of Gill and von Hippel (*126*) [ε_{280}(Y226F KatG) = 1.42 x 10^5 $M^{-1}cm^{-1}$ and ε_{280} (KatG$^{\Delta 209\text{-}228}$)=1.36 x 10^5 $M^{-1}cm^{-1}$, ε_{280} (KatG$^{\Delta 200\text{-}214}$)=1.37 x 10^5 $M^{-1}cm^{-1}$, and ε_{280} (KatG$^{\Delta LL1}$)=1.31 x 10^5 $M^{-1}cm^{-1}$].

3.2.4. Absorption spectra and activity assays

WtKatG and its variants were reconstituted with 0.9 equivalents of hemin. Following reconstitution, each protein was incubated for 24 hours at 4°C. The solution was then centrifuged to remove free hemin and other insoluble materials. The concentration of reconstituted enzyme was determined using the pyridine hemochrome assay (*124*). All spectra were obtained at room

temperature in 200 mM phosphate buffer, pH 7.0 using a Shmiadzu UV-1601 spectrophotometer (Columbia, MD) with a cell pathlength of 1.0 cm.

Catalase activity was evaluated by monitoring the decrease in H_2O_2 concentration in the presence of 10 nm enzyme at 240 nm (ε_{240}= 39.4 M^{-1} cm^{-1}) (*135*). All assays were carried out at room temperature using Shimadzu UV-1601 spectrophotometer using 200 mM phosphate buffer, pH 7.0. Peroxidase activity was measured by monitoring the production of ABTS radical at 417 nm (ε_{417} = 34.7 mM^{-1} cm^{-1}), initial concentration of ABTS was measured spectrophotometrically at 340 nm (ε_{340} = 3.66 x 10^4 M^{-1} cm^{-1}) (*136*).

3.2.5. Rapid Freeze Quench (RFQ) EPR

Rapid Freeze Quench (RFQ)-EPR experiments were performed in collaboration with Dr. Aimin Liu, Georgia State University. Solutions of wtKatG or Y226F KatG or $KatG^{\Delta 209\text{-}228}$ (~260 μM) and varying equivalents (1, 5, 10, and 50) of H_2O_2 in 50 mM phosphate buffer, pH 7.0 were mixed in 1:1 ratio. The mixture was then incubated for the indicated time periods followed by freeze quench in isopentane at -130°C. The frozen samples were then packed in precision bore EPR tubes immersed in an isopentane bath. EPR tubes were then transferred to liquid nitrogen and finally examined using Bruker ER200D spectrometer with 9.6 GHz modulation frequency with a 4116DM resonator. For temperature control an oxford ITC 503S temperature controller, an ESR910 helium cryostat and LLT650/13 liquid helium transfer tube (Oxford Instrument, Concord, MA). Data acquisition software was developed in house and Bruker WINEPR V 2.11 was used for data manipulation.

3.2.6. Stopped-flow analysis

3.2.6.1 in the presence of H_2O_2

In Single mixing experiments, Y226F KatG and KatG$^{\Delta 209\text{-}228}$ was allowed to react with excess of H_2O_2 to form higher oxidation states. In this mode, syringe 'A' contained 6 μM enzyme in 50 mM phosphate buffer, pH 7.0 and syringe 'B' contained varying concentrations of H_2O_2. Full spectra recorded by diode array indicated transient H_2O_2 concentration-dependent spectral shifts consistent with compound I formation followed by an H_2O_2-independent shift to a compound II-like spectrum. The rates of these two events provided a narrow H_2O_2 concentration range to measure a rate constant for compound I formation (5 to 30 equivalents or 7.5 μM to 45 μM H_2O_2). This rate was recorded at 412 nm using single wavelength detection. This wavelength allows more facile distinction between the formation and decay of the compound I intermediates. Similar results were obtained when absorption at 400 nm was monitored.

3.6.2*.2 in the presence of peroxidatic electron donors*

The return of ferryl heme intermediates to the ferric state in the presence of electron donors; ascorbate and ABTS, was evaluated using sequential mixing stopped-flow experiments. 6 μM of enzyme (Y226F KatG or KatG$^{\Delta 209\text{-}228}$) was mixed against 0.95 equivalent of H_2O_2 an allowed to react in the delay line for 10 s or 0.7 s, respectively. These delay times allowed accumulation of compound II like intermediates because accumulation of a large fraction of compound I intermediate under single turnover conditions is near impossible. The contents of the delay line were mixed with 50 mM phosphate buffer, pH 7.0, as well as 30 μM of ascorbate and

varying concentrations of ABTS. Thus, the final reaction mixture contained 1.5 μM enzyme, 15 μM ascorbate, 25 mM buffer, and 0-120 μM ABTS. The full spectra were recorded by diode array, and the rate constants for ABTS-dependent reactions were measured at 400 nm by single wavelength measurements. Ascorbate reduces ABTS radicals as rapidly as they are generated to its parent compound ensuring a constant substrate concentration during the reaction (*114*, *139*). Ascorbate is often a poor substrate for peroxidase enzymes and has been a very effective tool for measuring rapid peroxidase reactions with electron donors and minimizes the interference from the oxidized products. Moreover, the concentration of ascorbate was a constant in our ABTS stopped-flow studies making its contribution easy to account for.

3.3 Results

The importance of LL1 in positioning tyrosine 226 to participate in the W-Y-M covalent adduct (an essential feature for the catalase activity of KatG) has been extensively evaluated. Considerably less attention has been focused on other important roles which LL1 might be contributing in order to maintain the stability and functionality of KatGs.

In an attempt to decipher what additional contributions LL1 may make to KatG function, we targeted LL1 by deleting portions of the structure including or excluding the essential tyrosine. In case of Y226F variant, substitution with phenylalanine eliminated the possibility of W-Y-M formation. KatG$^{\Delta LL1}$ variant was deleted by removing amino acids from Leu193 to Asn228, and also lacked the ability to form the covalent adduct. KatG$^{\Delta 200\text{-}214}$ variant was created to leave out the Y226 by deleting Glu200-Lys214 at the N-terminal portion of LL1. The

KatG$^{\Delta 209\text{-}228}$ variant removed Ser209-Asn228 at C-terminal part of LL1 and it did include the essential tyrosine. These variants were investigated by steady-state and transient-state kinetics.

3.3.1. Steady-state kinetic analysis

The variants KatG$^{\Delta LL1}$, KatG$^{\Delta 209\text{-}228}$ and Y226F KatG exhibited no catalase activity whereas KatG$^{\Delta 200\text{-}214}$ retained catalase activity comparable to the wtKatG (Table 3.1). The substitution of tyrosine or its absence in KatG$^{\Delta LL1}$, and KatG$^{\Delta 209\text{-}228}$ is sufficient to explain the loss of catalase activity. As previously mentioned, this tyrosine is involved in covalent adduct required to maintain the catalase activity in wtKatG. It has been shown that the analogous replacement of tyrosine 226 with phenylalanine in KatG from several other organisms like *M. tuberculosis*, *B. pseudomallei* and *Synechocystis* eliminates the catalase activity (*108, 113*). Interestingly, the effect on peroxidase activity of tyrosine substitution of KatG from these organisms varied considerably ranging from little effect on peroxidase activity (*90*) to substantial increase (*108, 113*) or decrease in peroxidase activity (*89*). Our evaluation of Y226F from *E.coli* KatG indicated that any of these three outcomes may be observed depending upon the conditions used to measure peroxidase activity.

The dependence of the peroxidase activity of Y226F KatG, KatG$^{\Delta 200\text{-}214}$ and wtKatG on H_2O_2 is shown in Figure 3.2 (Panel A). Y226F KatG showed substantially greater peroxidase activity than either wtKatG or KatG$^{\Delta 200\text{-}214}$ provided that H_2O_2 concentrations were relatively low. The apparent second order rate constant (k_{cat}/K_M) for Y226F KatG (2.3×10^6 $M^{-1}s^{-1}$) with respect to H_2O_2 was nearly one order of magnitude greater than that determined for wtKatG

Table 3.1: Catalase kinetic parameters for wild-type KatG, Y226F KatG, and deletion variants

Protein	Kinetic Parameters		
	k_{cat} (s^{-1})	K_M (mM)	k_{cat}/K_M ($M^{-1}s^{-1}$)
wtKatG	11000 ± 200	3.4 ± 0.1	3.2×10^6
Y226FKatG	ND	ND	ND
$KatG^{\Delta 200\text{-}214}$	9600 ± 200	7.2 ± 0.2	1.3×10^6
$KatG^{\Delta 209\text{-}228}$	ND	ND	ND
$KatG^{\Delta LL1}$	ND	ND	ND

N/D: Not detected

(3.6×10^5 $M^{-1}s^{-1}$) (Table 3.2). This was due largely to a much lower apparent K_M of Y226F KatG for H_2O_2. Indeed, the maximum observed peroxidase activity for Y226F KatG was only 1.4 fold higher than that recorded for wtKatG. Along with this, Y226F KatG and wtKatG showed starkly different sensitivities toward H_2O_2-dependent inhibition. At higher concentrations of H_2O_2 (i.e., those exceeding 0.8 mM) Y226F KatG showed a progressive and substantial loss of peroxidatic activity, but H_2O_2 produced a much more modest decrease in the peroxidase activity of wtKatG. The H_2O_2-depedent peroxidase activity of $KatG^{\Delta 200\text{-}214}$ showed similar response to varying concentration H_2O_2 compared to wtKatG as can be observed from comparable apparent second order rate constants.

The effects of H_2O_2 on the peroxidase activity of the two deletion variants $KatG^{\Delta LL1}$ and $KatG^{\Delta 209\text{-}228}$ were compared to Y226F KatG (Figure 3.2, panel B). The apparent k_{cat} values for $KatG^{\Delta 209\text{-}228}$ and $KatG^{\Delta LL1}$ were 8- and 4-fold higher, respectively, when compared to that of Y226F KatG. Closer examination of kinetic data in Figure 3.2, panel B showed that these three variants depicted a very different response at low and high concentrations of H_2O_2. Even though, all the three variants showed similar response to lower concentrations of H_2O_2 (inset), they diverged dramatically at higher concentrations of H_2O_2 specifically in terms of their susceptibility to H_2O_2-dependent inhibition. Out of the three variants, $KatG^{\Delta 209\text{-}228}$ showed least susceptibility to inhibition as indicated by the largest K_I value (~10 mM) while Y226F KatG was the most susceptible variant with the lowest K_I value (~0.7 mM). $KatG^{\Delta LL1}$ showed intermediate

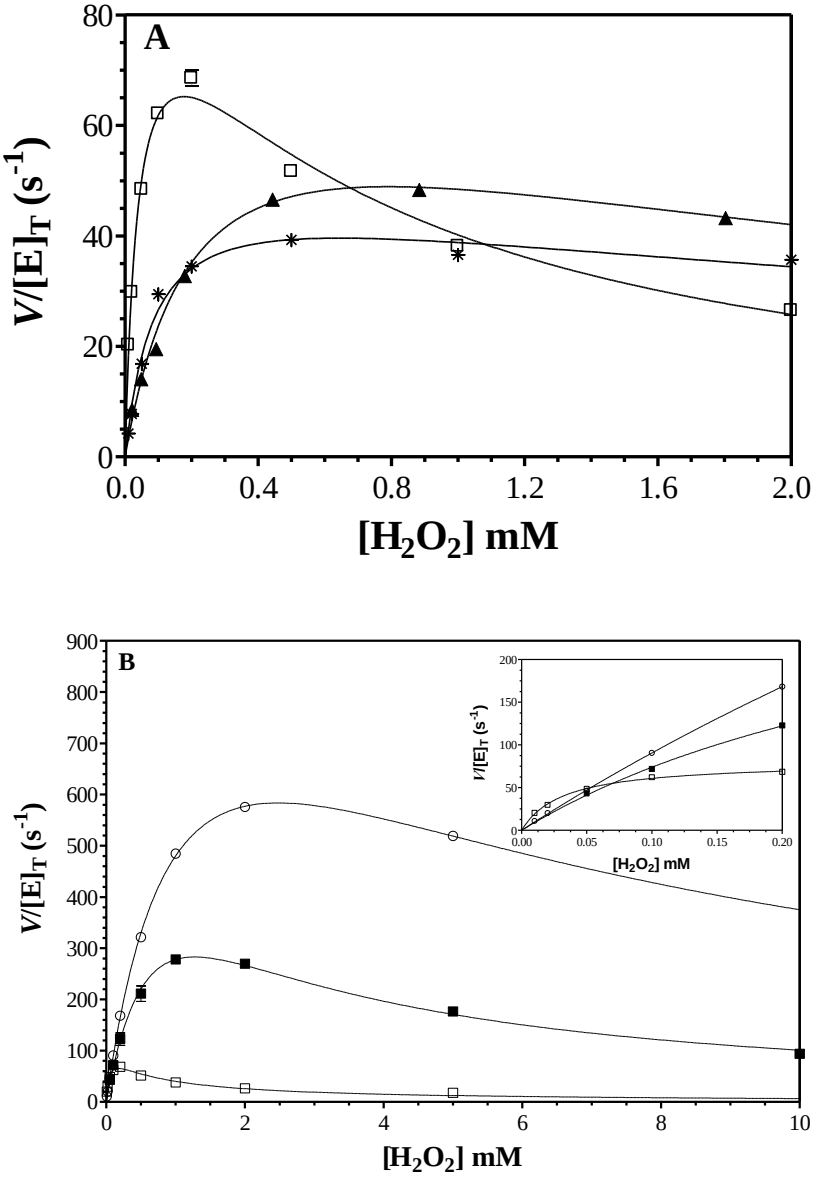

Figure 3.2: Effect of H_2O_2 concentration on the peroxidase activity of wild-type KatG, Y226F KatG, and deletion variants (KatG$^{\Delta LL1}$, KatG$^{\Delta 200\text{-}214}$, and KatG$^{\Delta 209\text{-}228}$). Panel A compares the activities of wild-type KatG (▲), KatG$^{\Delta 200\text{-}214}$ (*) and Y226FKatG (□). Panel B compares the activities of variants lacking observable catalase activities, these are KatG$^{\Delta 209\text{-}228}$ (○), KatG$^{\Delta LL1}$ (■), and Y226F KatG (□). Activities of catalase negative variants at low H_2O_2 concentrations are shown in the inset. All reaction contained 0.5 mM ABTS, 50 mM acetate buffer, pH 5.0, and were carried out at 23°C.

Table 3.2: Peroxidase kinetic parameters with respect to H_2O_2 for wild-type KatG, Y226F KatG, and deletion variants

Protein	Kinetic Parameters			
	k_{cat} (s^{-1})	K_M (mM)	k_{cat}/K_M ($M^{-1}s^{-1}$)	K_I (mM)
wtKatG	76 ± 9	0.22 ± 0.05	3.5×10^5	3 ± 1
Y226F KatG	97 ± 5	0.043 ± 0.005	2.3×10^6	0.73 ± 0.08
$KatG^{\Delta 200\text{-}214}$	50 ± 2	0.09 ± 0.01	5.6×10^5	5 ± 1
$KatG^{\Delta 209\text{-}228}$	904 ± 34	0.83 ± 0.06	9.6×10^5	10.0 ± 0.8
$KatG^{\Delta LL1}$	713 ± 86	0.97 ± 0.17	7.4×10^5	1.7 ± 0.3

sensitivity to inhibition with a K_I value of around 1.7 mM. It is likely that at least one contributor to the disparity between maximum observed activities and apparent k_{cat} values was the magnitude of the K_I with respect to H_2O_2.

The effect of reducing substrate (ABTS) on the peroxidase activity of KatG$^{\Delta 209\text{-}228}$, KatG$^{\Delta LL1}$, and Y226F KatG was also evaluated (Figure.3.3). When compared to H_2O_2-dependent activities, even though the data obtained for ABTS did not fit particularly well to a hyperbolic equation, a similar trend in the overall peroxidase activities was observed with the greatest activity displaced by KatG$^{\Delta 209\text{-}228}$ followed by KatG$^{\Delta LL1}$ and then Y226F KatG. However, in contrast to the H_2O_2–dependence where there was a different response to low and high concentrations of H_2O_2, ABTS-dependent activities of the variants maintained the same trend at all concentrations of ABTS tested (i.e., above and below the apparent K_M for ABTS).

3.3.2. UV-visible characterization

The UV-visible absorption spectra were recorded for the ferric form of Y226F KatG, and KatG$^{\Delta 209\text{-}228}$ following reconstitution with hemin and compared with those recorded previously for wtKatG and KatG$^{\Delta LL1}$ (*103*). The ferric state of both the variants showed a Soret maximum at ~407 nm and charge transfer maxima at 508 and 642 nm indicating a mixture of states dominated by pentacoordinate and hexacoordinate high-spin heme. All UV-visible features were comparable to wtKatG and KatG$^{\Delta LL1}$; except that KatG$^{\Delta LL1}$ showed a substantial contribution from hexacoordinate low-spin heme species (*103*).

Upon addition of 100 μM H_2O_2, the UV-Vis spectra of Y226F KatG and KatG$^{\Delta 209\text{-}228}$

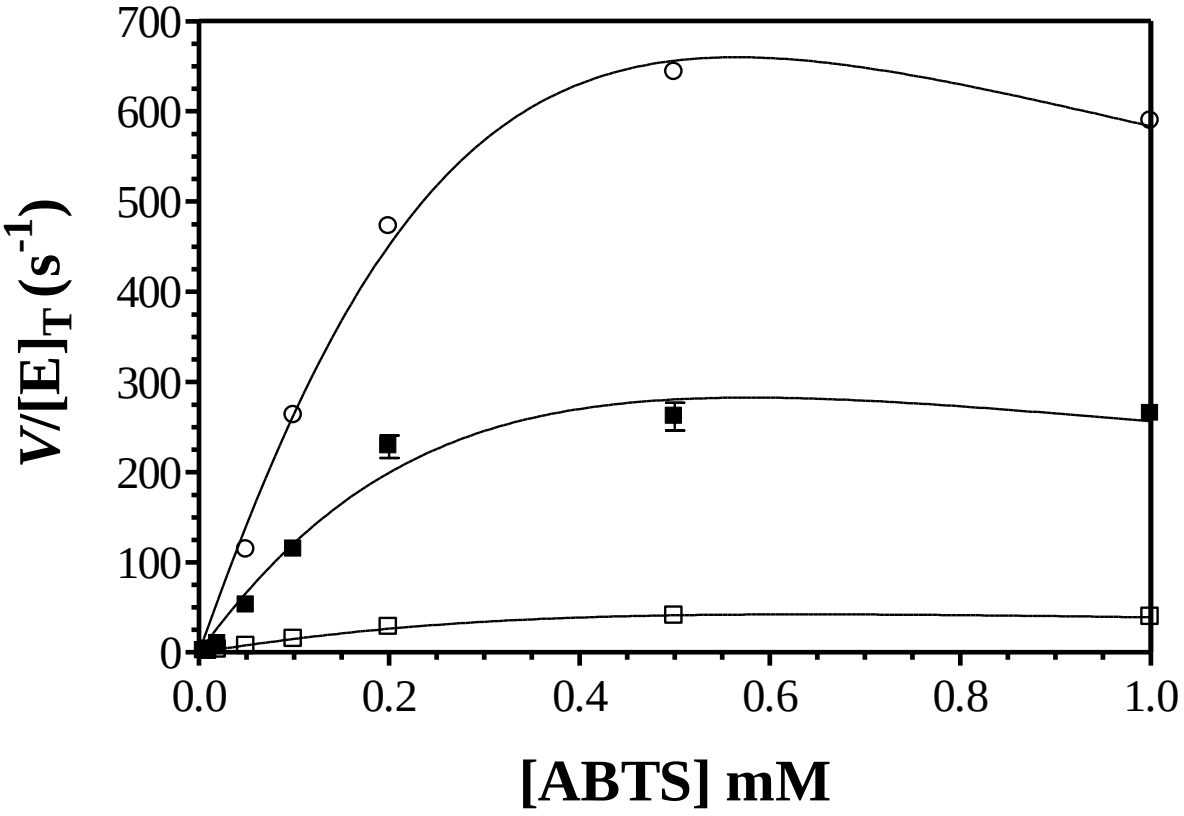

Figure 3.3: Effect of ABTS concentration on the peroxidase activities of the catalase negative variants KatG$^{\Delta 209\text{-}228}$ (○), KatG$^{\Delta LL1}$ (■), and Y226F KatG (□). All reactions for Y226FKatG, and KatG$^{\Delta LL1}$ contained1 mM H_2O_2. All reactions for KatG$^{\Delta 209\text{-}228}$ contained 2 mM H_2O_2. Regardless of variant all assays were performed using 50 mM acetate buffer, pH 5.0, and carried out at 23°C.

showed a red shift of the Soret band to 418 nm and emergence of β and α bands at 542 nm and 578 nm, respectively. This suggested that variants lacking tyrosine 226 either by substitution or deletion both easily formed the "inactive" compound III intermediate in the presence of H_2O_2 (Figure.3.4 A and B). As described earlier, formation of inactive species (Fe^{III}-$O_2^{\cdot -}$) or oxyperoxidase is a common mechanism by which H_2O_2 inhibits peroxidases. This species is formed when compound II (Fe^{IV}=O) reacts with H_2O_2 rather than the peroxidase reducing substrate. This formation of compound III with H_2O_2 in the absence of a reducing substrate has been reported in KatG enzymes from other organisms where the tyrosine analogous to tyrosine 226 was substituted with phenylalanine (*75, 95, 113, 142, 160*).

3.3.3. Transient-state kinetic analysis:

3.3.3.1. Single mixing reaction with H_2O_2

Though each of the variants formed compound III quite easily in the presence of relatively low concentration of H_2O_2 (100 μM), the steady-state kinetic studies clearly showed a different susceptibility to inactivation for each variant. In order to investigate this further, stopped-flow kinetic measurements were carried out to monitor the effect of H_2O_2 on the rates of interconversion between heme intermediates.

In general, KatG compound I is a difficult species to observe in the presence of H_2O_2 because of its rapid reduction by H_2O_2 in the catalase cycle. However, in catalase-negative variants it is conceivable that the reaction may be observed. Expected spectral changes would include 40-50% hypochromicity of Soret band and exponential decrease in the absorbance over

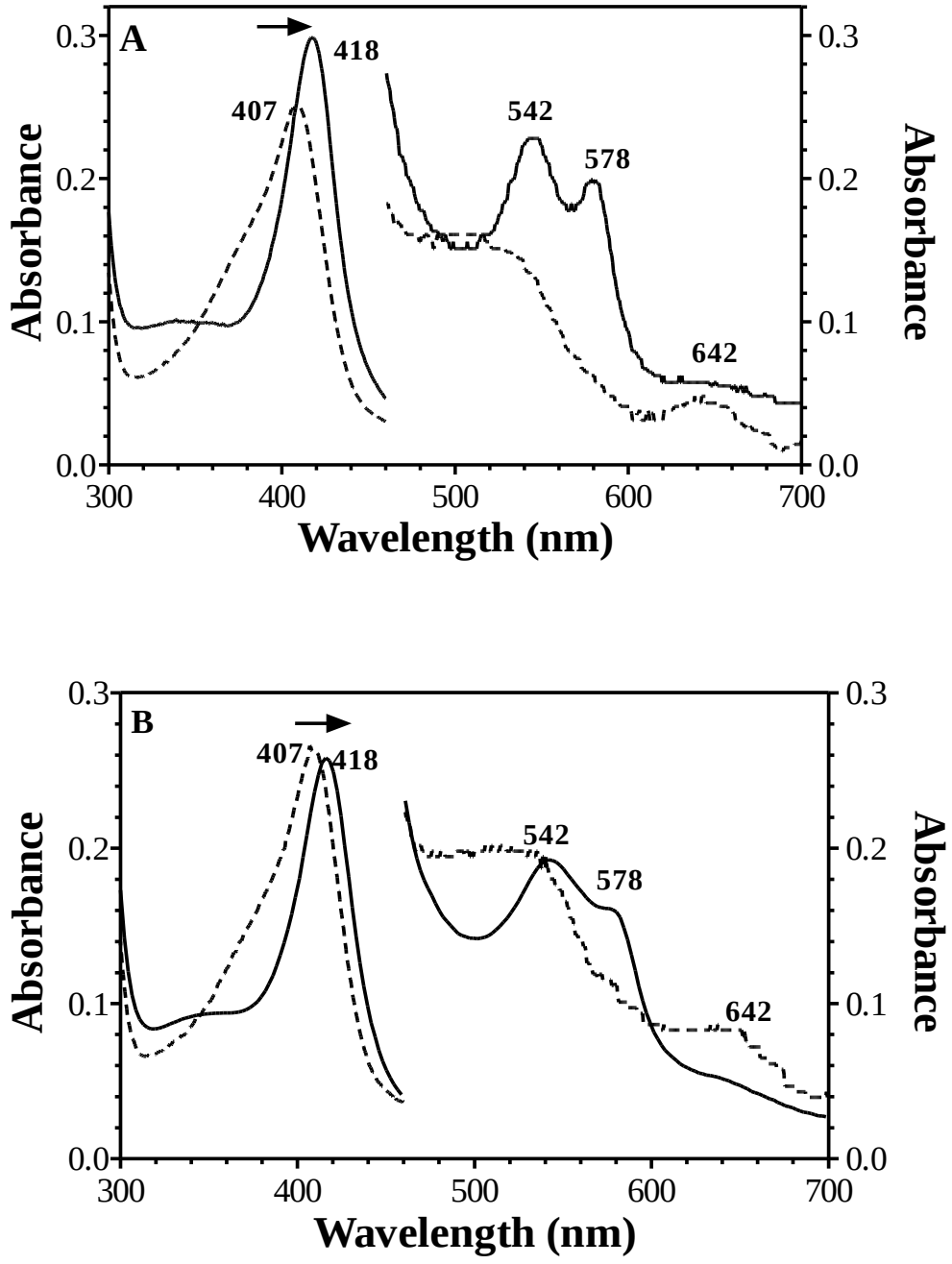

Figure 3.4: Effect of H_2O_2 on the absorbance spectra of Y226F KatG (A), and KatG$^{\Delta 209\text{-}228}$ (B). Spectral changes were recorded before (dashed line) and after (sold line) addition of 100 μM H_2O_2. All spectra were recorded using 50 mM phosphate buffer, pH 7.0, and at 25 °C

time at a wavelength closer to Soret maximum. When 3 μM of ferric Y226F KatG was reacted with 5 equivalents of H_2O_2, 20-30 % hypochromicity of Soret band was observed with two isosbestic points (341 and 420 nm) suggesting formation of a compound I-like species (Figure 3.5). Similar spectral changes were observed upon reaction of 3 μM of ferric $KatG^{\Delta 209-228}$ with 10 equivalents of H_2O_2 (Figure 3.6). In each case, the transition was monophasic as observed at 400 nm (see Figure 3.5 and 3.6 insets) indicating pseudo-first order conditions had been achieved. A plot of k_{obs} *versus* H_2O_2 concentration was linear for both the variants. However, the second order rate constant for the formation of the compound I-like species was two-fold higher for Y226F KatG (7.5×10^6 $M^{-1}s^{-1}$) compared to $KatG^{\Delta 209-228}$ (3.9×10^6 $M^{-1}s^{-1}$) (Figure.3.7).

The compound I-like species of both the variants was only transiently observed, and in the absence of an exogenous electron donor an intermediate with spectral features suggestive of compound II-like species appeared. This intermediate was characterized by Soret band at 418 nm and β and α bands at 530 and 560 nm, respectively. It was formed within ~0.045 s for Y226F KatG (Figure 3.8) and ~0.05 s for $KatG^{\Delta 209-228}$ (Figure 3.9). In reaction traces recorded at 412 nm, the formation of compound II-like intermediate comprised the second phase of a biphasic transition. The first phase corresponded to formation of compound I-like species followed by its decay and the formation of a compound-II like species in the second phase (insets, Figures 3.8 and 3.9).

The dependence of k_{obs} for the second phase on H_2O_2 concentration was evaluated. There was a hyperbolic response to H_2O_2 for Y226F KatG and and $KatG^{\Delta 209-228}$. Overall, rates were more rapid for Y226F KatG than $KatG^{\Delta 209-228}$ with the former approaching a maximum for a first

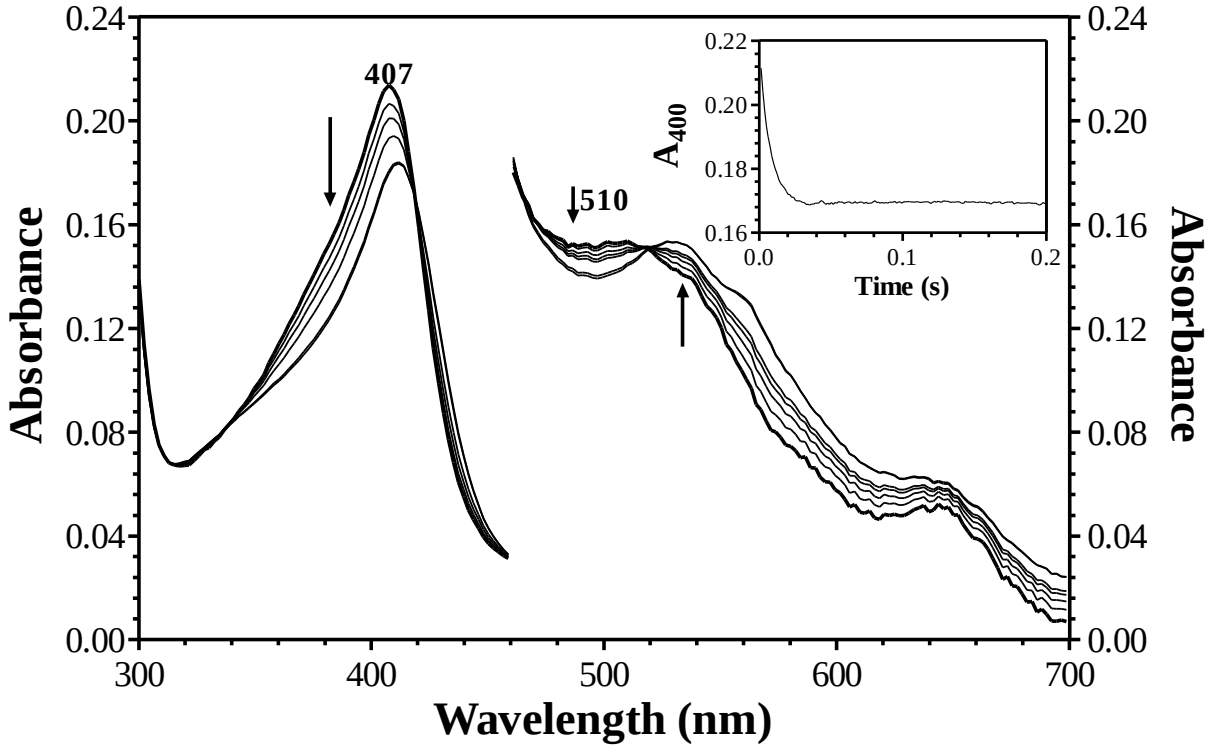

Figure 3.5: Compound I formation of Y226F KatG. Spectral changes observed upon addition of 15 μM H_2O_2 to 3 μM ferric Y226F. First spectrum is that of ferric enzyme. Following spectra were taken after 2.5, 3.8, 6.3 and 15 ms (bold), respectively. Reactions were carried out in 50 mM phosphate buffer, pH 7.0 and 4 °C. **T**ypical time trace between 3 μM Y226F and 15 μM H_2O_2 followed at 400nm shown in inset.

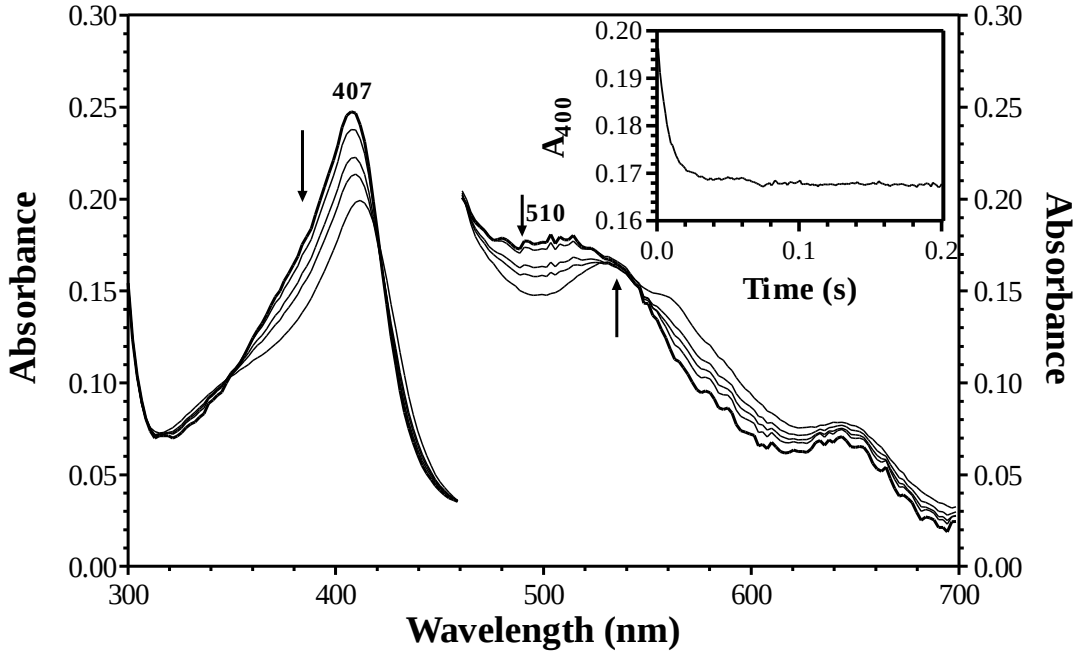

Figure 3.6: Compound I formation of KatG$^{\Delta 209\text{-}228}$. Spectral changes observed upon addition of 15 μM H_2O_2 to 3 μM ferric KatG$^{\Delta 209\text{-}228}$. First spectrum is that of ferric enzyme. Following spectra were taken after 2.5, 3.8, 5 and 13 ms (bold), respectively. Typical time trace between 3 μM KatG$^{\Delta 209\text{-}228}$ and 15 μM H_2O_2 followed at 400nm is shown in inset. Reactions were carried out in 50 mM phosphate buffer, pH 7.0 and 4 °C.

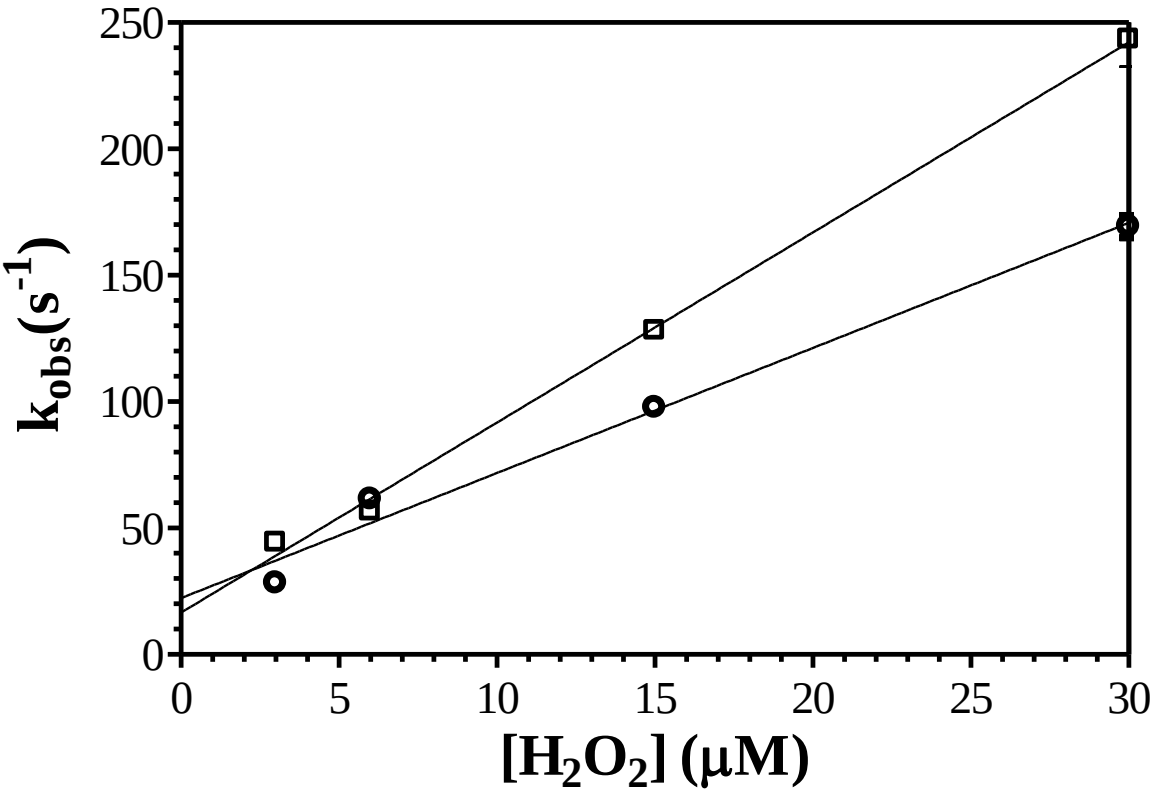

Figure 3.7: Rate constants for formation of compound I in Y226F KatG (□) and KatG$^{\Delta 209-228}$ (○) plotted against H_2O_2 concentration at 400 nm. Reactions were carried out using 3μM of enzymes in 50 mM phosphate buffer, pH 7.0 at 4°C

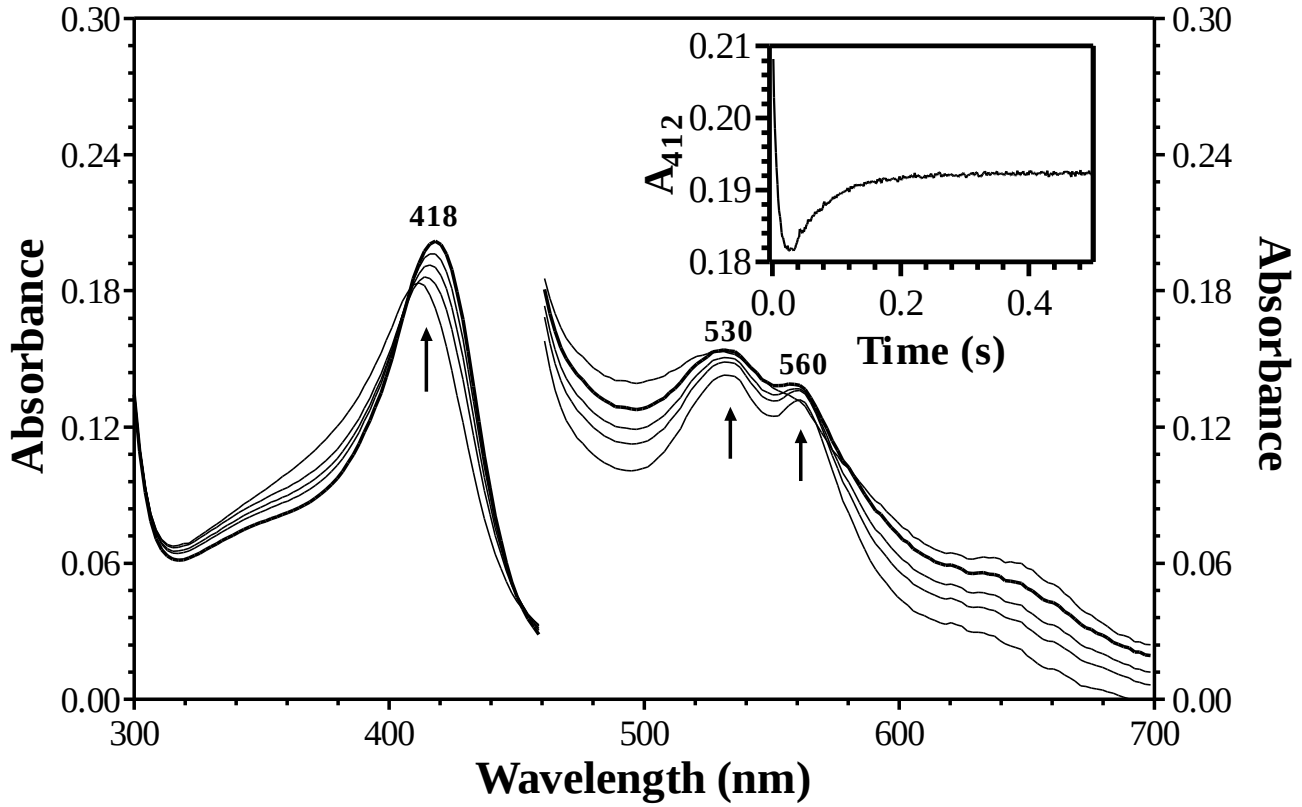

Figure 3.8: Compound I decay to compound II of Y226F KatG. Spectral changes observed upon addition of 15 μM H_2O_2 to 3 μM ferric Y226F. First spectrum is that of compound I taken at 15 ms. Following spectra were taken after 45, 78, 127, 500, and 620 ms (bold, peaks at 418, 530, and 560 nm, respectively). Reactions were carried out in 50 mM phosphate buffer, pH 7.0 and 4 °C. Typical time trace between 3 μM Y226F and 15 μM H_2O_2 followed at 412 nm showing decay of compound I to compound II is shown in inset.

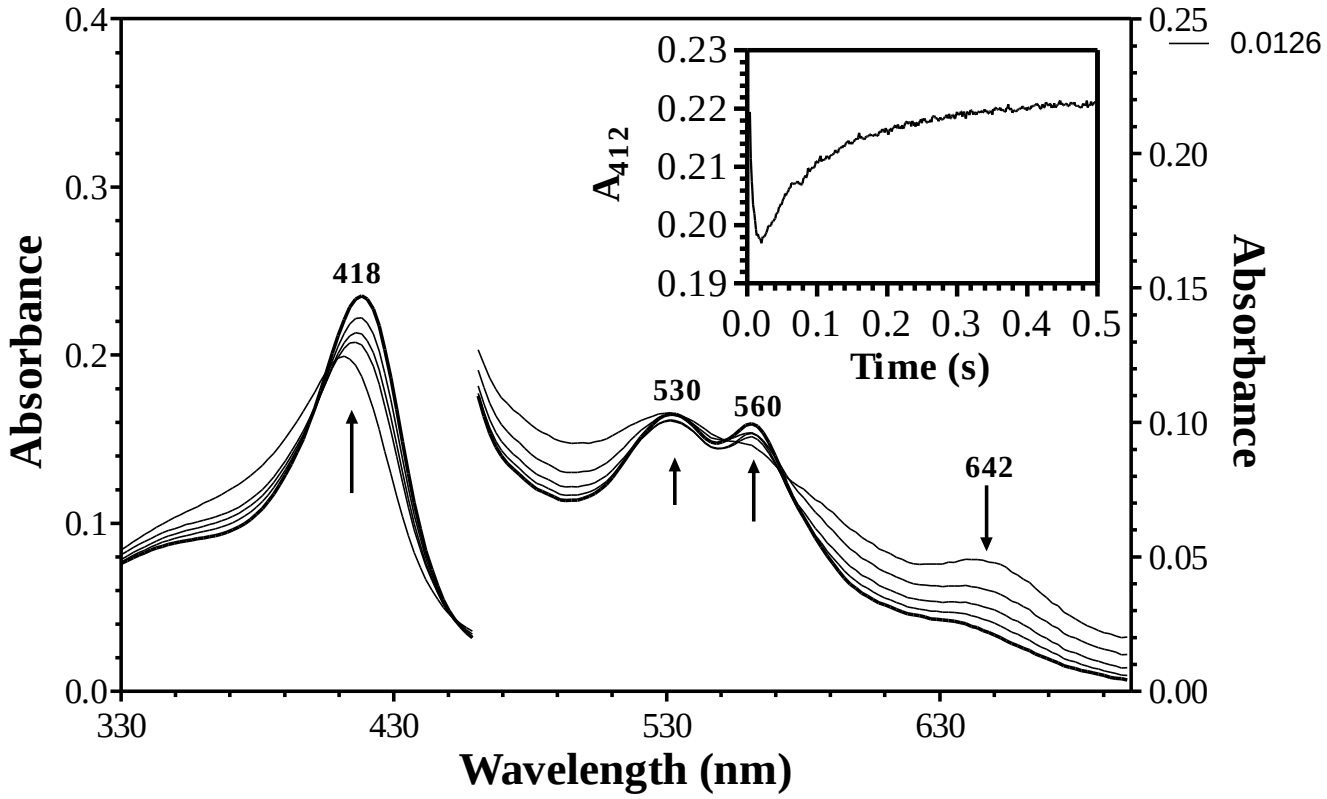

Figure 3.9: Compound I decay to compound II of KatG$^{\Delta 209\text{-}228}$. Spectral changes observed upon addition of 15 μM H_2O_2 to 3 μM ferric KatG$^{\Delta 209\text{-}228}$. First spectrum is that of compound I taken at 13 ms. Following spectra were taken after 50, 75, 126, and 500 ms (bold, peaks at 418, 530, and 560 nm, respectively). Reactions were carried out in 50 mM phosphate buffer, pH 7.0 and 4 °C. Typical time trace between 3 μM KatG$^{\Delta 209\text{-}228}$ and 15 μM H_2O_2 followed at 412 nm showing decay of compound I to compound II is shown in inset.

order rate constant of 23 ± 2s^{-1} while the latter approached 15 ± 1 s^{-1} (Figure 3.10).

One interpretation consistent with the data would be that of two sequential reactions. The first is a bimolecular reaction with H_2O_2 to form a compound I-like species. The rate constant corresponding to this step is 7.5 or 3.9 × 10^6 $M^{-1}s^{-1}$ for Y226F KatG and $KatG^{\Delta 209-228}$, respectively. The second is an intramolecular electron transfer resulting in radical transfer from the heme to the KatG protein. The first order rate constant corresponding to this step being 23 ± 2 s^{-1} for Y226F KatG and 15 ± 1 s^{-1} for $KatG^{\Delta 209-228}$ (reaction 3.10)

$$\mathbf{Fe^{III}(PPIX)(P)+H_2O_2} \xrightarrow[\substack{7.5\times10^6\ M^{-1}s^{-1}\\ 3.9\times10^6\ M^{-1}s^{-1}}]{k_1} \mathbf{Fe^{IV}{=}O(PPIX^{\cdot+})(P)} \xrightarrow[\substack{23\pm2\ s^{-1}\\ 15\pm1\ s^{-1}}]{k_2} \mathbf{Fe^{IV}{=}O(PPIX)(P^{\cdot})} \quad \mathbf{(3.10)}$$

Given the rate constants for each step, and the concentrations of H_2O_2 utilized, one would predict based on this model a change in rate determining step for the formation of the compound II-like species. At low H_2O_2 concentrations (less than 15 μM) the first step would be rate determining, none of the compound I-like species would accumulate, and the reaction would appear as a direct conversion to the compound II-like species. Conversely, at concentrations of H_2O_2 15 μM and above the rate of compound I formation would begin to exceed that of its conversion to the compound II-like species, and compound I would accommodate. Absorbance at 412 nm allows for monitoring of both steps. The effect of H_2O_2 on the character of the trace at 412 nm is precisely consistent with the mechanism proposed and the rate constants determined.

At the lowest H_2O_2 concentration tested for both variants a single phase conversion was observed. As H_2O_2 concentration increased, the biphasic character of the trace increased with the

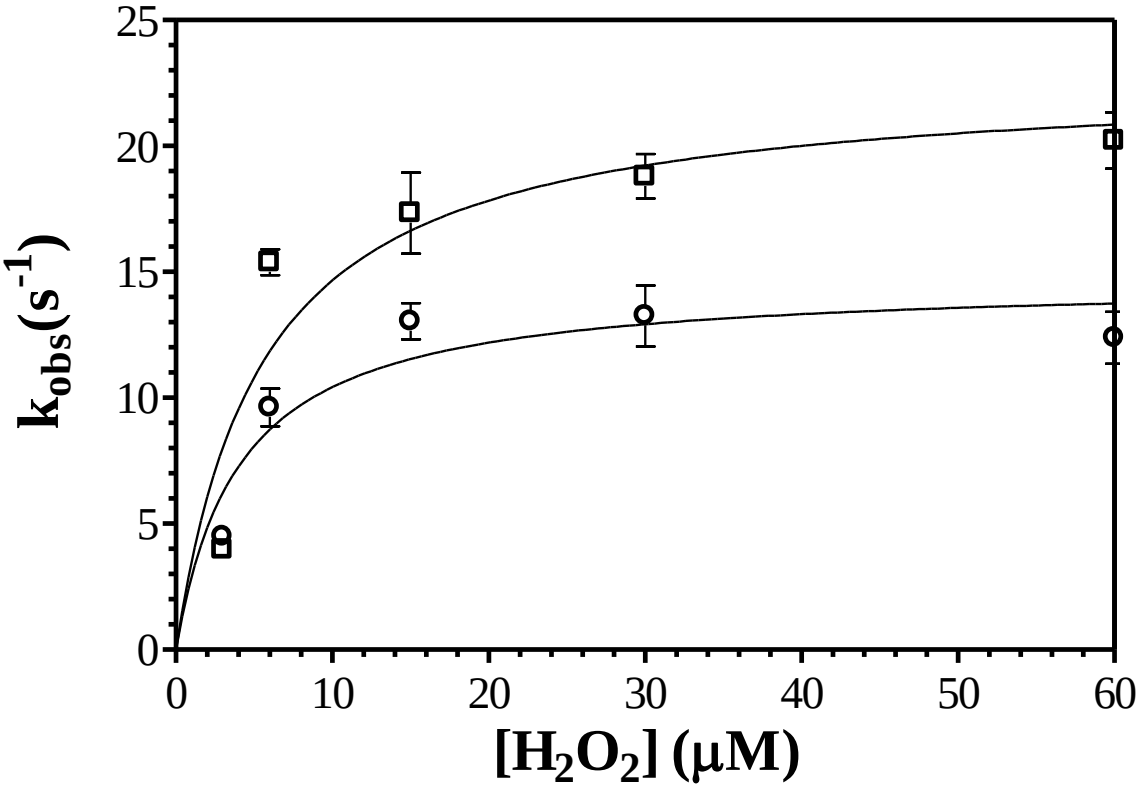

Figure 3.10: Rate constants for formation of compound II in Y226F KatG (□) and KatG$^{\Delta 209\text{-}228}$ (○) plotted against H_2O_2 concentration at 412 nm. Reactions were carried out using 3μM of enzymes, 50 mM phosphate buffer, pH 7.0 at 4°C.

pronounced decrease in absorbance followed by a subsequent increase in absorbance became more pronounced. The first phase of the reaction was clearly H_2O_2 dependent, just as the second-phase was H_2O_2 independent (Figure 3.11)

As mentioned earlier, both $KatG^{\Delta 209-228}$ and Y226F KatG reacted with 100 μM H_2O_2 to rather easily form an intermediate with spectral characteristics consistent with Fe^{III}-$O_2^{\cdot -}$ intermediate (compound III), in order to determine the relative rates of the formation of this species, we monitored reactions with 100 μM H_2O_2 by stopped-flow. Following accumulation of compound II-like intermediate a slow emergence of the Fe^{III}-$O_2^{\cdot -}$ intermediate was observed indicated by a shift in the β and α bands from 530 and 560 nm, respectively to 542 and 578 nm, respectively (Figure 3.12 panels A and B). Interestingly, the rate of compound III formation was more rapid with $KatG^{\Delta 209-228}$ thanY226F KatG.

Both Y226F KatG and $KatG^{\Delta 209-228}$ displayed similar mechanistic response to H_2O_2, and interestingly, the rate constants governing their reactions with H_2O_2 were very similar to one another. This would suggest that the profound differences between the two proteins in sensitivity to H_2O_2-dependent inactivation was not actually due to differences in the direct reaction with H_2O_2 or their relative rates.

3.3.3.2. *Rapid Freeze-quench EPR*

RFQ-EPR experiments were performed on Y226F KatG and $KatG^{\Delta 209-228}$ to determine the presence of protein-based radicals during the reaction of these with H_2O_2. These studies were to

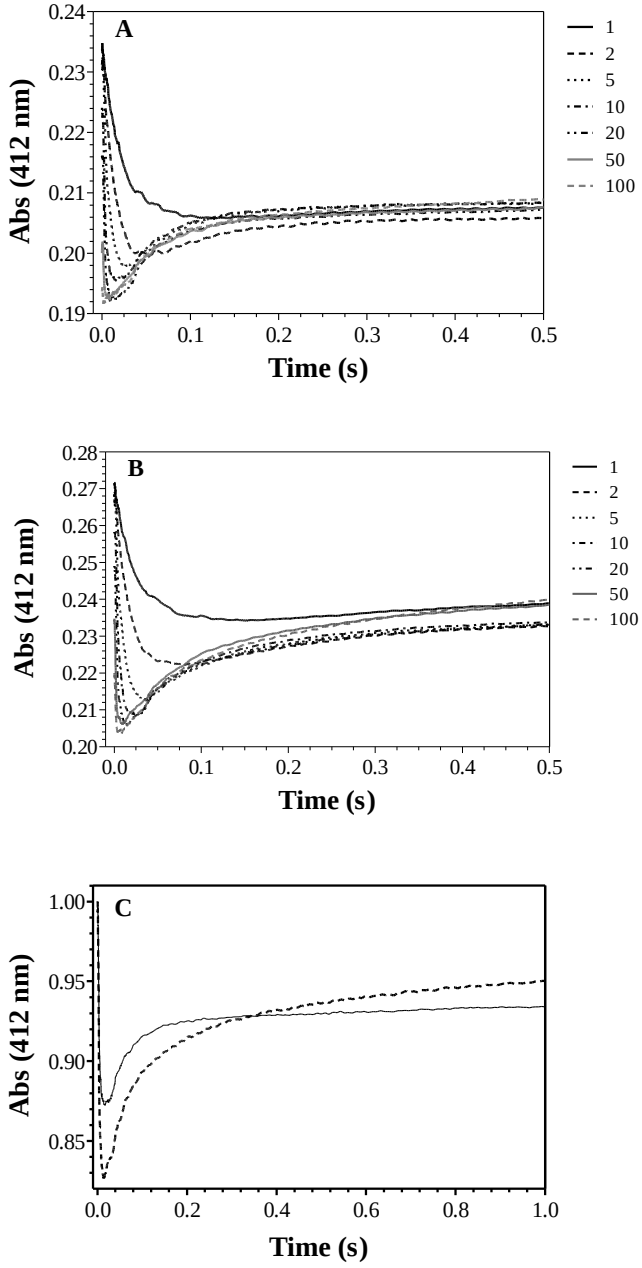

Figure 3.11: Typical time trace at 412 nm showing decay of compound I to compound II. Reaction of 3 μM of either Y226F KatG (A) or KatG$^{\Delta 209\text{-}228}$ (B) at different concentrations (μM) of H_2O_2 C, Overlay of the time traces of reaction of 3 μM of Y226F KatG with15 μM H_2O_2 (solid line) and 3 μM KatG$^{\Delta 209\text{-}228}$ with 30 μM H_2O_2 (dashed line). Reactions were carried out in 50 mM phosphate buffer, pH 7.0 and 4 °C.

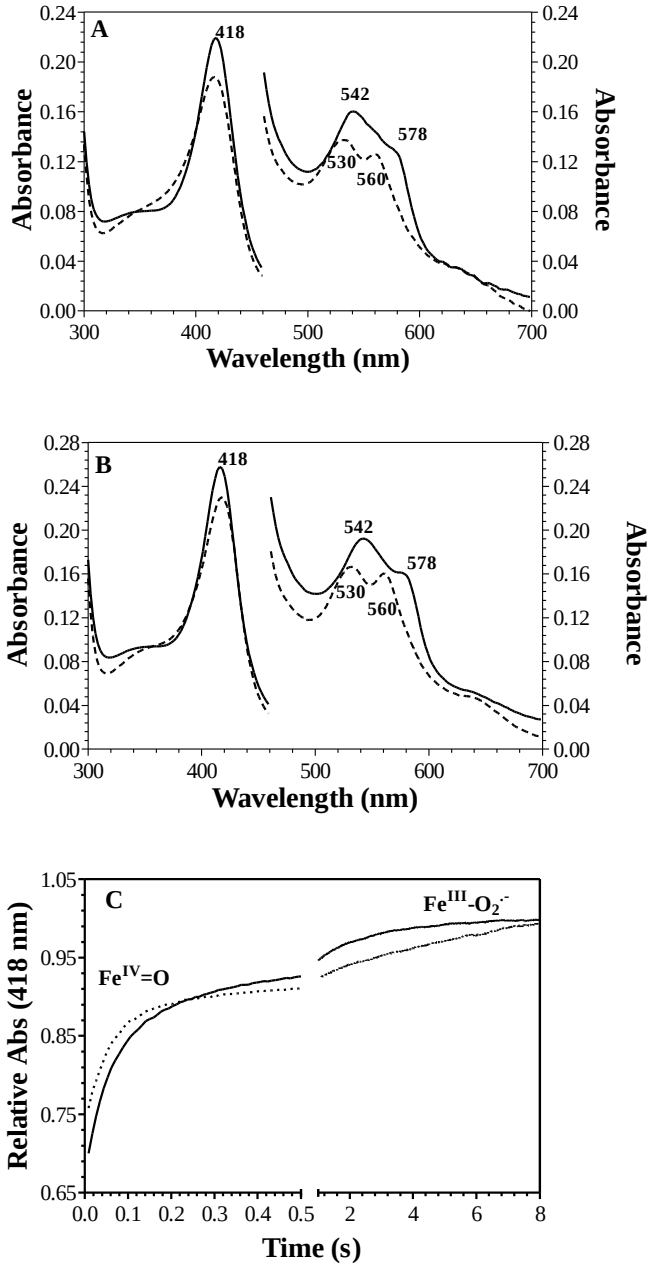

Figure 3.12: Heme intermediates observed during reactions with excess H_2O_2. Spectral changes upon addition of 100μM H_2O_2 to ferric Y226F (A) and KatG$^{\Delta 209\text{-}228}$ (B) recorded at 0.09 s (dashed line) and 7.5 s (solid line) for Y226F KatG and 0.2 s (dashed line) and 7 s (solid line) for KatG$^{\Delta 209\text{-}228}$. C, Time course of reaction of Y226F KatG (dashed line) and KatG$^{\Delta 209\text{-}228}$ (solid line) with H_2O_2 followed at 418 nm. All reactions were carried in 50 mM phosphate buffer, pH 7.0 at 4°C

complement the optical data for heme intermediates observed in our stopped-fow experiments. Both the variants were mixed with H_2O_2 and samples were frozen at an incubation times from 10 ms to 400 ms. These conditions corresponded well to optical stopped-flow measurements used to generate compound I and compound II (Figure 3.11).

Figure 3.13 shows the results obtained when KatG$^{\Delta 209\text{-}228}$ was mixed with 5 equivalents of H_2O_2 and frozen at the incubation times from 10 ms to 400 ms. At 5 equivalents of H_2O_2 an initial doublet with hyperfine splitting at ~21 gauss and line width of ~30 gauss was observed only after 10 ms (Trace A). On a longer time scale (300 ms) a singlet signal started to appear with much smaller hyperfine interaction and disappearance of doublet species (Trace B). At ten-fold higher H_2O_2 concentration (50 equivalents) and a longer reaction time (400 ms) only a narrow singlet with no hyperfine splitting was observed (Trace C).

The effect of reaction time and H_2O_2 concentration on radical species observed may reflect transition from the compound I-like to compound II-like spectra observed in our optical stopped-flow experiments. Moreover, the spectra clearly indicate the participation of protein components in oxidation even though the Tyrosine 226 side chain is absent and the W-Y-M covalent adduct cannot form. The Y226F variant presented substantially greater difficulty in the RFQ experiment. Nevertheless, qualitatively similar results were obtained when the protein was mixed with 10 equivalents of H_2O_2 and allowed to react for 13 ms (Figure 3.14).

3.3.3.3. Sequential mixing reaction with H_2O_2 and electron donors

Single mixing kinetic experiments showed a slower rate of compound I formation and a faster rate of compound III formation for KatG$^{\Delta 209\text{-}228}$ in the presence of H_2O_2 alone, indicating

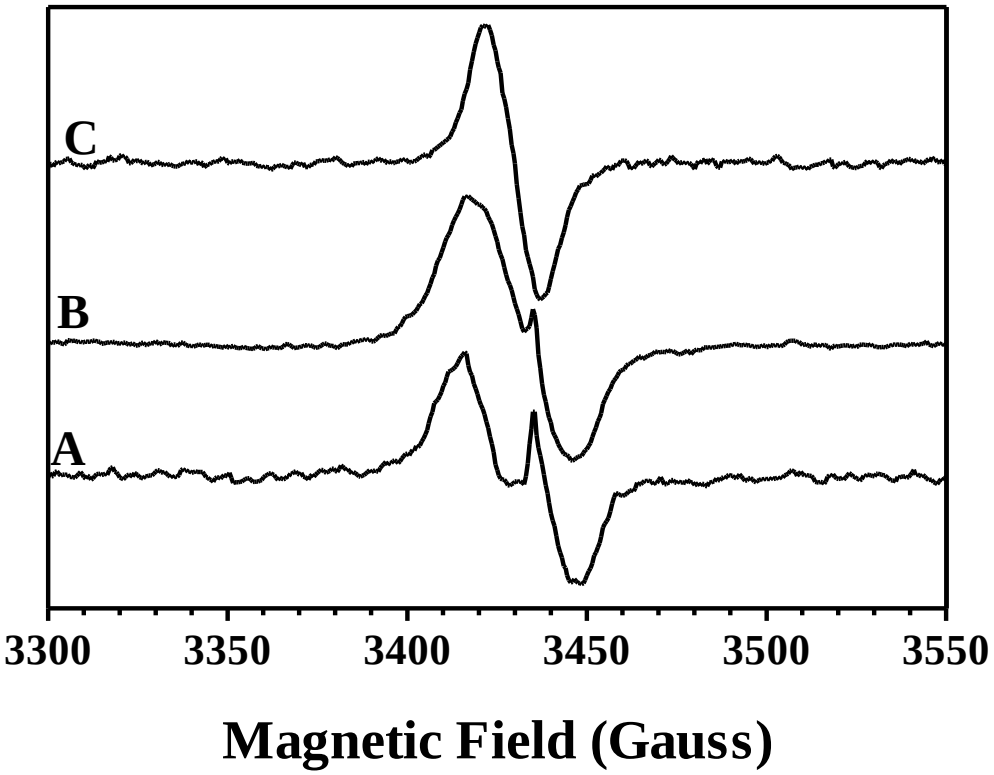

Figure 3.13: EPR spectra of appearance of different species in KatG$^{\Delta 209\text{-}228}$ during the reaction of resting enzyme with H_2O_2. KatG$^{\Delta 209\text{-}228}$ (141 μM) was reacted at 4°C with 5 equivalents (A and B) and 50 equivalents of H_2O_2 (C). Reaction mixtures were freeze quenched after (A) 10 ms; (B) 300 ms; and (C) 400 ms.

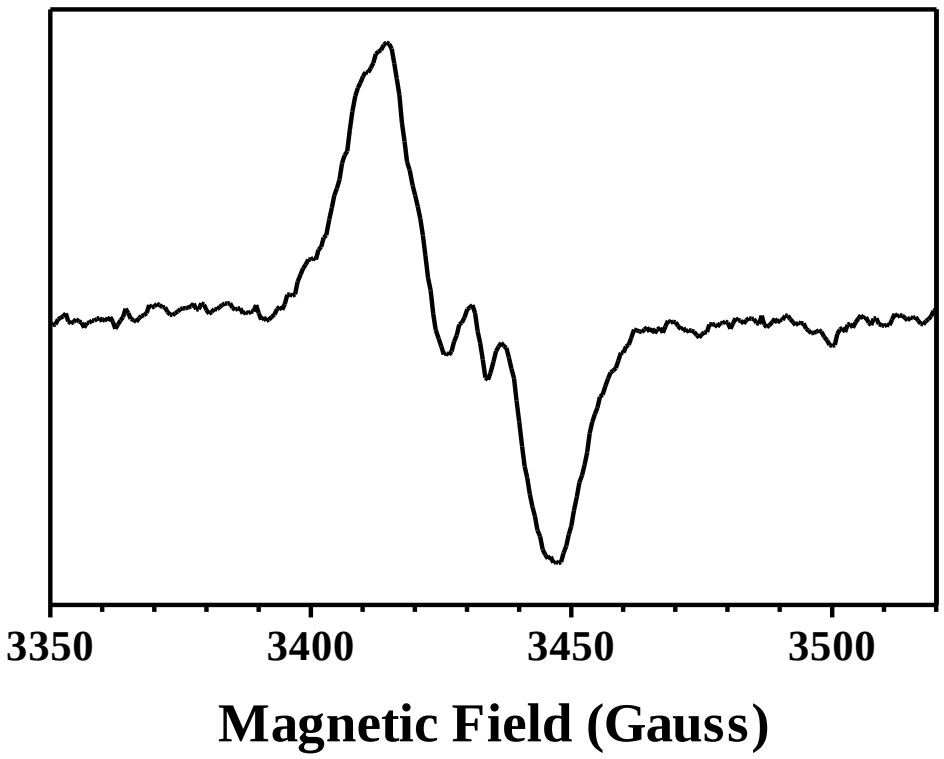

Figure 3.14: EPR spectra of appearance of doublet species in Y226F KatG during the reaction of resting enzyme with H_2O_2. Y226F KatG (131 μM) was reacted at 4°C with 10 equivalents of H_2O_2 and the reaction mixture was quenched after 13 ms.

lower peroxidase activity and greater susceptibility to H_2O_2-dependent inactivation. However, substantially higher peroxidase activity and greater resistance to H_2O_2-dependent inactivation was observed for KatG$^{\Delta 209\text{-}228}$. In order to account for these paradoxical findings, the reactions of KatG$^{\Delta 209\text{-}228}$ and Y226F KatG with electron donors were evaluated by stopped-flow experiments. In order to carry out these experiments a sequential mixing approach was required. In this, both the enzymes were first reacted with single equivalent of H_2O_2, and then following mixing with solution containing electron donor, the return of ferryl heme intermediates to the ferric state was followed. In order to allow for formation of higher oxidation heme states in the initial reaction with H_2O_2, a delay time of 0.7 s and 10 s for Y226F KatG and KatG$^{\Delta 209\text{-}228}$, respectively, was set to separate the initial mixing event and the final mixing event.

For both the variants, the first spectrum observed under these conditions was the ferryl species resembling compound II. Reduction of compound II to the ferric state in the presence of buffer alone, ascorbate, or ascorbate and ABTS was followed by monitoring the absorbance increase at 400 nm (Figure 3.15, Panels A and B). Irrespective of the identity of electron donor, the rate of conversion of KatG$^{\Delta 209\text{-}228}$ to the ferric state was substantially faster than Y226F KatG (Figure 3.15, Panel C). For the experiment including ascorbate and ABTS, we also evaluated the effect of ABTS concentration on the rate of enzyme reduction. The plot of pseudo first-order rate constants, k_{obs}, against ABTS concentration was linear and from the slope second order rate constants were determined to be 5.2×10^4 M^{-1} s^{-1} for KatG$^{\Delta 209\text{-}228}$, which was over an order of magnitude higher than that for Y226F KatG (1.8×10^3 M^{-1} s^{-1}) (Figure3.16).

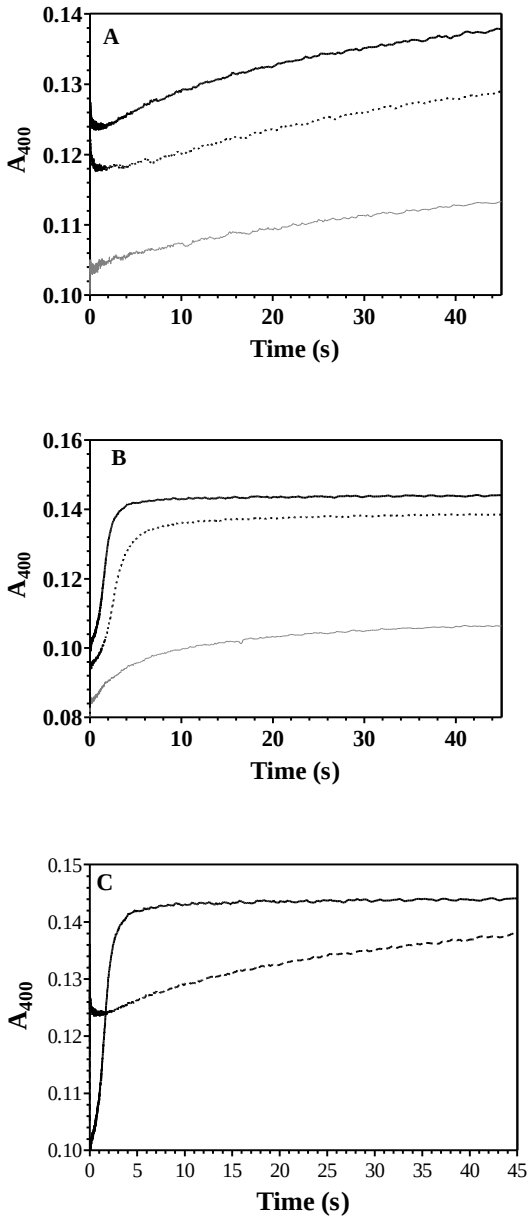

Figure 3.15: Reduction of compound II of Y226F KatG (A) and KatG$^{\Delta 209\text{-}228}$ (B). Sequential mixing experiment were performed to monitor the return of ferryl intermediate to the ferric state in the presence of buffer (gray line), 15 μM ascorbate (dotted line), and 15 μM ascorbate and 15 μM ABTS (solid line) under single turnover conditions. C, Effect of ABTS on the reduction of compound II of Y226F KatG (dotted line) and KatG$^{\Delta 209\text{-}228}$ (solid line) to the ferric state. All reactions were carried out in 50 mM phosphate buffer, pH 7.0 at 4°C

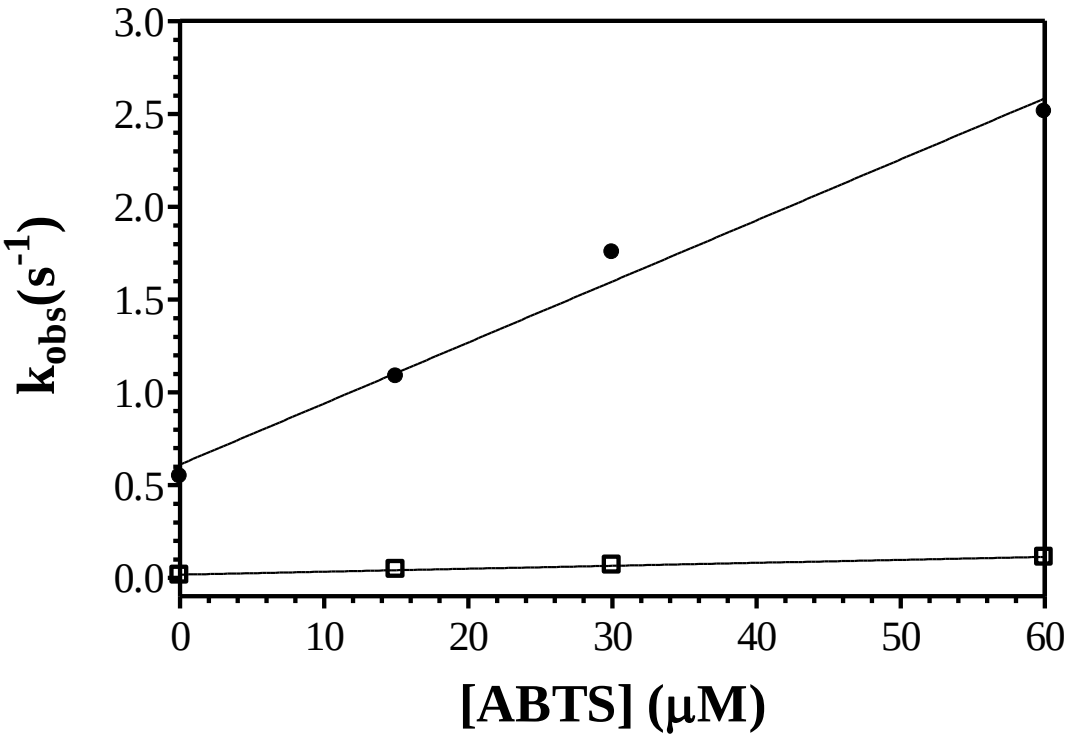

Figure 3.16: Rate constants for reaction of Y226F KatG (□) and KatG$^{\Delta 209\text{-}228}$ (●) to the ferric state plotted against ABTS concentration. Effect of ABTS concentration, in the presence of 15μM ascorbate, on reduction of ferryl intermediates of each enzyme was monitored using sequential mixing stopped-flow experiment. All the reactions were carried out in 50 mM phosphate buffer, pH 7.0 at 4°C

3.4. Discussion

Comparison of crystal structures and amino-acid sequences of catalase-peroxidases with their monofunctional peroxidase counterparts indicate the presence of a large loop 1 (i.e. LL1) between Asp192 and Pro229 (*E.coli* numbering). The LL1 structure forms part of substrate access channel and connects the distal and proximal halves of KatG active site. LL1 has been assigned an important role of supporting tyrosine (Y226) for the formation of Trp-Tyr-Met crosslink. This crosslink is an important feature that maintains the catalatic activity of KatG. However, the role of rest of the LL1 structure in KatG catalysis is not well defined.

In this research, we have presented evidences in support of other important roles of LL1 besides anchoring Y226 in its proper position. The variants involving Y226 have been created either by site-directed mutagenesis (Y226F KatG) or deletion mutagenesis ($KatG^{\Delta 209\text{-}228}$ and $KatG^{\Delta LL1}$) and these were evaluated by steady state and transient-state kinetic methods. The properties of these variants were compared against the wtKatG and another LL1 deletion variants which retains tyrosine. Our data indicated that the LL1 structure restricts the access of peroxidatic electron donors to the active site and also that at least part of LL1 is important for maintaining the structural integrity of KatG.

The importance of LL1 structure in stability of KatG protein was illustrated by comparison of $KatG^{\Delta LL1}$ to the variants where only part of the structure has been removed ($KatG^{\Delta 209\text{-}228}$). $KatG^{\Delta LL1}$ was expressed in inclusion bodies and required purification under denaturing conditions followed by refolding, whereas $KatG^{\Delta 209\text{-}228}$ was expressed in soluble form. Also, heme titration of apo $KatG^{\Delta LL1}$ produced a linear increase in activity only up to 0.25

equivalents, whereas wtKatG and KatG$^{\Delta 209\text{-}228}$ showed no defects in heme uptake. As in all available crystal structures for KatG enzymes, the N-terminal and C-terminal ends of LL1 are separated by a considerable distance (~25 Å) (*91-94*). This instability in the KatG structure can arise due to the strain imposed on the enzyme structure by forcing D192 and P229 to be sequentially and therefore, spatially adjacent to one another. When a portion of the LL1 structure which does not appear to have a particular catalytic function (note the properties of KatG$^{\Delta 200\text{-}214}$) is allowed to remain in the KatG structure as in KatG$^{\Delta 209\text{-}228}$ the stability issues are largely resolved.

Steady-state data showed that the LL1 variants involving Y226 either by deletion (KatG$^{\Delta LL1}$ and KatG$^{\Delta 209\text{-}228}$) or substitution (Y226F) retained no catalase activity due to absence of the W-Y-M adduct, however, they all differed substantially in their peroxidase activity. The main effect on peroxidase activity was seen with respect to H_2O_2. These variants showed similar response to lower H_2O_2 concentrations, however, at higher H_2O_2 concentrations they diverged dramatically specifically in terms of their susceptibility to H_2O_2-dependent inhibition. The increase in peroxidase activity at lower H_2O_2 concentration can suggest that in the absence of *catalatic* activity, the catalytic machinery of KatG is completely dedicated towards accomplishing the *peroxidatic* activity of KatG. Furthermore, the inhibition at higher concentrations of H_2O_2 is suggestive of formation of an inactive intermediate $Fe^{III}\text{-}O_2^{\cdot -}$ (compound III).

Apparent second-order rate constants for peroxidase turnover with respect to H_2O_2 were similar for each variant but with respect to the reducing substrate, ABTS, reactivity at low

concentrations varied considerably. The apparent second-order rate constant for Y226F KatG (1.7×10^5 $M^{-1}s^{-1}$) was an order of magnitude lower than either $KatG^{\Delta 209-228}$ (3.0×10^6 $M^{-1}s^{-1}$) or $KatG^{\Delta LL1}$ (1.5×10^6 $M^{-1}s^{-1}$).

Single-mixing stopped-flow data showed that even though Y226F KatG showed poor peroxidase activity as compared to $KatG^{\Delta 209-228}$, the rate of formation of compound II was twice as high for Y226F KatG than for $KatG^{\Delta 209-228}$. Compound II is inactive in the catalase cycle but active in peroxidase cycle and its presence enhances the formation of compound III in the presence of H_2O_2. Indeed, both variants showed different susceptibility to peroxide-dependent inhibition via compound III formation. However, stopped-flow data indicate that the rate of accumulation of this intermediate is similar in both the variants.

As the ferryl intermediate is able to react either with H_2O_2 forming compound III or ABTS leading to ferric state, a poor ability to accomplish latter would be expected to more facile accumulation of the Fe^{III}-$O_2^{\cdot -}$ state. In some respect this is reminiscent of the structural features of typical monofunctional catalase enzyme which have a long and narrow channel leading to heme limiting peroxidase activity. Indeed, in *S. cerevisiae* catalase substitution intended to widen the access channel have been shown to increase the peroxidase activity (*161*). Sequential mixing stopped-flow studies confirmed that ferryl heme intermediates specifically compound II like species were rapidly converted to the resting ferric state in the presence of ABTS. Among the two variants, the rate to return to the ferric state was an order of magnitude faster for $KatG^{\Delta 209-228}$ than for Y226F KatG.

Figure 3.17 represents the proposed intermediates for the catalase (inner pathway) and peroxidase (outer pathway) activities of wtKatG. The catalase reaction in wtKatG incorporates a radical on W-Y-M adduct. The reaction of formation W-Y-M radical is proposed to proceed via formation of compound I (porphyrin π-cation radical). This intermediate is rapidly converted to oxyferryl heme with simultaneous formation of W-Y-M radical (compound I*). The reaction of compound I* with second molecule of H_2O_2 produces an inactive intermediate (Fe^{III}-$O_2^{\cdot -}$). Electron transfer from the superoxide radical of Fe^{III}-$O_2^{\cdot -}$ to the WYM helps in decomposition of this intermediate to ferric enzyme and dioxygen (O_2). In the peroxidase cycle, formation of an external protein radical ($P^{\cdot}$) is suggested from compound I*, keeping in mind the narrowness of the access channel in KatG compared to the size of many peroxidatic electron donors (AH). The intermediate carrying the $P^{\cdot}$ was called compound I**. Compound I** was then reduced by two equivalents of AH generating ferric enzyme, two substrate radicals ($A^{\cdot}$) and a water molecule.

Figure 3.18 proposes the modifications in the catalytic cycle of wtKatG in the absence of tyrosine, either by mutation (Y226F) or by deletion ($KatG^{\Delta LL1}$ and $KatG^{\Delta 209-228}$). The absence of tyrosine prevents the formation of W-Y-M covalent adduct and this results in loss of catalase activity with variable effects on the peroxidase activity. In the absence of W-Y-M adduct, radical is proposed to transfer to external protein site generating $P^{\cdot}$ (compound I**). Due to formation of $P^{\cdot}$, the second reaction with H_2O_2 would form Fe^{III}-$O_2^{\cdot -}$ intermediate (inner dead end in Figure 3.18). The easy formation of Fe^{III}-$O_2^{\cdot -}$ in these variants, in the presence of low H_2O_2 concentration, was supported by our UV-Vis and stopped-flow data (Figures 3.4 and 3.12). Also, the variable effects on peroxidase activity in Y226F KatG can be seen due to the barrier imposed by rest of the LL1 which limits the ability of exogenous electron donors to reach the active site.

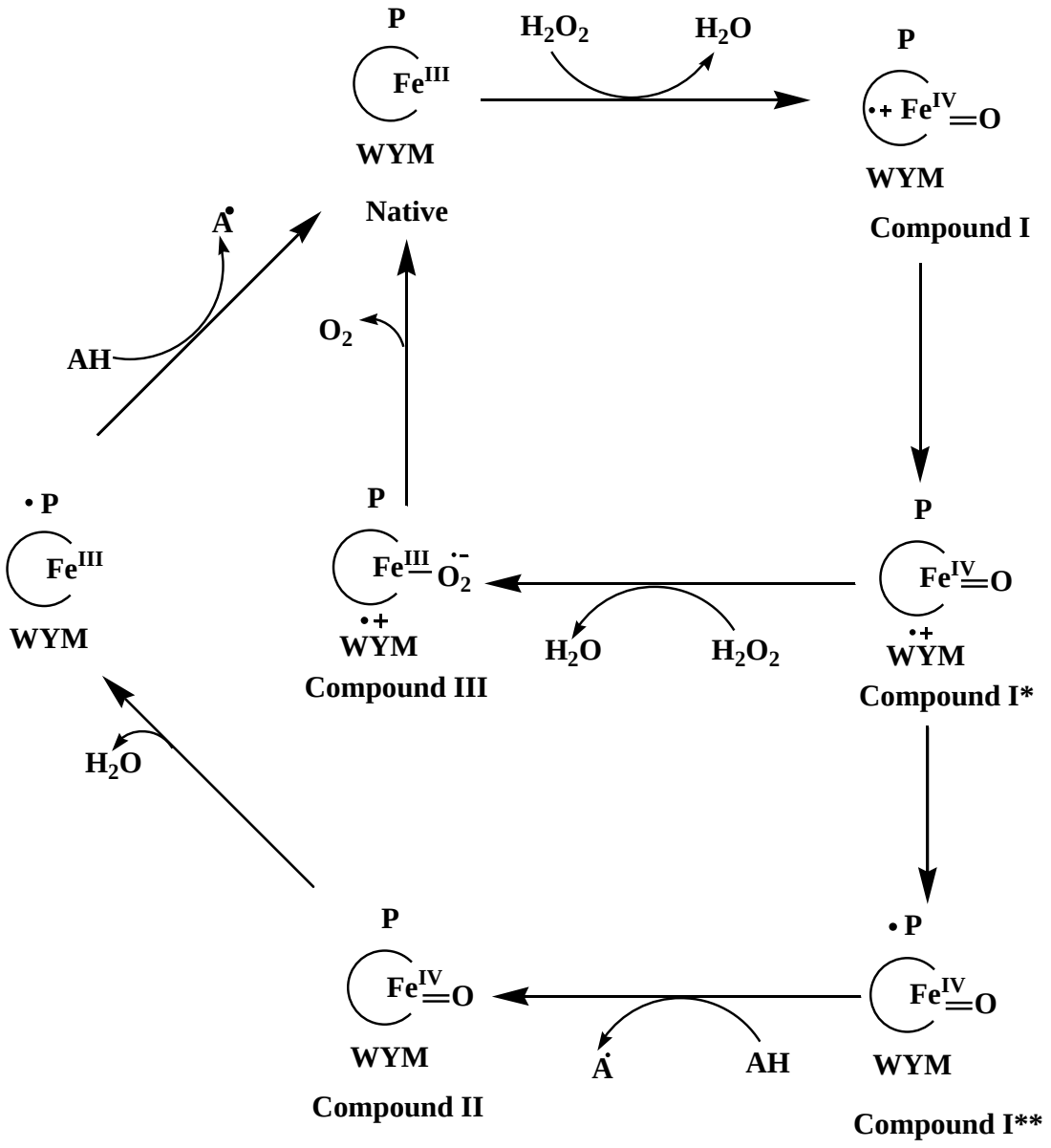

Figure 3.17: Proposed intermediates for catalatic (inner pathway) and peroxidatic (outer pathway) activities of wild-type KatG.

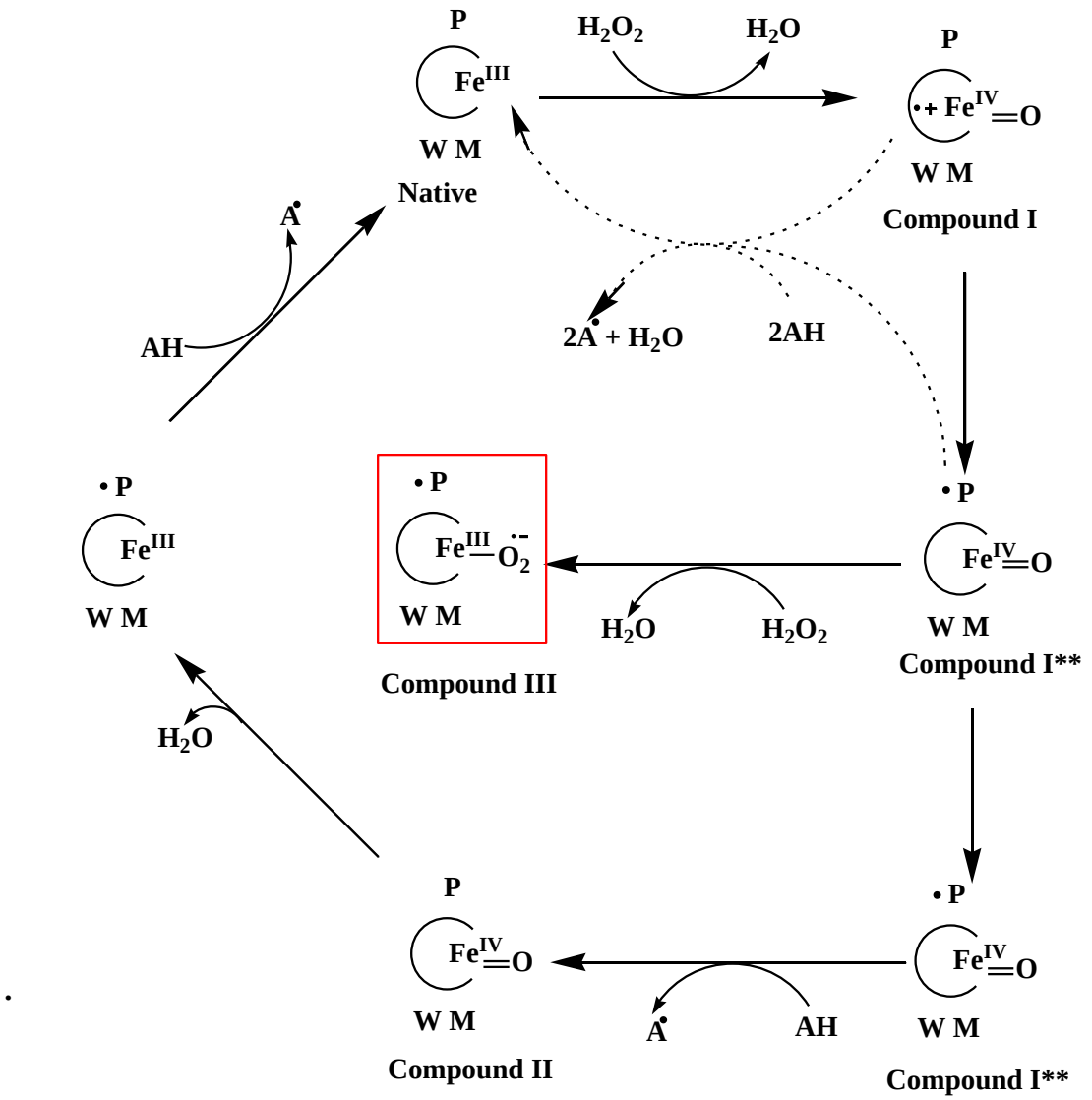

Figure 3.18: Proposed intermediates formed during the interrupted catalatic (inner dead end) and peroxidatic (outer pathway) activities of Y226F KatG and LL1 deletion variants.

This limited peroxidatic turnover can also favor the accumulation of Fe^{III}-$O_2^{\cdot -}$ intermediate due to reaction with H_2O_2. However, the deletion variants in spite of being catalase negative due to the absence of W-Y-M adduct showed substantial greater peroxidase activity than Y226F KatG. An order of magnitude increase in the rate of return of ferryl species to ferric form in the deletion variants compared to Y226F KatG may suggest that deletion of entire LL1 or part of it relives the barrier and allows the access of larger exogenous electron donor leading to more direct electron transfer pathway (represented by bold dotted lines in Figure 3.18). This direct electron transfer increases the peroxidatic turnover in the deletion variants and ultimately prevents the accumulation of Fe^{III}-$O_2^{\cdot -}$ intermediate.

In conclusion, we have shown that, LL1 act as a gate keeper to limit the peroxidatic activity in favor of catalase turnover. However, by obstructing the access of peroxidatic electron donor LL1 makes the enzyme prone to accumulation of inactive Fe^{III}-$O_2^{\cdot -}$ intermediate. Under normal circumstances, this would be profoundly disadvantageous; however, presence of Y226 in W-Y-M in close proximity to heme takes advantage of Fe^{III}-$O_2^{\cdot -}$ intermediate as a mechanism for release of oxygen and completion of novel catalatic mechanism.

Chapter Four: Dependence of Catalytic Ability of Catalase-peroxidases on Intersubunit Interactions

4.1. Introduction

Catalase-peroxidases (KatGs) are heme-dependent, bifunctional enzymes found in bacteria, archebacteria and some fungi (*21*). The catalase and peroxidase activities of these enzymes are similar to those of the robust monofunctional representatives found in nature. The catalase activity of KatG rivals that of bovine liver catalase (*32*), and the peroxidase activity is well within the range of those observed within the non-animal peroxidase superfamily (*105*). This presents three options for the advent of this unique bifunctionality: 1) Enhanced peroxidase function has been built into the framework of a pre-existing catalase active site, 2) enhanced catalase activity has been obtained from a peroxidase active site , or 3) a completely new structural scaffold has been utilized which allows for both functions.

The KatG active site is nearly identical to Class I of the non-animal peroxidases (e.g., cytochrome c peroxidase), but it has no resemblance to typical monofunctional catalases (*98*). Clearly, nature has taken the second option, modifying peroxidase scaffold to perform catalase activity orders of magnitude greater than any other members of its superfamily. The modifications in the peroxidase scaffold are immediately evident from the crystal structures and

amino acid sequence alignments of known KatGs in comparison to monofunctional peroxidases (*91-94*). On one hand KatGs are multimeric enzymes either homodimers or homotetramers. This is in contrast to most other non-animal peroxidases which are almost entirely monomeric. A direct monomer comparison reveals that the KatG subunit has three peripheral structures which are absent from the other monomeric peroxidases (*91-94, 99*) .

First, there is the gene duplicated C-terminal domain ≥ 30 Å away from the active site. Despite its substantial separation from the active site, it is essential for catalase-peroxidase function by preventing distal histidine coordination to the iron in the heme (*86*). Second, two large loops, called large loop 1 (LL1) and large loop 2 (LL2), are observed in all the KatGs and have been shown to be essential for catalase but not peroxidase activity (*43, 87, 98, 102, 162*). Parts of LL1 and LL2 contribute to a narrow access channel to the deeply buried heme in the active site (*103*). In terms of length and sequence conservation, LL1 and LL2 contrast with one another in noteworthy ways. On one hand, the LL1 structure varies considerably in length ranging from 37 to76. Across this structure there are stretches of sequence that show little if any conservation, but there are also portions which are virtually invariant across all catalase-peroxidases, such as the "MGLIYVNPEG" sequence that appears at the LL1 C-terminus (*98*). In contrast, LL2 varies little in its length, and yet at the same time, strictly conserved residues are far less prevalent in the structure than in LL1.

LL1 is positioned at one edge of the heme between D and E helices, and it connects the distal and proximal sides of the active site (*91-94*). The strictly conserved residues, e.g., Tyr249, Ile248, and Glu253 (*Synechocystis* numbering), have been identified as essential for the H_2O_2

oxidation required for catalase turnover (*91-94, 102*). Tyrosine 249 participates in a unique Trp122-Tyr249-Met275 covalent adduct found on the distal side of the active site heme. Site-specific substitutions preventing formation of the full adduct (e.g., Y249F (*90*), M275I (*114*), etc.) produce KatG variants with substantially diminished catalase activity. It has been reported that Ile248 maintains the heme architecture by forming a hydrogen bond with Asp152 (*105*), and Glu253 creates an acidic entrance to the access channel, which helpd to stabilize and orients the solute matrix essential for H_2O_2 oxidation (*102*).

Crystal structures of KatGs indicate that LL2 begins and terminates adjacent to the active site between the F and G helices. The ascending and descending limbs of LL2 run roughly parallel to a hydrogen bond network formed by distal histidine (His106), Asn136, and Leu130. A KatG variant entirely lacking LL2 showed a 200-fold decrease in catalase activity, but only a two fold reduction in peroxidase activity (*87*). However, the mechanism by which LL2 exerts active site control is still to be explored as the majority of effort has focused on understanding the role of LL1 in the catalytic versatility of KatG.

A consistent feature of LL2 in all solved structures for KatG enzymes is the contact of its apex with the C-terminal domain of another subunit. The LL2 apex contains six amino acids (Ala288-Pro289-Ile290-Glu291-Glu292-Gln293, *E.coli* residues and numbering) which interact with a hydrophobic cavity of C-terminal domain (Figure 4.1). In order to investigate the role of this point of contact in maintaining the active site architecture and catalytic ability of *E.coli* KatG, a series of site-specific and deletion variants were generated and the catalytic and spectroscopic properties were evaluated.

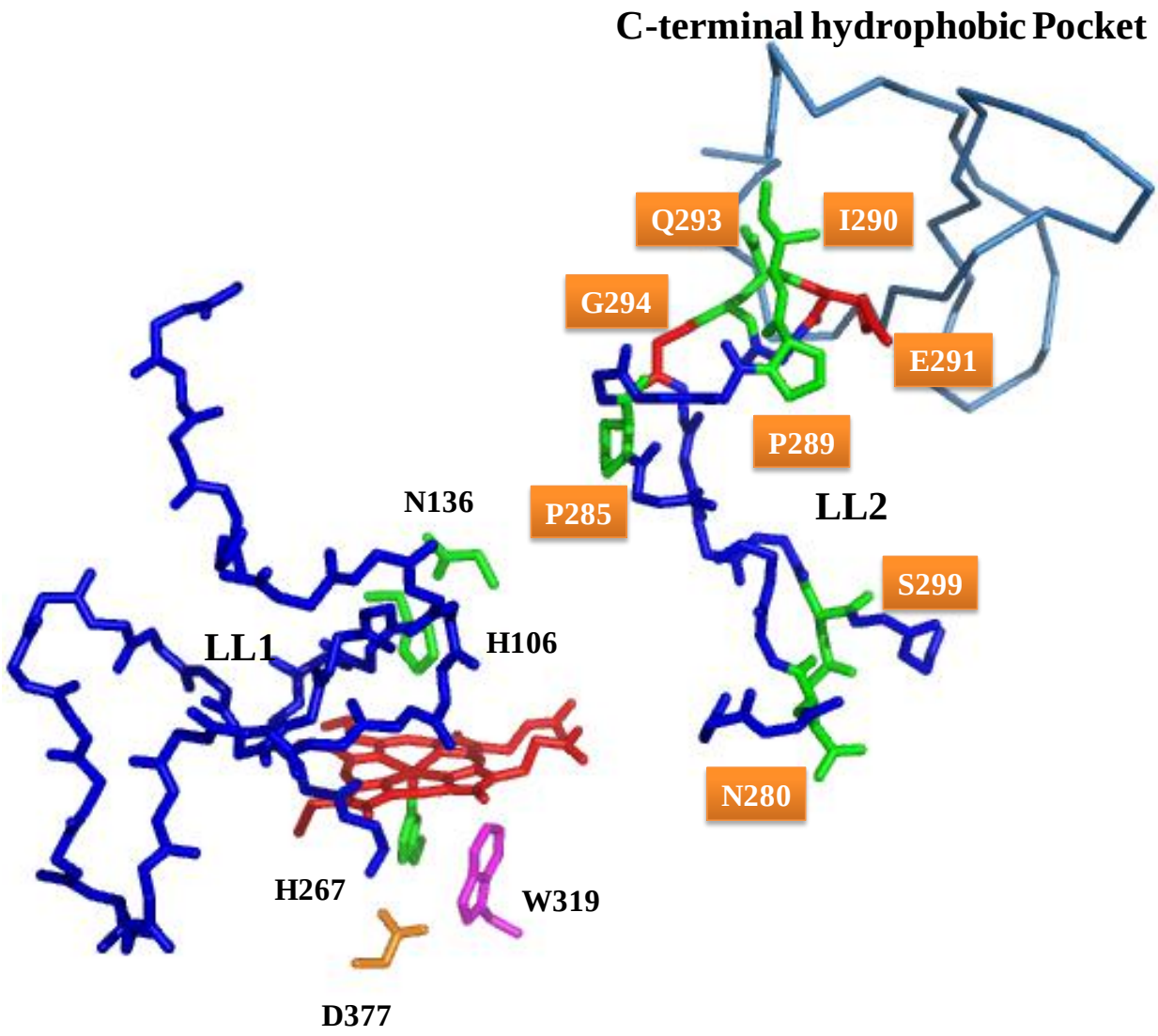

Figure 4.1: Position of LL2 with respect to the active site Heme. Structure was taken from PDB accession domain 1SJ2. LL2 starts and ends adjacent to the active site. IIe290, Glu291, and Gln293 (*E.coli* numbering) are located on the apex of LL2 forming a point of contact with hydrophobic cavity of C-terminal domain of another subunit. The residues investigated in this study are highlighted in orange.

Table 4.1: Classification of variants based on catalatic activity

Group I	Group II	Group III
I290A KatG	IEEQ-A KatG	KatG$^{\Delta 288\text{-}293}$
Q293A KatG	KatG$^{\Delta 291}$	
I290A/Q293A KatG		KatG$^{\Delta 290\text{-}293}$
I290V KatG	KatG$^{\Delta P285/\Delta G294}$	
Q293V KatG		KatG$^{\Delta 291\text{-}292}$
I290V/Q293V KatG	KatG$^{\Delta N280/\Delta S299}$	
Q293E KatG		KatG$^{\Delta LL2}$
E291A KatG		
E291K KatG		
E291K/E292A KatG		

The variants settled into three groups on the basis of their catalase activity (Table 4.1). Most variants generated by site-directed mutagenesis (i.e., substitution variants) showed similar catalase activity to wtKatG. Likewise, their spectroscopic characteristics changed little compared to wtKatG, suggesting little if any effect on the heme environment. Consistent with these results, the kinetics of peroxidase activity and CN^- binding were all similar to one another and wtKatG. Conversely, the majority of deletion variants showed catalytic and spectroscopic characteristics almost identical to the variant lacking the entire LL2 structure (*87*). The deletion variants had clearly impaired catalase activity and an altered active site structure. These proteins were dominated by high-spin pentacoordinate heme rather than the typical hexacoordinate state heme-dominated wtKatG. These results suggest that the strict length conservation of LL2 plays an important role in the formation of intersubunit interactions between LL2 apex and C-terminal domain; this interaction in turn maintains the appropriate heme environment for the multifunctional activity of KatG.

4.2. Materials and Methods:

4.2.1.Materials

All oligonucelotide primers were obtained from Invitrogen (Carlsbad, CA). *E.coli* strains (XL-1 Blue and BL-21 [DE3]) and *Pfu* polymerase were purchased from Agilent Technologies (La Jolla, CA). Restriction enzymes were obtained from New England Biolabs (Beverly, MA). QIAprep Spin Miniprep kit and nickel-nitriloacetic acid (Ni-NTA) resin were obtained from Qiagen (Valencia,CA). Isopropyl-B-D-thioglactopyranoside (IPTG) was obtained from Gold

Biotechnology Inc. (St. Louis, MO). Mono and di-basic sodium phosphate, acetic acid, and sodium acetate were purchased from Fisher (Pittsburgh,PA). Bugbuster and benzonase nuclease were purchased from EMD (Madison, WI). Ampicillin, chloramphenicol, imidazole, hemin, sodium dithionite, 2,2'-azino-bis(3-ethylbenzothiazoline-6-sulfonic acid) (ABTS), and hydrogen peroxide (30%), were obtained from Sigma (St. Louis, MO). Water purified through Barnstead Easy Pure II UV ultrapure water system (18.2 MΩ/cm resistivity) was used to make all buffers and media.

4.2.2. Cloning of Site-specific and deletion variants

The site-specific and deletion variants of the LL2 were generated using the "around the horn" approach as described in chapter 2, with the exception of I290V KatG and I290V/Q2393V KatG. For these two variants the QuikChange™ procedure was used. Table 4.2 lists the mutagenic primers used in this study. Amplification products were used to transform the *E. coli* XL-1 Blue by heat shock procedure. Colonies were selected on the basis of ampicillin resistance, and the desired plasmids were subjected to restriction endonuclease digestion as successful mutants must contain a specific alteration to the restriction endonuclease digest pattern (Table 4.2). Each restriction site is an addition either by silent mutation or by specific mutation. Restriction digest-positive candidates were subjected to DNA sequencing analysis to confirm that the desired mutation had occurred and no undesired mutations had taken place.

Table 4.2: List of primers used for making site-directed and deletion LL2 variants

Variant	Forward Primer	Reverse Primer	Restriction Enzyme
I290V KatG	5'-Phos- GCTGCACCG**GTT**GAAGAACAA-3'	5'-Phos- TTGTTCTTCAACCGGTGCAGC-3'	Age I
Q293V KatG	5'-Phos- CCGATTGAAGAA**GTT***GGCCTA*GGTTGGGCGAGC-3'	5'-Phos - GCTCGCCCAACCTAGGCCAACTTCTTCAATCGG-3'	Sty I
I290V/Q293V KatG	5'-Phos - GCTGCACCG**GTT**GAAGAA**GTT**GGTTTAGGTTGG-3'	5'-Phos - CCAACCTAAACCAACTTCTTCAACCGGTGCAGC-3'	Age I
I290A KatG	5'-Phos -CCG**GCG**GAAGAACAAGGTTTAGGTTGGGCG-3'	5'-Phos - *CGC*AGCTTCTGGATCAGGACCTACATTTGATGTC-3'	Nae I
Q293A KatG	5'-Phos - CCGATTGAAGAA**GCA***GGCCTA*GGTTGGGCG-3'	5'-Phos - *CGC*AGCTTCTGGATCAGGACCTACATTTGATGTC-3'	Sty I
I290A/Q293A KatG	5'-Phos - CCG**GCG**GAAGAA**GCG**GGTTTAGGTTGG-3'	5'-Phos - *CGC*AGCTTCTGGATCAGGACCTACATTTGATGTC-3'	Nae I
E291A KatG	5'-Phos - CCG*ATC***GCG**GAACAAGGTTTAGGTTGGGCG-3'	5'-Phos - *CGC*AGCTTCTGGATCAGGACCTACATTTGATGTC-3'	Pvu I
E291K KatG	5'-Phos- CCGATT**AAA**GAACAAGGTTTAGGTTGGGCGAGC-3'	5'-Phos - *CGC*AGCTTCTGGATCAGGACCTACATTTGATGTC-3'	N/A
E291K/E291A KatG	5'-Phos – CCGATT**AAAGCC**CAAGGTTTAGGTTGGGCG-3'	5'-Phos - *CGC*AGCTTCTGGATCAGGACCTACATTTGATGTC-3'	Sty I
Q293E KatG	5'-Phos - CCGATTGAAGAA**GAA***GGCCTA*GGTTGGGCG-3'	5'-Phos - *CGC*AGCTTCTGGATCAGGACCTACATTTGATGTC-3'	Sty I
KatG$^{\Delta 288-293}$	5'-Phos - *GGC*TTAGGTTGGGCGAGCACTTACGGC-3'	5'-Phos - *GGC*TTCTGGATCAGGACCTACATTTGATGTCGG-3'	Nae I
KatG$^{\Delta 290-293}$	5'-Phos - *GGT*TTAGGTTGGGCGAGCACTTACGGCAGC-3'	5'-Phos - CGG*GGC*AGCTTCTGGATCAGGACCTAC-3'	Sma I
KatG$^{\Delta 291-292}$	5'-Phos- CCG*ATCCAA*GGTTTAGGTTGGGCGAGC-3'	5'-Phos - *CGC*AGCTTCTGGATCAGGACCTACATTTGATGTC-3'	Sty I
KatG$^{\Delta 291}$	5'-Phos - CCG*ATCGAA*CAAGGTTTAGGTTGGGCGAGC-3'	5'-Phos - *CGC*AGCTTCTGGATCAGGACCTACATTTGATGTC-3'	Pvu I
KatG$^{\Delta 285/\Delta 294}$	5'-Phos - *GCG*CCGATTGAAGAACAA*TTG*GGTTGGGCGAGC-3'	5'-Phos- *CGCTTC*ATCAGGACCTACATTTGATGTCGGACCG-3'	Kas I / Sty I
IEEQ-A KatG	5'-Phos - CCG**GCGGCTGCAGCG**GGTTTAGG-3'	5'-Phos - *CGC*AGCTTCTGGATCAGGACCTACATTTGATGTC-3'	Pst I
KatG$^{\Delta 280/\Delta 299}$			
KatG $^{\Delta 280}$	5'-Phos- GGTCCG*ACGTCAGTA*GGTCCTGATCC-3'	5'-Phos- GGCACCGTGGGTTTTACCCAGCGTATG-3'	Aat II
KatG $^{\Delta 299}$	5'-Phos- GCG*ACG*TACGGCAGCGGCGTTGG-3'	5'-Phos- CCAACCTAAACCTTGTTCTTCAATCGGTGC-3'	
	(used KatG $^{\Delta 280}$ as template)		BsiW I

4.2.3. Expression and purification

Expression and purification of all the variants were carried out as described in chapter 2. Concentrations of purified enzyme was estimated according to the method of Gill and von Hippel (*126*) using ε_{280}= 1.44 x 10^5 $M^{-1}cm^{-1}$ for all the variants with the exception of $KatG^{\Delta LL2}$, where ε_{280}= 1.37 x 10^5 $M^{-1}cm^{-1}$ was used.

4.2.4. Circular Dichroism

Far-UV CD spectra (180-300 nm) were recorded for all the variants prior to reconstitution with hemin by using 5 μM of each enzyme in 5 mM phosphate buffer, pH 7.0. A Jasco J-180 spectropolarimeter was used to record all CD spectra by using 0.05 cm pathlength quartz cell, 0.05 nm data pitch, continuous scanning mode, scanning speed of 50 nm/min, and 8 accumulations. Baseline correction and data analysis were done using J-720 software from Jasco.

4.2.5. UV-visible absorption spectra and activity assays

Wild-type KatG and its variants were reconstituted using 0.9 equivalents of hemin. Following heme addition, each protein was allowed to incubate for 24 hrs at 4 °C. After 24 hrs, each reconstituted protein was centrifuged at 13,000 rpm for 5 minutes to remove any free hemin or insoluble proteins. All spectra were recorded between 800 nm to 250 nm at room temperature in 200 mM phosphate buffer, pH 7.0 using Shmiadzu UV-1601 spectrophotometer. Method of Falk was used to determine the concentration of reconstituted enzyme (*124*).

Catalase activity was evaluated by monitoring the decrease in H_2O_2 concentration at 240 nm (ε_{240}= 39.4 M^{-1} cm^{-1}) (*135*). Peroxidase activity was measured by monitoring the production of ABTS radical at 417 nm (ε_{417} = 34.7 mM^{-1} cm^{-1}), initial concentration of ABTS was measured spectrophotometrically at 340 nm (ε_{340} = 3.66 x 10^4 M^{-1} cm^{-1}) (*136*). All assays were carried out at room temperature using Shimadzu UV-1601 spectrophotometer using 10 nM enzyme, 200 mM phosphate buffer, pH 7.0.

4.2.6. Magnetic Circular Dichroism

A Jasco J-810 spectropolarimeter was used to record MCD spectra. All spectra were recorded using 15 μM of enzyme in 50 mM phosphate buffer, pH 7.0, and 50 mM NaCl. Samples were placed in a 0.5 cm pathlength cuvette, and the cuvette was placed in a magnetic cell holder with in 1.4 Tesla magnetic field generated by permanent magnet. All spectra were recorded at room temperature using the following instrument settings: wavelength, 700 nm to 350 nm; scanning mode, continuous; scanning speed, 50 nm/min; data pitch, 0.1 nm; and accumulations, 8. In order to obtain MCD spectra for the ferrous heme state, small amounts < 1 mg solid sodium dithionite was added to the sample cuvette and mixed. Only four spectral accumulations were collected for the ferrous state. The baseline correction and data analysis were done using Jasco J-720 software. For baseline correction, buffer spectrum was subtracted from the MCD spectrum, and the difference spectrum was used for data analysis. The data were fit to equation 4.1.

$$\varepsilon/\Delta H = \frac{\text{Delta OD}}{\text{(Enzyme concentration mM) x 1.4 Tesla x 0.5 cm pathlength}} \qquad \textbf{(4.1)}$$

4.2.7. Electron Paramagnetic Resonance Spectroscopy and Spin Quantification

EPR spectra were recorded using Bruker EMX instrument equipped with an Oxford ESR 900 cryostat equipped with an ITC temperature controller. Samples were concentrated to a final concentration of 150 μM in a final volume of 300 μl using Amicon Ultra-4 centrifuge filter devices. Spectrometer settings were as follows: temperature, 10K; center field, 3250 G; sweep width, 5500 g; start field, 3250 G; receiver gain, 1.0 x 10^5; microwave power, 9.38 GHz; modulation amplitude, 10 G; modulation frequency, 100 kHz; time constant, 655.36 ms; and conversion time, 655.36 ms. Spin quantification was carried out as described in chapter 2 using Biomolecular EPR spectroscopy software package available online (*134*).

4.2.8. Evaluation of cyanide binding by titration and by stopped-flow

Cyanide binding was evaluated by two methods: equilibrium titration, and stopped-flow kinetics.

Cyanide binding by titration was monitored using Shimadzu UV-1601 spectrophotometer. Titrations were performed by adding 1-2 μL aliquots of a potassium cyanide stock solution to 1 mL of each variant (1μM) held in a cuvette. After each portion of cyanide was added, the solution was thoroughly mixed, and the optical spectrum was recorded after 3 min to ensure completion of the binding reaction. Change in absorbance at 422 nm was plotted against [KCN] to obtain the dissociation constants. All cyanide binding studies were carried out in 50 mM phosphate buffer, pH 7.0, at room temperature.

For stopped-flow kinetics, SX.18 MV Stopped-flow Rapid Reaction Analyzer in single mixing mode was used. One syringe contained 6 μM of enzyme and the second contained KCN (0.03-3 mM). Spectra were recorded by diode array. Kinetic constants were determined form triplicate measurements of single wavelength data recorded at 400 nm (decay of high-spin ferric species) and at 428 nm (formation of low-spin hexacoordinate ferric species). All reactions were carried out at 25°C in 50 mM phosphate buffer, pH 7.0.

4.3. Results

Alignments were performed using sequences of 20 KatGs from across the phylogentic spectrum. Two or more representative samples were taken from each group viz., fungal, bacterial and archeal groups. The samples were chosen on the basis of their separation in phylogenetic relationship tree for catalase-peroxidases provided by Obinger, et.al. (*163*). The degree to which the sequence and length of three large loops are conserved is shown in Figure 4.2. The sequence alignment shows that the length of LL1 varied from 37-76 amino-acids among KatGs contained ~10 highly conserved amino acid residues. In contrast, LL2 was highly conserved in its length (35 amino-acids) with very little (4 invariant amino acids) residue conservation. Three out of the four strictly conserved residues in LL2, were either proline or glycine. These residues tend to have greatest impact on conformation rather than on catalysis. Also, the other strongly conserved residues are almost all hydrophobic (i.e. conservation is between otherwise hydrophobically equivalent residues viz. Leu, Ile, Val, Met, Phe, etc.). The only other strongly conserved residue which did not fit the second category is tryptophan at position 297. We did not observe any apparent structural or functional effects on substituting W297 to alanine. The W297A variant

behaved the same as wtKatG by having equivalent activity profile and spectroscopic features. In contrast, the strictly conserved residues of LL1 included several aromatic residues which have shown to be crucial for bifunctionality of KatGs (*90, 107, 116*). This indicated that length conservation of LL2 over residue conservation might be an important criterion in catalytic versatility of KatG.

Previously, Goodwin lab has shown that the LL2 structure is required to maintain the bifunctionality of KatG (*87, 103*). Indeed, the variant lacking the entire LL2 structure caused a two orders of magnitude loss of catalase activity but only two-fold reduction in peroxidase activity and also diminished the rate of cyanide binding (*87*). However, the mechanism behind this observation was not clearly understood. Closer examination of the LL2 structure indicated that the ascending and descending limbs of this loop run roughly parallel to the hydrogen bond network formed by distal histidine (His106), Asn136, and Leu130. Thus, removal of entire LL2 was suggested to disrupt the above mentioned hydrogen bond network as two of its residues Glu284 and Trp297 lie fairly close to this network (*87, 103*).

Given the essential nature of LL2, its lack of sequence conservation but striking length conservation, and the prominent interaction with the C-terminal domain at the apex of the structure, we targeted LL2 in two different ways. First, we targeted the individual residues (I290, E291, E292, and Q293) which make an intersubunit contact with the hydrophobic cavity of C-terminal domain. These residues were substituted individually and in combination using site-directed mutagenesis. The second approach was to target the length of LL2 by deleting residues either at its apex (A288-Q293) or along its ascending and descending limbs (P285 and G294,

A.

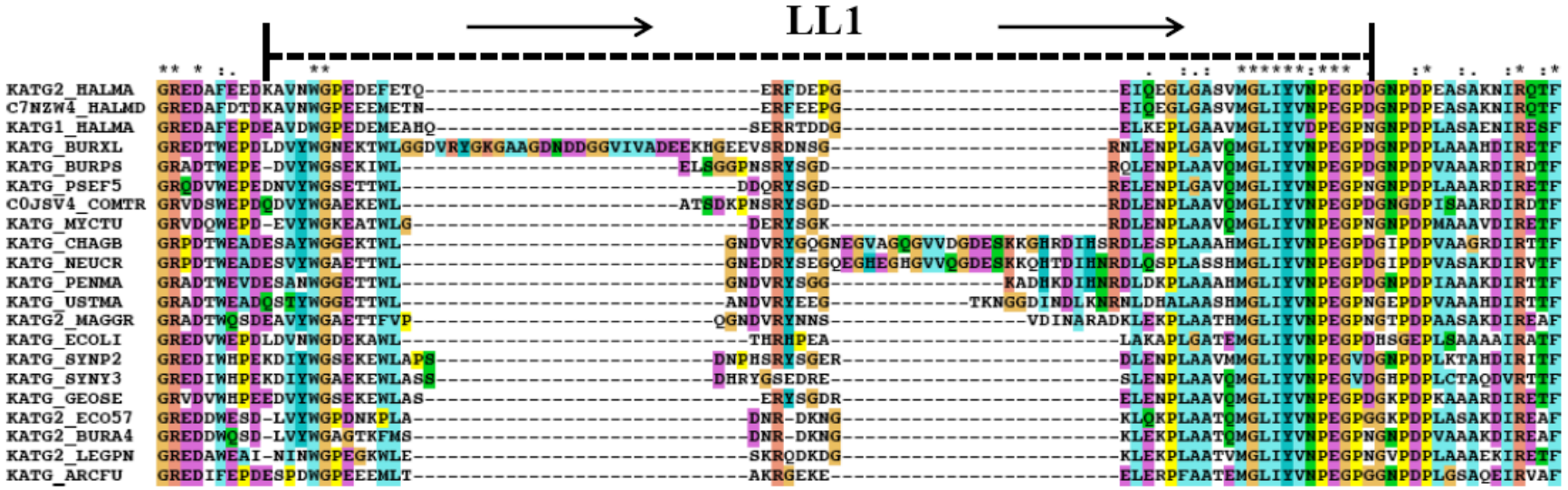

Figure 4.2: Multiple sequence alignment of 20 selected representatives from Class I families with one sequence from a typical Class II representative. Presented here are the three large loops of KatG; LL1 (A), LL2 (B), and LL3 (C). ClustalX version 2.0.11 was used as a tool for multiple alignments of protein sequences (*164, 165*). Dotted line represents length of the loops and arrows indicate their direction. '*' represents positions which have single, fully conserved residue, '·' represents that one of the "stronger' [STA, NEQK, NHQK, NDEQ, QHRK, MILV, MILF, HY, FYM] group is fully conserved, ':' represents that one of the 'weaker' [CSA, ATV, SAG, STNK, STPA, SGND, SNDEQK, NDEQHK, NDEQHRK, FVLIM, HFY] group is fully conserved. Abbreviations of species correspond with their names in UniProtKB (*166, 167*).

B.

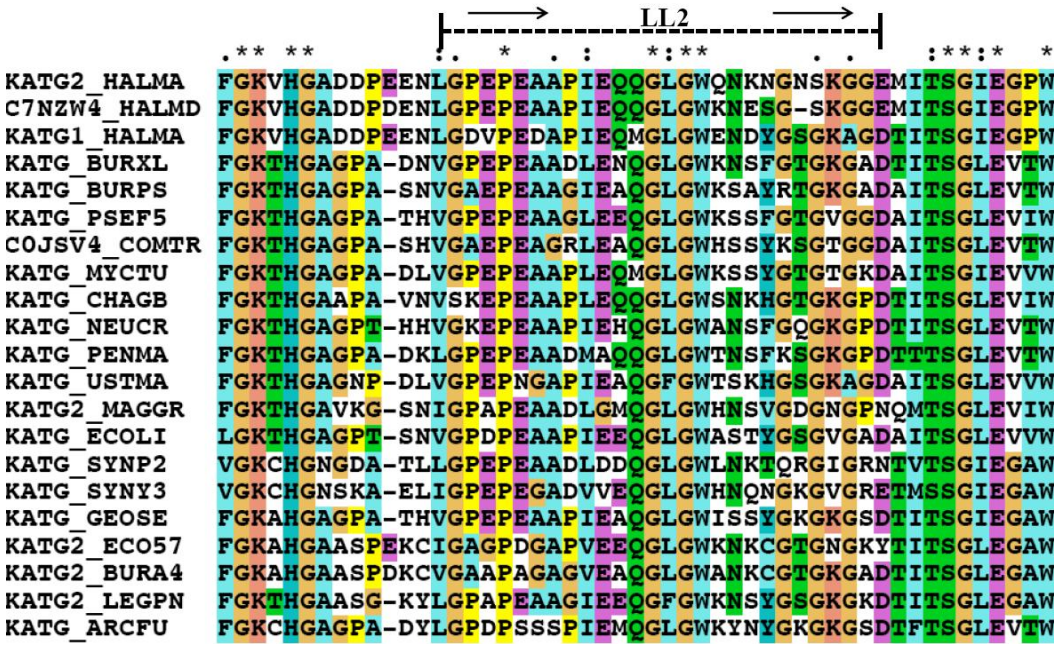

C.

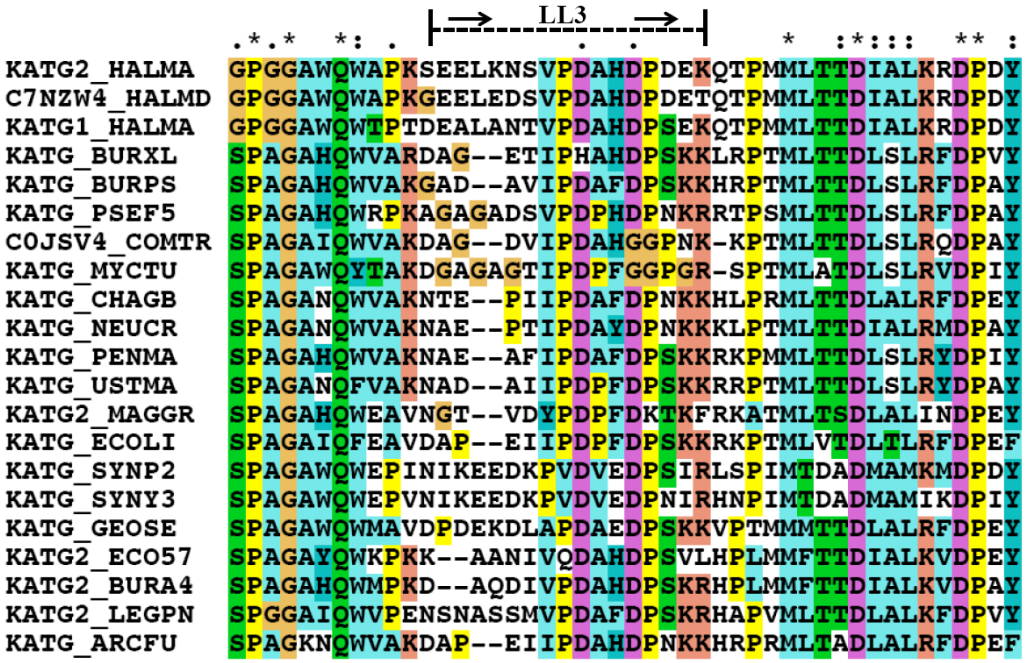

Figure 4.2: (Continued)

N280 and S299) (Figure 4.1). Each vectors for the expression of each variant was successfully produced and confirmed by DNA sequence analysis. Each of the variants were over-expressed in a soluble form and showed proper global folding of the protein as indicated by circular dichroism spectra when compared with the wtKatG (Figure 4.3).

4.3.1. Catalase activity

The catalase activity of the variants was compared with respect to the wtKatG and the variant lacking LL2 ($KatG^{\Delta LL2}$) (Table 4.3). The variants divided into three distinct groups based on their catalatic ability. The apparent second order rate constants (k_{cat}/K_M) of Group I variants were similar to wtKatG (i.e., 10^6 $M^{-1}s^{-1}$) suggesting minimal loss of catalase activity in these variants (Figure 4.4). In stark contrast, Group III variants showed catalase activity at least two orders of magnitude lower than wtKatG as indicated by their low turnover numbers (i.e., k_{cat}) (Figure 4.5). The apparent k_{cat}/K_M for group III variants was three orders of magnitude lower than wtKatG, but was similar to the variant which lacked the entire LL2 structure (*87*). The middle group of variants (i.e., Group II) retained minimal catalase activity as 80-90% reduction in their apparent k_{cat} values was observed when compared to wtKatG (Figure 4.6).

4.3.2. Peroxidase activity

The kinetic parameters for peroxidase activity with respect to H_2O_2 and ABTS are shown in Tables 4.4 and 4.5, respectively. The data obtained from activity assays were fit to standard

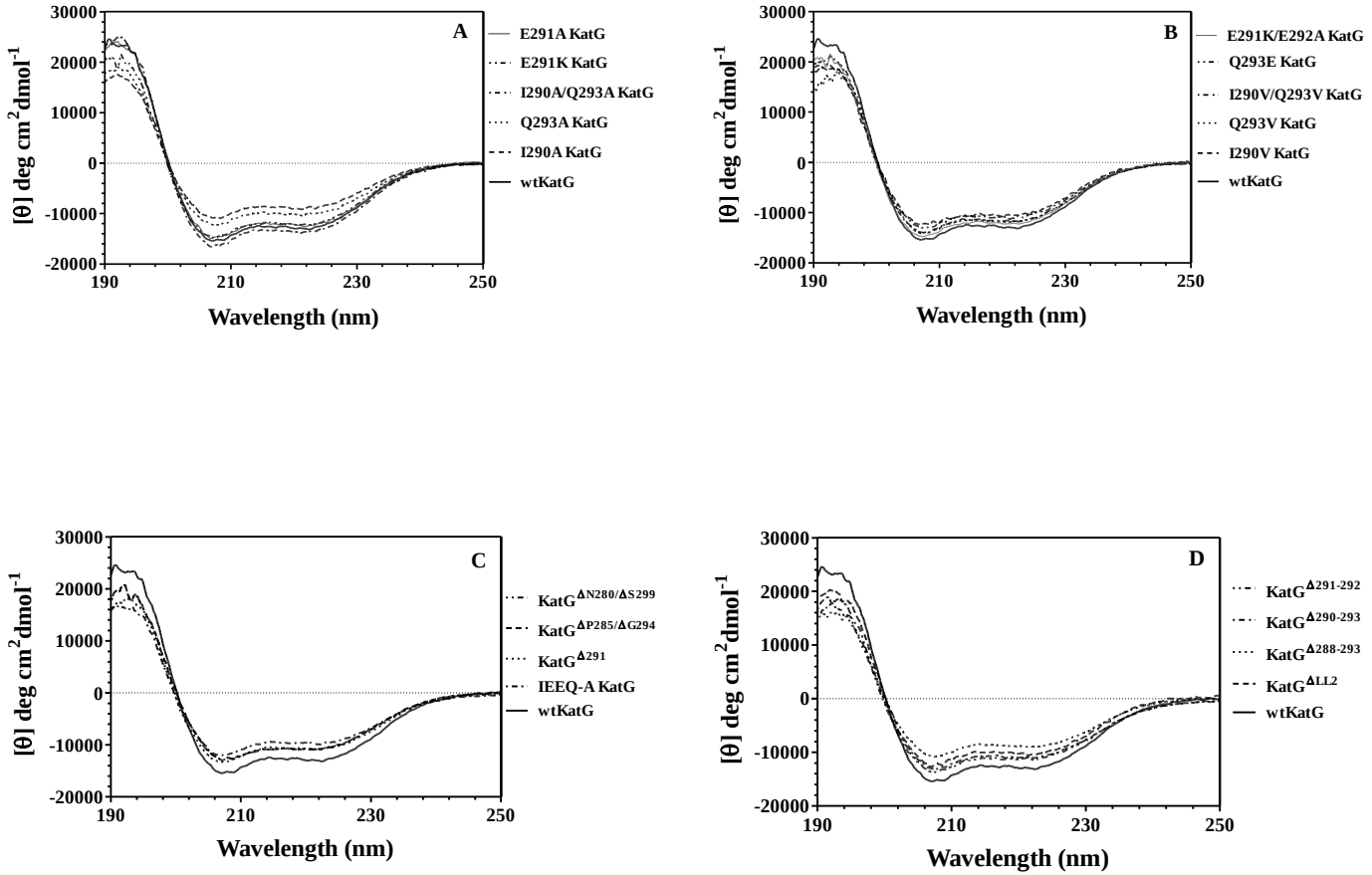

Figure 4.3: CD spectra of group I (A and B), group II (C), and group III (D) variants. Each spectrum was recorded with apo-enzyme in 5 mM phosphate buffer, pH 7.0 at room temperature.

Table 4.3: Apparent catalase kinetic parameters

	KatG	Catalase cycle parameters			
		k_{cat}(s^{-1})	K_M (mM H_2O_2)	k_{cat}/K_M (10^6 $M^{-1}s^{-1}$)	*Fraction (k_{cat})*
Group I	WT KatG	11000 ± 200	3.5 ± 0.2	3.2	1
	I290A KatG	10173 ± 309	3.7 ± 0.3	2.7	0.92
	Q293A KatG	12176 ± 621	4.6 ± 0.6	2.6	1.10
	I290A/Q293A KatG	7606 ± 440	4.1 ± 0.7	1.9	0.69
	I290V KatG	7981 ± 187	3.9 ± 0.3	2	0.72
	Q293V KatG	5309 ± 233	3.1 ± 0.4	1.7	0.48
	I290V/Q293V KatG	9540 ± 293	3.2 ± 0.4	1.8	0.86
	Q293E KatG	9624 ± 568	8 ± 1	1.2	0.87
	E291A KatG	16653 ± 487	5.9 ± 0.4	2.8	1.51
	E291K KatG	9540 ± 293	2.1 ± 0.2	4.5	0.86
	E291A/E2912K KatG	12184 ± 390	2.5 ± 0.3	4.8	1.10
Group II	IEEQ-A KatG	626 ± 28	3.4 ± 0.5	0.18	0.05
	$KatG^{\Delta 291}$	1983 ± 47	3.1 ± 0.2	0.64	0.18
	$KatG^{\Delta P285/\Delta G294}$	1766 ± 49	2.2 ± 0.2	0.8	0.16
	$KatG^{\Delta N280/\Delta S299}$	2535 ± 114	3.2 ± 0.4	0.79	0.23
Group III	$KatG^{\Delta 288\text{-}293}$	7 ± 7	3 ± 14	0.0023	0.0006
	$KatG^{\Delta 290\text{-}293}$	37 ± 5	5 ± 1	0.0074	0.0033
	$KatG^{\Delta 291\text{-}292}$	N/D	N/D	N/D	N/D
	$KatG^{\Delta LL2}$	N/D	N/D	N/D	N/D

N/D: Not Detected

Michaelis-Menten equation (4.1). However, in some variants substrate-dependent inhibition was observed and the data were fit to equation 4.2.

$$\frac{v}{[E]_T} = \frac{k_{cat}[S]}{K_M + [S]} \qquad \textbf{(4.1)}$$

$$\frac{v}{[E]_T} = \frac{k_{cat}[S]}{K_M + [S] + [S]^2 / K_I} \qquad \textbf{(4.2)}$$

In case of peroxidase activity with respect to H_2O_2 concentration, a two to four- fold reduction in apparent k_{cat} was observed for group I variants with a much more dramatic decrease in apparent K_M (Figure 4.7, Panel A). This decrease in both apparent k_{cat} and apparent K_M gave rise to similar apparent k_{cat}/K_M values compared to wtKatG. Conversely, group II (Figure 4.8, Panel A) and III (Figure 4.9, Panel A) variants showed a two to four-fold higher apparent k_{cat} with much higher apparent K_M values. The net result with respect to k_{cat}/K_M was 10-fold lower apparent second-order rate constants for these variants.

The apparent k_{cat} values measured for group I variants for ABTS concentration were reduced by two to four-fold with modest decrease in apparent K_M except some cases where it was either equal to (Q293A, Q293V, and I290V/Q293V) or slightly higher (I290A and I290V) than that for wtKatG (Figure 4.7, Panel B). In case of the group II (Figure 4.8, Panel B) and III (Figure 4.9, Panel B) variants, there was slight increase in apparent k_{cat} and decrease in K_M leading to overall higher apparent second order rate constant (~10^6 $M^{-1}s^{-1}$), with the exception of KatG$^{\Delta P285/\Delta G294}$ and KatG$^{\Delta N280/\Delta S299}$ which showed ~40 % decrease in apparent k_{cat}/K_M.

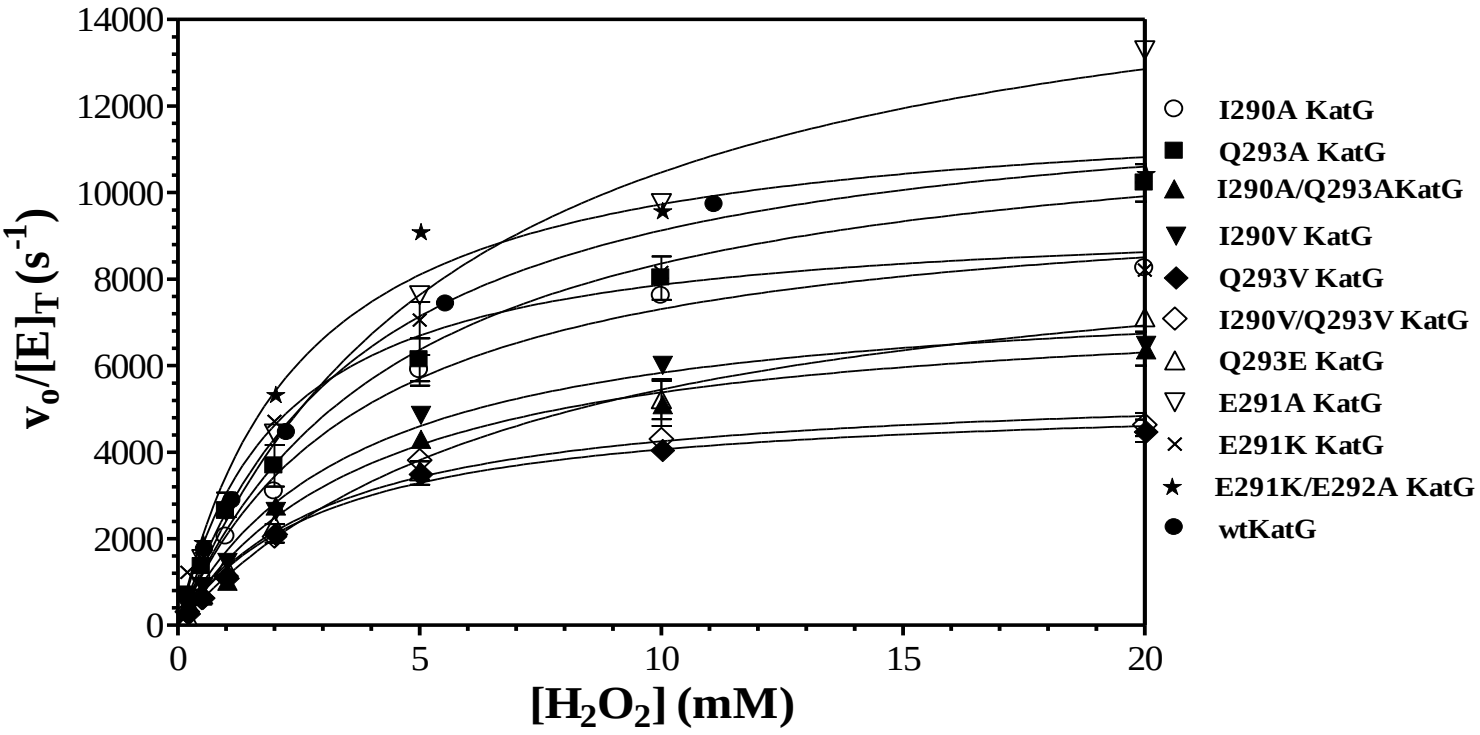

Figure 4.4: Effect of H_2O_2 concentration on the catalase activity of wtKatG and group I variants. Reactions were carried our using 10 nM enzyme and 0.2-20 mM H_2O_2 in 100 mM phosphate buffer, pH 7.0, at 23°C

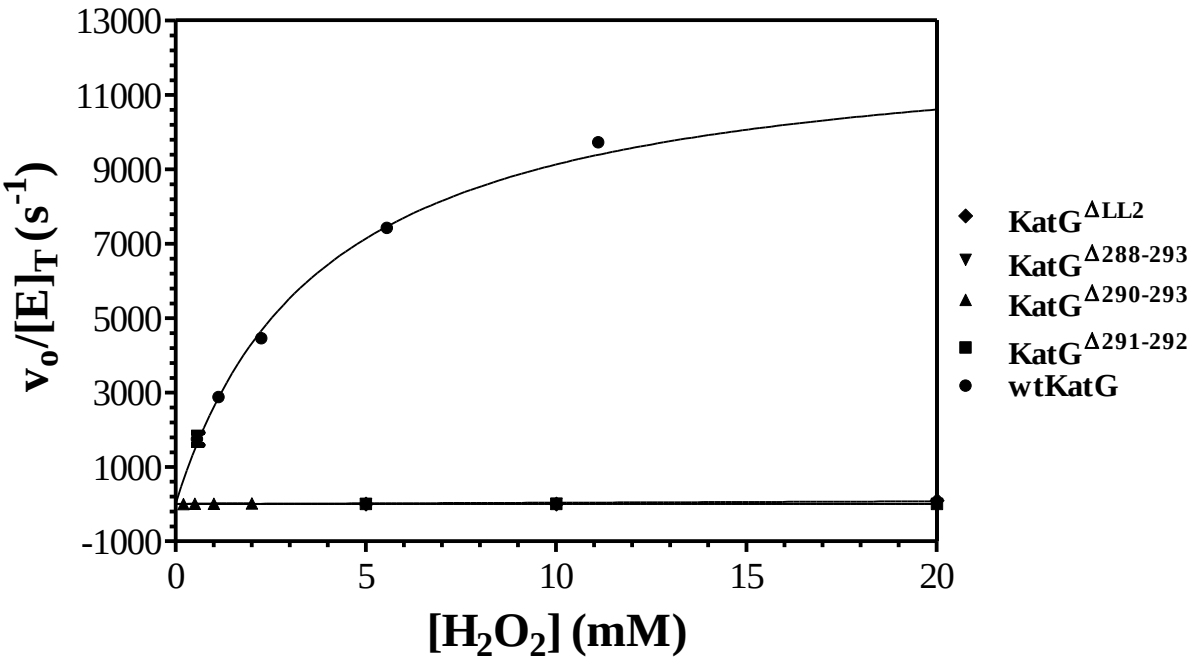

Figure 4.5: Effect of H_2O_2 concentration on the catalase activity of wtKatG, KatG$^{\Delta LL2}$ and group III variants. Reactions were carried our using 10 nM enzyme and 0.2-20 mM H_2O_2 in 100 mM phosphate buffer, pH 7.0, at 23°C.

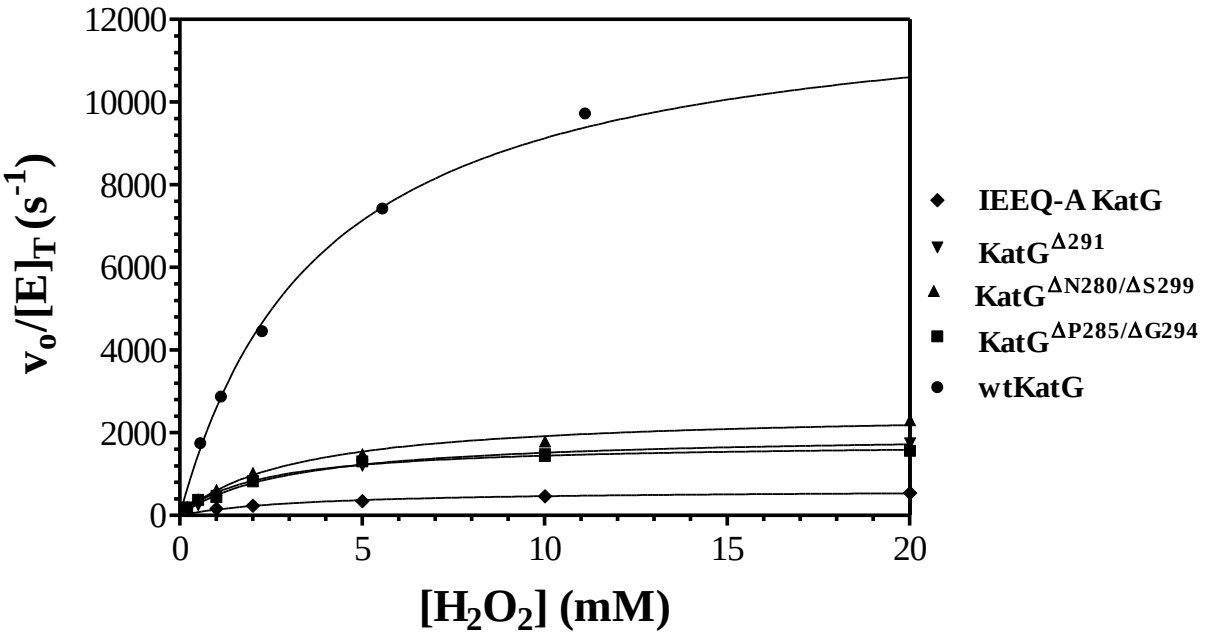

Figure 4.6: Effect of H_2O_2 concentration on the catalase activity of wtKatG and group II variants. Reactions were carried our using 10 nM enzyme and 0.2-20 mM H_2O_2 in 100 mM phosphate buffer, pH 7.0, at 23°C.

Table 4.4: Apparent peroxide-dependent peroxidase kinetic parameters

	KatG	Peroxide-dependent peroxidase cycle parameters			
		k_{cat}(s^{-1})	K_M (mM H_2O_2)	k_{cat}/K_M (10^5 $M^{-1}s^{-1}$)	K_I(mM H_2O_2)
Group I	WT KatG	65 ± 6	0.18 ± 0.04	3.6	N/D
	I290A KatG	26.3 ± 0.6	0.08 ± 0.01	3.3	N/D
	Q293A KatG	27.8 ± 0.6	0.07 ± 0.01	3.9	N/D
	I290A/Q293A KatG	13.5 ± 0.4	0.07 ± 0.01	1.9	N/D
	I290V KatG	14.66 ± 0.3	0.03 ± 0.01	4.9	N/D
	Q293V KatG	22.1 ± 1.3	0.30 ± 0.06	0.73	N/D
	I290V/Q293V KatG	22 ± 1	0.14 ± 0.03	1.6	N/D
	Q293E KatG	23.8 ± 0.5	0.089 ± 0.008	2.7	N/D
	E291A KatG	40.4 ± 0.9	0.104 ± 0.007	3.9	12 ± 1
	E291K KatG	34.1 ± 0.8	0.06 ± 0.01	5.7	N/D
	E291A/E292K KatG	35.3 ± 0.5	0.057 ± 0.004	5.9	N/D
Group II	IEEQ-A KatG	97 ± 6	73 ± 9	0.013	N/D
	$KatG^{\Delta 291}$	184 ± 8	40 ± 3	0.046	N/D
	$KatG^{\Delta P285/\Delta G294}$	247 ± 44	139 ± 32	0.018	N/D
	$KatG^{\Delta N280/\Delta S299}$	218 ± 9	56 ± 8	0.039	N/D
Group III	$KatG^{\Delta 288\text{-}293}$	46 ± 1.8	7.7 ± 0.7	0.059	N/D
	$KatG^{\Delta 290\text{-}293}$	422 ± 107	215 ± 65	0.019	N/D
	$KatG^{\Delta 291\text{-}292}$	261 ± 19	98 ± 12	0.027	N/D
	$KatG^{\Delta LL2}$	27.8 ± 0.2	2.2± 0.2	0.13	N/D

N/D: Not Detected

Table 4.5: Apparent ABTS-dependent peroxidase kinetic parameters

	KatG	ABTS-dependent peroxidase cycle parameters			
		k_{cat}(s^{-1})	K_M (mM ABTS)	k_{cat}/K_M (10^5 $M^{-1}s^{-1}$)	K_I (mM ABTS)
Group I	WT KatG	55.2 ± 1.3	0.087 ± 0.008	6.3	N/D
	I290A KatG	32.5 ± 0.9	0.16 ± 0.02	2.0	N/D
	Q293A KatG	29.7 ± 0.5	0.08 ± 0.01	3.7	N/D
	I290A/Q293A KatG	13.3 ± 0.4	0.037 ± 0.06	3.6	N/D
	I290V KatG	28.4 ± 0.7	0.13 ± 0.01	2.2	N/D
	Q293V KatG	17.4 ±0.5	0.09 ± 0.01	1.9	N/D
	I290V/Q293V KatG	22.7 ± 0.3	0.09 ± 0.01	2.7	N/D
	Q293E KatG	20.2 ± 0.6	0.052 ± 0.008	3.9	N/D
	E291A KatG	39.7 ± 0.8	0.07 ± 0.01	5.7	N/D
	E291K KatG	29.6 ± 0.3	0.023 ± 0.02	13	N/D
	E291K/E292A KatG	38.2 ± 0.8	0.030±0.003	13	N/D
Group II	IEEQ-A KatG	70 ± 3	0.029 ± 0.003	24	0.9 ± 0.2
	$KatG^{\Delta 291}$	68 ± 1	0.062 ± 0.05	11	N/D
	$KatG^{\Delta P285/\Delta G294}$	29 ± 1	0.069 ± 0.007	4.2	4.3 ± 0.8
	$KatG^{\Delta N280/\Delta S299}$	54.3 ± 0.9	0.074 ± 0.005	7.3	N/D
Group III	$KatG^{\Delta 288\text{-}293}$	65 ± 1	0.041 ± 0.004	16	N/D
	$KatG^{\Delta 290\text{-}293}$	37.7 ± 0.9	0.022 ± 0.002	17	N/D
	$KatG^{\Delta 291\text{-}292}$	54 ± 1	0.019 ± 0.002	28	N/D
	$KatG^{\Delta LL2}$	25.7 ± 0.9	0.012 ± 0.001	22	N/D

N/D: Not Detected

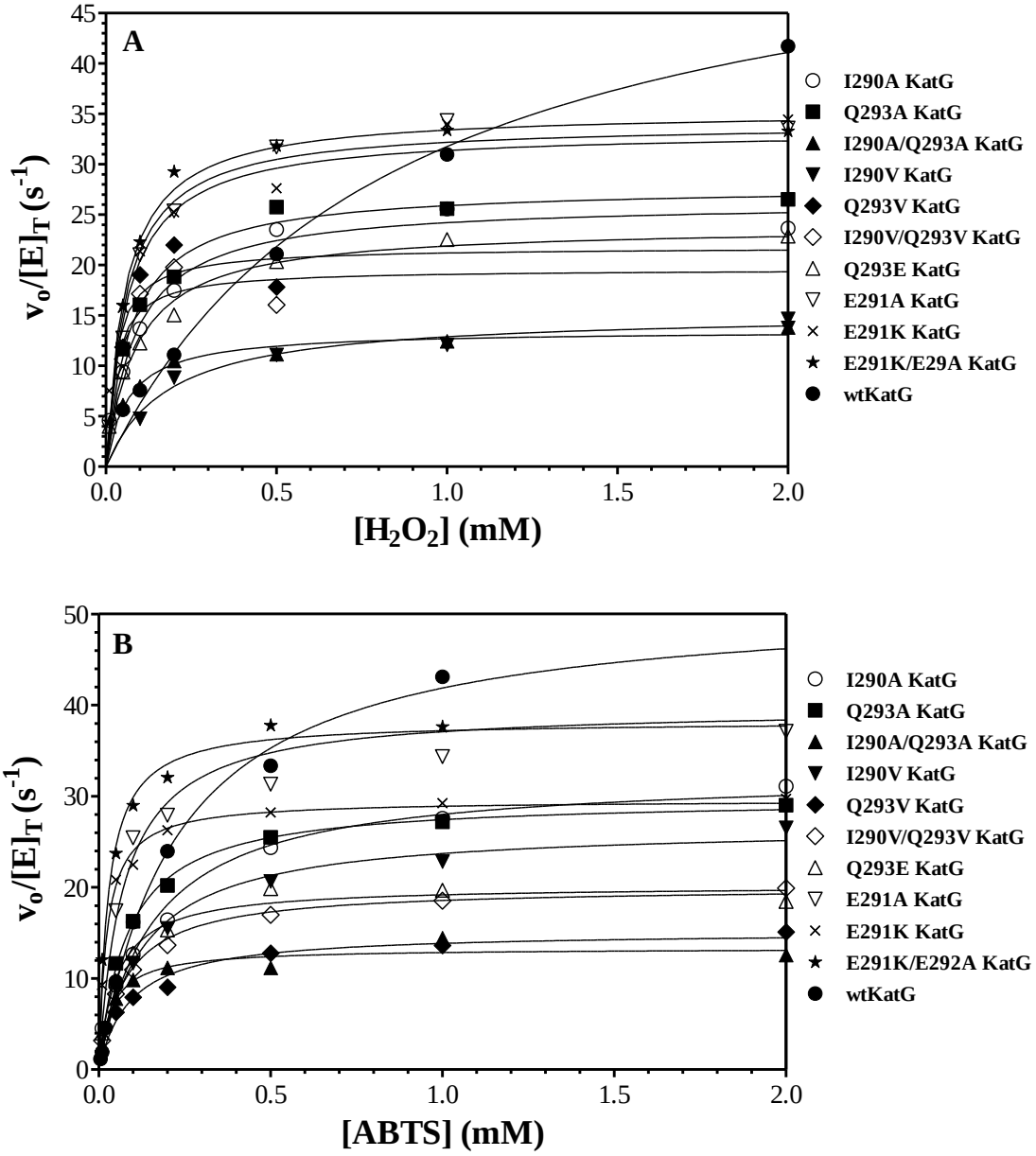

Figure 4.7: Comparison of peroxidase activities of wtKatG and group I variants. The effects of H_2O_2 (A) and ABTS (B) concentrations on the rate of ABTS oxidation by wtKatG and group III variants were evaluated. (A) All reactions contained 0.5 mM ABTS. (B) All reactions contained 0.5 mM H_2O_2. All reactions were carried out at 23°C in 50 mM acetate buffer, pH 5.0, using 10 nM of enzyme.

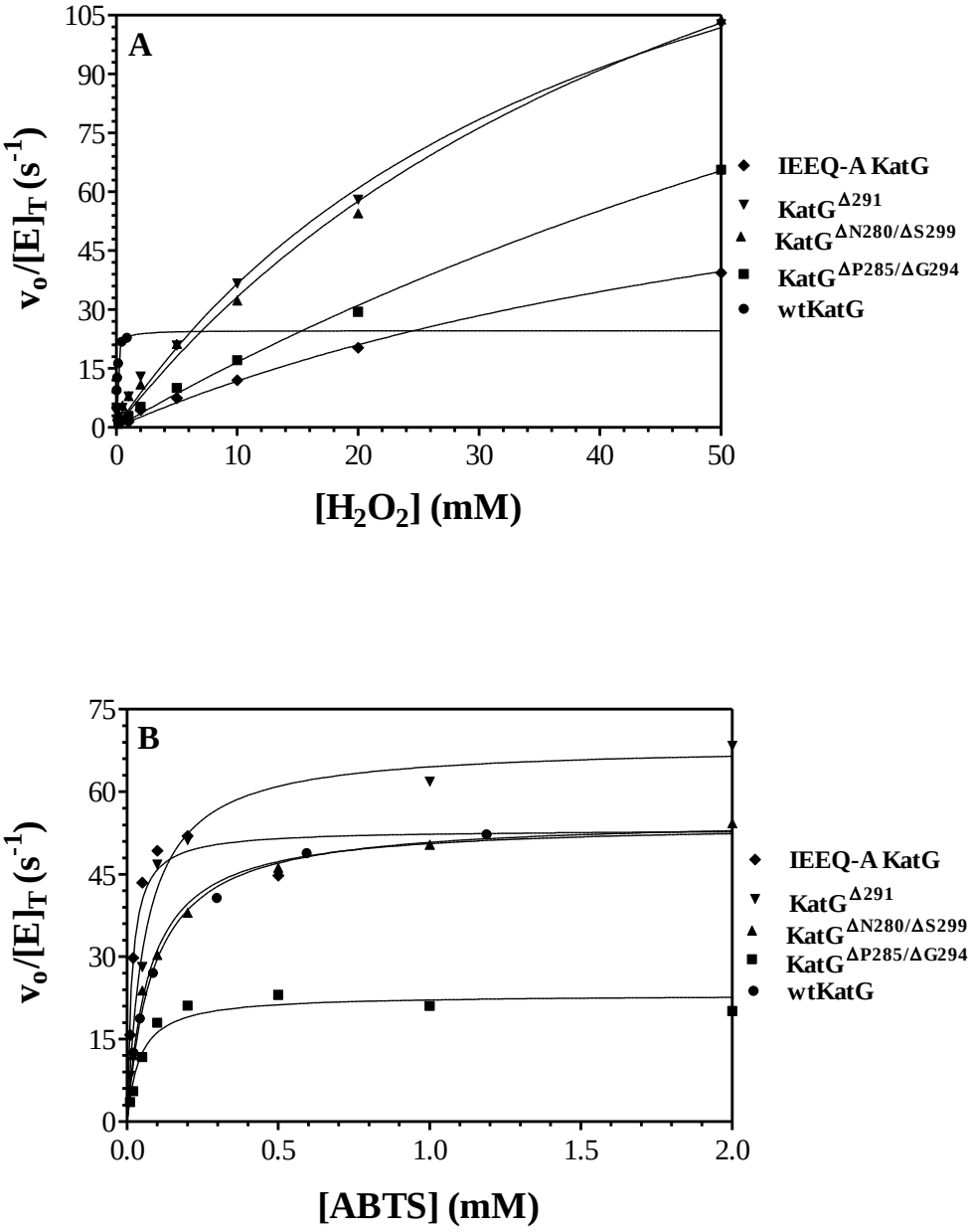

Figure 4.8: Comparison of peroxidase activities of wtKatG and group II variants. The effects of H_2O_2 (A) and ABTS (B) concentrations on the rate of ABTS oxidation by wtKatG and group III variants were evaluated. (A) All reactions contained 0.5 mM ABTS. (B) 0.5 mM H_2O_2 for wtKatG and 20 mM H_2O_2 for the variants. All reactions were carried out at 23°C in 50 mM acetate buffer, pH 5.0, using 10 nM of enzyme.

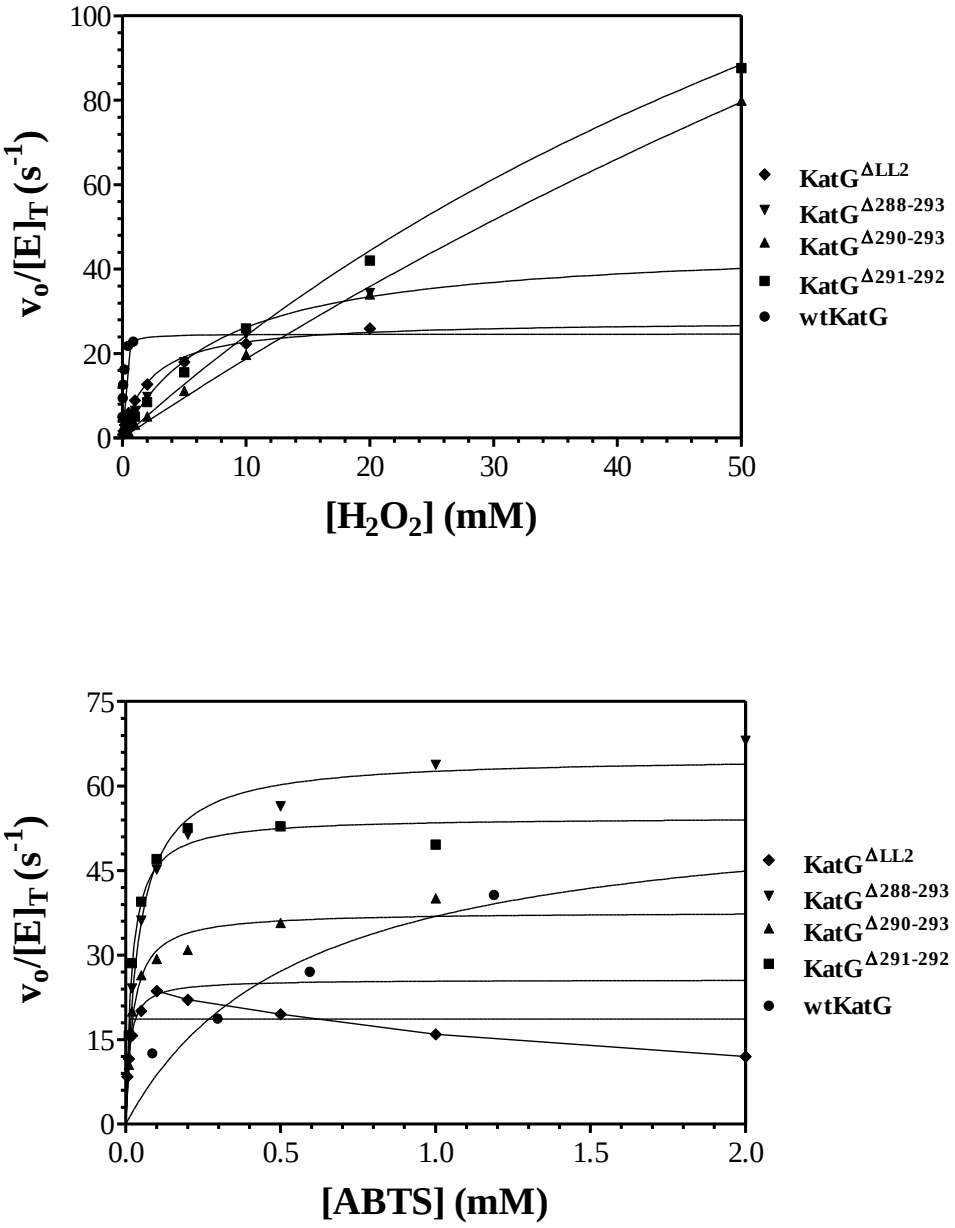

Figure 4.9: Comparison of peroxidase activities of wtKatG and group III variants. The effects of H_2O_2 (A) and ABTS (B) concentrations on the rate of ABTS oxidation by wtKatG and group III variants were evaluated. (A) All reactions contain 0.5 mM ABTS. (B) 0.5 mM H_2O_2 for wtKatG and 20 mM H_2O_2 for the variants. All reactions were carried out at 23°C in 50 mM acetate buffer, pH 5.0, using 10 nM of enzyme.

4.3.3 Spectroscopic evaluation of KatG LL2 variants

The typical UV-Vis spectrum for ferric KatG shows a Soret band absorption maximum at 408 nm with charge transfer transitions near 500 nm (shoulder) and 642 nm. These features generally refer to a mixture of coordination states dominated by hexacoordinate high-spin heme with contributions from the pentacoordinate high-spin state (*87, 88, 101*). Generally, the absorption spectra for the ferric forms of the group I substitution variants were highly similar to wtKatG (Figure 4.10). For variants in group II (Figure 4.11, Panels A and B) and group III (Figure 4.11, Panels C and D), the tendency was for a more substantial shoulder (~380 nm) to the Soret band. These variants tended to show a slight red-shift in the charge transfer and CT1 to 645 nm. These spectral shifts are consistent with a greater contribution from pentacoordinate heme states (*102, 168*). However, similar spectral shifts would be observed for free heme, thus, on the basis of UV-Vis absorption spectra alone assignment of coordination environment for these variants could not be made.

Magnetic Circular Dichroism is a useful approach for hemoproteins and because the transitions measured are π- π^* transitions from the porphyrin, it is an approach that can be applied at room temperature. Moreover, there is less ambiguity in the interpretation of some aspects of the spectra (particularly when applied to the ferrous state) aiding in a more definitive assignment of heme coordination. MCD spectra of the ferric state of the variants were consistent with domination by high-spin species (Figures 4.12 and 4.13) (*168, 169*). Each variant was reduced with dithionite and MCD spectra for the ferrous state was measured. For the variants in group I, the spectra for the ferrous state was virtually invariant. The maximum corresponding to the Soret

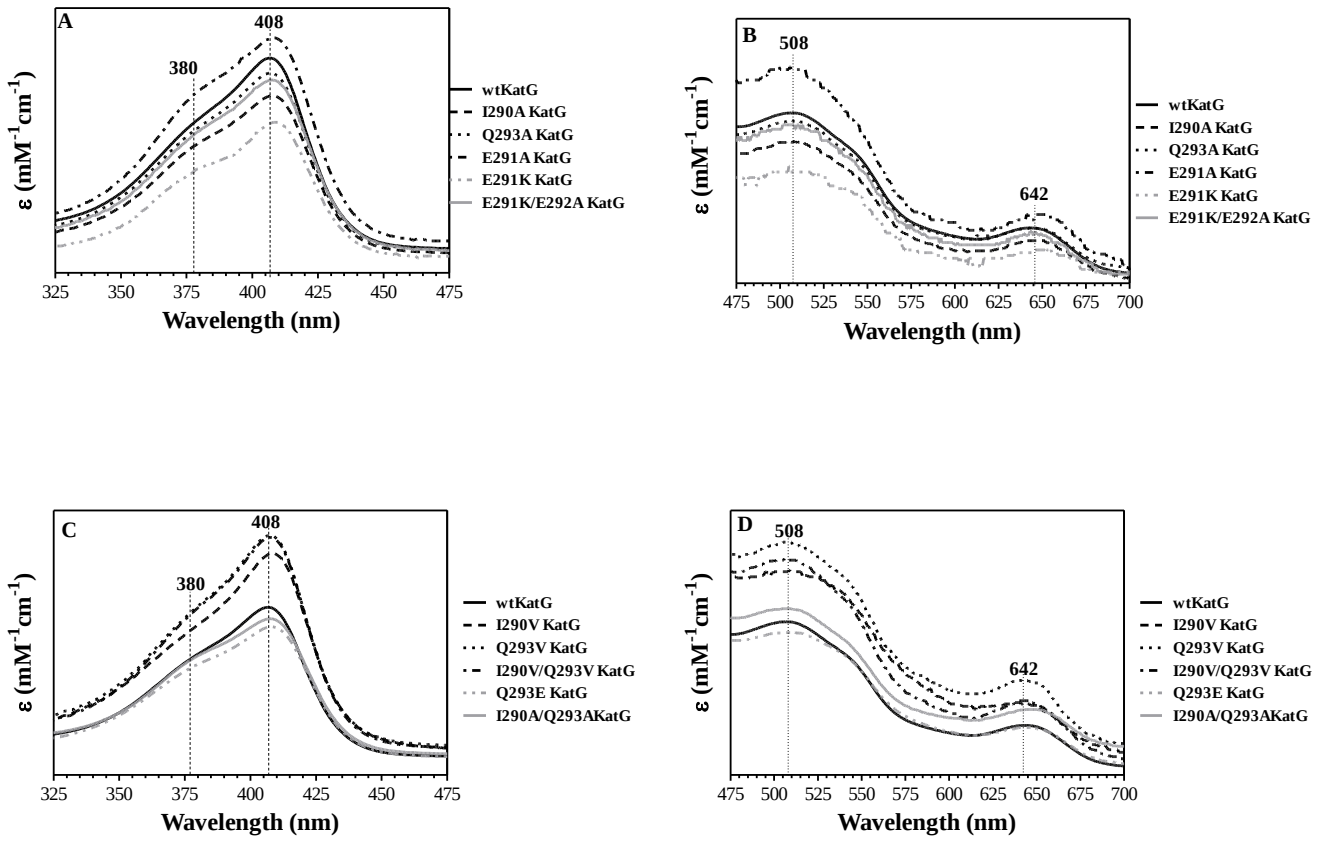

Figure 4.10: UV-Visible spectral comparison of ferric wtKatG and group I variants. Spectra were obtained for ferric wtKatG and the variants. Panels (A) and (C) show these spectra from 325 to 475 nm, and Panels (B) and (D) show them from 475 to 700 nm. All the spectra were recorded at 23 °C in 100 mM phosphate buffer, pH 7.0.

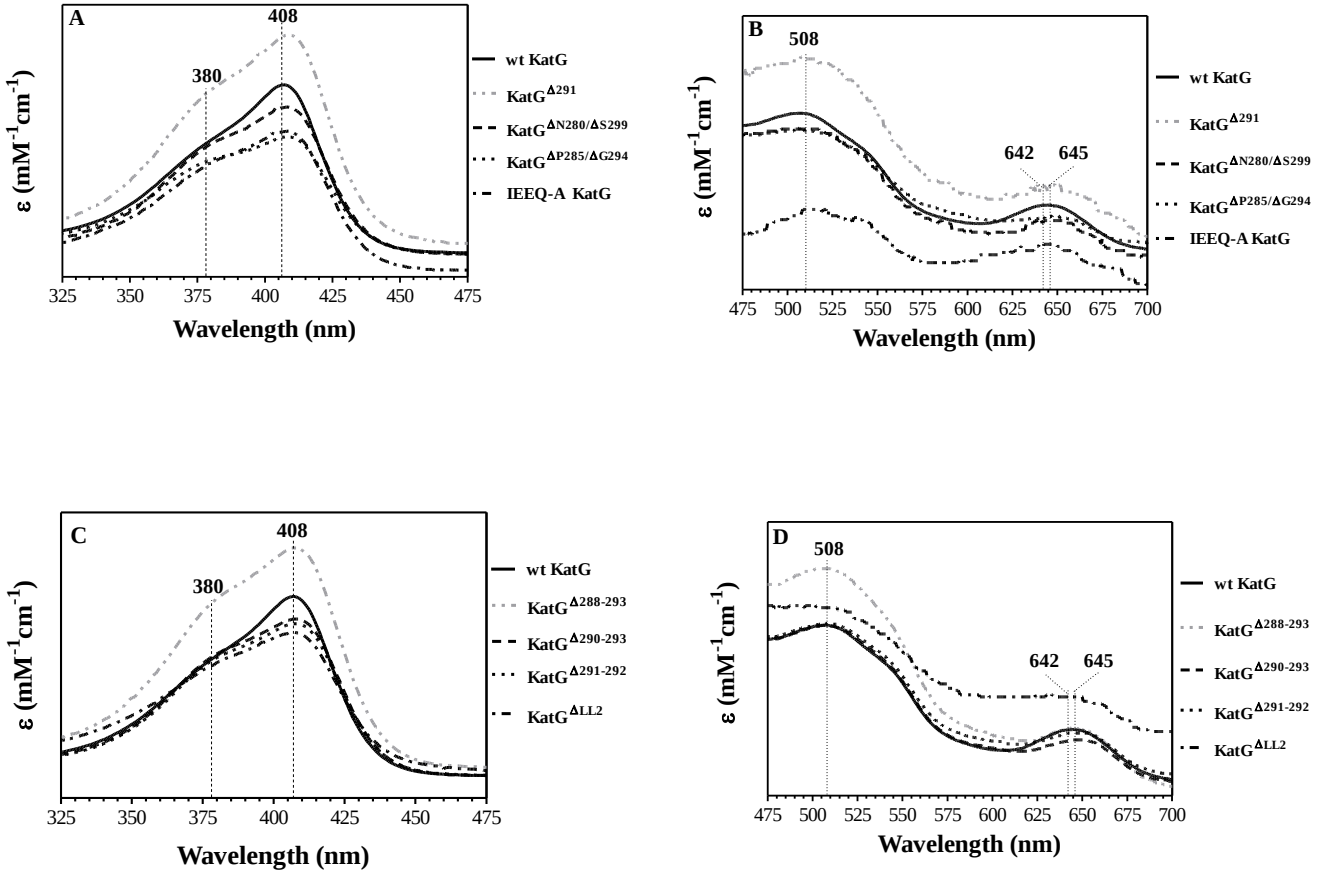

Figure 4.11: UV-Visible spectral comparison of ferric wtKatG with group II (A and B), and group III (C and D) variants. Spectra were obtained for ferric wtKatG and the variants. Panels (A) and (C) show these spectra from 325 to 475 nm, and Panels (B) and (D) show them from 475 to 700 nm. All the spectra were recorded at 25 ˚C in 100 mM phosphate buffer, pH 7.0.

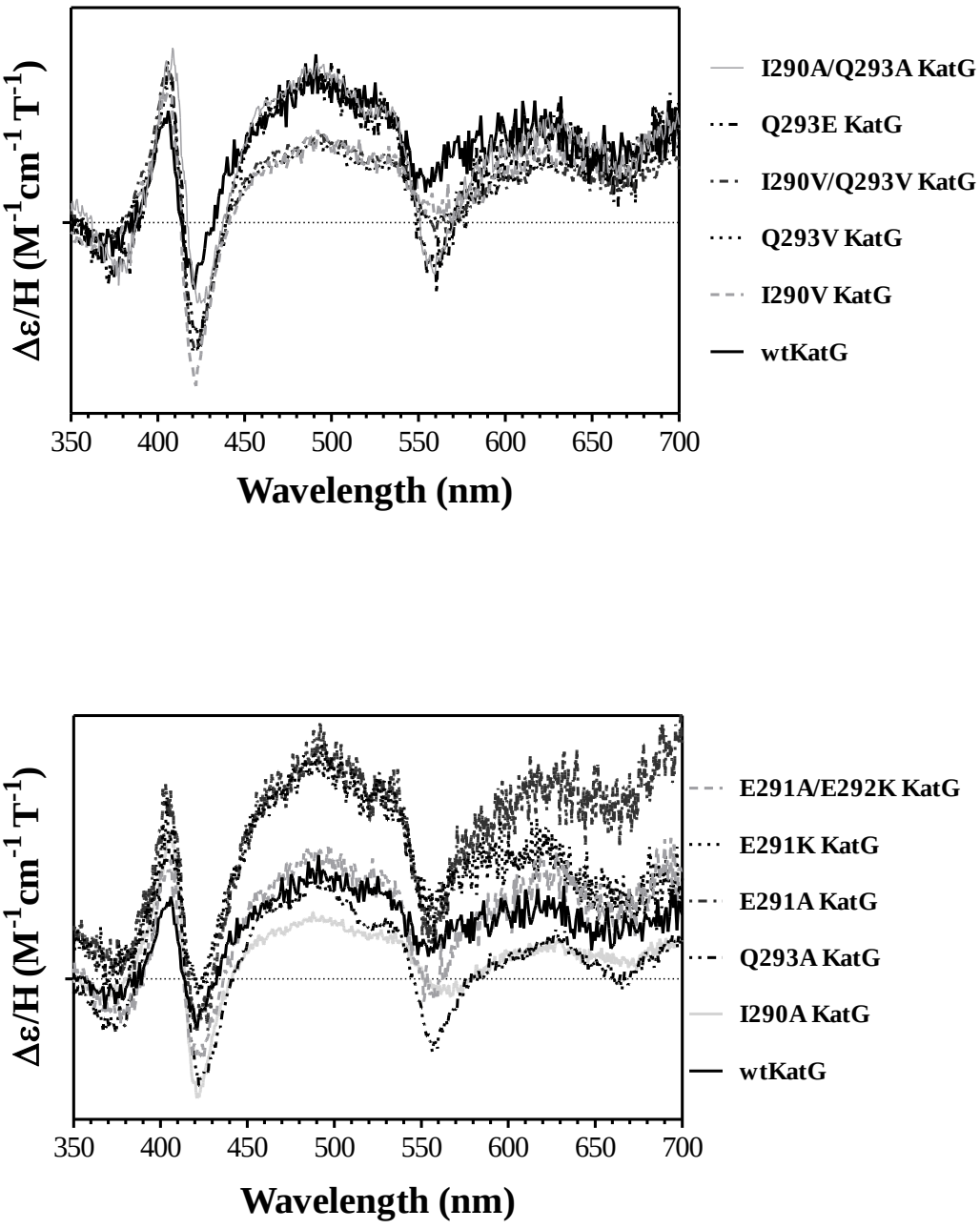

Figure 4.12: Overlay of ferric MCD of wtKatG and group I variants. Spectra were recorded at room temperature using 15uM of each enzyme, in 50 mM phosphate buffer, pH 7.0.

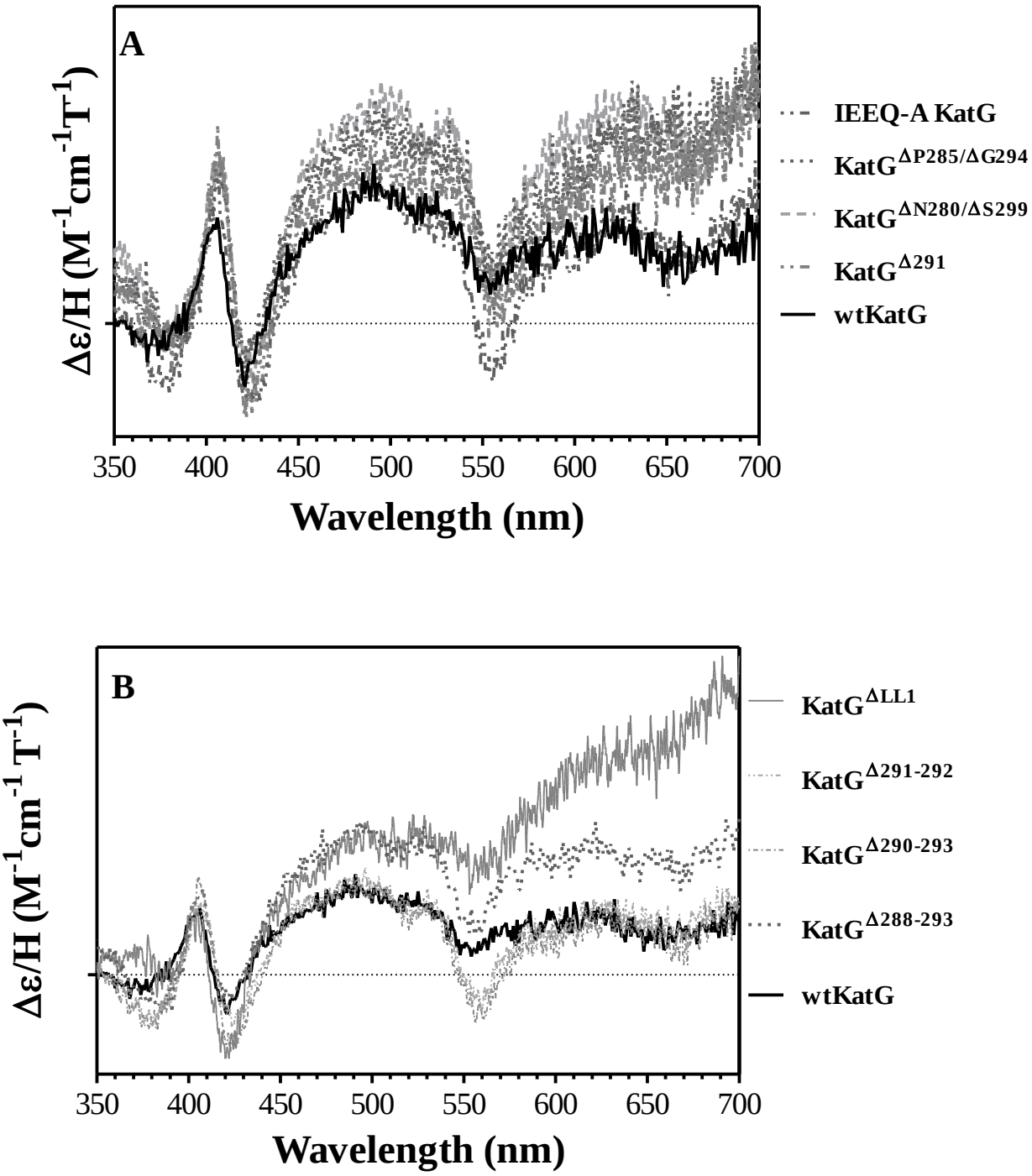

Figure 4.13: Overlay of ferric MCD wtKatG, group II (A) and group III (B) variants. Spectra were recorded at 25 ˚C using 15uM of each enzyme, in 50 mM phosphate buffer, pH 7.0.

band was singular and consistently observed near 440 nm. Likewise, transitions corresponding to the β and α bands were consistently observed near at 557 nm and 585 nm (Figure 4.14). In contrast, group II (Figure 4.15) and III (Figure 4.16) were distinct from group I in that the feature around 440 nm was split, with a higher intensity feature at ~ 430 nm and a lower intensity feature at ~ 445 nm.

Figure 4.16 represents an overlay of the typical ferrous MCD spectrum of group III variants which clearly shows the splitting of Soret band. Interestingly, KatG$^{\Delta 290\text{-}293}$ did not show the same split feature, but the wavelength maximum was not consistent with wtKatG in that it had blue shifted to 432 nm and at 445 nm there was a notable negative cotton effect. Although every group II and III variants were distinct form wtKatG, they all (with the exception of KatG$^{\Delta 290\text{-}293}$) were highly similar to KatG$^{\Delta LL2}$.

The coordination states of the three groups were further evaluated by electron paramagnetic resonance (EPR) spectroscopy. The EPR spectra of all the variants, except I290A KatG, showed mixed populations of high spin ferric heme species with contribution from an axial component ($g_{\perp}$ = 6.00; $g_{\parallel}$ = 1.99) as well as rhombic component (g = 6.64, 4.95, 1.95). However, there was a marked difference in *distribution* of high spin species among the variants. Group I variants showed greater contribution from the axial component and comparatively less from rhombic component consistent with wtKatG, indicating domination by the hexacoordinate high-spin ferric state (Figure 4.17) (*101*). In contrast, spectra for the group II (Figure 4.18) and III (Figure 4.19) variants were dominated by the rhombic component with a comparatively diminished axial component. These spectra bear a striking resemblance to KatG$^{\Delta LL2}$.

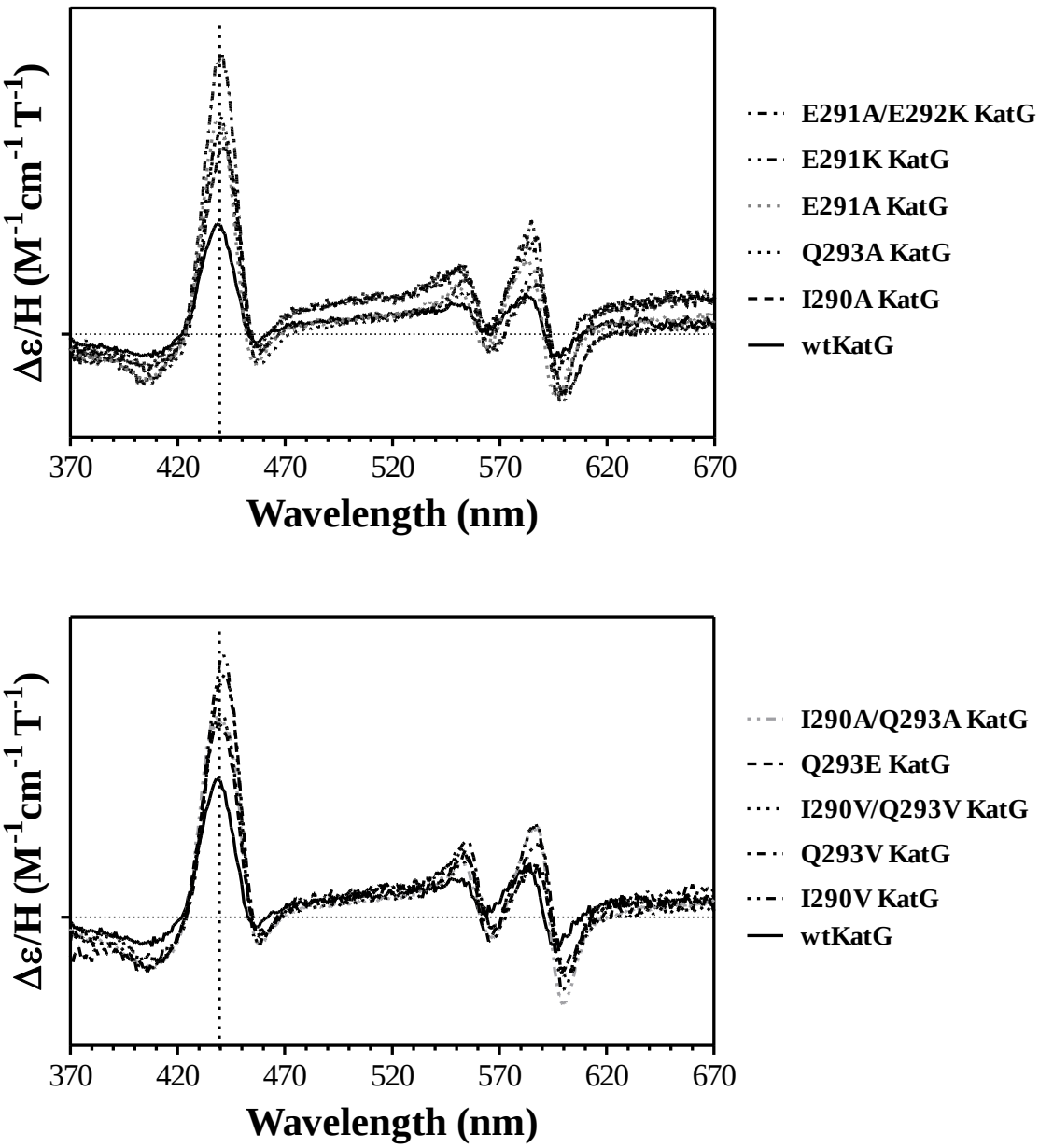

Figure 4.14: Overlay of ferrous MCD spectra wtKatG and group I variants. Spectra were recorded at 25 ˚C using 15 μM of each enzyme, in 50 mM phosphate buffer, pH 7.0.

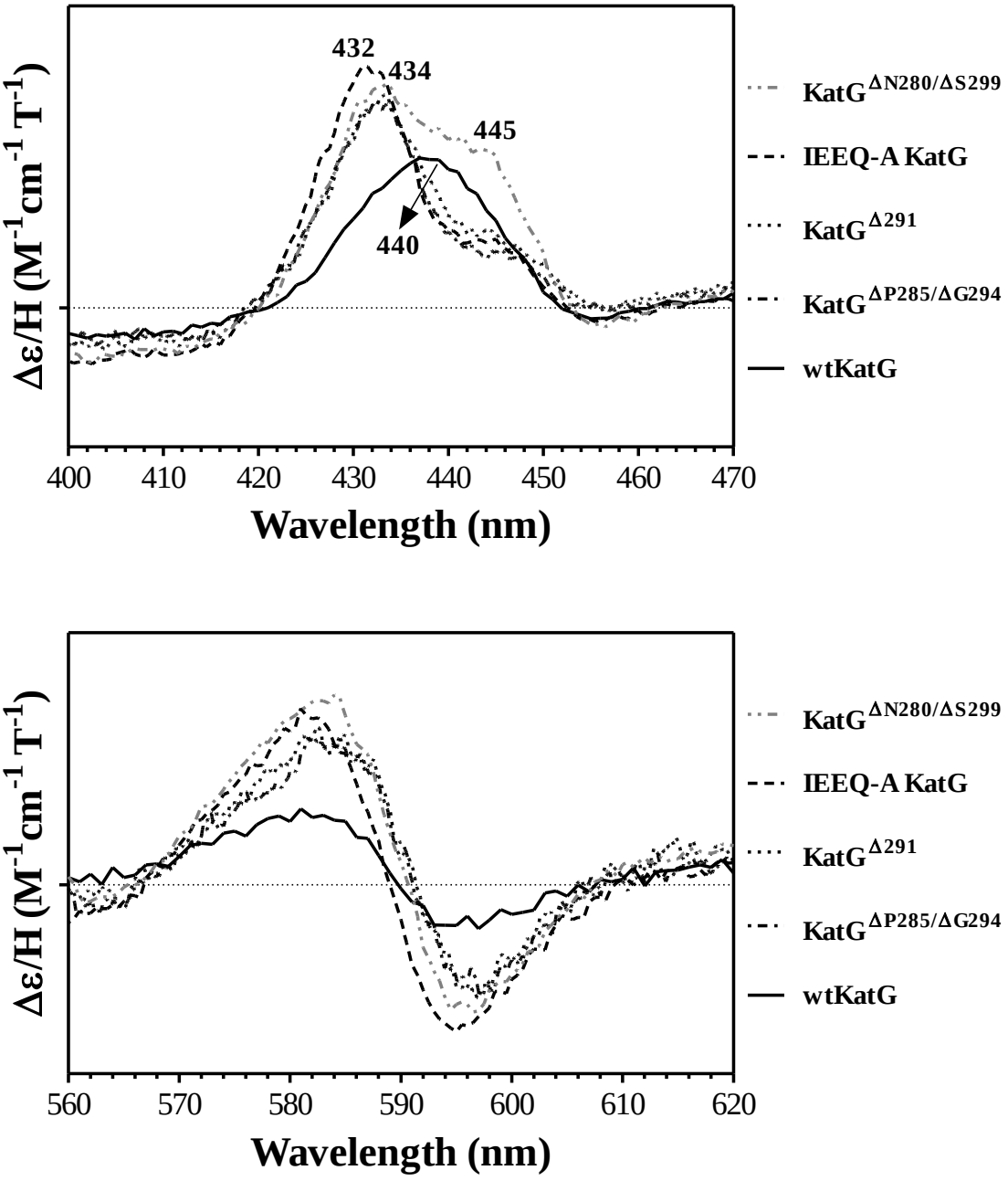

Figure 4.15: Overlay of ferrous MCD comparison of wtKatG, and group II variants. Spectra were recorded at 25 ˚C using 15 μM of each enzyme, in 50 mM phosphate buffer, pH 7.0.

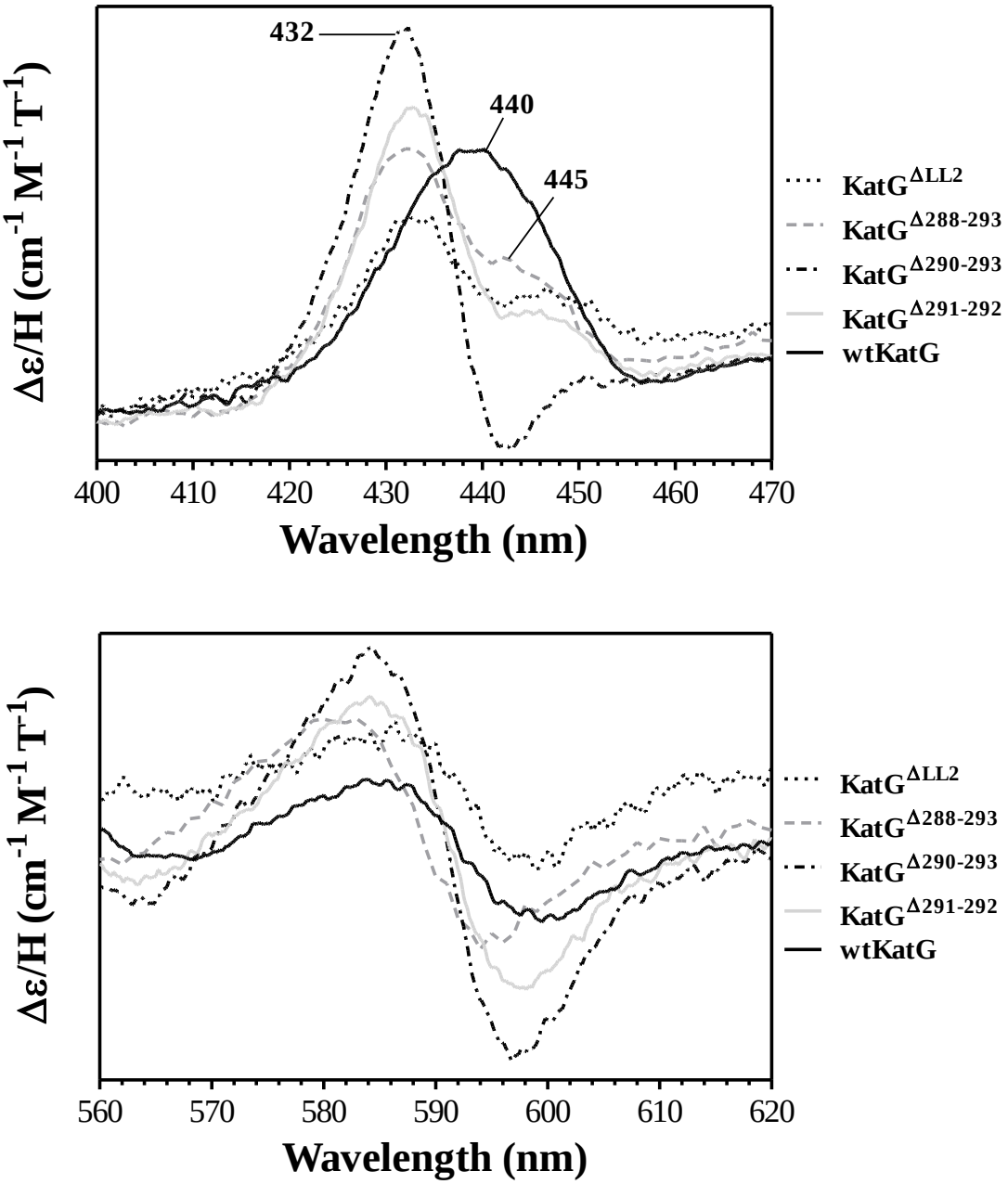

Figure 4.16: Overlay of ferrous MCD spectra of wtKatG, KatG$^{\Delta LL2}$ and group III variants. Spectra were recorded at room temperature using 15 μM of each enzyme, in 50 mM phosphate buffer, pH 7.0.

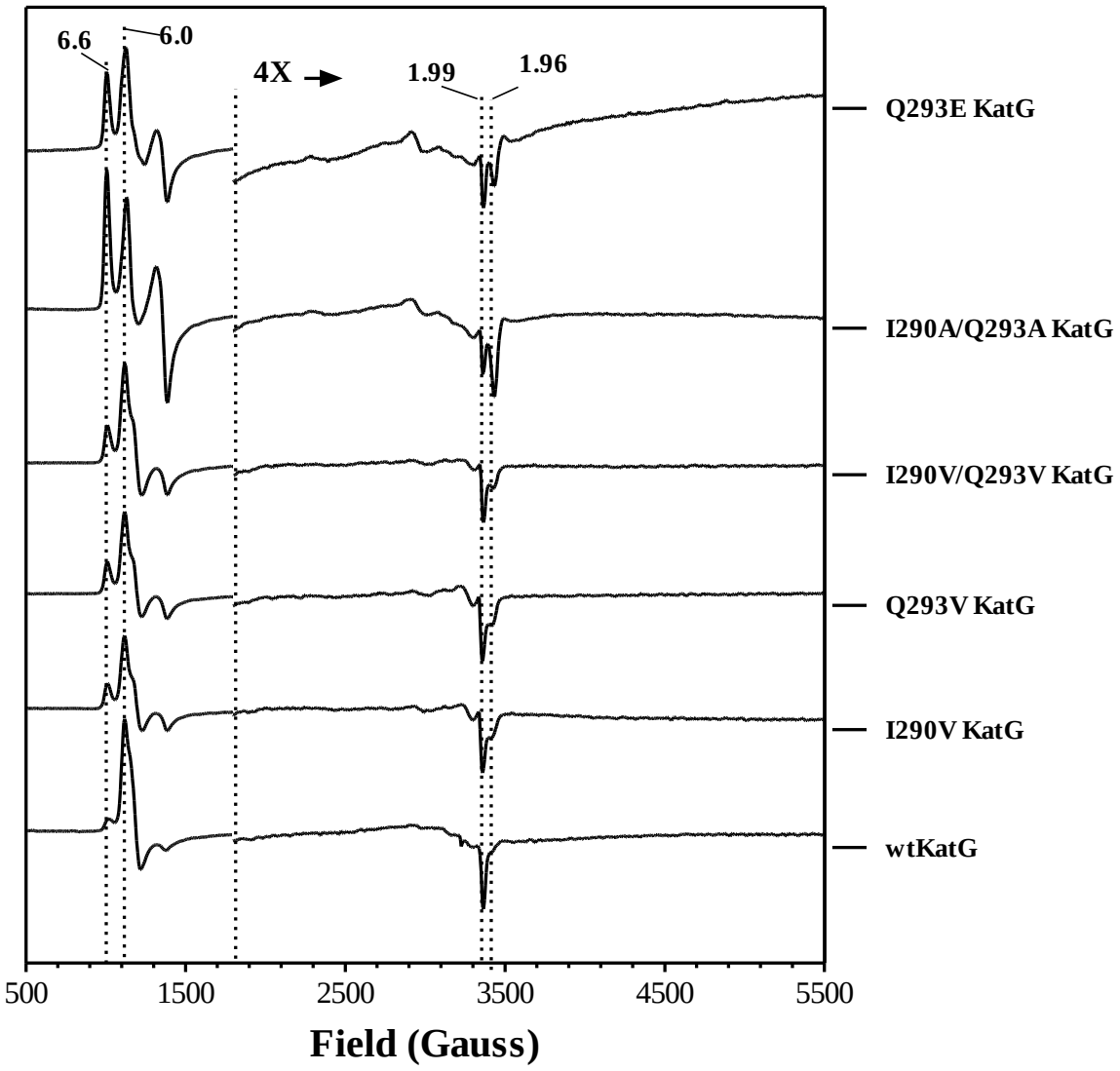

Figure 4.17: Comparison of EPR spectra of wtKatG and group I variants. Relative intensity magnified by 4 at field strength greater than 1700 Gauss. EPR settings were identical to those described in materials and methods.

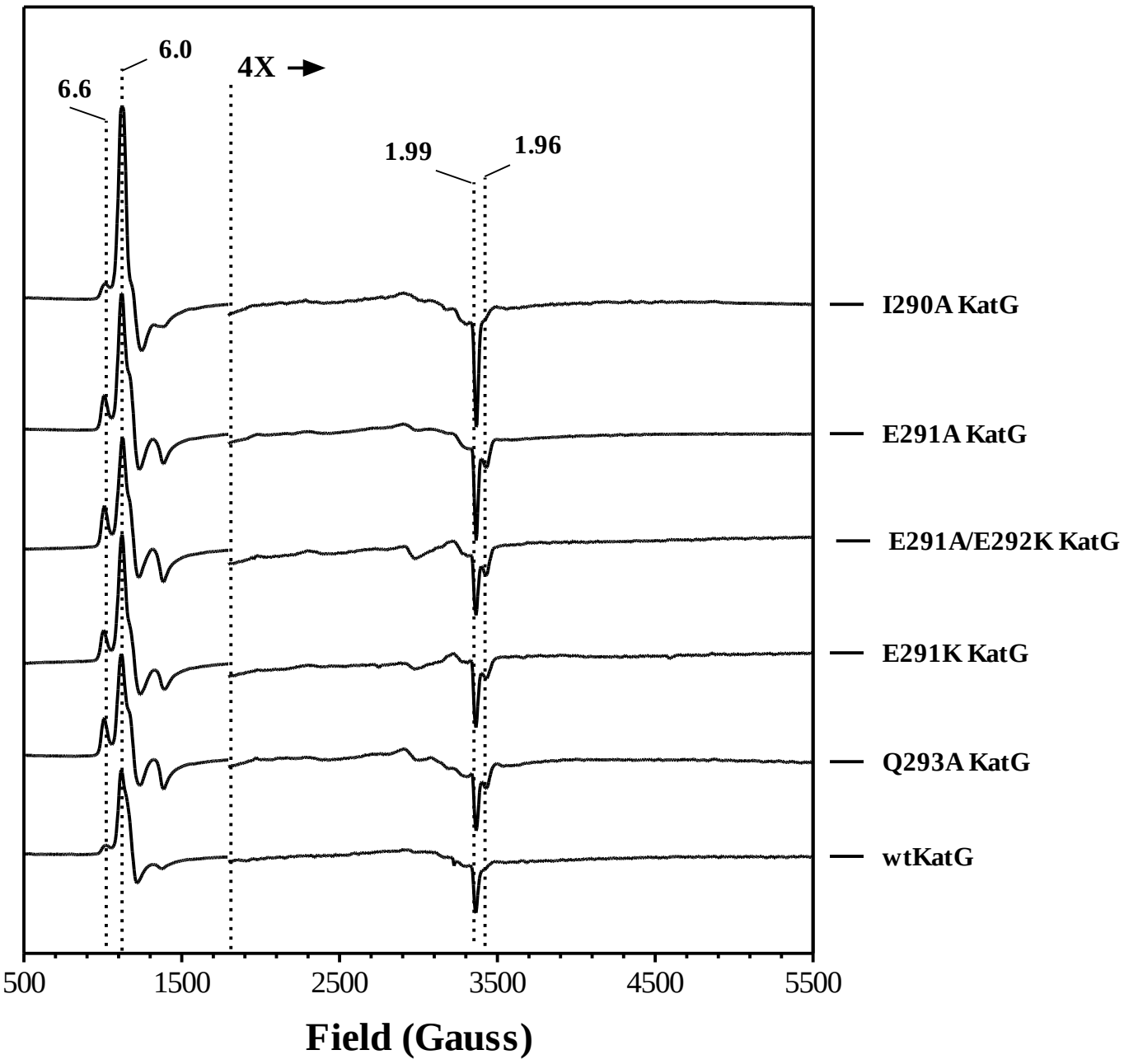

Figure 4.17: Continued

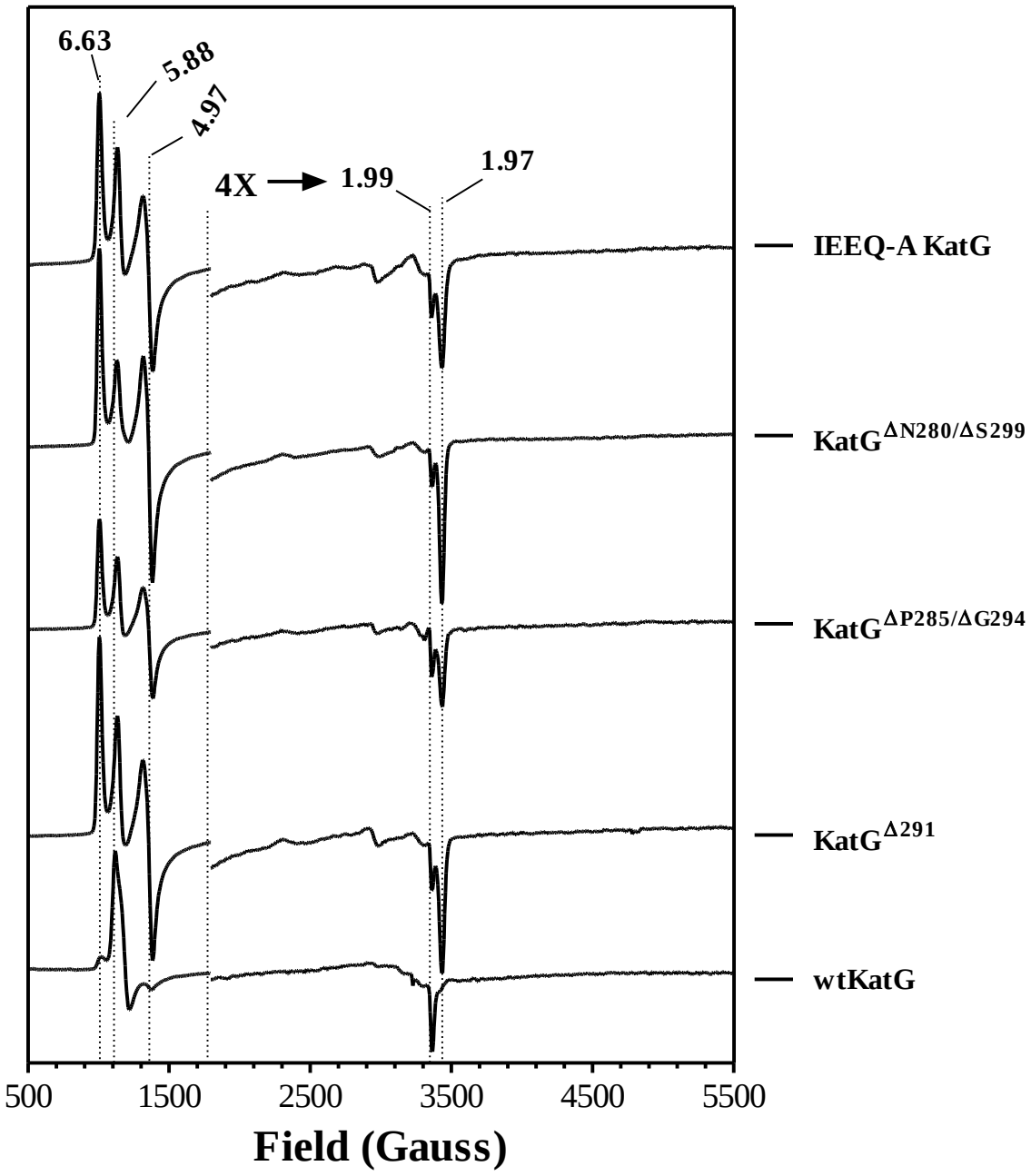

Figure 4.18: Comparison of EPR spectra of wtKatG and group II variants. Relative intensity magnified by 4 at field strength greater than 1700 Gauss. EPR settings were identical to those described in materials and methods.

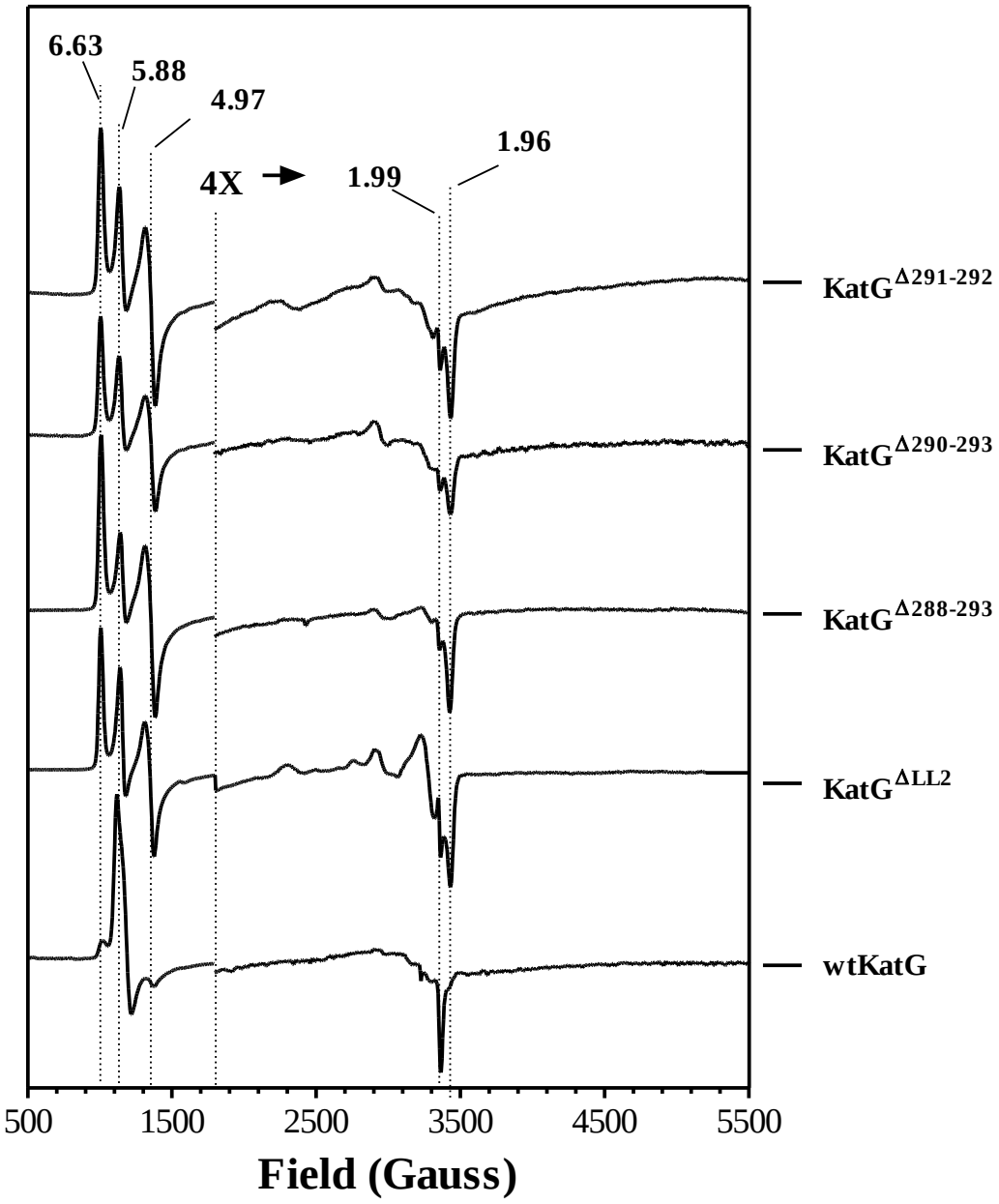

Figure 4.19: Comparison of EPR spectra of wtKatG and group III variants. Relative intensity magnified by 4 at field strength greater than 1700 Gauss. EPR settings were identical to those described in materials and methods.

Together, the UV-Vis, MCD, and EPR spectra indicated that substitution variants to LL2 has little effect on heme coordination, but deletions to the structure substantially shifted coordination from hexacoordinate to pentacoordinate high-spin heme.

The next step was to quantify the relative proportion of each coordinating species, and in order to accomplish this, EPR spectral simulations and integrations was carried out. The most accurate simulations were obtained by accounting for three high spin signals and one low-spin signal. The high spin signals included: two axial components (AHS1 with g-values of 5.85 and 1.99, and AHS2 with g-values of 5.69 and 1.99) and one rhombic component (RHS) with g-values of 6.65, 4.95, and 1.95. The low-spin component was simulated rhombic (RLS) with g-values of 2.93, 2.27, and 1.53. Table 4.6 represents the ratios of various EPR signals expressed as a percentage contribution of each species in wtKatG and each variant. EPR spectra of all the variants irrespective of their groups were dominated by high-spin species. The group I variants all showed higher percentage contribution from AHS signal over RHS, a feature common with wtKatG. I290A/Q293A KatG and the quadruple alanine (IEEQ-A KatG) variants were the exceptions with slightly higher RHS state over AHS state. In contrast, all of the deletion variants were dominated by the RHS state. In case of KatG$^{\Delta 290\text{-}293}$, the RHS:AHS ratio was almost 50:50 which might have some relation to no Soret splitting in MCD ferrous spectrum of this variant. But the overall higher rhombic contribution in the deletion variants corroborated well with the prominent shoulder at 380 nm in the UV-Vis ferric spectra of these variants.

Table 4.6: Ratios, expressed as percentages, of various EPR signal observed in wtKatG and variants

KatG		HS - LS	RHS - AHS	AHS1 - AHS2	AHS1 – AHS2 – RHS - RLS
	Wt KatG	99.98 – 0.02	14.9 – 85.9	49.9 – 35.1	49.9 – 35.1-14.9 – 0.02
	I290V KatG	99.93 – 0.07	39.7 – 60.2	23.4 – 36.8	23.4 – 36.8 - 39.7 – 0.07
	Q293V KatG	99.98 – 0.02	40.3 – 59.6	22.5 – 37.0	22.5 – 37.0 - 40.3 -0.02
	I290V/Q293V KatG	97.88 – 0.07	39.4 – 58.5	22.6 – 35.9	22.6 – 35.9 – 39.4 – 0.07
	I290A KatG	100 – 0	11 – 89	62.3 – 26.5	62.3 – 26.5 – 11 – 0
Group I	Q293A KatG	99.7 – 0.3	35.4 – 64.3	33.8 – 30.5	33.8 – 30.5 – 35.4- 0.3
	I290A/Q293A KatG	99.9 – 0.1	61.3 – 38.6	19.6 – 19.0	19.6 – 19.0 – 61.3 – 0.1
	Q293E KatG	99.9 – 0.1	35.1 – 64.8	36.9 – 27.8	36.9 – 27.8 – 35.1- 0.1
	E291A KatG	99.92 – 0.07	39.1 – 60.9	24.6 – 36.3	24.6 – 36.3 – 39.1 – 0.07
	E291K KatG	99.8 – 0.2	26.4 – 73.4	47.1 – 26.3	47.1 – 26.3 – 26.4 – 0.2
	E291KE292A KatG	99.9 – 0.1	37.7 – 62.1	34.4 – 27.7	34.4 – 27.7 – 37.7 – 0.1
	IEEQ-A KatG	99.7 – 0.3	58.2 – 41.5	21.0 – 20.4	21.0 – 20.4 – 58.2 – 0.3
Group II	$KatG^{\Delta 291}$	99.7 – 0.3	54.4 – 45.3	23.3 – 21.9	23.3 – 21.9 – 54.4 – 0.3
	$KatG^{\Delta P285/\Delta G294}$	99.8 – 0.2	58.5 – 41.2	20.9 – 20.2	20.9 – 20.2-58.5 – 0.2
	$KatG^{\Delta N280/\Delta S299}$	99.8 – 0.2	68.4 – 31.3	16.2 – 15.2	16.2 - 15.2 – 68.4 – 0.2
	$KatG^{\Delta LL2}$	99.9 – 0.1	77.1 – 22.9	11.6 – 11.2	11.6 – 11.2 – 77.1 – 0.1
	$KatG^{\Delta 288-293}$	99.7 – 0.3	73.5 – 26.2	10.1 – 16.0	10.1 – 16.0 – 73.5 – 0.3
GroupIII	$KatG^{\Delta 290-293}$	99.3 – 0.7	56.2 – 43.0	20.5 – 22.5	20.5 – 22.5 – 56.2 – 0.7
	$KatG^{\Delta 291-292}$	99.7 – 0.3	75.7 – 24.0	12.0 – 11.9	12.0 – 11.9 – 75.7 – 0.3

4.3.4. Cyanide binding studies

4.3.4.1 Cyanide titrations

Cyanide binding is a useful probe to investigate the changes in structure and accessibility of the active site. The spectral changes upon the addition of cyanide to wtKatG and variants from all the three groups showed a shift in Soret band maximum to 424 nm from 408 nm along with appearance of a new band at 540 nm and disappearance of charge transfer bands at 510 and 645 nm. These features indicated formation of a hexacoordinate low spin Fe^{III}-CN complex. In wtKatG and group I variants first evidence of formation of Fe^{III}-CN complex was observed at lower concentration of KCN (~ 2 μM) (Figure 4.20, A and B). In contrast, the variants from group II and III showed an initial decrease in absorbance at 380 nm at lower KCN concentration followed by a shift in Soret absorption maximum to 424 nm at higher KCN concentrations (> 10 μM) (Figure 4.20, C and D). The shift of Soret absorption maximum was accompanied by a small decrease in intensity in wtKatG and group I variants, whereas in group II and III variants greater absorption intensity was observed for the Fe^{III}-CN complex than the unligated Fe^{III} state. Figure 4.21 shows the ligand binding curves for wtKatG, Q293A KatG (representing group I), IEEQ-A KatG and $KatG^{\Delta 291}$ (representing group II) and all the other deletion variants (representing group III). Dissociations constants were determined by least-squares analysis of the absorption at 422 nm was fit to a single-ligand binding model. The K_D values were for group I variants were similar to wtKatG but were significantly lower compared to the group II and III variants (Table 4.7).

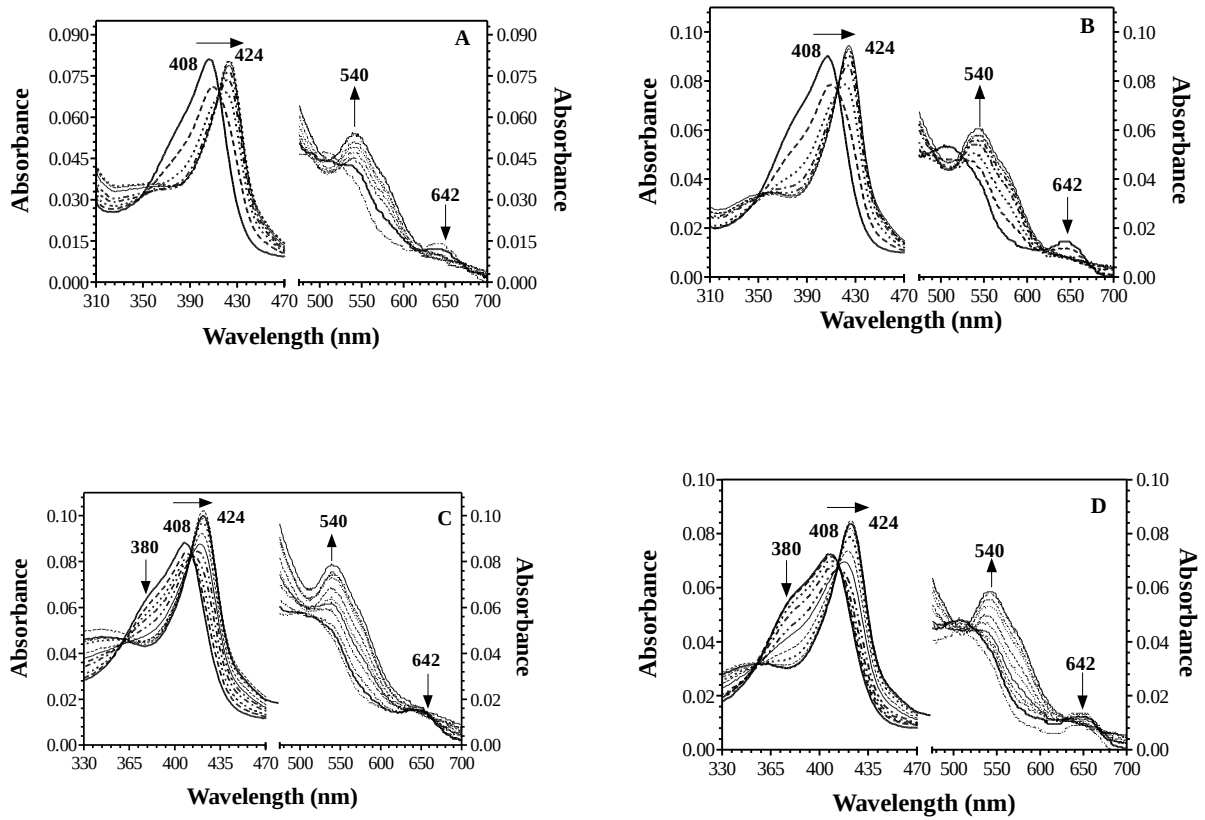

Figure 4.20: Titration of wtKatG (A), Q293A KatG (B), KatG$^{\Delta 291}$ (C), and KatG$^{\Delta 288\text{-}293}$ (D) with potassium cyanide. Spectra were recorded 3 min after each addition of cyanide. All the reactions were carried out at 25°C in 100 mM phosphate buffer, pH 7.0

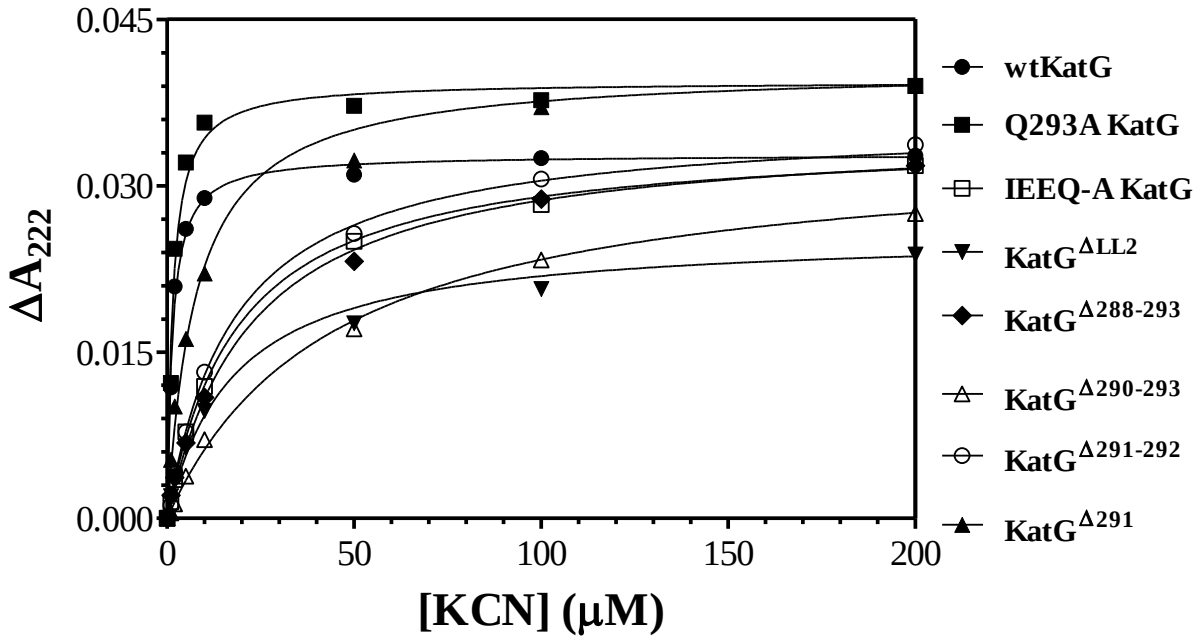

Figure 4.21: Titration of wtKatG and group I, II, and III variants with potassium cyanide. The data point on the graph show ΔA_{422} values as a function of the concentration of cyanide. The data were fit to a one binding site model to obtain K_D values. All the reactions were carried out at 25°C, in 100 mM phosphate buffer, pH 7.0

Table 4.7: Dissociation constants for cyanide binding of wtKatG and the variants obtained from equilibrium titration studies

	K_D (μM)
WT KatG	1.4 ± 0.1
Q293A KatG	1.5 ± 0.2
$KatG^{\Delta 291}$	8 ± 5
IEEQ-A KatG	18.9 ± 0.6
$KatG^{\Delta LL2}$	18 ± 2
$KatG^{\Delta 288\text{-}293}$	22 ± 1
$KatG^{\Delta 290\text{-}293}$	43 ± 2
$KatG^{\Delta 291\text{-}292}$	17.7 ± 0.7

4.3.4.2 Cyanide binding kinetics

Diode array spectra recorded upon reaction with KCN showed the similar changes as observed in cyanide titration experiments. The Soret absorption maximum was shifted from 408 nm to 424 nm (isosbestic point 413) and a prominent new peak appeared at 540 nm in wtKatG and all three groups of variants. All the variants, including wtKatG, showed biphasic cyanide binding kinetics. In wtKatG and Q293A KatG (Figure 4.22 A), the biphasic cyanide binding included a rapid first phase whereas the first phase was much slower in group II (Figure 4.22 B) and III (Figure 4.22 C) variants.

The obtained pseudo first order rate constants for CN^- binding by wtKatG and its variants increased linearly with KCN concentration (Figure 4.23). The apparent second-order rate constant (k_{on}) for cyanide binding was calculated from the slope. For wtKatG and Q293A KatG the k_{on} values were 4.3 x 10^5 $M^{-1}s^{-1}$ and 4.7 x 10^5 $M^{-1}s^{-1}$, respectively. Indeed, similar results were observed for all group I variants. In contrast, all the deletion variants as well as the quadruple substitution variant showed a three order of magnitude reduction in k_{on} . The finite intercept gave the k_{off} values, which are reported in Table 4.8. The k_{off} / k_{on} gave values for the dissociation constants (K_D) of the cyanide complexes of each protein. K_D values of 25 μM were calculated for wtKatG and Q293A KatG whereas a much higher K_D values (in mM) were obtained for group II and III variants (Table 4.8).

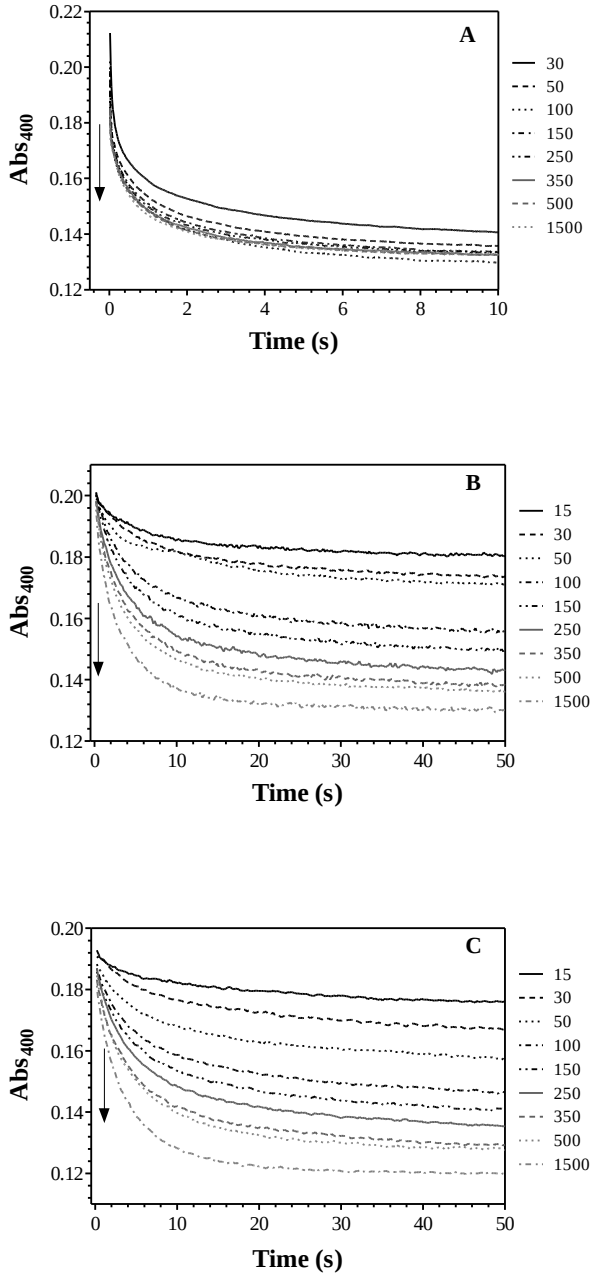

Figure 4.22: Cyanide binding studies of Q293A KatG (A), IEEQ-A KatG (B), and KatG$^{\Delta 288-293.}$ Panels A, B and C show the time course of formation of the ferri-cyano complex in the presence of varying concentrations (μM) of potassium cyanide at 400 nm. All reactions were carried out in single mixing mode at 25°C using 50mM phosphate buffer, pH 7.0

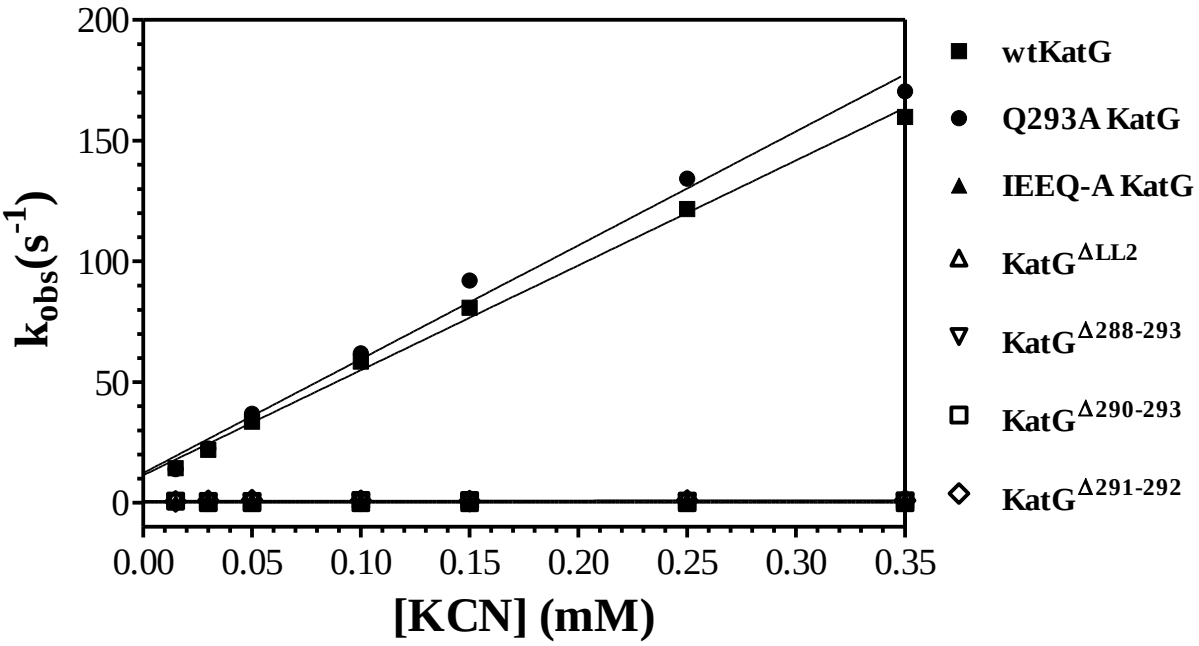

Figure 4.23: Pseudo-first-order-rate constants for the formation of cyanide complex of wtKatG and variants as a function of cyanide concentration. Absorbance increase at 428 nm was fit to double exponential equation, and k_{obs} values for the fast phase were plotted versus potassium cyanide concentration. All reactions were carried out in single mixing mode at 25°C using 50mM phosphate buffer, pH 7.0.

Table 4.8: k_{on}, k_{off}, and K_D for cyanide binding by wtKatG, and its LL2 variants

KatG	k_{on} (10^3 $M^{-1}s^{-1}$)	k_{off} (s^{-1})	K_D (μM)
WT KatG	434 ± 7	11 ± 1	25
Q293A KatG	471 ± 11	12 ± 2	25
IEEQ-A KatG	0.97 ± 0.07	0.27 ± 0.01	278
$KatG^{\Delta LL2}$	0.018 ± 0.002	0.0189 ± 0.0003	952
$KatG^{\Delta 288-293}$	0.36 ± 0.03	0.254 ± 0.006	705
$KatG^{\Delta 290-293}$	0.6 ± 0.4	0.65 ±0.09	1083
$KatG^{\Delta 291-292}$	0.7 ± 0.4	0.74 ± 0.09	1057

4.4. Discussion

KatG has a buried active site and more defined water matrix on the distal side of the heme compared to monofunctional peroxidases (*102, 170-172*). LL1 and LL2 help define a deep and narrow access channel to this buried active site. This architecture is typical for catalatic activity and its manipulation usually decreases the catalase but increases the peroxidase activity (*43, 102*). In this report, we introduced substitutions and deletions to the residues in the LL2 structure of *E.coli* catalase-peroxidase to determine their influence on the active site architecture and function. Our previous studies on a variant obtained by deletion of the entire LL2 structure have shown that absence of LL2 results in a near complete loss of catalase activity with little effect on peroxidase activity (*87*). This suggests that LL2 in provides an architectural framework that is necessary for maintaining catalase-peroxidase bifunctionality.

Sequence alignments of different KatGs indicate a striking conservation of length in LL2 rather than the identity of particular residues. Moreover, when the amino acid identity is conserved, with one exception (i.e., W297), glycine and proline are the conserved residues. When the amino acid character is conserved, it is in hydrophobicity. This is in contrast to the other large loop (LL1) where there is great variation in length, but at the same time, positions of sequence which are virtually invariant. Crystal structures indicate a point of contact between apex of LL2 and hydrophobic pocket of intersubunit C-terminal domain. The strict conservation of length and *conformationally* important residues suggests that the length is necessary to maintain this specific interaction. In this report, we explored the interaction of LL2 with the intersubunit C-terminal domain more closely to examine the role of this interaction on active site

function of KatG. We hypothesized that this interaction contributes to active site fine tuning for catalase activity and anticipated that any perturbation of this interaction would cause changes in heme coordination and consequently, activity of the protein.

Out of the six residues present at the apex of LL2, side chains Ile290 and Gln293 protrude directly into a cavity provided by the C-terminal domain (Figure 4.1), whereas Glu291 and Glu292 are both anticipated to point away from the pocket. Single and double substitutions of these amino acids produced variants that were catalytically and spectroscopicly similar to the wild-type enzyme. The catalase and peroxidase activities were more or less equivalent to the wild-type with apparent second-order rate constants around 10^6 $M^{-1}s^{-1}$ for catalase and 10^5 $M^{-1}s^{-1}$ for peroxidase activities. Preservation of both the activities correlated well with unchanged spectroscopic characteristics. All of these variants contain predominantly hexacoordinate high-spin heme as suggested by UV-Vis spectroscopy, and confirmed by MCD and EPR. Unchanged spectral features and activity profile might suggest that identity of the residue at the point of contact is not a particularly important criterion for maintaining the bifunctionality of KatG.

Conversely, deletion variants including the apex and limb residues differ drastically in catalytic and spectroscopic characteristics in comparison to the wild-type enzyme. Four apex deletion variants ($KatG^{\Delta 288-293}$, $KatG^{\Delta 290-293}$, $KatG^{\Delta 291-292}$, and $KatG^{\Delta 291}$) and two limb deletion variants ($KatG^{\Delta 285/\Delta 294}$, and $KatG^{\Delta 280/\Delta 299}$) were subjected to spectroscopic and kinetic analyses. The largest apex deletion variant i.e., $KatG^{\Delta 288-293}$ had negligible catalase activity and with this came a notable shift in heme coordination environment toward the pentacoordinate state. These properties were essentially identical to the variant lacking the entire LL2 structure. Interestingly,

a similar pattern (i.e., shifts in heme coordination to pentacoordinate heme state and negligible catalase activity) was also observed for KatG$^{\Delta 290\text{-}293}$ and KatG$^{\Delta 291\text{-}292}$. The smallest apex deletion variant (KatG$^{\Delta 291}$) and both the limb deletion variants retained around 20% of catalase activity but in terms of the heme coordination environment these resembled the rest of the deletion variants. All the deletion variants demonstrated decreased peroxidase activity with respect to H_2O_2 with very little effect on the ABTS-dependent peroxidase activity.

In contrast, the substitution variants had little effect, if any, on the catalase activity and consistent with these data, the spectroscopic features of these variants were comparable to those of the wild-type enzyme. It was not until, four of the apex residues were substituted with alanine (i.e., IEEQ-A KatG) that the effects similar to those seen for the deletion variants were observed. This quadruple substitution variant was dominated by pentacoordinate heme environment and retained only 6% of the catalase activity compared to wild-type enzyme. These observations emphasize on the fact that length conservation of LL2 is an important criterion to maintain the intersubunit interaction with C-terminal domain. This interaction, despite being 35Å away from the active site, is essential for maintaining the bifunctionality.

In the absence of appreciable catalase activity, it is difficult to assess the specific reasons for the loss of catalytic function. Here, evaluation of remaining peroxidase activity and evaluation of small ligand (CN^-) binding provide useful probes of important catalytic steps. Peroxidase kinetic parameters with respect to H_2O_2 provide insight into the ability to form compound I and other highly oxidized states necessary for catalysis. Kinetic parameters with

respect to the electron donor (e.g., ABTS) are informative to investigate electron transfer into the active site heme system.

The effect on H_2O_2-dependent peroxidase parameters was dramatic for all the deletion variants. The apparent second order rate constants with respect to H_2O_2 were two orders of magnitude lower than wild type enzyme. However, substantial rates of turnover (even in excess of wtKatG) could be observed at sufficiently high H_2O_2 concentration. This suggests a deficiency in the correct association of H_2O_2 in the active site leading toward its reduction to H_2O. On the other hand, the kinetic parameters with respect to ABTS suggest that electron transfer to the heme by exogenous donors is unaffected and in some cases enhanced.

Attempts to use the stopped-flow to directly measure the formation of compound I were unsuccessful. The variants were insufficiently reactive at low peroxide concentrations, and at higher concentrations of peroxide, the variants showed signs of heme bleaching. However, small ligand binding to the ferric state, especially that of CN^- mimics in many ways H_2O_2-dependent formation of compound I. We observed dramatically diminished rates of CN^- binding for all the variants with LL2 deletions, both k_{on} and k_{off} decreased substantially with the net effect on K_D being considerably larger for the deletion variants. Equilibrium titration experiments confirmed the same decrease in affinity for CN^- as a ligand. Conversely, substitution variants (i.e., group I variants) showed CN^- binding kinetics indistinguishable from wild type KatG. Equilibrium titration of CN^- to determine K_D for CN^- for these variants confirmed the results of our stopped-flow study.

Interestingly, the diminished rates of CN^- binding correlate with an increase in the proportion of heme in its pentacoordinate high-spin state and decrease in the hexacoordinate high-spin species. It is at first glance counterintuitive that the absence of a sixth ligand would diminish binding of CN^- as a sixth ligand. After all, the presence of a pre-existing sixth ligand would be expected to compete with CN^- for its binding site. However, it has been observed elsewhere that diminished rates of CN^- binding by *M. tuberculosis* KatG go with increased proportions of the pentacoordinate state (*70*). Specifically, increased rates (1000-fold higher) of cyanide binding were observed in aged enzyme preparations due to higher proportions of hexacoordinate heme where a distal water molecule occupied the sixth position. On the contrary, freshly prepared enzyme dominated by pentacoordinate heme had lower affinity for cyanide as a heme ligand (*70*). Also, low temperature EPR spectroscopy and resonance Raman studies demonstrated favor ligand binding (cyanide or peroxide) to hexacoordinate heme. These results were suggested to provide evidence for the participation of a distal water molecule weakly bound at the sixth position of heme iron in the first phase of the reaction mechanism of KatG is important for the reaction of cyanide binding (*70*).

The distal water molecules have also been implicated in proton transfer within the distal cavity during the H_2O_2 - dependent compound I formation which is an initial step in both catalase and peroxidase turnover. QM/MM calculations addressing the compound I formation in HRP suggests an energetic advantage of specific distal water molecule in the active site (*173*). In *Burkholderia pseudomallei* KatG, mutation of Asp141, which is present at the acidic entrance channel and forms a hydrogen bond with Ile237, increases the K_M for H_2O_2 oxidation. This was suggested to occur due to release of water molecule, which alters the solvent matrix in the

substrate channel for efficient H_2O_2 oxidation (*143*). So, it is reasonable to speculate that the displacement of distal water molecule from the sixth position in the deletion variants results in a loss of catalase activity by influencing H_2O_2 oxidation.

The first step of peroxidase turnover involves diffusion of H_2O_2 in to the active site and its deprotonation by the distal histidine acting as general base. Thus, the increased K_M for H_2O_2 in most of the deletion variants and two-order of magnitude lower apparent k_{cat}/K_M of all the deletion variants may suggests a deficiency in the correct association of H_2O_2 in the active site leading toward its reduction to H_2O. This also suggests that deletion of parts of LL2 can disrupt the ordered matrix of oriented water dipole present in the narrow KatG access channel and this in turn can hamper the diffusion of H_2O_2 into the active site. These observations were further supported by cyanide binding experiments. Lower k_{on} rates for cyanide binding for deletion variants also suggested the importance of distal water molecule in ligand access and binding. Moreover, lower K_D values of wild-type enzyme and site-specific variants further supported that the hexacoordinate heme is the preferential species for cyanide binding.

In conclusion, the presented data suggest that length conservation of LL2 structure in KatGs is an important criterion with respect to maintaining the bifunctionality. Furthermore, the length conservation is highly essential to preserve the intersubunit interaction with the C-terminal domain and this interaction despite of its distant location efficiently fine tune the active site structure of KatG to catalyze catalase and peroxidase reactions. Catalase activity parameters clearly demonstrate that deletion of any part of LL2 structure dramatically reduces / eliminates the catalase activity in contrast to site-specific substitutions. The lower apparent k_{cat}/K_M for

H_2O_2-dependent peroxidase activity along with diminished rates of catalase activity suggests that there are some difficulties in allowing the peroxide substrate access to the active site. This observation was further supported by cyanide binding studies which indicated that compound I formation is hampered in deletion variants. This may be due to disruption of the ordered network of water molecules especially at the distal part of the active site. The dominance of pentacoordinate high-spin heme species in all the deletion variants further helped us in suggesting that distal water molecule is displaced from the sixth ligand position which is preventing the efficient binding of peroxide substrate to the active site heme. Moreover, this work demonstrated that even the smallest deletion of LL2 structure was able to replicate the results as was seen in case of the enzyme lacking the entire LL2 structure. Thus, this work not only supported our previous findings that LL2 plays a major role in modulating the active site architecture and catalytic versatility of KatG but also provided sufficient evidences to support nature's strategy to choose length conservation in this structure over the residue conservation.

Chapter Five: Summary

Enzymes are nature's catalysts, tremendously accelerating the rates of a wide range of biochemical reactions, often with exquisite specificity. Clearly, nature is an accomplished enzyme engineer, and a central strategy employed by biological systems is the co-opting of existing structures for new catalytic purposes. One could envision several approaches for doing just that. For example, the direct substitution of active site amino acid residues, changing the geometric and electronic properties of the active site, could conceivably produce catalysts for as yet unaddressed reactions. Interestingly, since the advent of site-directed mutagenesis, biochemists the world over have tried just that approach. The result has been a near uniform failure. The virtually invariant result has been the loss of the existing catalytic abilities with no new added catalytic function. As such, it has been extraordinarily useful for understanding the mechanisms of existing enzymes, but uniformly poor for engineering new ones.

This raises an important question: Is this the way nature has done enzyme engineering? While a definitive answer for all enzymes is not currently available, it is safe to say that in the case of catalase-peroxidases, the answer is clearly “no”. With more than ample time to make substantial substitution of active site functional groups very little has changed between KatG and its fellow class I non-animal peroxidases (e.g., cytochrome c peroxidases), indeed, even comparisons to much more distantly related class II and III enzymes show very similar

active-site structures. Yet, KatG alone has catalase activity rivaling that of structurally unrelated monofunctional catalases. All the rest of the non-animal peroxidases have catalase activity at least three orders of magnitude lower. That ample time for active site substitutions has elapsed is easily evident from KatG's C-terminal domain. Itself derived from a monofunctional peroxidase through gene duplication and fusion, the C-terminal domain shows substantial active site substitution such that it no longer even binds heme.

This point to a strategy employed for the development of KatG as a catalase that can be understood in two ways. First, it represents the improvisation of a new mechanism for catalase activity. This improvised mechanism does not require substantial active site changes to accommodate it; rather this mechanism capitalizes on the strengths afforded by the active site structure as it is. In other words, the physical features of the peroxidases structure favor certain intermediates, interactions with substrates and chemical events. These are being used to accomplish catalase turnover in a new way. Second, a nearly identical active site indicates that where structural modifications have been made, these have primarily been carried out peripheral or external to the active. These must account for the subtle perturbation and fine adjustments necessary for the emergence of new catalytic function.

The focus of the research described in this dissertation has been on the latter. In this regard, there are three structural components: a gene duplicated C-terminal domain, and two large loops- LL1 and LL2. The work in the Goodwin laboratory, including that described in this dissertation, demonstrates that all three structures play an important role in maintaining the bifunctionality of KatG enzymes. Moreover, this study demonstrates that KatG's amenability to

structural fine-tuning makes it an ideal system for enzyme engineering. Based on the evidences provided in this dissertation and from the previous work in Goodwin lab, it is reasonable to suggest that catalase-peroxidases are fruitful models to study how enzyme functions are regulated by the fourth (i.e., global) structural level. Disruption of structural features unique to LL1 and LL2 (e.g., The W-Y-M covalent adduct or intersubunit noncovalent interactions, respectively) confirms that the changes to the structures distant to the active site would affect heme coordination state and catalytic properties of the enzyme.

5.1. Effect on KatG catalytic versatility: Residue conservation of Large Loop 1

The most obvious feature of the LL1 structure is its contribution of an invariant tyrosine to the W-Y-M covalent adduct. This seems rather a very small role for a structure which is 35-76 amino acids long. Indeed, the LL1 structure is far more than is necessary to position tyrosine for participation in the adduct. KatG crystal structures show that this loop forms the part of substrate access channel and regulates the access of reducing substrates to the heme edge. Because of its location and its important role in supporting tyrosine this loop has been thoroughly investigated. Studies have shown that manipulation of the conserved residues of this loop present at the substrate entrance channel either diminishes or removes the *catalatic* activity of KatG but has varied effects on the peroxidase activity, ranging from no effect, decrease, or enhancement of the peroxidase activity. Also, the Goodwin lab has previously shown that removal of entire LL1 causes complete loss of catalase activity and changes the rate limiting step to compound II reduction but increases the peroxidase activity compared to wild-type enzyme.

This suggested that there are some additional roles filled by this loop, which help to maintain the overall catalytic performance of KatG. The work in this dissertation has provided evidence in support of this hypothesis. The study involving the partial deletion of LL1 ($KatG^{\Delta 209-228}$) and its comparison to Y226F KatG and $KatG^{\Delta LL1}$, helped elucidate not only the mechanism for loss of catalase activity but also the substantial enhancement of peroxidase activity. It has become clear that the LL1 structure is essential for maintaining the structural integrity of KatG, as deletion of the entire structure makes the protein insoluble during expression. Furthermore, this loop favors catalase turnover by obstructing direct access of reducing substrates to the heme center. Simultaneously, it rescues the enzyme from inactivation which would normally arise due to reducing substrate unavailability, by cleverly providing a tyrosine for the formation of the W-Y-M adduct. This has been proposed to facilitate the release of molecular oxygen to complete a novel *catalatic* cycle.

The effect of the LL1 structure on the catalytic activity of KatG would be interpreted as uncovering a mutual competition between catalase and peroxidase turnover. However, recent work from the Goodwin laboratory, involving mechanistic studies of KatG catalytic cycle in *M. tuberculosis* have suggested that peroxidase activity acts as a synergistic mechanism for catalase activity. This mechanistic study forces one to look at the peroxidase and catalase activities of KatG from a whole new perspective. Up to now, the general consensus of the fields is that both the activities are competitive in nature and this has led to the classical representation of catalase-peroxidase mechanistic scheme of KatGs, which is just an overlay of individual catalase and peroxidase cycles. And more so, the conditions used to measure one activity (e.g., pH, buffer conditions, availability of substrates, etc.) eliminate contribution from the second. This suggests

that at any given point of time enzyme is favoring one activity over the other. Thus, in the absence of one activity (e.g., catalase) no change or even enhancement of the other (e.g., peroxidase activity) is seen which again emphasizes the competitiveness between the two activities. However, the data from recent mechanistic studies suggested that the presence of peroxidase activity or more importantly the presence of reducing substrates enhance the catalase activity instead of diminishing or eliminating it. This has led to the new hypothesis that the peroxidase activity has been folded into making catalase activity of KatG operate by a novel mechanism producing more efficient catalyst over a broader range of conditions. The work, though in its initial stages, has provided enough data to reveal the devotion of peroxidase machinery towards enhancement of the catalase activity, especially under conditions where catalase activity is assumed to be absent. Under this paradigm, the presence of LL1 structure and its constraints for the electron donors to enhance the catalase activity can help us envision the presence of peroxidase activity as a catalase activity enhancer.

5.2. Effect on KatG catalytic versatility: Length Conservation of Large Loop 2

Previously it has been shown that LL2 is critical for the bifunctionality of KatG. Deletion of entire LL2 caused a 99% loss of catalase activity along with dominance of pentacoordinate high spin heme species over the hexacoordinate that dominates in the wild type enzyme. This showed that removal of entire loop has a profound impact on the KatG catalytic activity and its absences make this bifunctional enzyme like monofunctional peroxidases.

To explore how LL2 affects KatG function, the effects of the disruption of this peripheral structure were examined. Sequence comparison of 20 widely phylogenetically dispersed KatGs showed a remarkable length conservation of LL2 but relatively little sequence conservation. The LL2 is ~35 amino-acid long, starts and ends near the active site, and spans between F and G helices. Most importantly, the apex of LL2 forms a unique intersubunit interaction with the C-terminal domain. Deletion of the entire LL2 ($KatG^{\Delta LL2}$) changed the coordination state of the enzyme to pentacoordinate ferric heme and rendered the enzyme catalase negative. $KatG^{\Delta LL2}$ showed mixed populations of high spin ferric heme with 77% rhombic contribution and 23% axial contribution in contrast to 99% axial contribution in wild type enzyme. This suggested that LL2 preserves the catalatic activity of KatG by maintaining the proper active site architecture. This role of LL2 was further strengthened by the fact that disruption of intersubunit interactions between LL2 and C-terminal domain were sufficient to duplicate the results of $KatG^{\Delta LL2}$. indeed, just deleting two amino acid residues at the point of interaction. Even the elimination of one amino acid out of 35 reduced catalase activity by 80%. The importance of length conservation of this loop was strengthened by the fact that deletion variants had greater impact on overall catalytic activity and heme coordination of KatG compared to the site specific variants involving the apex residues.

The deletion variants showed the heme species population mixture of $KatG^{\Delta LL2}$. This was confirmed by UV-Vis, MCD, and EPR spectroscopy. In contrast, site-specific variants showed higher percentage of hexacoordinate high spin heme similar to the wild-type enzyme. The steady state kinetics showed that deletion variants retained little if any catalase activity whereas site-specific variants were more or less catalase active. The effect on peroxidase activity

of deletion variants was variable. The apparent k_{cat}/K_M with respect to H_2O_2 was diminished by two orders of magnitude with very little effect on ABTS- dependent parameters. The rates of cyanide binding were dramatically diminished in deletion variants whereas the rates were indistinguishable from wild-type enzyme for the substitution variants.

In conclusion, the dominance of pentacoordinate high-spin heme species, near absence of catalase activity, decreased rates of H_2O_2-dependent peroxidase activity, and finally diminished rates of cyanide binding in all the deletion variants suggested that length conservation of LL2 is an important criterion to maintain the distant intersubunit interaction. And, this intersubunit interaction between LL2 structure and intersubunit C-terminal domain preserves the catalatic activity to KatG by retaining the proper active site architecture.

5.3. Conclusions

In summary, this research has helped to identify how nature has gone about engineering a new catalytic activity from an old structural scaffold. The importance of global structures in balancing the catalytic performance of KatG suggests that nature's decision to manipulate KatG's global structure has made this enzyme a better catalyst and opened up many doors for engineering a new catalyst. Nature's strategy to use a peroxidase scaffold and manipulate through the action of peripheral structures to build a new function is an elegant one. On one hand, residue conservation in LL1 has provided an excellent gateway to enhance the catalase function by using peroxidase machinery. On the other hand, length conservation in LL2 has maintained a necessary active-site structural framework by interacting with the C-terminal

domain of another subunit some 35Å away. This is the kind of interaction that would typically be overlooked due to its distant location. But this research has clearly shown that this distant interaction is crucial in order to maintain the bifunctionality of KatG. This research points toward the necessity of understanding peripheral structures and distant protein-protein interactions for controlling catalytic function.

References

1. Paoli, M., Marles-Wright, J., and Smith, A. (2002) Structure-function relationships in heme-proteins, *DNA and Cell Biology 21*, 271-280.

2. Reedy, C. J., and Gibney, B. R. (2004) Heme protein assemblies, *Chemical Reviews 104*, 617-649.

3. The PubChem Project. http://pubchem.ncbi.nlm.nih.gov/. June 2009.

4. Mogi, T., Saiki, K., and Anraku, Y. (1994) BIOSYNTHESIS AND FUNCTIONAL-ROLE OF HEME-O AND HEME-A, *Molecular Microbiology 14*, 391-398.

5. Salemme, F. R. (1977) STRUCTURE AND FUNCTION OF CYTOCHROMES-C, *Annual Review of Biochemistry 46*, 299-329.

6. DiCarlo, C. M., Vitello, L. B., and Erman, J. E. (2007) Effect of active site and surface mutations on the reduction potential of yeast cytochrome c peroxidase and spectroscopic properties of the oxidized and reduced enzyme, *Journal of Inorganic Biochemistry 101*, 603-613.

7. Vainshtein, B. K., Melikadamyan, W. R., Barynin, V. V., Vagin, A. A., Grebenko, A. I., Borisov, V. V., Bartels, K. S., Fita, I., and Rossmann, M. G. (1986) 3-DIMENSIONAL STRUCTURE OF CATALASE FROM PENICILLIUM-VITALE AT 2.0 A RESOLUTION, *Journal of Molecular Biology 188*, 49-61.

8. Murshudov, G. N., Grebenko, A. I., Barynin, V., Dauter, Z., Wilson, K. S., Vainshtein, B. K., MelikAdamyan, W., Bravo, J., Ferran, J. M., Ferrer, J. C., Switala, J., Loewen, P. C., and Fita, I. (1996) Structure of the heme d of Penicillium vitale and Escherichia coli catalases, *Journal of Biological Chemistry 271*, 8863-8868.

9. Chida, H., Yokoyama, T., Kawai, F., Nakazawa, A., Akazaki, H., Takayama, Y., Hirano, T., Suruga, K., Satoh, T., Yamada, S., Kawachi, R., Unzai, S., Nishio, T., Park, S. Y., and Oku, T. (2006) Crystal structure of oxidized cytochrome c(6A) from Arabidopsis thaliana, *Febs Letters 580*, 3763-3768.

10. Poulos, T. L., Finzel, B. C., and Howard, A. J. (1987) HIGH-RESOLUTION CRYSTAL-STRUCTURE OF CYTOCHROME-P450CAM, *Journal of Molecular Biology 195*, 687-700.

11. Sono, M., Dawson, J. H., Hall, K., and Hager, L. P. (1986) LIGAND AND HALIDE BINDING-PROPERTIES OF CHLOROPEROXIDASE - PEROXIDASE-TYPE ACTIVE-SITE HEME ENVIRONMENT WITH CYTOCHROME-P-450 TYPE ENDOGENOUS AXIAL LIGAND AND SPECTROSCOPIC PROPERTIES, *Biochemistry 25*, 347-356.

12. Carpena, X., Soriano, M., Klotz, M. G., Duckworth, H. W., Donald, L. J., Melik-Adamyan, W., Fita, I., and Loewen, P. C. (2003) Structure of the clade 1 catalase, CatF of Pseudomonas syringae, at 1.8 angstrom resolution, *Proteins-Structure Function and Bioinformatics 50*, 423-436.

13. Demontellano, P. R. O., Choe, Y. S., Depillis, G., and Catalano, C. E. (1987) STRUCTURE-MECHANISM RELATIONSHIPS IN HEMOPROTEINS - OXYGENATIONS CATALYZED BY CHLOROPEROXIDASE AND HORSERADISH-PEROXIDASE, *Journal of Biological Chemistry 262*, 11641-11646.

14. Ator, M. A., and Demontellano, P. R. O. (1987) PROTEIN CONTROL OF PROSTHETIC HEME REACTIVITY - REACTION OF SUBSTRATES WITH THE HEME EDGE OF HORSERADISH-PEROXIDASE, *Journal of Biological Chemistry 262*, 1542-1551.

15. Masters, C., and Holmes, R. (1977) PEROXISOMES - NEW ASPECTS OF CELL PHYSIOLOGY AND BIOCHEMISTRY, *Physiological Reviews 57*, 816-882.

16. Nicholls, P., Fita, I., and Loewen, P. C. (2001) Enzymology and structure of catalases, *Advances in Inorganic Chemistry, Vol 51 51*, 51-106.

17. Rorth, M., and Jensen, P. K. (1967) DETERMINATION OF CATALASE ACTIVITY BY MEANS OF CLARK OXYGEN ELECTRODE, *Biochimica Et Biophysica Acta 139*, 171-&.

18. Beers, R. F., a nd Sizer, I .W. (1952) A spectrophotometric method for measuring the breakdown of hydrogen peroxide by catalase, *Journal of Biological Chemistry 95*, 133-149.

19. Press, N. Y. C. u., (Ed.) (1995) *The Peroxisome: A Vital Organelle*, Cambridge.

20. Klotz, M. G., Klassen, G. R., and Loewen, P. C. (1997) Phylogenetic relationships among prokaryotic and eukaryotic catalases, *Molecular Biology and Evolution 14*, 951-958.

21. Klotz, M. G., and Loewen, P. C. (2003) The molecular evolution of catalatic hydroperoxidases: Evidence for multiple lateral transfer of genes between prokaryota and from bacteria into Eukaryota, *Molecular Biology and Evolution 20*, 1098-1112.

22. Kirkman, H. N., and Gaetani, G.F. (1984) Catalase: a tetrameric enzyme with four tightly bound molecules of NADPH, *PNAS 81*, 4343-4347.

23. Fita, I., and Rossmann, M.G. (1985) The NADPH binding site on beef liver catalase, *PNAS 82*, 1604-1608.

24. Murshudov, G. N., Melikadamyan, W. R., Grebenko, A. I., Barynin, V. V., Vagin, A. A., Vainshtein, B. K., Dauter, Z., and Wilson, K. S. (1992) 3-DIMENSIONAL STRUCTURE OF CATALASE FROM MICROCOCCUS-LYSODEIKTICUS AT 1.5 A RESOLUTION, *Febs Letters 312*, 127-131.

25. Gouet, P., Jouve, H. M., and Dideberg, O. (1995) CRYSTAL-STRUCTURE OF PROTEUS-MIRABILIS PR CATALASE WITH AND WITHOUT BOUND NADPH, *Journal of Molecular Biology 249*, 933-954.

26. Vainshtein, B. K., Melikadamyan, V. P., Barynin, V. V., Vagin, A. A., and Grebenko, A. I. (1981) THE STRUCTURE OF PENICILLIUM-VITALE CATALASE, *Kristallografiya 26*, 1003-1016.

27. Berthet, S., Nykyri, L. M., Bravo, J., Mate, M. J., BerthetColominas, C., Alzari, P. M., Koller, F., and Fita, I. (1997) Crystallization and preliminary structural analysis of catalase A from Saccharomyces cerevisiae, *Protein Science 6*, 481-483.

28. Bravo, J., Mate, M.J., Schneider, t., Switala, J., Wilson, K., Loewen, P.C., and Fita, I. (1999) Structure of catalase HPII from Escherichia coli at 1.9 Å resolution, *Proteins-Structure Function and Bioinformatics 34*, 155-166.

29. Bravo, J., Verdaguer, N., Tormo, J., Betzel, C., Switala, J., Loewen, P. C., and Fita, I. (1995) CRYSTAL-STRUCTURE OF CATALASE HPII FROM ESCHERICHIA-COLI, *Structure 3*, 491-502.

30. Melikadamyan, W. R., Barynin, V. V., Vagin, A. A., Borisov, V. V., Vainshtein, B. K., Fita, I., Murthy, M. R. N., and Rossmann, M. G. (1986) COMPARISON OF BEEF-LIVER AND PENICILLIUM-VITALE CATALASES, *Journal of Molecular Biology 188*, 63-72.

31. Switala, J., O'Neil, J. O., and Loewen, P. C. (1999) Catalase HPII from Escherichia coli exhibits enhanced resistance to denaturation, *Biochemistry 38*, 3895-3901.

32. Zamocky, M., and Koller, F. (1999) Understanding the structure and function of catalases: clues from molecular evolution and in vitro mutagenesis, *Progress in Biophysics & Molecular Biology 72*, 19-66.

33. Loewen, P. C., Switala, J., Vonossowski, I., Hillar, A., Christie, A., Tattrie, B., and Nicholls, P. (1993) CATALASE HPII OF ESCHERICHIA-COLI CATALYZES THE CONVERSION OF PROTOHEME TO CIS-HEME-D, *Biochemistry 32*, 10159-10164.

34. Obinger, C., Maj, M., Nicholls, P., and Loewen, P. (1997) Activity, peroxide compound formation, and heme d synthesis in Escherichia coli HPII catalase, *Archives of Biochemistry and Biophysics 342*, 58-67.

35. Chelikani, P., Carpena, X., Fita, I., and Loewen, P. C. (2003) An electrical potential in the access channel of catalases enhances catalysis, *Journal of Biological Chemistry 278*, 31290-31296.

36. Kalko, S. G., Gelpi, J. L., Fita, I., and Orozco, M. (2001) Theoretical study of the mechanisms of substrate recognition by catalase, *Journal of the American Chemical Society 123*, 9665-9672.

37. Amara, P., Andreoletti, P., Jouve, H. M., and Field, M. J. (2001) Ligand diffusion in the catalase from Proteus mirabilis: A molecular dynamics study, *Protein Science 10*, 1927-1935.

38. Koua, D., Cerutti, L., Falquet, L., Sigrist, C. J. A., Theiler, G., Hulo, N., and Dunand, C. (2009) PeroxiBase: a database with new tools for peroxidase family classification, *Nucleic Acids Research 37*, D261-D266.

39. Dunford, H. B. (1999) *Heme Peroxidases*, John Wiley.

40. Welinder, K. G. (1992) Superfamily of plant, fungal and bacterial peroxidases, *Current Opinion in Structural Biology 2*, 388-393.

41. Zamocky, M., Jakopitsch, C., Furtmuller, P. G., Dunand, C., and Obinger, C. (2008) The peroxidase-cyclooxygenase superfamily: reconstructed evolution of critical enzymes of the innate immune system, *Proteins-Structure Function and Bioinformatics 72*, 589-605.

42. Taurog, A. (1999) Molecular evolution of thyroid peroxidase, *Biochimie 81*, 557-562.

43. Smulevich, G., Jakopitsch, C., Droghetti, E., and Obinger, C. (2006) Probing the structure and bifunctionality of catalase-peroxidase (KatG), *Journal of Inorganic Biochemistry 100*, 568-585.

44. Jespersen, H. M., Kjaersgard, I. V. H., Ostergaard, L., and Welinder, K. G. (1997) From sequence analysis of three novel ascorbate peroxidases from Arabidopsis thaliana to structure, function and evolution of seven types of ascorbate peroxidase, *Biochemical Journal 326*, 305-310.

45. Dalton, D. A. (1991) *Peroxidases in Chemistry and Biology*, Vol. 1-2, CRC Press, Boca Raton, FL.

46. Skulachev, V. P. (1998) Cytochrome c in the apoptotic and antioxidant cascades, *Febs Letters 423*, 275-280.

47. Yonetani, T., and Ohnishi, T. (1966) CYTOCHROME C PEROXIDASE A MITOCHONDRIAL ENZYME OF YEAST, *Journal of Biological Chemistry 241*, 2983

48. Piontek, K., Smith, A. T., and Blodig, W. (2001) Lignin peroxidase structure and function, *Biochemical Society Transactions 29*, 111-116.

49. Bindschedler, L. V., Dewdney, J., Blee, K. A., Stone, J. M., Asai, T., Plotnikov, J., Denoux, C., Hayes, T., Gerrish, C., Davies, D. R., Ausubel, F. M., and Bolwell, G. P. (2006) Peroxidase-dependent apoplastic oxidative burst in Arabidopsis required for pathogen resistance, *Plant Journal 47*, 851-863.

50. Schuller, D. J., Ban, N., vanHuystee, R. B., McPherson, A., and Poulos, T. L. (1996) The crystal structure of peanut peroxidase, *Structure 4*, 311-321.

51. Banci, L. (1997) Structural properties of peroxidases, *Journal of Biotechnology 53*, 253-263.

52. Poulos, T. L., and Kraut, J. (1980) THE STEREOCHEMISTRY OF PEROXIDASE CATALYSIS, *Journal of Biological Chemistry 255*, 8199-8205.

53. Goodin, D. B., and McRee, D. E. (1993) THE ASP-HIS-FE TRIAD OF CYTOCHROME-C PEROXIDASE CONTROLS THE REDUCTION POTENTIAL, ELECTRONIC-STRUCTURE, AND COUPLING OF THE TRYPTOPHAN FREE-RADICAL TO THE HEME, *Biochemistry 32*, 3313-3324.

54. Vitello, L. B., Erman, J. E., Miller, M. A., Wang, J., and Kraut, J. (1993) EFFECT OF ARGININE-48 REPLACEMENT ON THE REACTION BETWEEN CYTOCHROME-C PEROXIDASE AND HYDROGEN-PEROXIDE, *Biochemistry 32*, 9807-9818.

55. Edwards, S. L., Xuong, N. H., Hamlin, R. C., and Kraut, J. (1987) CRYSTAL-STRUCTURE OF CYTOCHROME-C PEROXIDASE COMPOUND-I, *Biochemistry 26*, 1503-1511.

56. Finzel, B. C., Poulos, T. L., and Kraut, J. (1984) CRYSTAL-STRUCTURE OF YEAST CYTOCHROME-C PEROXIDASE REFINED AT 1.7-A RESOLUTION, *Journal of Biological Chemistry 259*, 3027-3036.

57. edwards, S. L. R., R., Wariishi, H., Gold, M.H., and Poulos, T.L. (1993) Crystal structure of lignin peroxidase, *Proceedings of the National Academy of Sciences of the United States of America-Biological Sciences 90*, 750-754.

58. Gajhede, M., Schuller, D.J., Henriksen, A., Smith, A.T., and Poulos, T.L. (1997) Crystal structure of horseradish peroxidase C at 2.15 Å resolution, *Nature Structural Biology 4*, 1032-1038.

59. Huyett, J. E., Doan, P. E., Gurbiel, R., Houseman, A. L. P., Sivaraja, M., Goodin, D. B., and Hoffman, B. M. (1995) COMPOUND ES OF CYTOCHROME-C PEROXIDASE

CONTAINS A TRP PI-CATION RADICAL - CHARACTERIZATION BY CW AND PULSED Q-BAND ENDOR SPECTROSCOPY, *Journal of the American Chemical Society 117*, 9033-9041.

60. Sivaraja, M., Goodin, D. B., Smith, M., and Hoffman, B. M. (1989) IDENTIFICATION BY ENDOR OF TRP191 AS THE FREE-RADICAL SITE IN CYTOCHROME-C PEROXIDASE COMPOUND ES, *Science 245*, 738-740.

61. Fishel, L. A., Farnum, M. F., Mauro, J. M., Miller, M. A., Kraut, J., Liu, Y. J., Tan, X. L., and Scholes, C. P. (1991) COMPOUND-I RADICAL IN SITE-DIRECTED MUTANTS OF CYTOCHROME-C PEROXIDASE AS PROBED BY ELECTRON-PARAMAGNETIC RESONANCE AND ELECTRON NUCLEAR DOUBLE-RESONANCE, *Biochemistry 30*, 1986-1996.

62. Patterson, W. R., and Poulos, T. L. (1995) CRYSTAL-STRUCTURE OF RECOMBINANT PEA CYTOSOLIC ASCORBATE PEROXIDASE, *Biochemistry 34*, 4331-4341.

63. Patterson, W. R., Poulos, T. L., and Goodin, D. B. (1995) IDENTIFICATION OF A PORPHYRIN PI-CATION-RADICAL IN ASCORBATE PEROXIDASE COMPOUND-I, *Biochemistry 34*, 4342-4345.

64. Poulos, T. L., Edwards, S. L., Wariishi, H., and Gold, M. H. (1993) CRYSTALLOGRAPHIC REFINEMENT OF LIGNIN PEROXIDASE AT 2-ANGSTROM, *Journal of Biological Chemistry 268*, 4429-4440.

65. Sutherland, G. R. J., Zapanta, L. S., Tien, M., and Aust, S. D. (1997) Role of calcium in maintaining the heme environment of manganese peroxidase, *Biochemistry 36*, 3654-3662.

66. Vanhuystee, R. B., Xu, Y. J., and Odonnell, J. P. (1992) VARIATION IN SORET BAND ABSORPTION OF PEROXIDASE DUE TO CALCIUM, *Plant Physiology and Biochemistry 30*, 293-297.

67. Howes, B. D., Feis, A., Raimondi, L., Indiani, C., and Smulevich, G. (2001) The critical role of the proximal calcium ion in the structural properties of horseradish peroxidase, *Journal of Biological Chemistry 276*, 40704-40711.

68. Banci, L., Carloni, P., and Savellini, G. G. (1994) MOLECULAR-DYNAMICS STUDIES ON PEROXIDASES - A STRUCTURAL MODEL FOR HORSERADISH-PEROXIDASE AND A SUBSTRATE ADDUCT, *Biochemistry 33*, 12356-12366.

69. Thomas L. Poulos, S. T. F., Richard A. Alden, Steven L. Edwards, Ulf Skogland, Koji , and Takio, B. E., Nguyen-huu Xuong, Takashi Yonetani, and Joseph Kraut. (1980) The Crystal Structure of Cytochrome c Peroxidase, *The journal of Biological Chemistry 255*, 575-580.

70. Ranguelova, K., Suarez, J., Metlitsky, L., Yu, S. W., Brejt, S. Z., Zhao, L., Schelvis, J. P. M., and Magliozzo, R. S. (2008) Impact of Distal Side Water and Residue 315 on Ligand Binding to Ferric Mycobacterium tuberculosis Catalase-Peroxidase (KatG), *Biochemistry 47*, 12583-12592.

71. Hiner, A. N. P., Ruiz, J. H., Lopez, J. N. R., Canovas, F. G., Brisset, N. C., Smith, A. T., Arnao, M. B., and Acosta, M. (2002) Reactions of the class II peroxidases, lignin peroxidase and Arthromyces ramosus peroxidase, with hydrogen peroxide - Catalase-like activity, compound III formation, and enzyme inactivation, *Journal of Biological Chemistry 277*, 26879-26885.

72. Wariishi, H., and Gold, M. H. (1989) LIGNIN PEROXIDASE COMPOUND-III - FORMATION, INACTIVATION, AND CONVERSION TO THE NATIVE ENZYME, *Febs Letters 243*, 165-168.

73. Barr, D. P., and Aust, S. D. (1994) CONVERSION OF LIGNIN PEROXIDASE COMPOUND-III TO ACTIVE ENZYME BY CATION RADICALS, *Archives of Biochemistry and Biophysics 312*, 511-515.

74. Barr, D. P., and Aust, S. D. (1994) CONVERSION OF LIGNIN PEROXIDASE COMPOUND-III TO ACTIVE ENZYME, *Faseb Journal 8*, A1367-A1367.

75. Jakopitsch, C., Wanasinghe, A., Jantschko, W., Furtmuller, P. G., and Obinger, C. (2005) Kinetics of interconversion of ferrous enzymes, compound II and compound III, of wild-type Synechocystis catalase-peroxidase and Y249F, *Journal of Biological Chemistry 280*, 9037-9042.

76. Dunford, H. B. a. S., J.S. (1976) On the function and mechanism of action of peroxidases, *Coordination Chemistry Review 19*, 187-251.

77. Hulquist, D. E., and Morrison, M. (1963) Lactoperoxidase. I. The Prosthetic Group of Lactoperoxidase, *Journal of Biological Chemistry 238*, 2843-2846.

78. Zederbauer, M., Furtmueller, P. G., Brogioni, S., Jakopitsch, C., Smulevich, G., and Obinger, C. (2007) Heme to protein linkages in mammalian peroxidases: impact on spectroscopic, redox and catalytic properties, *Natural Product Reports 24*, 571-584.

79. Furtmuller, P. G., Zederbauer, M., Jantschko, W., Helm, J., Bogner, M., Jakopitsch, C., and Obinger, C. (2006) Active site structure and catalytic mechanisms of human peroxidases, *Archives of Biochemistry and Biophysics 445*, 199-213.

80. Sundaramoorthy, M., Kishi, K., Gold, M. H., and Poulos, T. L. (1994) THE CRYSTAL-STRUCTURE OF MANGANESE PEROXIDASE FROM PHANEROCHAETE-CHRYSOSPORIUM AT 2.06-ANGSTROM RESOLUTION, *Journal of Biological Chemistry 269*, 32759-32767.

81. Zeng, J., and Fenna, R. E. (1992) X-RAY CRYSTAL-STRUCTURE OF CANINE MYELOPEROXIDASE AT 3 ANGSTROM RESOLUTION, *Journal of Molecular Biology 226*, 185-207.

82. Fiedler, T. J., Davey, C. A., and Fenna, R. E. (2000) X-ray crystal structure and characterization of halide-binding sites of human myeloperoxidase at 1.8 angstrom resolution, *Journal of Biological Chemistry 275*, 11964-11971.

83. Furtmuller, P. G., Burner, U., and Obinger, C. (1998) Reaction of myeloperoxidase compound I with chloride, bromide, iodide, and thiocyanate, *Biochemistry 37*, 17923-17930.

84. Singh, A. K., Singh, N., Sharma, S., Singh, S.B., Kaur, P., Bhushan, A., Srinivasan, A., Singh, T.P. (2008) Crystal structure of lactoperoxidase at 2.4 A resolution, *Journal of Molecular Biology 376*, 1060-1075.

85. Furtmuller, P. G., Jantschko, W., Regelsberger, G., Jakopitsch, C., Arnhold, J., and Obinger, C. (2002) Reaction of lactoperoxidase compound I with halides and thiocyanate, *Biochemistry 41*, 11895-11900.

86. Baker, R. D., Cook, C. O., and Goodwin, D. C. (2004) Properties of catalase-peroxidase lacking its C-terminal domain, *Biochemical and Biophysical Research Communications 320*, 833-839.

87. Li, Y. J., and Goodwin, D. C. (2004) Vital roles of an interhelical insertion in catalase-peroxidase bifunctionality, *Biochemical and Biophysical Research Communications 318*, 970-976.

88. Varnado, C. L., Hertwig, K. M., Thomas, R., Roberts, J. K., and Goodwin, D. C. (2004) Properties of a novel periplasmic catalase-peroxidase from Escherichia coli O157 : H7, *Archives of Biochemistry and Biophysics 421*, 166-174.

89. Singh, R., Wiseman, B., Deemagarn, T., Donald, L. J., Duckworth, H. W., Carpena, X., Fita, I., and Loewen, P. C. (2004) Catalase-peroxidases (KatG) exhibit NADH oxidase activity, *Journal of Biological Chemistry 279*, 43098-43106.

90. Jakopitsch, C., Auer, M., Ivancich, A., Ruker, F., Furtmuller, P. G., and Obinger, C. (2003) Total conversion of bifunctional catalase-peroxidase (KatG) to monofunctional peroxidase by exchange of a conserved distal side tyrosine, *Journal of Biological Chemistry 278*, 20185-20191.

91. Bertrand, T., Eady, N. A. J., Jones, J. N., Nagy, J. M., Jamart-Gregoire, B., Raven, E. L., and Brown, K. A. (2004) Crystal structure of Mycobacterium tuberculosis catalase-peroxidase, *Journal of Biological Chemistry 279*, 38991-38999.

92. Carpena, X., Loprasert, S., Mongkolsuk, S., Switala, J., Loewen, P. C., and Fita, I. (2003) Catalase-peroxidase KatG of Burkholderia pseudomallei at 1.7 A resolution, *Journal of Molecular Biology 327*, 475-489.

93. Wada, K., Tada, T., Nakamura, Y., Kinoshita, T., Tamoi, M., Shigeoka, S., and Nishimura, K. (2002) Crystallization and preliminary X-ray diffraction studies of catalase-peroxidase from Synechococcus PCC 7942, *Acta Crystallographica Section D-Biological Crystallography 58*, 157-159.

94. Yamada, Y., Fujiwara, T., Sato, T., Igarashi, N., and Tanaka, N. (2002) The 2.0 angstrom crystal structure of catalase-peroxidase from Haloarcula marismortui, *Nature Structural Biology 9*, 691-695.

95. Regelsberger, G., Jakopitsch, C., Ruker, F., Krois, D., Peschek, G. A., and Obinger, C. (2000) Effect of distal cavity mutations on the formation of compound I in catalase-peroxidases, *Journal of Biological Chemistry 275*, 22854-22861.

96. Hillar, A., Peters, B., Pauls, R., Loboda, A., Zhang, H. M., Mauk, A. G., and Loewen, P. C. (2000) Modulation of the activities of catalase-peroxidase HPI of Escherichia coli by site-directed mutagenesis, *Biochemistry 39*, 5868-5875.

97. Regelsberger, G., Jakopitsch, C., Furtmuller, P. G., Rueker, F., Switala, J., Loewen, P. C., and Obinger, C. (2001) The role of distal tryptophan in the bifunctional activity of catalase-peroxidases, *Biochemical Society Transactions 29*, 99-105.

98. Zamocky, M., Regelsberger, G., Jakopitsch, C., and Obinger, C. (2001) The molecular peculiarities of catalase-peroxidases, *Febs Letters 492*, 177-182.

99. Welinder, K. G. (1991) BACTERIAL CATALASE-PEROXIDASES ARE GENE DUPLICATED MEMBERS OF THE PLANT PEROXIDASE SUPERFAMILY, *Biochimica Et Biophysica Acta 1080*, 215-220.

100. Baker, R. D., Cook, C. O., and Goodwin, D. C. (2006) Catalase-peroxidase active site restructuring by a distant and "inactive" domain, *Biochemistry 45*, 7113-7121.

101. Moore, R. L., Cook, C. O., Williams, R., and Goodwin, D. C. (2008) Substitution of strictly conserved Y111 in catalase-peroxidases: Impact of remote interdomain contacts on active site structure and catalytic performance, *Journal of Inorganic Biochemistry 102*, 1819-1824.

102. Jakopitsch, C., Droghetti, E., Schmuckenschlager, F., Furtmuller, P. G., Smulevich, G., and Obinger, C. (2005) Role of the main access channel of catalase-peroxidase in catalysis, *Journal of Biological Chemistry 280*, 42411-42422.

103. Li, Y. (2005) Roles of two Interhelical Insertions in Catalase-Peroxidase Catalysis: Tracing the Impact of Peripheral Protein Strctures on the Heme Enzyme Function, In *Chemistry and Biochemistry*, Auburn University, Auburn.

104. Vlasits, J., Furtmuller, P. G., Jakopitsch, C., Zamocky, M., and Obinger, C. (2010) Probing hydrogen peroxide oxidation kinetics of wild-type Synechocystis catalase-peroxidase (KatG) and selected variants, *Biochimica Et Biophysica Acta-Proteins and Proteomics 1804*, 799-805.

105. Santoni, E., Jakopitsch, C., Obinger, C., and Smulevich, G. (2004) Comparison between catalase-peroxidase and cytochrome c peroxidase. The role of the hydrogen-bond networks for protein stability and catalysis, *Biochemistry 43*, 5792-5802.

106. Jakopitsch, C., Auer, M., Regelsberger, G., Jantschko, W., Furtmuller, P. G., Ruker, F., and Obinger, C. (2003) Distal site aspartate is essential in the catalase activity of catalase-peroxidases, *Biochemistry 42*, 5292-5300.

107. Jakopitsch, C., Kolarich, D., Petutschnig, G., Furtmuller, P. G., and Obinger, C. (2003) Distal side tryptophan, tyrosine and methionine in catalase-peroxidases are covalently linked in solution, *Febs Letters 552*, 135-140.

108. Ghiladi, R. A., Knudsen, G. M., Medzihradszky, K. F., and de Montellano, P. R. O. (2005) The Met-Tyr-Trp cross-link in Mycobacterium tuberculosis catalase-peroxidase (KatG) - Autocatalytic formation and effect on enzyme catalysis and spectroscopic properties, *Journal of Biological Chemistry 280*, 22651-22663.

109. Ghiladi, R. A., Medzihradszky, K. F., and de Montellano, P. R. O. (2005) Role of the Met-Tyr-Trp cross-link in Mycobacterium tuberculosis catalase-peroxidase (KatG) as revealed by KatG(M255I), *Biochemistry 44*, 15093-15105.

110. Donald, L. J., Krokhin, O. V., Duckworth, H. W., Wiseman, B., Deemagarn, T., Singh, R., Switala, J., Carpena, X., Fita, I., and Loewen, P. C. (2003) Characterization of the catalase-peroxidase KatG from Burkholderia pseudomallei by mass spectrometry, *Journal of Biological Chemistry 278*, 35687-35692.

111. Varnado, C. (2006) ENHANCING EXPRESSION OF RECOMBINANT HEMOPROTEINS: PROGRESS TOWARD UNDERSTANDING STRUCTURE/FUNCTION AND THERAPEUTIC APPLICATION, In *Chemistry and Biochemistry*, Auburn University, Auburn.

112. Ghiladi, R. A., Medzihradszky, K. F., Rusnak, F. M., and de Montellano, P. R. (2005) Correlation between isoniazid resistance and superoxide reactivity in Mycobacterium tuberculosis KatG, *Journal of the American Chemical Society 127*, 13428-13442.

113. Yu, S. W., Girotto, S., Zhao, X. B., and Magliozzo, R. S. (2003) Rapid formation of Compound II and a tyrosyl radical in the Y229F mutant of Mycobacterium tuberculosis

catalase-peroxidase disrupts catalase but not peroxidase function, *Journal of Biological Chemistry 278*, 44121-44127.

114. Jakopitsch, C., Ivancich, A., Schmuckenschlager, F., Wanasinghe, A., Poltl, G., Furtmuller, P. G., Ruker, F., and Obinger, C. (2004) Influence of the unusual covalent adduct on the kinetics and formation of radical intermediates in Synechocystis catalase peroxidase - A stopped-flow and EPR characterization of the MET275, TYR249, and Arg(349) variants, *Journal of Biological Chemistry 279*, 46082-46095.

115. Yu, S. W., Girotto, S., Lee, C., and Magliozzo, R. S. (2003) Reduced afflinity for isoniazid in the S315T mutant of Mycobacterium tuberculosis KatG is a key factor in antibiotic resistance, *Journal of Biological Chemistry 278*, 14769-14775.

116. Santoni, E., Jakopitsch, C., Obinger, C., and Smulevich, G. (2004) Manipulating the covalent link between distal side tryptophan, tyrosine, and methionine in catalase-peroxidases: An electronic absorption and resonance Raman study, *Biopolymers 74*, 46-50.

117. Suarez, J., Ranguelova, K., Jarzecki, A. A., Manzerova, J., Krymov, V., Zhao, X. B., Yu, S. W., Metlitsky, L., Gerfen, G. J., and Magliozzo, R. S. (2009) An Oxyferrous Heme/Protein-based Radical Intermediate Is Catalytically Competent in the Catalase Reaction of Mycobacterium tuberculosis Catalase-Peroxidase (KatG), *Journal of Biological Chemistry 284*, 7017-7029.

118. Sambrook, J. M., and Fritsch, E.F. (1989) *Molecular Cloning: a laboratory manual*, Cold Spring Harbor, NY.

119. Lundberg, K. S., Shoemaker, D. D., Adams, M. W. W., Short, J. M., Sorge, J. A., and Mathur, E. J. (1991) HIGH-FIDELITY AMPLIFICATION USING A THERMOSTABLE DNA-POLYMERASE ISOLATED FROM PYROCOCCUS-FURIOSUS, *Gene 108*, 1-6.

120. Geier, G. E., and Modrich, P. (1979) RECOGNITION SEQUENCE OF THE DAM METHYLASE OF ESCHERICHIA-COLI-K12 AND MODE OF CLEAVAGE OF DPN-I ENDONUCLEASE, *Journal of Biological Chemistry 254*, 1408-1413.

121. Szybalski, W., Kim, S. C., Hasan, N., and Podhajska, A. J. (1991) CLASS-IIS RESTRICTION ENZYMES - A REVIEW, *Gene 100*, 13-26.

122. Novagen. (2003) pET System Manual.

123. Link, A. J., LaBaer, J. (2011) Trichloroacetic acid (TCA) precipitation of proteins, *Cold Spring harbor Protocols 2011*, 993-994.

124. Falk, J. K. (1964) *Porphyrins and Metalloporphyrins*, Elsevier Publishing, New York.

125. Kelly, S. M., Jess, T. J., and Price, N. C. (2005) How to study proteins by circular dichroism, *Biochimica Et Biophysica Acta-Proteins and Proteomics 1751*, 119-139.

126. Gill, S. C., and Vonhippel, P. H. (1989) CALCULATION OF PROTEIN EXTINCTION COEFFICIENTS FROM AMINO-ACID SEQUENCE DATA, *Analytical Biochemistry 182*, 319-326.

127. Sutherland, J. C. (1980) Magnetic Circular Dichroism of Biological Molecules, *Ann. Rev. Biophys. Bioeng. 9*, 293-326.

128. Caldwell, D., Thorne, J.M., and Eyring,H. (1971) Magnetic Circular Dichroism, *Annual Review of Physical Chemistry 22*.

129. Vickery, L., Nozawa, T., and Sauer, K. (1975) Magnetic Circular Dichroism Studies of Myoglobin Complexes. Correlation with Heme Spin State and Axial Ligation, *Journal of American Chemical Socitey 98*, 343-350.

130. Treu, J. I., and Hopfield, J.J. (1975) Magnetic circular dichroism in hemoglobin, *The Journal of Chemical Physics 63*, 613-623.

131. Palmer, G. (1979) Electron Paramagnetic Resonance of Hemoproteins, In *The Porphyrins*, pp 313-353.

132. Hagen, W. R. (2009) *Biomolecular EPR Spectroscopy*, CRC press.

133. Que, L., Jr., (Ed.) (2000) *Physical Methods in Bioinorganic Chemistry, Spectroscopy and Magnetism*, University Science Book, Sausalito, CA.

134. Hagen, W. Biomolecular EPR spectroscopy, Tu Delft.

135. Nelson D.P., K. L. A. (1972) Enthalpy of decomposition of hydrogen peroxide by catalase at 25 degrees C (with molar extinction coefficients of H_2O_2 solutions in the UV), *Analytical Biochemistry 49*, 474-478.

136. Scott, S. L. C. W. J., Bakac A., Espenson, J.H. (1993) Spectroscopic parameters, electrode potentials, acid ionization constants, and electron exchange rates of the 2,2'-azinobis(3-ethylbenzothiazoline-6-sulfonate) radicals and ions, *The Journal of Physical chemistry 97*, 6710-6714.

137. Fersht, A. (1998) *Structure and Mechanism in Protein Science: A guide to Enzyme Catalysis and Protein Folding*, 1st ed., Freeman, W.H. and Company.

138. http://www.hi-techsci.com/techniques/stoppedflow.

139. Goodwin, D. C., Yamazaki, I., Aust, S. D., and Grover, T. A. (1995) DETERMINATION OF RATE CONSTANTS FOR RAPID PEROXIDASE REACTIONS, *Analytical Biochemistry 231*, 333-338.

140. Bray, R. C. (1961) Sudden Freezing as a Technique for the Study of Rapid Reactions

Biochemical Journal 81, 189-193.

141. Bray, R. C., and Pettersson, R. (1961) Electron-Spin-Resonance Measurements, *Biochemical Journal 81*.

142. Chouchane, S., Lippai, I., and Magliozzo, R. S. (2000) Catalase-peroxidase (Mycobacterium tuberculosis tuberculosis KatG) catalysis and isoniazid activation, *Biochemistry 39*, 9975-9983.

143. Deemagarn, T., Wiseman, B., Carpena, X., Ivancich, A., Fita, I., and Loewen, P. C. (2007) Two alternative substrate paths for compound I formation and reduction in catalase-peroxidase KatG from Burkholderia pseudomallei, *Proteins-Structure Function and Bioinformatics 66*, 219-228.

144. Jakopitsch, C., Vlasits, J., Wiseman, B., Loewen, P. C., and Obinger, C. (2007) Redox intermediates in the catalase cycle of catalase-peroxidases from Synechocystis PCC 6803, Burkholderia pseudomallei, and Mycobacterium tuberculosis, *Biochemistry 46*, 1183-1193.

145. Chouchane, S., Girotto, S., Yu, S. W., and Magliozzo, R. S. (2002) Identification and characterization of tyrosyl radical formation in Mycobacterium tuberculosis catalase-peroxidase (KatG), *Journal of Biological Chemistry 277*, 42633-42638.

146. Wengenack, N. L., Jensen, M. P., Rusnak, F., and Stern, M. K. (1999) Mycobacterium tuberculosis KatG is a peroxynitritase, *Biochemical and Biophysical Research Communications 256*, 485-487.

147. Zhang, Y., Heym, B., Allen, B., Young, D., and Cole, S. (1992) THE CATALASE PEROXIDASE GENE AND ISONIAZID RESISTANCE OF MYCOBACTERIUM-TUBERCULOSIS, *Nature 358*, 591-593.

148. Hazbon, M. H., Brimacombe, M., del Valle, M. B., Cavatore, M., Guerrero, M. I., Varma-Basil, M., Billman-Jacobe, H., Lavender, C., Fyfe, J., Garcia-Garcia, L., Leon, C. I., Bose, M., Chaves, F., Murray, M., Eisenach, K. D., Sifuentes-Osornio, J., Cave, M. D., de Leon, A. P., and Alland, D. (2006) Population genetics study of isoniazid resistance mutations and evolution of multidrug-resistant Mycobactetium tuberculosis, *Antimicrobial Agents and Chemotherapy 50*, 2640-2649.

149. van Soolingen, D., de Haas, P. E. W., van Doorn, H. R., Kuijper, E., Rinder, H., and Borgdorff, M. W. (2000) Mutations at amino acid position 315 of the katG gene are associated with high-level resistance to isoniazid, other drug resistance, and successful transmission of Mycobacterium tuberculosis in The Netherlands, *Journal of Infectious Diseases 182*, 1788-1790.

150. Mokrousov, I., Narvskaya, O., Otten, T., Limeschenko, E., Steklova, L., and Vyshnevskiy, B. (2002) High prevalence of KatG Ser315Thr substitution among isoniazid-resistant Mycobacterium tuberculosis clinical isolates from northwestern Russia, 1996 to 2001, *Antimicrobial Agents and Chemotherapy 46*, 1417-1424.

151. Mokrousov, I., Otten, T., Filipenko, M., Vyazovaya, A., Chrapov, E., Limeschenko, E., Steklova, L., Vyshnevskiy, B., and Narvskaya, O. (2002) Detection of isoniazid-resistant Mycobacterium tuberculosis strains by a multiplex allele-specific PCR assay targeting katG codon 315 variation, *Journal of Clinical Microbiology 40*, 2509-2512.

152. Leung, E. T. Y., Kam, K. M., Chiu, A., Ho, P. L., Seto, W. H., Yuen, K. Y., and Yam, W. C. (2003) Detection of katG Ser315Thr substitution in respiratory specimens from patients with isoniazid-resistant Mycobacterium tuberculosis using PCR-RFLP, *Journal of Medical Microbiology 52*, 999-1003.

153. Arnao, M. B., Acosta, M., Delrio, J. A., and Garciacanovas, F. (1990) INACTIVATION OF PEROXIDASE BY HYDROGEN-PEROXIDE AND ITS PROTECTION BY A REDUCTANT AGENT, *Biochimica Et Biophysica Acta 1038*, 85-89.

154. Arnao, M. B., Acosta, M., Delrio, J. A., Varon, R., and Garciacanovas, F. (1990) A KINETIC-STUDY ON THE SUICIDE INACTIVATION OF PEROXIDASE BY HYDROGEN-PEROXIDE, *Biochimica Et Biophysica Acta 1041*, 43-47.

155. Baynton, K. J., Bewtra, J. K., Biswas, N., and Taylor, K. E. (1994) INACTIVATION OF HORSERADISH-PEROXIDASE BY PHENOL AND HYDROGEN-PEROXIDE - A KINETIC INVESTIGATION, *Biochimica Et Biophysica Acta-Protein Structure and Molecular Enzymology 1206*, 272-278.

156. Hiner, A. N. P., Rodriguez-Lopez, J. N., Arnao, M. B., Raven, E. L., Garcia-Canovas, F., and Acosta, M. (2000) Kinetic study of the inactivation of ascorbate peroxidase by hydrogen peroxide, *Biochemical Journal 348*, 321-328.

157. Singh, R., Wiseman, B., Deemagarn, T., Jha, V., Switala, J., and Loewen, P. C. (2008) Comparative study of catalase-peroxidases (KatGs), *Archives of Biochemistry and Biophysics 471*, 207-214.

158. Carpena, X., Melik-Adamyan, W., Loewen, P. C., and Fita, I. (2004) Structure of the C-terminal domain of the catalase-peroxidase KatG from Escherichia coli, *Acta Crystallographica Section D-Biological Crystallography 60*, 1824-1832.

159. Zhao, X. B., Yu, S. W., Ranguelova, K., Suarez, J., Metlitsky, L., Schelvis, J. P. M., and Magliozzo, R. S. (2009) Role of the Oxyferrous Heme Intermediate and Distal Side Adduct Radical in the Catalase Activity of Mycobacterium tuberculosis KatG Revealed by the W107F Mutant, *Journal of Biological Chemistry 284*, 7030-7037.

160. Regelsberger, G., Jakopitsch, C., Engleder, M., Ruker, F., Peschek, G. A., and Obinger, C. (1999) Spectral and kinetic studies of the oxidation of monosubstituted phenols and anilines by recombinant Synechocystis catalase - Peroxidase compound I, *Biochemistry 38*, 10480-10488.

161. Zamocky, M., Herzog, C., Nykyri, L. M., and Koller, F. (1995) SITE-DIRECTED MUTAGENESIS OF THE LOWER PARTS OF THE MAJOR SUBSTRATE CHANNEL OF YEAST CATALASE-A LEADS TO HIGHLY INCREASED PEROXIDATIC ACTIVITY, *Febs Letters 367*, 241-245.

162. Cade, C. E., Dlouhy, A. C., Medzihradszky, K. F., Salas-Castillo, S. P., and Ghiladi, R. A. (2010) Isioniazid-resistance conferring mutations in Mycobacterium tuberculosis KatG: Catalase, peroxidase, and INH-NADH adduct formation activities, *Protein Science 19*, 458-474.

163. Zamocky, M., Furtmuller, P. G., and Obinger, C. (2010) Evolution of structure and function of Class I peroxidases, *Archives of Biochemistry and Biophysics 500*, 45-57.

164. Larkin, M. A., Blackshields, G., Brown, N. P., Chenna, R., McGettigan, P. A., McWilliam, H., Valentin, F., Wallace, I. M., Wilm, A., Lopez, R., Thompson, J. D., Gibson, T. J., and Higgins, D. G. (2007) Clustal W and clustal X version 2.0, *Bioinformatics 23*, 2947-2948.

165. Thompson, J. D., Gibson, T. J., Plewniak, F., Jeanmougin, F., and Higgins, D. G. (1997) The CLUSTAL_X windows interface: flexible strategies for multiple sequence alignment aided by quality analysis tools, *Nucleic Acids Research 25*, 4876-4882.

166. Apweiler, R., Martin, M. J., O'Donovan, C., Magrane, M., Alam-Faruque, Y., Antunes, R., Barrell, D., Bely, B., Bingley, M., Binns, D., Bower, L., Browne, P., Chan, W. M., Dimmer, E., Eberhardt, R., Fazzini, F., Fedotov, A., Foulger, R., Garavelli, J., Castro, L. G., Huntley, R., Jacobsen, J., Kleen, M., Laiho, K., Legge, D., Lin, Q. A., Liu, W. D., Luo, J., Orchard, S., Patient, S., Pichler, K., Poggioli, D., Pontikos, N., Pruess, M., Rosanoff, S., Sawford, T., Sehra, H., Turner, E., Corbett, M., Donnelly, M., van Rensburg, P., Xenarios, I., Bougueleret, L., Auchincloss, A., Argoud-Puy, G., Axelsen, K., Bairoch, A., Baratin, D., Blatter, M. C., Boeckmann, B., Bolleman, J., Bollondi, L., Boutet, E., Quintaje, S. B., Breuza, L., Bridge, A., deCastro, E., Coudert, E., Cusin, I., Doche, M., Dornevil, D., Duvaud, S., Estreicher, A., Famiglietti, L., Feuermann, M., Gehant, S., Ferro, S., Gasteiger, E., Gateau, A., Gerritsen, V., Gos, A., Gruaz-Gumowski, N., Hinz, U., Hulo, C., Hulo, N., James, J., Jimenez, S., Jungo, F., Kappler, T., Keller, G., Lara, V., Lemereier, P., Lieberherr, D., Martin, X., Masson, P., Moinat, M., Morgat, A., Paesano, S., Pedruzzi, I., Pilbout, S., Poux, S., Pozzato, M., Redaschi, N., Rivoire, C., Roechert, B., Schneider, M., Sigrist, C., Sonesson, K., Staehli, S., Stanley, E., Stutz, A., Sundaram, S., Tognolli, M., Verbregue, L., Veuthey, A. L., Wu, C. H., Arighi, C. N., Arminski, L., Barker, W. C., Chen, C. M., Chen, Y. X., Dubey, P., Huang, H. Z., Mazumder, R., McGarvey, P., Natale, D. A., Natarajan, T. G., Nchoutmboube, J.,

Roberts, N. V., Suzek, B. E., Ugochukwu, U., Vinayaka, C. R., Wang, Q. H., Wang, Y. Q., Yeh, L. S., Zhang, J. A., and UniProt, C. (2011) Ongoing and future developments at the Universal Protein Resource, *Nucleic Acids Research 39*, D214-D219.

167. Jain, E., Bairoch, A., Duvaud, S., Phan, I., Redaschi, N., Suzek, B. E., Martin, M. J., McGarvey, P., and Gasteiger, E. (2009) Infrastructure for the life sciences: design and implementation of the UniProt website, *Bmc Bioinformatics 10*.

168. Pond, A. E., Sono, M., Elenkova, E. A., Goodin, D. B., English, A. M., and Dawson, J. H. (1999) Influence of protein environment on magnetic circular dichroism spectral properties of ferric and ferrous ligand complexes of yeast cytochrome c peroxidase, *Biospectroscopy 5*, S42-S52.

169. Pond, A. E., Sono, M., Elenkova, E. A., McRee, D. E., Goodin, D. B., English, A. M., and Dawson, J. H. (1999) Magnetic circular dichroism studies of the active site heme coordination sphere of exogenous ligand-free ferric cytochrome c peroxidase from yeast: effects of sample history and pH, *Journal of Inorganic Biochemistry 76*, 165-174.

170. Wiseman, B., Colin, J., Smith, A. T., Ivancich, A., and Loewen, P. C. (2009) Mechanistic insight into the initiation step of the reaction of Burkholderia pseudomallei catalase-peroxidase with peroxyacetic acid, *Journal of Biological Inorganic Chemistry 14*, 801-811.

171. Zamocky, M., Furtmuller, P. G., and Obinger, C. (2008) Evolution of catalases from bacteria to humans, *Antioxidants & Redox Signaling 10*, 1527-1547.

172. Vlasits, J., Bellei, M., Jakopitsch, C., De Rienzo, F., Furtmuller, P. G., Zamocky, M., Sola, M., Battistuzzi, G., and Obinger, C. (2010) Disruption of the H-bond network in the main access channel of catalase-peroxidase modulates enthalpy and entropy of Fe(III) reduction, *Journal of Inorganic Biochemistry 104*, 648-656.

173. Derat, E., Shaik, S., Rovira, C., Vidossich, P., and Alfonso-Prito, M. (2007) The effect of a water molecule on the mechanism of formation of compound 0 in horseradish peroxidase, *J. Am. Chem. Soc. 129*, 6346.